GEOCHEMISTRY OF ARSENIC IN MAGMATIC SYSTEMS WITH SOME RESULTS FOR ANTIMONY

by

Bryan J. Maciag

Submitted in partial fulfillment of the requirements
for the degree of Doctor of Philosophy

at

Dalhousie University
Halifax, Nova Scotia
August 2022

To Mom, Dad, and beer, without you this would not have been possible.

TABLE OF CONTENTS

LIST OF TABLES

LIST OF FIGURES

ABSTRACT

This thesis reports on the results of high-temperature experiments and detailed chemical analysis of natural samples that assess the oxidation state of As and Sb, and the distribution of As in the solidification products of felsic magmas.

In the first study of this thesis, X-ray absorption near edge structure (XANES) determined that As and Sb are predominantly in the trivalent state in basaltic glasses synthesized at 1200°C, 0.1 MPa, and oxygen fugacity (fO_2) of FMQ -3.3 to +5.7 (FMQ is the Fayalite-Magnetite-Quartz redox buffer). Additionally, extended X-ray absorption fine structures spectroscopy (EXAFS) revealed that the configuration of both elements is $Me^{III}O_3E$ trigonal pyramids (Me = metal; E is the lone pair of electrons). As trivalent As and Sb are a poor match for most major elements based on charge and ionic radius, common rock-forming minerals will reject these metalloids during crystallization.

The second study of this thesis explores the unexpected enrichment of As in apatite observed in a number of felsic plutonic rock suites. Piston-cylinder experiments were used to measure apatite/melt partitioning and speciation of As in a range of felsic melt compositions at 900-1050°C, 0.75 GPa, and FMQ -0.4 to +7.5. Results indicate that As is incompatible in apatite, except at extraordinarily high fO_2. Arsenic-enriched apatite could form from melts after protracted crystallization generates high As levels. Combining the experimental results with crystallization models shows that this process is consistent with the enrichment of incompatible trace elements observed in apatites from the South Mountain Batholith, Nova Scotia.

The final study of this thesis determined the geogenic sources of As contamination in groundwater from granitic bedrock terranes in southwestern Nova Scotia. Trace element analysis of the major and accessory minerals from representative bedrock samples and calculation of mineral stability were used to assess the lability of As at near-surface conditions. Pyrite and cordierite are phases with elevated As concentrations and oxidation (pyrite), or dissolution (cordierite) of these phases could release As into the groundwater. This process is consistent with the occurrence of high As concentrations in groundwater associated with cordierite and oxidized pyrite-bearing granitic bedrock. The best predictor of elevated As in groundwater is a combination of the identity and low-temperature stability of the As host minerals and secondary factors such as the permeability of the sample.

Collectively, these three studies show that As is likely incompatible in most phases that crystallize from both felsic and mafic magmas over the known range of terrestrial redox conditions. The highest As concentrations will therefore be associated with the most evolved melts and produce the most As-enriched minerals. If these minerals are unstable at low-temperature conditions, then they will become geogenic sources of As contamination after the igneous rocks are brought to the surface by erosion and uplift.

LIST OF ABBREVIATIONS AND SYMBOLS USED

a_i	activity of phase i
a.u.	arbitrary units
Al	aluminosilicates
ALK	peralkaline
Ap	apatite
As^{III}	trivalent As
As^{V}	pentavalent As
APS	Advanced Photon Source
ASI	Alumina Saturation Index
ARD	acid rock drainage
$B_{Mineral}$	mass fraction of the mineral in the crystallizing assemblage
BSE	backscattered electron image
BGD	biotite granodiorite
Bi	biotite
BMG	biotite monzogranite
BT	biotite tonalite
C_i	concentration in phase i
C_l	melt concentration after crystallization,
C_0	initial melt composition
CG	coarse grained (>2 mm)
Chl	chlorite
CLS	Canadian Light Source
CMAS	$CaO\text{-}MgO\text{-}Al_2O_3\text{-}SiO_2$
cm^{-1}	per centimeter
cm^3	centimeter cubed
CN	coordination number
Crd	cordierite
Crd-Alt	altered cordierite
Cpy	chalcopyrite

CSEG	Canadian Society of Economic Geologists
$D^{\text{Apatite/Whole-rock}}$	apatite/whole-rock partition coefficient
$D^{\text{Apatite/Melt}}$	apatite/melt partition coefficient
$D_{\text{As(V)}}$	As^{V} apatite/melt partition coefficient
$D_{\text{As(III)}}$	As^{III} apatite/melt partition coefficient
D^{Bulk}	bulk partition coefficient
$D^{\text{Cpx/melt}}$	clinopyroxene/melt partition coefficients
$D^{\text{Mineral/Melt}}$	partition coefficient between the mineral and the melt.
dG	change in Gibbs free energy
dP	change in pressure
DNRR	Nova Scotia Department of Natural Resources and Renewables
DOE	Department of Energy
E	energy
E^0	standard cell voltage
e^-	electron
Eh	redox potential
EDS	energy dispersive spectroscopy
Ep	epidote
EPMA	electron probe microanalyzer
EXAFS	extended X-ray absorption fine structures
eV	electron volts
F	fraction of liquid remaining
f	fugacity
$\mathscr{F}$	Faraday constant
FG	fine grained (<1 mm)
FMQ	fayalite- magnetite-quartz buffer
fO_2	oxygen fugacity
FOH	ferric oxide and hydroxides
fS_2,	sulfur fugacity
FT-IR	Fourier transform infrared spectroscopy
g	grams

g/cm^3	grams per centimeter cubed
Gl	glass
GPa	gigapascal
GSA	Geological Society of America
H	entropy
h	hours
HERC	Health and Environments Research Centre
HP	Halifax Pluton
HREE	heavy rare earth elements
HXMA	Hard X-ray Micro-Analysis
I	X-ray intensity
I_0	incident X-ray intensity
IAB	island arc basalt
IR	ionic radius
J/cm^2	joules per centimeter squared
K	degrees Kelvin
k	wave number
K_{eq}	equilibrium constant
K’	effective equilibrium constant
kJ/mol	kilojoule per mole
kV	kilovolts
LA-ICP-MS	laser ablation inductively coupled plasma mass spectrometry
LFB	Lachlan Fold Belt, Australia
LMG	leucomonzogranite
LOD	limit of detection
LREE	light rare earth elements
M^i_x	mass of element x in phase i
m^i	mass of the phase i
Ma	million years
MAC	maximum acceptable concentration
MAL	metaluminous

MB	Musquodoboit Batholith, Nova Scotia, Canada
MBMG	muscovite biotite monzogranite
MBT	muscovite biotite tonalite
Me	either As or Sb
MG	medium grained (1-2mm)
mg	milligram
mm	millimeters
mol/kg	moles per kilogram
MORB	mid-ocean ridge basalts
MPa	megapascal
MREE	middle rare earth elements
Ms	muscovite
Mz	monazite
n	number of electrons transferred
N	count/number of analyses
nA	nanoamps
NBO/T	non-bridging oxygen over tetrahedral cations
Nd:YAG	neodymium doped yttrium alumina garnet
NIST	National Institute of Standards and Technology
nm	nanometer
NSERC	Natural Sciences and Engineering Research Council of Canada
OIB	ocean island basalt
P	pressure
PAL	peraluminous
PGE	platinum group element
pH	power of hydrogen
PMP	Port Mouton Pluton, Nova Scotia, Canada
Pn	pinite
Py	pyrite
R	gas constant
$R^{glass/Vapour}$	volume ratio of glass to vapor

REE	rare earth element
S	enthalpy
s	seconds
S_o^2	amplitude reduction factor
Sb^{III}	trivalent Sb
Sb^{V}	pentavalent Sb
SMB	South Mountain Batholith, Nova Scotia, Canada
SI	supplementary information
t	sample thickness
T	temperature
U	measured value for calculating statistical tests
VESPERS	Very Sensitive Elemental and Structural Probe Employing Radiation from a Synchrotron
Vp	vapor
wt.%	weight precent
X_i	mole fraction of phase i
XANES	X-ray absorption near edge structures
XAS	X-ray absorption spectroscopy
XPS	X-ray photoelectron spectroscopy
XRD	X-ray diffraction spectroscopy
XRF	X-ray fluorescence
Y	value of modelled data for statistical tests
y	charge of Me
ZAF	atomic number-absorption effect-fluorescence excitation
Zr	zircon
Å	angstroms
$Å^{-1}$	per angstrom
°C	degrees Celsius
$\Delta_r G^o$	Gibbs free energy of the reaction at the standard state
$\Delta_r H^o_{298}$	change in enthalpy of the reaction at 298K
$\Delta_r S^o_{298}$	change in entropy of the reaction at 298K

ΔFMQ	log deviation from the FMB buffer
g_i	fugacity/activity coefficient of i
Γ	activity factor (reaction production ratio of activity coefficients)
μ	absorption coefficient.
μg/g	microgram per gram
μg/L	micrograms per liter
μm	micrometers
ρ^i	density of phase i
Ψ	melt molar (Al/(Na+K))
σ	Standard deviation
σ^2	mean square relative displacement
χ^2	chi squared
$\forall^i$	volume of phase i

ACKNOWLEDGEMENTS

Doing a Ph.D. is like an epic fantasy quest. There are hundreds of characters who make the story possible. First and foremost, I would like to thank James Brenan, the mentor of this adventure. The journey was long, but I could not have made it to the end without your unflinching support and ruthless criticism. Thank you for giving me this opportunity and letting to carry out my research the way I wanted to without regard for money. I appreciate you always being there to drag me backdown to reality when I reached too far (like thinking I could study As, Sb, Bi, and N). Also thank you for not shouting at me when I would interrupt you at your office, broke all your blue chairs (I think it's a design flaw) or when I nearly burnt down the LSC.

A special thanks to the council of elders, Mike and Yana, who oversaw this quest. The discussions with you on the approach, direction and implications of my research over the years were invaluable. You were right, doing a third experimental project would have been a bad idea. I would like to thank the organizations who provided me with resources on this quest: the Society of Economic Geologists, the Geological Society of America the Canadian Light Source and the Mineralogical Association of Canada.

My quest took an exciting turn when I had the opportunity to pursue research at a synchrotron. I would like to thank the Canadian Light Source and the Advanced Photon Source for that experience. My time at the beamlines would not have been possible or as smooth without the support and guidance of the beamline scientists Ning Chen, Peter Blanchard, Renfei Feng, Zou Finfrock, and Debroa Motta Meira. I also would like to thank David Morris and Dr. Peng Zhang at Dalhousie University for helping me get a handle on how to process the results.

A hero needs tools to complete their quest. I am thankful for the assistance provided by Erin Keltie, Dan MacDonald and James Brenan for their support in the LA-ICP-MS, EMPA and experimental labs respectively. I would also like to thank Norma and Darlene, for being patient with me when I would constantly pop by the main office looking for James. Also thank you, Norma, for getting me reimbursed and for the help with all the invoices, without you I'm sure there would be a bounty on my head.

A hero must be expected to enter unknown waters on their journey. I want to thank Gavin Kennedy, Mike Parsons, Anne-Marie Ryan and Neal Sullivan for helping a

high-temperature geochemist understand something about environmental geochemistry and groundwater.

No hero travels alone. Thanks to each traveller who walked beside me, even briefly. I especially want to thank Ana who walked beside me and push me towards the end of this journey from day one, Sean for coffee and beer side quests, and my fellow experimentalists Erin, Kate and Tashi who would meet with me at the local tavern to commiserate over failed experiments.

The last years would have been different if not for the friendly Ettin Lexie-Chris. Discussions with you two on geochemistry and GIS were invaluable, even if one of your heads has the wrong opinions on statistics. I am thankful for your support in and outside of science. The many lunches and coffee break these last 6 years made the time fly by. I will miss the pedantry.

The end of this quest was a particular hard mountain to climb. A special thanks to James, Lexie, and my companion Claire for dropping everything and hauling me up the mountain to the end.

Chapter 1

INTRODUCTION

Elements that are present at the trace level, here loosely defined as less than 10,000 μg/g, offer a unique window on a variety of geochemical processes, as their distribution is independent of phase stoichiometry. Instead, thermodynamically defined partitioning relationships control the allocation of these so-called trace elements. The phases that trace elements prefer to occupy define their geochemical affinities, which include atmophile, lithophile, chalcophile or siderophile (Goldschmidt, 1954). The use of trace elements to understand high- and low-temperature geochemical processes is far-ranging: from research into planetary differentiation to identifying geogenic sources of groundwater contamination. Trace elements with multiple oxidation states are a particularly interesting subgroup as their geochemical properties, including ionic radii, charge, and coordination environment may shift depending on the redox conditions of the system. The combination of the oxidation state and the nature of the binding ligands define a geochemical species. In some cases, the inventory of a particular trace element within a sample may comprise multiple species, resulting in diverse geochemical behavior. Hence, the chemical characteristics and relative abundance of each species are essential to the accurate interpretation of trace element behavior. A number of intensive variables may control the abundance of species, or speciation, with the most important at conditions of magma formation and differentiation being temperature and the fugacities of oxygen and sulfur (fO_2 and fS_2, respectively).

Amongst the more geochemically complex group of elements are the metalloids, defined by their transitional electronic properties between metals and non-metals. This group of elements has the propensity to form both anions and cations and a potentially wide range of oxidation states. Within this group are the elements As and Sb, typically present at trace levels in natural systems. The behavior of these two metalloids related to high-temperature magmatic processes is not well-studied; however, As and Sb exhibit chalcophile, lithophile and even siderophile tendencies (Goldschmidt, 1954), likely dictated by the prevailing fO_2 and fS_2 conditions (see Chapter 2, section 2.1). Therefore, interpreting the natural variation of As and Sb abundances more fully in igneous rocks requires information on which chemical states, or speciation, exist for a specific range of conditions. The major focus of this thesis is to provide such information through calibration by high temperature laboratory experiments in which the relevant intensive parameters can be varied in a systematic way. Emphasis is on the behavior of As, with more limited results for Sb as the lower natural abundances of Sb limit the data available for interpretation. This thesis also documents the distribution and groundwater lability of As in the solidification products of a felsic plutonic magma; thus, linking the knowledge of igneous partitioning with environmental mobility.

Chapter 2 provides the necessary background information to aid in the understanding and interpretation of this thesis. Information is provided on the general geochemical properties of As and Sb, background on the concept of oxygen fugacity, the geochemistry of apatite, as well as the physical basis for the spectroscopic methods employed to assess the speciation of As and Sb.

Chapter 2

BACKGROUND

2.1. Geochemistry of Arsenic and Antimony

2.1.1. Chemical Properties and Abundances

Arsenic, Sb, Bi, P and N are collectively called the "pnictogens" and occupy Group 15 on the periodic table. Pnictogens have three stable electron configurations for ionic bonding (+III or +V cations or as a -III anion). Other nominal charges are possible through covalent bonding. As both As and Sb are metalloids they will behave as either metals or non-metals depending on the system conditions. A summary of the oxidation states and ionic radii for As and Sb is provided in Table 2.1.

The concentration of As and Sb in most geochemical reservoirs is low (Table 2.2), but these elements can be enriched in sedimentary rocks, particularly shales (As: 100 µg/g; Sb: 15 µg/g; Ketris and Yudovich, 2009). Additionaly, the concentration of these metalloids in the mantle (As: 0.07 µg/g, Sb: 0.01 µg/g; Palme and O'Neill, 2003) is 1-2 orders of magnitude lower than in the crust (As: 2.5 µg/g; Sb: 0.2 µg/g; Rudnick and Gao, 2003), suggesting that As and Sb behaved incompatibly during crust-mantle fractionation. Arsenic also has an affinity for PGE, with immiscible arsenide-melts preferentially sequestering Pt, Rh, and Ir over to the co-existing sulfide-melt (Gervilla et al. 1996; Hanley 2007; Helmy et al. 2013; Piña et al. 2015; Bai et al. 2017). Arsneic and PGEs can form PGE-arsenides that may segregate from the base metal sulfides like at the Serranía de Ronda deposit, Spain (Piña et al. 2015) or form early sperrylite [$PtAs_2$] like at the Monts de Cristal complex, Gabon (Maier et al. 2015).

Table 2.1 Ionic charge and radii of As and Sb

	Charge	Ionic Radii (Å)	Reference
Arsenic	5+ (6-fold)	0.46	(Shannon, 1976)
	5+ (4-fold)	0.335	(Shannon, 1976)
	3+ (6-fold	0.58	(Shannon, 1976)
	3+ (3-fold)	0.42*	(Shannon, 1976; Soignard et al., 2008)
	0	1.48	(Railsback, 2003)
	3-	2.22	(Railsback, 2003)
Antimony	5+ (6-fold)	0.6	(Shannon, 1976)
	3+ (4-fold)	0.76	(Shannon, 1976)
	3+ (5-fold)	0.8	(Shannon, 1976)
	3+ (6-fold)	0.76	(Shannon, 1976)
	0	1.61	(Railsback, 2003)
	3-	2.45	(Railsback, 2003)

**Calculated as As-O bond length -IR of oxygen in 3-fold coordination (1.38Å)*

Table 2.2 Concentrations of As and Sb in select geochemical reservoirs

Reservoir	Arsenic concentration (μg/g)	Antimony concentration (μg/g)	Reference
CI Chondrite	1.85	0.14	(McDonough and Sun, 1995)
Bulk Silicate Earth	0.05	0.0055	(McDonough and Sun, 1995)
Primitive Mantle	0.066	0.012	(Jochum and Hofmann, 1997; Palme and O'Neill, 2003)
Average Crust	2.5	0.2	(Rudnick and Gao, 2003)
Upper Crust	4.8	0.4	(Rudnick and Gao, 2003)
Mid-ocean Ridge Basalt	0.20	0.02	(Jochum and Hofmann, 1997; Jenner and O'Neill, 2012)
Ocean Island Basalt	0.46	0.2	(Jochum and Hofmann, 1997; Jenner and O'Neill, 2012)
Granite	0.77	0.13	(Gao et al., 1998)
Felsic Volcanics	4.53	0.3	(Gao et al., 1998)
Black Shale	30	5	(Ketris and Yudovich, 2009)

2.1.2. Speciation and Partitioning at the Magmatic Stage

Limited quantitative data is currently available on the speciation of As and Sb in silicate melts that is applicable to terrestrial magmatic systems. Although model dependent, the oxidation state of As and Sb has been inferred from studies of interphase partitioning between sulfide and silicate melt (Li and Audétat, 2012, 2015; Kiseeva and Wood, 2013, 2015), rutile and silicate melt (Klemme et al., 2005) and metal and silicate melt (Righter et al., 2009; Siebert et al., 2011).

Direct measurements of speciation for As are limited to the studies of: Borisova et al. (2010), who determined that As has the form of $As^{III}(OH)_3$ in a natural peraluminous rhyolite glass using X-ray near-edge structures (XANES) and extended X-ray absorption fine structures (EXAFS); Canali et al. (2017), who used XANES to determine that As is only in the III+ oxidation state in synthetic basaltic melts at 1200°C, 0.1 MPa over the range of redox conditions found in terrestrial systems; and Guo (2008), who used X-ray photoelectron spectroscopy to determine that As is As^{III} in synthetic hydrous granitic glasses produced at 800°C and 200 MPa. Antimony speciation in silicate melts was studied in Fe-free basaltic analogues, where the oxidation state was found to be Sb^{III} over the terrestrial range of redox conditions (Miller et al.,2019). Chapter 3, Table 3.5 provides a full summary of the studies done to measure the speciation of As and Sb in silicate melts.

In addition to the past work on speciation, other aspects of the high-temperature geochemistry of As and Sb include studies of the partitioning amongst melts, vapor and coexisting crystalline phases. Guo (2008) measured vapor-granitic melt partitioning in experiments done at 800°C and 200 MPa and determined a value of ~1 for As, which is insensitive to changes in melt composition, while the partition coefficient for Sb increases from 0.1 to 1.3 as the melt alumina saturation index increases from 0.65 to 1.31. A similar partition coefficient for As between low salinity vapor and rhyolite melt was obtained by Simon et al. (2007) from experiments done at 800°C, 120 MPa, with a ~2-fold increase in the partition coefficient with the addition of 0.7 molar sulfur to the vapor. Experimentally-determined vapor/basaltic melt partition coefficients reported by Guo and Audétat (2017) are between 0.8 and 6 (As) and 0.1 and 3 (Sb), for experiments done at 850°C, 200 MPa. D'Souza and Canil (2018) found that the As and Sb partition coefficients between fluid and a sediment melt are 2.5 ± 1.7 and 12 ± 5.1, in sulfate saturated systems. Augmenting these experimental partitioning studies is the work of Zajacz et al. (2008) who measured the As and Sb content of coexisting melt and vapor inclusions trapped in pegmatite quartz crystals. Vapor/melt partition coefficients inferred from the inclusion pairs are 0.2-15 (As) and 1-10 (Sb). Partition coefficients for low salinity vapors decrease with increasing chlorinity, consistent with As and Sb forming hydroxy complexes in the vapor phase. However, in extremely chlorine-rich brines (>12 mol/kg Cl) the brine/melt partition coefficients increase to over 20, likely due to the formation of hydroxy-chloride complexes.

In terms of the chalcophile behavior of As and Sb, sulfide melt/silicate partition coefficients range from 20 to 50 (As) and 10 to 30 (Sb), from experiments done at 1.5 GPa and 1200°C, with values decreasing with silicate melt FeO content and temperature (Li and Audétat, 2012, 2015). Kiseeva and Wood (2013) report a somewhat greater, but overlapping, range of values for Sb (4 to 100) from experiments done at 1.5 GPa and 1400°C, with a similar dependence on melt FeO content. In terms of partitioning between crystalline sulfide (monosulfide solid solution) and sulfide melt, As and Sb are more strongly partitioned into sulfide liquid relative to monosulfide solid solution, with values for sulfide melt/ monosulfide solid solution partitioning of 10-20 (As) and 50-200 (Sb) (Li and Audétat 2015). Arsenic and Sb also exhibit siderophile behavior at reducing conditions, with Fe-Ni metal/silicate melt partition coefficients of ~100 to ~60,000 reported by Siebert et al. (2011) and Righter et al. (2009) over the P-T range of 1-3 GPa and 1500-2600°C and FMQ-1.5 to -12.

The lithophile behavior of As and Sb is observed by their dissolution into accessory minerals commonly associated with igneous rocks. For example, Klemme et al. (2005) report rutile/melt partition coefficients for Sb of 0.2 to 2, from experiments done at 1250-1300°C, 0.1 MPa, FMQ-3 to +7. The oxidized arsenate [$As^{V}O_4^{3-}$] species can readily substitute for phosphate [$P^{V}O_4^{3-}$], allowing the incorporation of As into phosphate minerals such as apatite [$Ca_{10}(PO_4)_6F_2$], monazite [$CePO_4$] and xenotime [YPO_4] (Pan and Fleet, 2002; Majzlan et al., 2014). Experimentally-determined partition coefficients for As between monazite and rhyolitic melt at 100-500 MPa and 750-1200°C are between 60 and 100 (Stepanov et al., 2012). Although no direct measurements of apatite/melt partitioning for As exist, empirical estimates have been reported from apatite/whole-rock ratios for granites from the Lachlan Fold Belt, Australia (Sha and Chappell, 1999). Median values determined in this way are ~1 for S-type granites, and 14 for I-type granites. The difference in partitioning was attributed to the more oxidized nature of the I-type compared to the S-type occurrences.

2.1.3. Controls on Arsenic Mobility in Groundwaters

Both the mobility and toxicity of As in surface and groundwater are a function of its chemical form, with trivalent As being significantly more toxic than pentavalent As (National Research Council, 1977; Stoeppler, 1992; Jain and Ali, 2000). A number of studies have found that the speciation of As in aqueous systems is strongly dependent on the pH and redox conditions of the system with both trivalent and pentavalent As species being present as oxyanions (Bowell et al., 2014). The release of As into groundwater is primarily attributed to four mechanisms: 1) sulfide oxidation, 2) geothermal input, 3) alkali desorption from Fe-oxides, and 4) reductive dissolution of Fe-oxide phases (Nickson et al., 2000; Smedley and Kinniburgh, 2002; Ravenscroft et al., 2011; Ali et al., 2018). Mechanisms 3 and 4 incorporate the desorption of As oxyanions from Fe, Al, and Mn oxides, thus the sorption behavior of As is critical to understanding groundwater contamination. Arsenic will readily desorb from Fe-oxides if there is: 1) a shift to high pH at oxidizing conditions, 2) reduction, 3) a decrease in the surface area of the oxide mineral, 4) the complete dissolution of the oxide host, or 5) changes in As speciation due to microbial activity (Smedley and Kinniburgh, 2002; Dixit and Hering, 2003; Ohtsuka et al., 2013; Chen et al., 2017). The sorption strength of As^{III} and As^{V} is strongly dependent on the solution composition and the nature of the oxide substrate. In general, As^{III} is sorbed similarly or stronger than As^{V} in waters with a pH between 6 to 9 (Dixit and Hering, 2003). At pH less than 6, As^{V} is more strongly sorbed than As^{III} (Dixit and Hering, 2003). Additionally, competition for sorption sites with other oxyanions can reduce the amount of As sorbed to oxides. Phosphate is a common competitor for sorption sites and is much more abundant in natural groundwater than As. Arsenite sorption is suppressed more than arsenate in the presence of phosphates (Dixit and Hering, 2003). Regardless of the species, goethite (FeO[OH]) has a greater capacity to adsorb oxyanions than hydrous ferric oxides (Dixit and Hering, 2003).

2.2. Apatite Geochemistry

Apatite is a ubiquitous accessory phase in a variety of rock types and comprises a compositionally diverse mineral supergroup. The three main end members of apatite are fluorapatite [$Ca_{10}(PO_4)_6F_2$], hydroxyapatite [$Ca_{10}(PO_4)_6(OH)_2$], and chlorapatite [$Ca_{10}(PO_4)_6Cl_2$]. The general chemical formula for apatite is $M1_4M2_6(TO_4)_6X_2$, where M1 and M2 are divalent cation sites both filled by Ca; T is a pentavalent tetrahedra site primarily occupied by PO_4^{3-} tetrahedra; and X is an anion site containing F, Cl or OH (Pan and Fleet, 2002; Hughes and Rakovan, 2015). The M1 site is a tricapped-trigonal prism with a coordination number of 9, while the M2 site is coordinated to six oxygens and the halogen site (Hughes and Rakovan, 2015). The multiple crystallographic sites are structurally accommodating to allow a large suite of element substitutions (Hughes and Rakovan, 2015). A detailed summary of the trace elements that are compatible within the apatite structure can be found in Pan and Fleet (2002). Some of the more important substitutions include Na^{I}, Mn^{II}, REE^{III}, Y^{III}, U^{IV} and Th^{IV} into the M sites; CO_3^{2-}, SO_4^{2-} and SiO_4^{4-} into the T site; and CO_3^{2-}, S^{2-} and O^{2-} into the X site. The anions in the X site form a column along the edges of the unit cell parallel to the c-axis.

Fluorine-rich apatite is the primary phosphate phase in igneous systems (Webster and Piccoli, 2015) despite being an accessory phase. The composition of F-rich apatite reflects the geochemistry and geologic history of its crystallizing or re-equilibrated environment (Patiño Douce and Roden, 2006; Boyce and Hervig, 2008). Fluorine-rich apatite is important for investigations based on trace-element geochemistry (Campbell and Henderson, 1997; Pan and Fleet, 2002; Klemme and Dalpé, 2003; Harlov and Förster, 2003). Apatite geochemistry can be used to understand a number of aspects of the environment in which it has grown, including the behavior of volatiles (F, Cl, H_2O) (Piccoli and Candela, 1994), the trace element composition of the host magma (Sha and Chappell, 1999), magma redox state by S speciation (Konecke et al., 2019) or the relative Eu and Ce anomalies (Belousova et al., 2002; Cao et al., 2012; Bromiley, 2021), and as a geochronometer (Chew and Spikings, 2015).

Arsenic is compatible in apatite in the form of arsenate [$As^{V}O_4^{3-}$] substituting for phosphate [$P^{V}O_4^{3-}$] in the T site, given by the reaction:

$$6As^{V}O_4^{3-} + Ca_{10}(P^{V}O_4)_6F_2 \leftrightarrow 6P^{V}O_4^{3-} + Ca_{10}(As^{V}O_4)_6F_2 \tag{2.1}$$

Complete replacement of phosphate with arsenate is possible for each halogen end member of apatite. The resulting “arsenate apatites” are svabite [$Ca_{10}(AsO_4)_6F_2$], johnbaumite [$Ca_{10}(AsO_4)_6(OH)_2$], and turneaureite [$Ca_{10}(AsO_4)_6Cl_2$] (Pan and Fleet, 2002). Liu et al. (2017) conducted a series of dynamic crystallization experiments which demonstrated that arsenite [$As^{III}O_3^{3-}$] can be incorporated into apatite in the phosphate site, but only if As^{III} is the only species in the fluid. The incorporation of As^{III} was ascribed to the process of “dynamic uptake”. However, As^{III} rapidly converts to As^{V} during recrystallization if As^{V} is available in the fluid. As an example of this process occurring in the natural environment, Liu et al. (2017) found that the As in apatite from the Ernest Henry Iron Oxide Copper Gold deposit, Australia is primarily As^{V}, but a few of these grains have cores of As^{III}, suggesting initial growth in the presence of the arsenite oxyanion.

2.3. Representation of the Redox State of a Natural System

The relative proportion of oxidized and reduced species characterizes the redox state of a natural system. There are two ways to represent the redox state of such systems in common use, either redox potential (Eh) or oxygen fugacity (fO_2). These expressions of the system's redox state are interchangeable. Converting between Eh and fO_2 uses the half cell reaction:

$$4H^{+} + O_{2\,(Gas)} + 4e^{-} \leftrightarrow 2H_2O_{\,(liquid)} \tag{2.2}$$

and its related Nernst equation:

$$Eh = E^{o} - \frac{RT}{n\mathcal{F}}\ln(fO_2 a^{4}_{H+}) \tag{2.3}$$

where $\mathscr{F}$ is the Faraday constant, a_{H+} is the hydrogen ion activity, n is the number of electrons transferred and E^{0} is the standard cell voltage. In petrology, fO_2 is the standard metric for system redox state, mainly because values of Eh are linked to reactions with pH. Additionally, any redox reaction can be written to include oxygen (Anderson, 2017).

Fugacity is a thermodynamic quantity that was originally introduced by G.N. Lewis in 1901. This term is used to describe the flow of matter, or "escaping tendency" between phases to equalize chemical potentials and attain equilibrium (Anderson, 2017).

Fugacity, *f*, is a measurable quantity defined as:

$$dG = \forall dP = RT\ln f \tag{2.4}$$

where *dG* is the change in Gibbs free energy, *dP* is the change in pressure, ∀ is the volume, R is the gas constant and T is the temperature in Kelvin.

As gases behave more ideally under low pressures, the fugacity is related to the pressure by:

$$\lim_{P\to 0}\frac{f}{P} = 1 \tag{2.5}$$

The ratio of $\frac{f}{P}$ is the fugacity coefficient, γ_f, therefore:

$$f_i = \gamma_{f_i} P \tag{2.6}$$

in which f_i is the fugacity of component i in the fluid or gas phase. In natural systems, the fO_2 is an intensive parameter (like temperature and pressure) that affects the stability of mineral assemblages, and gas phase compositions. Oxygen fugacity is the primary control on the oxidation state of redox-sensitive elements, which in turn impacts element partitioning and solubility behavior. The fO_2 control on As speciation is illustrated by the following reactions:

$$As^0 + \frac{3}{2}O_2 \leftrightarrow As^{III}O_{3/2} \tag{2.7}$$

$$As^{III}O_{3/2} + \frac{1}{2}O_2 \leftrightarrow As^{V}O_{5/2} \tag{2.8}$$

Reaction 2.8 can also be expressed as:

$$\mathrm{K_{eq}} = \frac{a_{\mathrm{As^V}O_{5/2}}}{a_{\mathrm{As^{III}}O_{3/2}} \cdot fO_2{}^{1/2}} \tag{2.9}$$

where $\mathrm{K_{eq}}$ is the equilibrium constant, a_i is the activity of phase i.

$$\log\mathrm{K_{eq}} = \log a_{\mathrm{As^V}O_{5/2}} - \log a_{\mathrm{As^{III}}O_{3/2}} - \frac{1}{2}\log f\mathrm{O_2}$$

$$\log\mathrm{K_{eq}} = \log\frac{a_{\mathrm{As^V}O_{5/2}}}{a_{\mathrm{As^{III}}O_{3/2}}} - \frac{1}{2}\log f\mathrm{O_2} \tag{2.10}$$

Substituting the thermodynamic relationship

$$\Delta_r G^o = -\mathrm{RT}\ln \mathrm{K} = -2.303 \cdot \mathrm{RT}\log \mathrm{K} = \Delta_r H^o_{298} - \mathrm{T}\Delta_r S^o_{298} \tag{2.11}$$

(where $\Delta_r G^o$ is the Gibbs free energy of the reaction at the standard state, $\Delta_r H^o_{298}$ is the enthalpy of the reaction at 298K, $\Delta_r S^o_{298}$ is the entropy of the reaction at 298K, T is the temperature in kelvin, and R is the gas constant) into equation 2.10 gives:

$$\frac{-\Delta_r H^o_{298}}{2.303 \cdot \mathrm{RT}} + \frac{\Delta_r S^o_{298}}{2.303 \cdot \mathrm{R}} = \log\frac{a_{\mathrm{As^V}O_{5/2}}}{a_{\mathrm{As^{III}}O_{3/2}}} - \frac{1}{2}\log f\mathrm{O_2} \tag{2.12}$$

Assuming both the enthalpy and entropy change of this reaction are constant, then examination of equation 2.12 shows that at a fixed species ratio the value of fO_2 will depend upon the temperature. Referencing fO_2 to a redox buffer assemblage largely removes the temperature dependence and the remaining differences reflect oxidized or reduced conditions *relative* to the chosen reference reaction. In this thesis, fO_2 is cast in terms of the Fayalite-Magnetite-Quartz (FMQ) oxygen buffer defined by the equilibrium:

$$\underset{\text{Fayalite}}{3\mathrm{Fe_2SiO_4}} + \underset{\text{Oxygen}}{\mathrm{O_2}} \leftrightarrow \underset{\text{Quartz}}{3\mathrm{SiO_2}} + \underset{\text{Magnetite}}{2\mathrm{Fe_3O_4}} \tag{2.13}$$

This thesis uses ΔFMQ notation, defined as the difference between the sample logfO_2 and the log fO_2 of reaction 2.13 at the same temperature. The calibration for the fO_2 of the FMQ buffer is from O'Neill (1987). The redox state of iron is the primary control on a magma redox state (Carmichael, 1991), and therefore the speciation of all redox-sensitive trace elements. Referencing to the FMQ buffer is convenient, in that it relates the fO_2 to the ferric-ferrous equilibrium. The extent of fO_2 variation in terrestrial magmas (Fig. 2.1) is significant, spanning approximately nine orders of magnitude from FMQ -3 to FMQ +5.7 (Carmichael, 1991) with felsic melts occupying a range between FMQ -2 to FMQ +3.2.

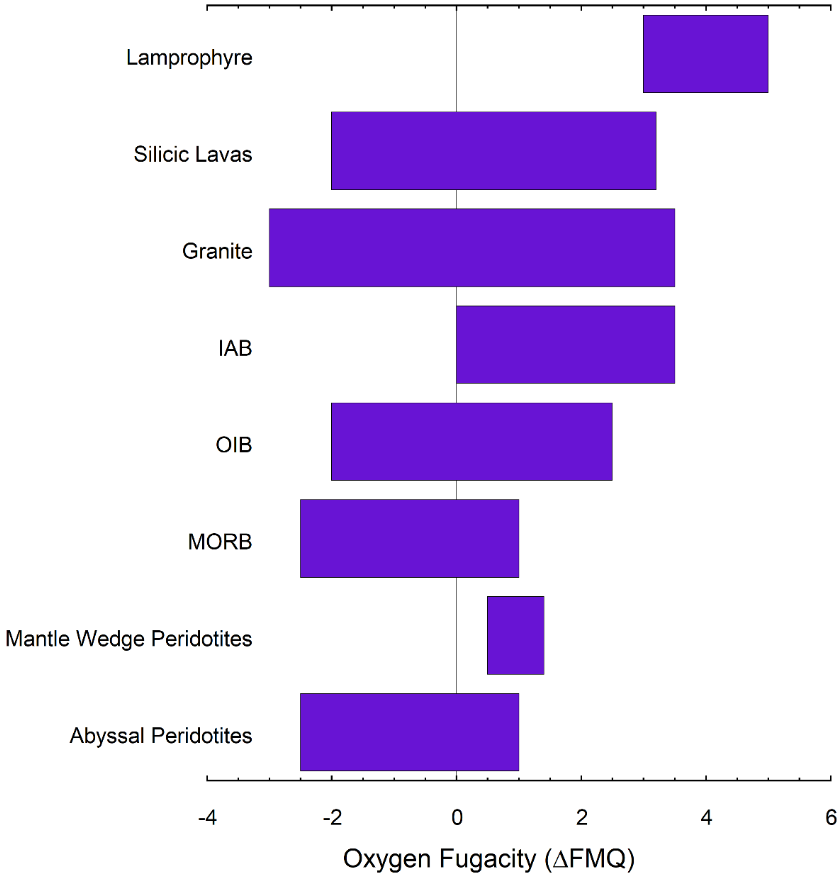

Figure 2.1 Range of oxygen fugacity for various terrestrial igneous rocks and their source regions. Modified from Miller et al. (2019). Data from: Abyssal peridotites (Bryndiza and Wood, 1990; Balhaus 1993); Mantle Wedge Peridotites (Wood and Virgo, 1989; Ballhaus, 1993; Brandon and Draper, 1996; Parkinson and Arculus, 1999; McInnes et al., 2001); MORB is mid ocean ridge basalt (Jugo et al., 2010 and references therein); OIB is ocean island basalt (Jugo et al., 2010 and references therein); IAB is island arc basalt (Jugo et al., 2010 and references therein); Granites (Cerny et al., 2005); Slilicic Lavas (Carmichael, 1991); and Lampropyres (Carmichael, 1991).

2.4.X-ray Absorption Spectroscopy

X-ray absorption spectroscopy (XAS) has emerged as the best technique for determining the speciation of As in solids (Foster and Kim, 2014). Other methods of measuring As speciation are high-performance liquid chromatography coupled with mass spectrometry. High-performance liquid chromatography has excellent detection limits but there is the possibility of changes in speciation during sample preparation (Nearing et al., 2014). X-ray photoelectron spectroscopy can also be used to determine the oxidation state in solids, but this method is only sensitive to the surface of the sample. X-ray absorption spectroscopy includes two different methods: 1) X-ray absorption near edge structures (XANES) which determines the oxidation state of an element and sometimes its coordination and 2) Extended X-ray absorption fine structures (EXAFS) which determines bond lengths, coordination numbers and elemental nearest neighbors (Newville, 2014).

2.4.1. Physical Basis for XAS

There are three modes of X-ray interaction with materials: absorption, scattering and transmission. If an X-ray is absorbed, the change in intensity, I, is governed by the Beer-Lamberts law:

$$I = I_0 e^{-\mu t} \tag{2.14}$$

in which I_0 is the incident X-ray intensity, t is the sample thickness and μ is the absorption coefficient. The probability of an X-ray absorption event is a function of energy, with the greatest probability of an event occurring at the binding energy.

If the X-ray energy absorbed is greater than or equal to the binding energy of the atom's core electron, that electron will escape as a photoelectron. The electron-hole created by this process is unstable and an electron from a higher energy shell will fill the "core hole" and emit a fluorescence X-ray. The intensity of the fluorescent X-ray produced is directly proportional to the intensity of the incident X-ray and the absorption coefficient. Released photoelectrons can scatter elastically off the nearby atoms and return to the absorbing atom creating constructive or destructive interference that modulates the absorption coefficient (Newville 2014).

The absorption coefficient can be calculated by measuring either the intensity of the X-rays transmitted through the sample using equation 2.14 or by the intensity of the element-specific fluorescent X-rays. Both the binding energy and the fluorescence X-ray energy are unique to the electronic structure of the atoms present in the sample, making XAS an element-specific analytical technique (Newville, 2014).

The XAS spectrum is collected by varying the energy of the incident X-ray beam through discrete energy steps and measuring the resulting absorption (Foster and Kim, 2014). When the incident energy is close to the binding energy there is a discrete increase in the absorption coefficient, called the absorption edge. This edge is often characterized by a sharp absorption maximum, or peak, referred to as the white line. The XANES part of the absorption spectra focuses on the energy range that includes the absorption edge and the interval within 50-80 eV of the edge.

The transition from the XANES to the EXAFS region of the absorption spectrum is usually taken as ~50 eV past the absorption edge (Foster and Kim, 2014). In this region, the constructive and destructive interference of scattered photoelectrons creates oscillations in the absorption spectra. The frequencies of these oscillations represent different scattering paths amongst the atoms present. Spectral analysis of the EXAFS plots absorption as a function of wave number k (in $Å^{-1}$) instead of energy, where k $\approx(E/4)^{1/2}$. For the case of As, the EXAFS measurements typically include up to 1000 eV or 16 $Å^{-1}$ above the absorption edge (Foster and Kim, 2014). Oscillations in the EXAFS spectrum decay with increasing energy, so the spectra are often multiplied by a power of k for analysis (Newville, 2014). This decay also requires that count times scale with k to maintain measurable signal-to-noise ratios (Calvin, 2013).

2.4.2. X-ray Absorption Near-Edge Structures

The XANES spectrum explores the binding energy of the core electrons of the element of interest within a sample. An increase in the oxidation state results in a decrease in the number of outer shell electrons, thus the nucleus binds the remaining electrons more tightly (Foster and Kim, 2014). This changes the binding energy of the electron and the absorption edge experiences a shift in energy (Fig. 2.2). The type of bonding can also change the binding energy of the core electrons. Covalent bonds typically have lower binding energies than ionic bonds. Thus, more than one factor can shift the absorption edge and interpretation of the XANES spectra for species identification requires caution (Foster and Kim, 2014).

Data reduction for XANES involves deadtime corrections, removing random spectral aberrations, pre-edge background removal, and normalization of the spectra (Newville, 2014). X-ray absorption near-edge structures uses linear combination fitting of various reference spectra to determine the oxidation states and their relative proportions in the samples under analysis (Foster and Kim, 2014). For spectral fingerprinting at the As K-edge, uncertainties reported for species identification are typically ± 10% but can range from 2 to 30% (Foster and Kim, 2014). Additionally, while the analytical sensitivity of XANES is at the µg/g level, a species must comprise >5% of the element of interest to be detectable (Foster and Kim, 2014). Unsuitable spectral reference materials, such as crystalline materials for aqueous fluids, can significantly reduce the accuracy and precision of the spectral match.

Beam-induced changes to the oxidation state of an element can occur during the collection of XANES spectra by photo-oxidation/reduction (Fig. 2.3). This effect is sometimes referred to as "beam damage". For the case of As, this often results in the oxidation of As^{-I} or As^{III} to As^{V}. Beam damage can be avoided by decreasing the scan time, relocating the analysis area after each scan or enclosing the sample in a cryogenic cell (Foster and Kim, 2014).

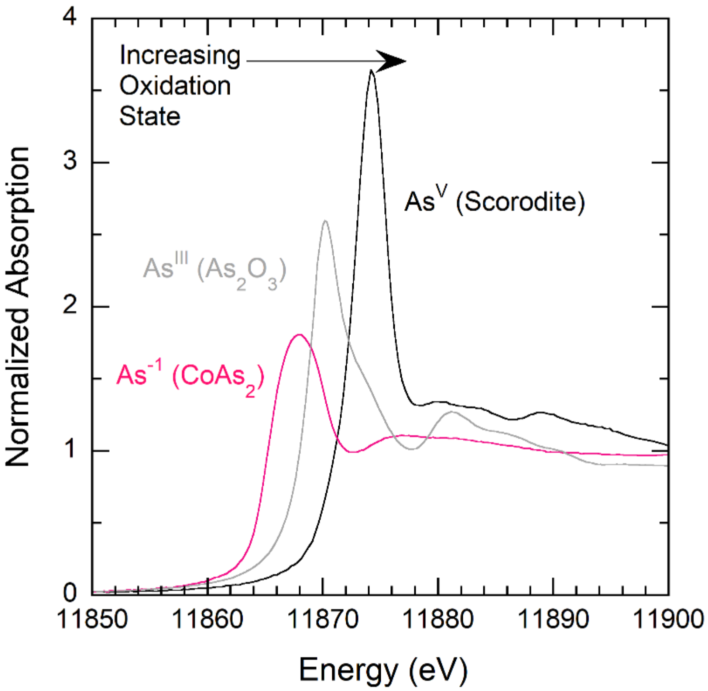

Figure 2.2 Normalized X-ray absorption near edge structures spectra at the As K-edge as a function of energy (eV) for As-bearing compounds with different oxidation states (as labelled).

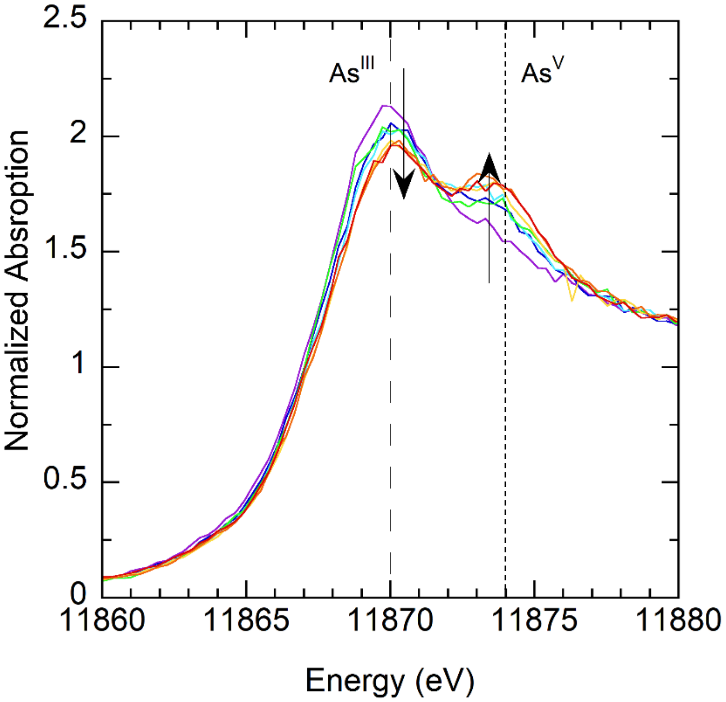

Figure 2.3 Normalized X-ray absorption near edge structures spectra at the As K-edge as a function of energy (eV). Spectra are individual scans of experimental glass AAO24 from chapter 4. Vertical lines indicate the white line position for As^{III} and As^{V}. This glass underwent photo-oxidation, with the intensity of the As^{III} peak decreasing as the As^{V} peak increases with time as shown by the arrows. Each scan lasted 4 min and 20 s. The first scan is in purple followed by blue, cyan, green, yellow, orange and finally red.

2.4.3. Extended X-ray Absorption Fine Structures Theory

As the origin of the EXAFS is interference created by scattering photoelectrons, spectral analysis of this energy region provides information on bond distances and coordination numbers. The amplitude of EXAFS features represents the intensity of the scattering event thus, the number of atoms surrounding the target atom. The distance a photoelectron travels dictates the wavelength of the oscillations, thus the bond length.

EXAFS spectra are processed similarly to XANES, but with the additional step of subtracting the background absorption features from the data to isolate the scattering events. As the EXAFS spectrum is a combination of scattering events that result in multiple sinusoidal functions, spectral deconvolution is done by Fourier transform. Analysis of EXAFS involves either linear combination fitting, as with XANES, or sequentially fitting theoretical scattering paths (called shells) to the data (Newville, 2014) to replicate the Fourier transform.

2.5.Contributions to Earth Science knowledge

The primary objective of this thesis is to provide a better understanding of the natural variation of As and Sb abundances in igneous rocks and their weathering products. This requires information on the speciation, which is the distribution of chemical forms over a specific range of conditions, as well as the predominant host phase(s) for these elements. Emphasis has been on the behavior of As, with only limited results for Sb. The thesis is comprised of three studies that document 1) the speciation of As and Sb in a mafic melt composition, 2) apatite/melt partitioning of As as a function of fO_2, temperature and melt composition with results for As speciation in a series of felsic compositions and 3) identifying the geogenic sources of As in groundwater associated with granite terranes in southwestern Nova Scotia. Each study's contributions are highlighted below.

2.5.1. Speciation of Arsenic and Antimony in Basaltic Magmas

Arsenic and Sb are amongst the metalloid group of elements, defined by their transitional electronic properties between metals and non-metals, and a large number of oxidation states. Knowledge of the oxidation state of these elements, and their variation with fO_2, provides a powerful tool for predicting mineral/melt partitioning behavior in a general way. This knowledge has potential applications for studying changes in the redox state of magmatic systems. Only a few studies evaluate the importance of oxygen fugacity on the oxidation state of As and Sb in geologically relevant melt compositions. These studies are limited by either the range of fO_2 investigated, methods of speciation measurement or the range of melt compositions employed.

Using synchrotron-based spectroscopic methods (XANES and EXAFS) this study reports the speciation of As and Sb in basaltic glasses produced in experiments done at 1200°C, 0.1 MPa and over the fO_2 range of FMQ -3.3 to +5.7. The dominant oxidation state in the samples is trivalent As and Sb, with pentavalent As contributing to less than 10% of the budget of As except at the highest fO_2 studied (FMQ +5.7). Pentavalent Sb was not observed in any of the samples studied, nor were any reduced oxidation states of As or Sb found in the glasses even at the lowest fO_2 investigated. Results paint a simple picture for predicting the geochemical behavior of these elements in magmatic systems, with the expectation that each will be rejected by most rock-forming minerals because of the poor match of As^{III} and Sb^{III} in ionic radius and charge for the major cation sites. Changes in the behavior of As and Sb in a magmatic system are unlikely to be fO_2-related, but instead reflect differences in other intensive parameters, such as fS_2, P and T.

2.5.2. Arsenic-rich Apatite as a Recorder of Local Crystallization Processes in Felsic Plutonic Systems.

The speciation measurements from the previous study indicate that As^{III} should prevail over the entire fO_2 range of terrestrial magmas, and therefore As should be incompatible in most rock-forming minerals, with the exception of sulfides. However, the As concentrations measured in apatite from several felsic plutonic suites exceed the whole rock, suggesting As is compatible in apatite. As As^{V} is much more compatible in apatite than As^{III}, the high apatite As concentrations suggest a greater presence of As^{V} in felsic melts. Based on the previous speciation study the amount of As^{V} in the melt to produce the necessary As enrichment in apatite would not be sufficient until the fO_2 exceeds the terrestrial range, creating a paradox in the geochemical behavior of As.

This study resolves the As-apatite paradox by performing apatite/melt partitioning experiments over a range of fO_2 and involving different felsic melt compositions. Results provide information on both the speciation of As in the melt and the fO_2-dependence of the partition coefficient for As, from which a general apatite/melt partitioning model is developed. From this, first-order crystallization models illustrate that for a reasonable range of fO_2, apatite/whole-rock ratios for As exceeding unity can only be reproduced by extreme levels of crystallization. Therefore, apatite with As concentrations enriched over the whole rock provides clear evidence for protracted crystallization, arguing for the presence of highly fractionated melts in some granitic systems.

2.5.3. Sources of Geogenic Arsenic in Well Water Associated with Granitic Bedrock from Nova Scotia, Canada

The origin of geogenic As contamination of groundwater derived from granite bedrock can be enigmatic. Peraluminous granites including the South Mountain Batholith, Musquodoboit Batholith and the Port Mouton Pluton dominate the bedrock of southwestern Nova Scotia. Over 30% of drinking water wells located in the South Mountain Batholith and Musquodoboit Batholith have As concentrations above the drinking water standard of 10 μg/L, while the Port Mouton Pluton aquifers have As concentrations less than 5 µg/L. The source of As in the groundwater associated with granite bedrock in Nova Scotia is poorly constrained, as is the origin of the disparity in well water concentration between the intrusions. To understand the geogenic As sources from within the granites, all mineral phases in samples of the three plutons were measured for As (and other trace elements). Results showed that cordierite is a previously unidentified source of As in the South Mountain Batholith, and Musquodoboit Batholith but is absent from the Port Mouton Pluton. Although As-rich pyrite is present in samples from all three plutons, only the South Mountain Batholith and Musquodoboit Batholith samples show evidence for pyrite oxidation, with variable As enrichment or depletion in the oxide alteration minerals. The origin of the elevated As well water concentrations for the South Mountain Batholith and Musquodoboit Batholith bedrock terranes is due to labile As released by cordierite weathering and sulfide oxidation. These results emphasize that the presence or absence of key bedrock mineral phases and their state of alteration is important to predicting well water contamination.

2.6.Contributions to Authorship

Bryan J. Maciag (BJM) and James M. Brenan (JMB) contributed to the overall design of this thesis. All experiments were done by BJM, except for SP4, SP6, SP7, SP8, SP9, SP21 and SP28 (Chapter 3) which were done previously by JMB. All Synchrotron measurements were done by BJM with the assistance of Erin Keltie and Juan Chavez Cabrera while at the beamlines. Data reduction, interpretation, and modelling of XANES and EXAFS were performed by BJM. Major and trace element analyses of samples SP4, SP6, SP7, SP8, SP9, SP21 and SP28 were done by JMB. Major and trace element analyses of apatite and biotite reported in Chapters 4 and 5 were done by BJM with the assistance of Rosa Toutah and Natalie Shields, both supervised by BJM. All other major and trace element measurements were completed by BJM. Whole-rock analyses reported in Chapter 4 were done as fee for service at Activation Laboratories in Ancaster, Ontario. All calculations and models were performed by BJM. BJM and JMB contributed to the writing of this thesis. Michael Parsons and Gavin Kennedy provided additional editorial and scientific input on Chapter 5. Chapter 3 has been published in Geochimica et Cosmochimica Acta as Maciag and Brenan (2020). Chapter 4 has been formatted for submission to American Mineralogist. Chapter 5 has been formatted for submission to either Environmental Science and Technology or Science of the Total Environment.

Chapter 3

SPECIATION OF ARSENIC AND ANTIMONY IN BASALTIC MAGMAS

Bryan J. Maciag[a]*, James M. Brenan[a]
[a]Department of Earth and Environmental Sciences, Dalhousie University, Halifax, NS, Canada
*Corresponding author: Bryan J. Maciag (bmaciag@dal.ca)

Key Words: Arsenic, Antimony, XANES, Oxygen fugacity, Redox State
Published in Geochimica et Cosmochimica Acta, Volume 276,1 May 2020

Abstract

This study applies X-ray absorption near edge structure (XANES) and extended X-ray absorption fine structures (EXAFS) spectroscopy at the K-edge to determine the speciation of As and Sb in a suite of basaltic glasses synthesized over a range of oxygen fugacity (fO_2) at 1200°C and 0.1 MPa. Experiments were executed in evacuated fused silica ampoules using a variety of solid metal metal-oxide buffers to achieve fO_2's ranging from FMQ -3.3 to FMQ +5.7 (where FMQ is the fayalite magnetite quartz buffer). The oxidation state was calculated using linear combination fitting to spectral reference material with known oxidation states using the XANES spectra. Speciation results were corrected for the quench effect of iron. Trivalent As and Sb were determined to be the dominant oxidation state in the samples, with pentavalent As contributing to less than 10% of the budget of As unless the fO_2 is greater than FMQ +5.3±0.9, while pentavalent Sb was not observed. Additionally, no reduced oxidation states of As or Sb were found in the glasses even at the lowest fO_2 investigated. Structural parameters such as the coordination number and bond length were determined by fitting theoretical electron scattering paths to the EXAFS spectra. Arsenic is coordinated by three oxygens at 1.78±0.01 Å forming $As^{III}O_3E$ (where E is the lone pair of electrons) trigonal pyramids. Antimony is coordinated by three oxygens at 1.98±0.01 Å, interpreted to be in a trigonal pyramid structure similar to As^{III}. As both metalloids are primarily present in the trivalent state over the range of terrestrial fO_2 (FMQ -3 to FMQ +5) it is expected that each will behave incompatibly during basaltic melting or crystallization, owing to 1) the tendency for these elements to form oxyanions, and 2) their poor match in ionic radius and charge for the major cation sites in mafic minerals.

3.1. Introduction

Arsenic (As) and Sb (Sb) are metalloids that occupy Group 15 on the Periodic Table collectively called the “pnictogens”. Apart from bismuth, the pnictogens form stable ionic bonds as +III and +V cations or as a -III anion, although covalency may occur especially with sulfur. Additionally, the cationic forms of these elements tend to form oxyanions (e.g. $As^{III}O_3^{-3}$, $As^VO_4^{3-}$) in oxygen-rich environments. Arsenic and Sb are present at trace levels in the mantle (As: 0.07 µg/g, Sb: 0.01 µg/g; Palme and O’Neill, 2003), and despite being enriched during crust-mantle differentiation these elements are still present at low concentrations in the crust (As: 2.5 µg/g; Sb: 0.2 µg/g; Rudnick and Gao, 2003). Elevated concentrations of As and Sb can be found in sedimentary rocks, particularly shales (As: 100µg/g; Sb: 15µg/g; Ketris and Yudovich, 2009). Significant enrichment of As and Sb is also associated with hydrothermal alteration related to gold mineralization, (As: >1000 µg/g Sb: >100 µg/g; Craw et al., 2004) such that As is considered a pathfinder element. In some cases, magmatic and hydrothermal processes can enrich both As and Sb such that they become accessory phases related to ore deposition. This is particularly important for the platinum group elements (PGE), as platinum shows a stronger affinity for arsenide phases over coexisting sulfide phases in magmatic systems. (Gervilla et al., 1996, Hanley, 2007, Helmy et al., 2013, Piña et al., 2015, Bai et al., 2017)

Arsenic and Sb are trace elements with diverse geochemical properties, thus their partitioning behavior can potentially be used to study the evolution of magmatic systems, including changes in intensive parameters such as redox state. Additionally, as both As and Sb are toxic, understanding their behavior in igneous systems is important for identifying potential sources of environmental contaminants during subsequent exhumation, weathering, and erosion. Knowledge of speciation is crucial to this issue, as both the mobility and toxicity of As in surface and groundwater is a function of the chemical form, with trivalent As being significantly more toxic than pentavalent As (Ferguson and Gavis, 1972; National Research Council, 1977; Stoeppler, 1992; Jain and Ali, 2000). While less toxic than As, the toxicity of Sb is also a function of the speciation, with trivalent Sb being more toxic than pentavalent Sb (Winship, 1987; Gebel, 1997; World Health Organization, 2006; Filella et al., 2007).

One of the main controls on the speciation of an element in silicate melt is the redox condition, whose metric is oxygen fugacity (fO_2). Of the intensive variables that control magmatic behavior, fO_2 has the largest range of values, spanning nine orders of magnitude (approximately -3.0 to +5.7 log units from the fayalite-magnetite-quartz buffer (FMQ)) (Carmichael, 1991; Mallmann and O'Neill, 2007) in terrestrial magmatic systems. As such, it is critical to quantify how fO_2 affects the speciation of As and Sb in silicate melts.

There is limited quantitative data currently available on the speciation of As and Sb for silicate melts compared to the more numerous studies involving aqueous fluids (the latter summarized by Pokrovski et al., 2013). The most systematic work on the speciation of these elements in silicate melts is that of Schreiber and Coolbaugh (1995), who measured the redox potential of As and Sb along with a number of other elements in Na-rich borosilicate melts at 1150°C and 0.1 MPa. This was accomplished by determining the redox ratio using colorimetric/complexometric titrations for glasses quenched from a specific fO_2. Other studies have utilized X-ray near-edge structures (XANES) and extended X-ray absorption fine structures (EXAFS) to measure the As speciation directly in a natural rhyolite (Borisova et al., 2010) and in a synthetic basaltic melt at 1200°C, 0.1 MPa (Canali et al., 2017). Antimony speciation has been measured by XANES and EXAFS in a range of synthetic melts at 1300-1400°C, 0.1 MPa and 1 GPa (Miller et al., 2019). Guo (2008) used X-ray photoelectron spectroscopy on synthetic hydrous granitic glasses produced at 800°C and 200 MPa to infer the As and Sb speciation but never quantified the species abundances. In addition to direct measurements of speciation, studies of interphase partitioning between sulfide and silicate melt (Kiseeva and Wood, 2013; Kiseeva and Wood, 2015; Li and Audétat, 2012; Li and Audétat, 2015), rutile and silicate melt (Klemme et al., 2005), and metal and silicate melt (Righter et al., 2009; Siebert et al., 2011) have been used to infer the As and Sb oxidation state, although these estimates are model dependent.

The importance of oxygen fugacity on the oxidation state of As and Sb in geologically-relevant melt compositions has only been evaluated in a few studies, and with some limitations. Whereas the work of Borisova et al (2010) provides important insight into As speciation in a natural rhyolite glass, the chosen sample represents only a single oxygen fugacity, whose value is somewhat imprecise (estimated to be between ~FMQ -3 to 0). Measurement of As speciation over the fO_2 range of FMQ -3.3 to +5.5 in the work of Canali et al. (2017) was done using the L_{III}-edge, which had limited sensitivity for As^V due to spectral interference from the magnesium K-edge. Miller et al. (2019) provide a thorough assessment of Sb speciation over the fO_2 range of FMQ -4.7 to +7.3, but with a focus on the basalt-analogue CMAS (CaO-MgO-Al_2O_3-SiO_2) system (although a single iron-bearing sample was investigated). The results presented here revisit the work of Canali et al. (2017) to measure the same samples but at the interference-free As K-edge, and serve to extend the results of Miller et al. (2019) to investigate Sb speciation to a more complex alkali- and iron-bearing basaltic melt composition.

3.2. Experimental Methods

3.2.1. Overview

The overall objective of these experiments was to generate a series of basaltic glasses containing dissolved Sb that had been equilibrated over the range of fO_2 that encompass terrestrial magmas at 1200°C and 0.1 MPa. The source of Sb in the experiments was synthetic $PtSb_2$ (geversite), which decomposed to form a PtSb melt with the excess Sb dissolving into the silicate melt or lost to the buffer phase. Two experiments (Sb06 and Sb21) did not contain sufficient $PtSb_2$ to reach saturation in a platinum-Sb phase. As the intent of this study is to measure speciation, not solubility, experiments that did not saturate in an antimonide phase are still considered successful. Glasses saturated in an antimonide melt phase are listed as having $PtSb_{melt}$ in Table 3.1. Control of fO_2 by traditional gas mixing was not a viable option in these experiments as Sb is volatile at elevated temperatures and lost from the experiment; therefore, a closed system was required. To achieve this objective, sealed silica ampoules containing solid metal metal-oxide or oxide-oxide fO_2 buffers and a chromite crucible were used. The buffers employed (i.e. Mo-MoO_2, Ni-NiO, MnO-Mn_3O_4, Fe_3O_4-Fe_2O_3) allowed the fO_2 to be fixed at FMQ -3.2, +0.7, +4.3 and +5.5 respectively in the experiments. The Co-CoO buffer was found to be too volatile, with a significant concentration (>20 wt.%) of CoO entering the melt. At the Ru-RuO_2 buffer, chromite was found to be unstable and failed as a crucible. Additionally, two "sliding" buffers using (Ni,Mg)O and NiPd alloys were employed to achieve intermediate fO_2 of FMQ -1.6 and +2.8 (see section 2.3.1 and the Supplementary Information for more details).

Table 3.1 Summary of experiments to measure As and Sb speciation.

Exp. ID	Buffer	ΔFMQ	Duration (h)	Phases Present
Sb06	Ni-NiO	0.67	98.3	Glass+ Ol
Sb08	$MnO-Mn_3O_4$	4.28	97.2	Glass + $PtSb_{melt}$ (X_{Sb}:0.25)
Sb16	$Mo-MoO_2$	-3.25	61.3	Glass + Px + $PtSb_{melt}$ (X_{Sb}:0.60)
Sb21	$Fe_3O_4-Fe_2O_3$	5.70	93.3	Glass
Sb24	NiPd-NiO	2.8±0.1	77.5	Glass + Ol + $PtSb_{melt}$ (X_{Sb}:0.01)
Sb25	Ni-(Ni,Mg)O	-1.5±0.1	77.5	Glass + $PtSb_{melt}$ (X_{Sb}:0.36)
SP4*	Ni-NiO/no buffer	0.68/0.7	96	Glass + $PtAs_{melt}$ (X_{As}:0.46)
SP6*	$MnO-Mn_3O_4$/no buffer	4.3/3.6	96	Glass + $PtAs_{melt}$ (X_{As}:0.47)
SP7^{a}	$MnO-Mn_3O_4$	4.3	87.3	Glass + $PtFe_{alloy}$
SP8*	$CO-CO_2$/ no buffer	0.68/4.3	92.5	Glass + $PtAs_{melt}$ (X_{As}:0.32)+ $PtAs_2$
SP9*	$CO-CO_2$/ no buffer	0.68/5.4	92.5	Glass + $PtAs_{melt}$ (X_{As}:0.37)
SP21*	$Mo-MoO_2$/no buffer	-3.25	48.5	Glass + $PtAs_{melt}$ + $PtFe_{alloy}$
SP28*	CO-CO2/no buffer	5.4/5.5	90	Glass + $PtAs_{melt}$ (X_{As}:0.22)

Temperature: 1200°C; Pressure; 0.1MPa

Ol- olivine; Px- Pyroxene; $PtSb_{melt}$ or $PtAs_{melt}$- platinum Sb or As melt; X_{Sb} is mole fraction Sb in the $PtSb_{melt}$. X_{As} is mole fraction As in the $PtAs_{melt}$.

*Two-stage experiments from Canali et al. 2017. In order to simplify experimental names, the M2 was dropped from all experimental names. Thus, SP21 corresponds to M2SP21 in Canali et al. 2017. The buffer utilized and fO_2 of the first experimental stage are separated from the conditions of the second experimental stage by a "/".

^{a}Single stage experiment from Canali et al. 2017. SP7 corresponds to SP7 in Canali et al. 2017

An additional six samples of basalt saturated in $PtAs_2$ (sperrylite) were obtained from the study of Canali et al. (2017), which were previously measured using XANES at the As L_{III}-edge. For the data reported in this study, the M2SP# experimental prefix from Canali et al. (2017) was simplified to SP#, except for SP7 in which the original experiment name was retained. The starting material and method used to synthesize the Sb-bearing samples (summarized below) is similar to that of Canali et al. (2017) although those workers employed a sample pre-equilibration step not used in the current work. A summary of experiments, including those done by Canali et.al. (2017) is provided in Table 3.1.

3.2.2. Materials

The basalt starting material for this study was prepared by weighing high purity (> 99.5%) oxides (MgO, Fe_2O_3, SiO_2, Al_2O_3, MnO, and TiO_2) and carbonates (K_2CO_3,

Na_2CO_3, and $CaCO_3$) within +/- 0.1 mg of the target values for the required composition. Reagents were ground together under ethanol in an agate mortar for at least 30 minutes to achieve a homogenous mixture then calcined in a box furnace by ramping from 500^{o}C to 1000^{o}C over 5 hours, followed by an isothermal soak for at least 8 hours at 1000^{o}C. After cooling to room temperature, the oxide mixture was then re-homogenized by grinding under ethanol for another 30 minutes before being placed in a platinum crucible and fused at 1500^{o}C for 30 minutes. The resulting melt was quenched in water, reground, and fused for an additional 30 minutes. This final glass was checked for crystals then ground into a fine powder. Several shards of glass were saved for analysis with the electron probe microanalyzer (EPMA) to confirm glass homogeneity.

The platinum antimonide geversite ($PtSb_2$) was synthesized by vacuum-sealing stoichiometric amounts of high purity (>99.95%) Pt and Sb powder in a silica ampoule then slow heating to 800^{o}C followed by an isothermal soak for 96 hours (see section 2.3 for ampoule preparation). The composition was confirmed by analyzing the run-product material using energy dispersive spectroscopy (EDS) on the EPMA.

Chromite from the New Caledonia ultramafic massif (Royal Ontario Museum Reference M4557), was made into crucibles to contain the melt during the experiments. Chromite was used to contain the melt because the solubility of chromite in basaltic melts is relatively low (< 0.3 wt.%; Roeder and Reynold, 1991), thus it would not change the melt composition significantly. Additionally, Sb is incompatible in chromite, meaning the elements of interest would not be lost to the crucible. These crucibles were cored from slabs of adcumulate chromitite using a diamond coring bit or fragments were ground into a cylindrical shape (outer diameter 4-4.9 mm by 5-10 mm long) using a diamond grinding wheel. A hole (diameter 1.3-2.3 mm by 3-6 mm deep) was drilled down the center of the resulting chromite cylinders using a diamond drill bit. To remove volatile-bearing phases and reduce any ferric iron, the chromite crucibles were fired at 1200^{o}C-1300^{o}C for 45 to 60 minutes in a vertical tube furnace at the FMQ buffer with the fO_2 fixed using a CO-CO_2 mixture.

3.2.3. Experiment Preparation

Silica ampoules were made by initially sealing the end of a 127 mm long high purity fused silica tube (internal diameter: 5 mm outer diameter: 9 mm) with an oxy-acetylene torch, then thoroughly cleaning the tube with soap and water before rinsing with water then ethanol followed by drying at 100°C. Silica ampoules were prepared according to Fig. 3.1, with a 50-100 mg layer of solid buffer at the base, then a 2-4 mm thick layer of coarse SiO_2 glass followed by the chromite crucible containing the basaltic glass powder and the Sb source ($PtSb_2$ aggregates). Initially, the $PtSb_2$ was added beneath the basalt (Sb06); however, several experiments saturated in $PtSb_2$ resulted in a trapped gas bubble that inhibited chemical exchange across the sample. To mitigate this effect, $PtSb_2$ was placed atop the melt in the remaining experiments. A silica ring (5 mm diameter 1-2 mm thick) was placed above the chromite crucible to prevent the melt from wicking out, followed by an approximately 30 mm long, 5mm thick silica spacer. The entire tube was evacuated for at least 30 minutes using a vacuum pump then sealed with an oxy-acetylene torch. Sealing the ampoule reduced the tube length to 50-80 mm. The sealed silica ampoules were placed vertically in 5 ml (19 by 26 mm) cylindrical alumina crucibles and then both the crucible and ampoule were placed in a box furnace at 1200°C for the experiment duration. Samples were quenched by removing the ampoule and crucible from the furnace, knocking free the crucible, and dropping the experimental ampoule into cold water.

3.2.3.1. Sliding Buffer Experiments

So-called "sliding" fO_2 buffers were used in two experiments to fix the fO_2 to approximately FMQ -2 and +2.5. These buffers are based on the equilibrium:

$$\mathrm{Ni_{metal}} + \frac{1}{2}\mathrm{O_2} \leftrightarrow \mathrm{NiO_{oxide}} \tag{3.1}$$

Which has an equilibrium constant of the form:

$$\mathrm{K_{eq}} = \frac{\mathrm{a_{NiO}^{oxide}}}{\mathrm{a_{Ni}^{metal}} \cdot \mathrm{fO_2}^{1/2}} \tag{3.2}$$

Where $\mathrm{a_{NiO}^{oxide}}$ and $\mathrm{a_{Ni}^{metal}}$ are the activity of NiO and Ni in the oxide and metal phases, respectively. The K_{eq} of this equation can be related to the standard state free energy of the reaction by:

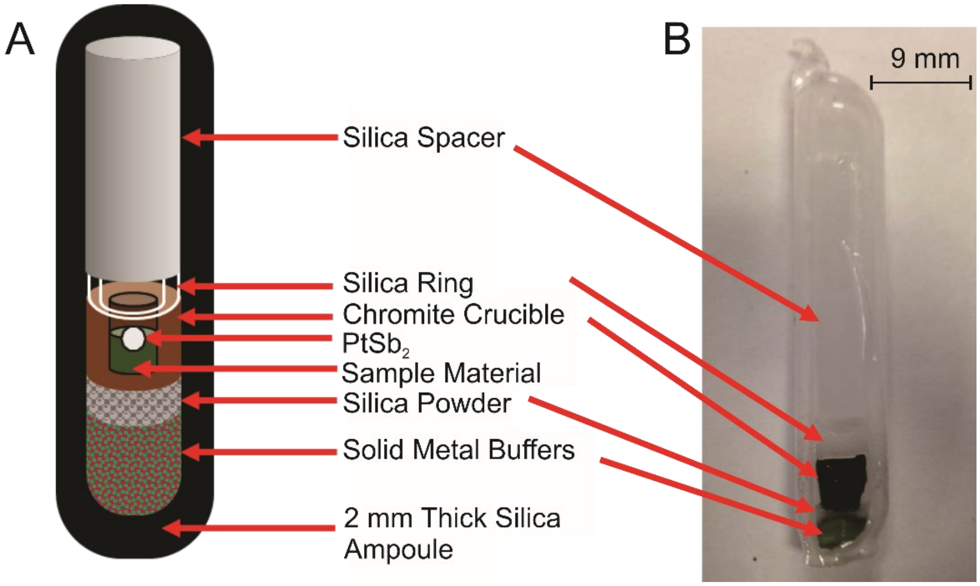

Figure 3.1 Illustration of the fused silica ampoule configuration employed in experiments. A) Schematic depiction of a sealed ampoule (not to scale) B) Photo of completed experiment containing the nickel nickel-oxide (NNO) buffer.

$$-\mathrm{RT}\ln \mathrm{K_{eq}} = \Delta_r \mathrm{G}^\circ \tag{3.3}$$

which when combined with equation 3.2 yields:

$$\ln \mathrm{K_{eq}} = \frac{-\Delta_r \mathrm{G}^\circ}{\mathrm{RT}} = \ln \mathrm{a}_{\mathrm{NiO}}^{\mathrm{oxide}} - \ln \mathrm{a}_{\mathrm{Ni}}^{\mathrm{metal}} - \frac{1}{2}\ln f\mathrm{O}_2 \tag{3.4}$$

equation 3.4 can be rearranged and solved for $f\mathrm{O}_2$ to yield:

$$\ln f\mathrm{O}_2 = 2\left[\ln \mathrm{a}_{\mathrm{NiO}}^{\mathrm{oxide}} - \ln \mathrm{a}_{\mathrm{Ni}}^{\mathrm{metal}} + \frac{\Delta_r \mathrm{G}^\circ}{\mathrm{RT}}\right] \tag{3.5}$$

Inspection of equation 3.5 shows that dilution of the Ni with Pd or the NiO with MgO will displace the $f\mathrm{O}_2$ to either a more reduced (addition of MgO) or more oxidized (addition of Pd) value than the assemblage involving only the pure phases. Information on the activity-composition relations required to calculate $f\mathrm{O}_2$ is obtained from Taylor et al. (1992) and Pownceby and O'Neill (1994a). The NiPd buffer has been previously used to monitor $f\mathrm{O}_2$ in experiments at the Re-ReO_2 buffer (Pownceby and O'Neill, 1994b). For a particular combination of m'tal and oxide to serve as a buffer rather than simply as a sensor, a significant amount of material was used relative to the experimental charge (10-15x). The buffer material was analyzed post-experiment by EPMA (see section 3.2) to calculate the $f\mathrm{O}_2$ (for more details see Supplementary Information).

3.3. Analytical Methods

3.3.1. Sample Preparation

After quenching, the silica ampoule was cracked open, and the chromite crucible and buffer materials were extracted, then mounted separately in 25.4 mm epoxy round pucks. After the epoxy hardened, the pucks were ground by hand using 220, 400, and 600 grit silicon carbide paper to expose the run-products or fresh buffer material. Samples were then polished in water using 1 μm followed by 0.3 μm alumina powder.

3.3.2. Electron Probe Micro-Analyzer (EPMA)

The major element composition of run-product phases was determined using the JEOL JXA-8200 EPMA housed in the Robert M. MacKay Electron Microprobe Laboratory at Dalhousie University. Silicate glass analyses were done using an accelerating voltage of 15 kV, a beam current of 10 nA and a 10 μm defocused beam to limit glass damage. Standards for silicate melt analysis were a natural basalt (Si, Al, Na, Mg, Fe and Ca), K-kaersutite (K), pyrolusite (Mn), chromite (Cr), rutile (Ti) and stibnite (Sb). Antimony metal was used for the interference corrections of the Sb Lα peak on the Ca Kα peak and the Sb Lγ3 peak on the Ti Kα peak, while magnetite was used for the interference correction of the 2nd order Fe Kβ1peak on the Sb Lα peak. Count times were 20 seconds for most elements but were increased to 60 seconds to obtain more precise Sb data. Raw count rates were converted to concentrations using the ZAF data reduction scheme. The major and trace element concentrations of the run-product glasses can be found in Table 3.2.

3.3.3. Laser Ablation Inductively Coupled Plasma Spectrometry (LA-ICP-MS)

Trace element concentrations were determined using the laser ablation inductively coupled plasma mass spectrometry (LA-ICP-MS) facility located in the Health and Environments Research Centre [HERC] Laboratory at Dalhousie University. The system employs a frequency quintupled Nd: YAG laser operating at 213 nm, coupled to a Thermo Scientific iCAP Q ICP-MS quadrupole mass spectrometer with He flushing the ablation cell to enhance sensitivity (Eggins et al., 1998). Silicate glasses were analyzed using a laser repetition rate of 5-10 Hz and a spot size of 40-50 microns with the analysis area moving back and forth during ablation to reduce ablation depth.

Table 3.2 Summary of run-product glasses compositions.

Exp. ID	Electron Microprobe Results (wt.%)												LA-ICP-MS Results (μg/g)			
	SiO_2	TiO_2	Al_2O_3	FeOt	MgO	CaO	Na_2O	K_2O	MnO	Cr_2O_3	Total	N	^{121}Sb	^{51}V	^{75}As	N
Sb06	47.8	5.62	9.00	12.3	10.3	13.0	0.77	0.13	0.14	0.14	99.5	14	3390	28	0.12	5
1σ	0.29	0.11	0.11	0.58	0.13	0.12	0.04	0.01	0.03	0.09	0.46		98	1	0.04	
Sb08	47.3	5.20	9.41	10.5	9.72	12.0	0.47	0.11	0.12	0.09	99.7	9	44200	190	0.42	7
1σ	0.16	0.07	0.07	0.07	0.08	0.18	0.02	0.01	0.02	0.03	0.37		4300	15.8	0.08	
Sb16	50.5	5.24	8.75	11.5	10.8	12.4	0.34	0.07	0.14	0.38	100	11	217	14	0.19	7
1σ	0.15	0.08	0.13	0.20	0.08	0.10	0.02	0.01	0.02	0.03	0.41		17	2	0.02	
Sb21	51.4	5.33	10.4	9.69	8.88	11.9	0.25	0.08	0.09	0.07	99.4	8	24	560	1.08	5
1σ	0.39	0.10	0.13	0.19	0.08	0.08	0.03	0.01	0.01	0.03	0.43		2.0	83	0.05	
Sb24	48.6	6.11	10.2	8.88	8.37	14.4	0.75	0.12	0.09	0.08	99.7*	8	11100	95	0.61	5
1σ	0.17	0.10	0.08	0.08	0.08	0.17	0.02	0.02	0.03	0.02	0.32		1400	14	0.15	
Sb25	50.9	5.97	9.49	7.23	11.1	14.0	0.81	0.14	0.10	0.25	99.9	7	243	11	0.68	8
1σ	0.21	0.10	0.08	0.24	0.09	0.09	0.03	0.01	0.02	0.03	0.35		47	1	0.12	

N is the number of analyses; σ is the standard deviation of the analyses.

* sample contains 2.01± 0.03 wt.% NiO

Beam irradiance was optimized for each material depending on photon-coupling characteristics with a target value of 5-10 J/cm^2. Factory-supplied time-resolved software was used for the acquisition of individual analyses. A typical analysis involved 20 seconds of background acquisition with the ablation cell being flushed with He, followed by ablation for 60 seconds, then 60 seconds of cell washout. Analyses were collected in a sequence in which two analyses were done on a standard reference material at the start of the acquisition cycle, then after every 16-18 analyses on the unknown samples. Four to five analyses were done on each run-product glass. Data reduction was done off-line using the Iolite version 3.6 software package. Antimony, As, and vanadium concentrations in the silicate glass were quantified using the NIST 610 silicate glass, which contains 396 µg/g Sb, 325 µg/g As, and 450 µg/g V (Jochum et al., 2011). Ablation yields were corrected by reference to the known concentration of Ca as determined by EPMA, using ^{43}Ca as an internal standard. The following isotopes were measured: ^{43}Ca, ^{51}V, ^{75}As, ^{121}Sb, ^{125}Sb, ^{194}Pt, ^{195}Pt. Concentrations were determined using the isotopes in italics and are reported in Table 3.2. Platinum was not quantified as the signal was very heterogeneous due to micro-inclusions contained within the glasses (see sections 4.2 and 4.3). The accuracy of the LA-ICP-MS protocol was assessed to be 15-20% relative to the published values of standard reference glasses (BHVO-1, BCR-2, BIR-1).

3.3.4. X-ray Absorption Spectroscopy

X-ray absorption spectra were collected at the Canadian Light Source, Saskatoon using the HXMA beamline with Si(220) crystal monochromators for the Sb K-edge (edge position: 30,491 eV; Samples: Sb06, Sb08, Sb16, Sb21, Sb24, and Sb25) and the VESPERS beamline with Si(111) monochromators for the As K-edge (edge position:11,867 eV; Samples: SP4, SP6, SP7, SP8, SP9, and SP28). Additional spectra at the As K-edge (Samples: SP4, SP21 and SP28) were collected at the Advanced Photon Source (APS), Argonne, USA at the sector 20-ID beamline using the Si(111) monochromators. No harmonic rejection was used on either beamline at the CLS as it is incapable of generating higher harmonics at the Sb K-edge and the flux on the VESPERS beamline was too low to generate interference from harmonics. At sector 20-ID the monochromators were detuned by 10% (30% for SP28) to reduce harmonics.

All unknowns were measured in fluorescence mode *in-situ* on polished samples using a 32 element Ge detector on HXMA, a 4 element Ge detector on VESPERS, and a 4 element vortex silicon drift detector at the APS. A 6-micron spot was used on VESPERS and a variable spot size (100 to 500 microns) was used on HXMA (optimized for counts and detector deadtime). The spot size at the APS was 100 by 120 microns. Spectral reference materials were measured in transmission mode. For measurements on the HXMA beamline, reference materials were prepared by dilution with boron nitride in a 1:3 proportion then packing the mixture tightly in a Teflon sample holder. On the VESPERS beamline and at the APS, reference materials were ground to a fine powder in a fumehood 2-3 hours prior to analysis to limit oxidation, then spread evenly across a piece of Kapton® tape. Spectra for reference materials $As^{V}{}_2O_5$, $As^{III}{}_2O_3$, $As^{III}{}_2S_3$, arsenopyrite [FeAsS], $Ca_3(As^{V}O_4)_2$ and $Na_2HAs^{V}O_4$, were obtained from the VESPERS spectral library (acquired by Dr. Peter Blanchard). These reference scans use similar parameters to those in this study, were performed on powders with purities greater the 99% (except for the arsenopyrite standard) and were also used as reference materials for the XANES analysis on VESPERS spectra. Spectra for the trivalent and pentavalent aqueous species at various fluid pH were also used as reference materials. The aqueous As standards are from Borisova et al. (2010) and aqueous Sb standards are from Tella and Pokrovski (2012) for pentavalent Sb and Pokrovski et al. (2006) for trivalent Sb.

An Sb foil reference material (edge position: 30,491 eV) was collected at the K-edge simultaneously with each sample on the HXMA beamline for use in energy calibration. For measurements on the VESPERS beamline and APS, energy calibration scans were done periodically on gold foil at the L_{III}-edge (edge position: 11,919 eV). Energy calibrations were done using the maximum derivative of the absorption spectra on the appropriate reference foil. The energy drift on the VESPERS and the APS beamlines were negligible and determined to be less than the energy resolution of the beamlines (1 eV) over the course of the analysis. Of concern during XANES analysis are spectral shifts caused by changes in speciation arising from beam induced oxidation/reduction of the sample. This process, termed "beam damage" was evaluated by comparing multiple scans completed on the same location, which is irradiated continuously for over 2 hours.

Figure 3.8 in the Supplement Information shows the peak position of multiple scans, and the lack of spectral change indicates that beam damage was not measurable.

Signal aberrations caused by defects in the monochromators were removed from individual scans. Scans were then aligned manually before merging. Each merged spectrum was calibrated and normalized. Linear combination fitting was performed on the individual spectrum using the reference materials as standards to determine the speciation in each sample. The processing of the data was completed using ATHENA from the DEMETER software package, version 0.9.26 (Ravel and Newville, 2005).

Linear combination fitting was performed on the XANES spectra in absorption vs energy space from -20 to +30 eV around the absorption edge for As and in both absorption vs energy and derivative of the absorption vs energy space for Sb (Fawcett et al., 2009). No significant difference in the species proportions from these methods was found for this study. Small shifts (±1 eV) in the energy spectra were allowed during linear combination fitting to account for energy drift during the collection of the sample spectra and the reference materials. The linear combination fitting reference materials for Sb included GaSb, $Sb^{III}_2O_3$, aqueous $KSb^V(OH)_5$, aqueous $Sb^V(OH)_5$ and aqueous $Sb^{III}(OH)_3$. The As reference materials were $As^{III}_2O_3$, skutterudite ($CoAs_2$), $Ca_3(As^VO_4)_2$, native As, scorodite [$FeAs^VO_4 \bullet 2H_2O$], aqueous $As^VO(OH)_3$ and aqueous $As^{III}(OH)_3$. Several aqueous standards were used during fitting; however, the results containing different combinations of aqueous standards were often statistically indistinguishable from each other in terms of quality of fit according to the Hamilton test (Hamilton, 1965) at a >95% confidence interval.

Detection limits for individual As species were assumed to be 10% based on past reported estimates (Foster and Kim, 2014). Detection limits for individual Sb species were determined by merging pentavalent Sb or metallic Sb spectra with the trivalent spectrum at 5%, 7%, 10%, and 15% species abundance. The resultant spectrum was fit with linear combination fitting using a number of reference materials. The detection limit was chosen as the combination at which the software could first distinguish the added species from the trivalent species, with zero-valent and more reduced Sb oxidation states having a detection limit of 7% and pentavalent Sb having a detection limit of 10%.

The ARTEMIS package from DEMETER (Ravel and Newville, 2005) was used to fit theoretical standards to the EXAFS portion of the spectra for samples SP4, SP28, Sb6, and Sb21. The standards were generated using IFEFFIT (Newville, 2001) based on the crystal structures of forsterite [Mg_2SiO_4] (Boström, 1987), diopside [$MgCaSi_2O_6$] (Cameron et al., 1973), asbecasite [$Ca_3TiAs^{III}{}_6Be_2Si_2O_{20}$] (Sacerdoti et al., 1993), scorodite [$FeAs^{V}O_6H_4$] (Hawthorne, 1976), native As (Wyckoff, 1963), arsenolite (Ballirano and Maras, 2002), native Sb (Schiferl et al., 1981), Sb pentoxide (Jansen, 1979), and valentinite [$Sb^{III}{}_2O_3$] (Buerger and Hendricks, 1938). The chemistry of the forsterite and diopside standards was modified to include either As or Sb as the absorbing element in a variety of crystallographic sites. The amplitude reduction factor (S_o^2) was determined by fitting theoretical standards to the corresponding reference materials then fixing this value in the unknown fits. The scorodite and $As^{III}{}_2O_3$ reference materials were used to determine S_o^2 for the As samples acquired at APS, while $Sb^{III}{}_2O_3$ was used for the Sb samples acquired at HXMA. Fitting to the standard was completed in R-space using k weights of 1, 2, and, 3 simultaneously. The fitting range for the unknown spectra was from 3.0-3.5Å^{-1} to 10-12Å^{-1} in k-space and 1-1.3Å to 3-3.5Å in R-space resulting in 7 to 11 independent points as determined by the Nyquist method. Fitting was done using a Hanning window with sills of 1 in k-space and 0.5 in R-space. Modelling of the EXAFS was done by fitting the first shell to the data, followed by subsequent attempts to fit a second shell, resulting in 4 to 8 variables being used in the fitting procedure.

3.4. Results

3.4.1. Control of Oxygen Fugacity

The target fO_2s of experiments Sb24 and 25 were FMQ +2.5 and -2.0, respectively based on the composition of the initial metal-oxide mixture. These experiments used the "sliding buffer" method (see section 2.3.1). In both cases, the final fO_2 is shifted from values expected from the initial mixture, with the composition of the buffer phases after the experiments (Table 3.6 in SI) yielding fO_2 of FMQ +2.8±0.1 for Sb24 and FMQ -1.5±0.1 for Sb25. The fO_2 of the remaining experiments was fixed by the presence of both pure metal and metal oxide or a combination of two metal oxides. The value of the fO_2 as well as the buffer phases are provided in Table 3.1 and were calculated using the equations from O'Neill and Pownceby (1993a) for the Ni-NiO buffer, O'Neill (1986) for the Mo-MoO_2 buffer, O'Neill (1988) for the Fe_3O_4-Fe_2O_3 buffer, and O'Neill and Pownceby (1993b) for the MnO-Mn_3O_4 buffer. The presence of metal and metal oxides in the other fO_2 buffers was confirmed by a combination of EPMA, XRD and reflected light microscopy. Experiment Sb08 contained a manganese Sb oxide phase in addition to MnO and Mn_3O_4.

3.4.2. Run-Product Phases

The run-products from experiments consist of homogeneous glasses (Fig. 3.2a), which contained sub-micron sized particles of Pt or Pt+Sb. These particles are observed in backscattered electron images and in the time-resolved LA-ICP-MS spectra for platinum (Fig. 3.3c). Crystals of olivine or a low calcium pyroxene were also observed in some run-products. Several samples (Sb08, Sb16, Sb24, and Sb25) were saturated in an immiscible antimonide melt phase (Fig. 3.2b) which always segregated to the melt-vapor interface due to surface tension.

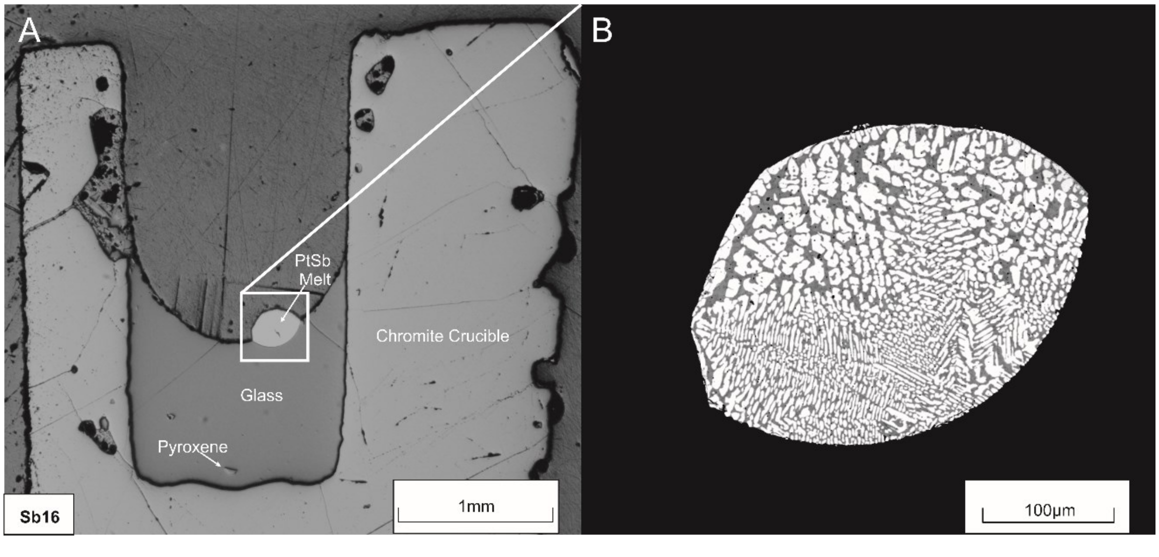

Figure 3.2 A) Reflected light image of a typical run-product with homogenous glass within a chromite crucible. The PtSb-melt is situated at the melt-vapor interface B) Backscatter electron image showing the quench exsolution phases of the PtSb melt bead. Dark phases are $PtSb_2$, while the lighter phases have a composition closer to PtSb. All images are from experiment Sb16 done at 1200°C, 0.1 MPa and FMQ -3.3.

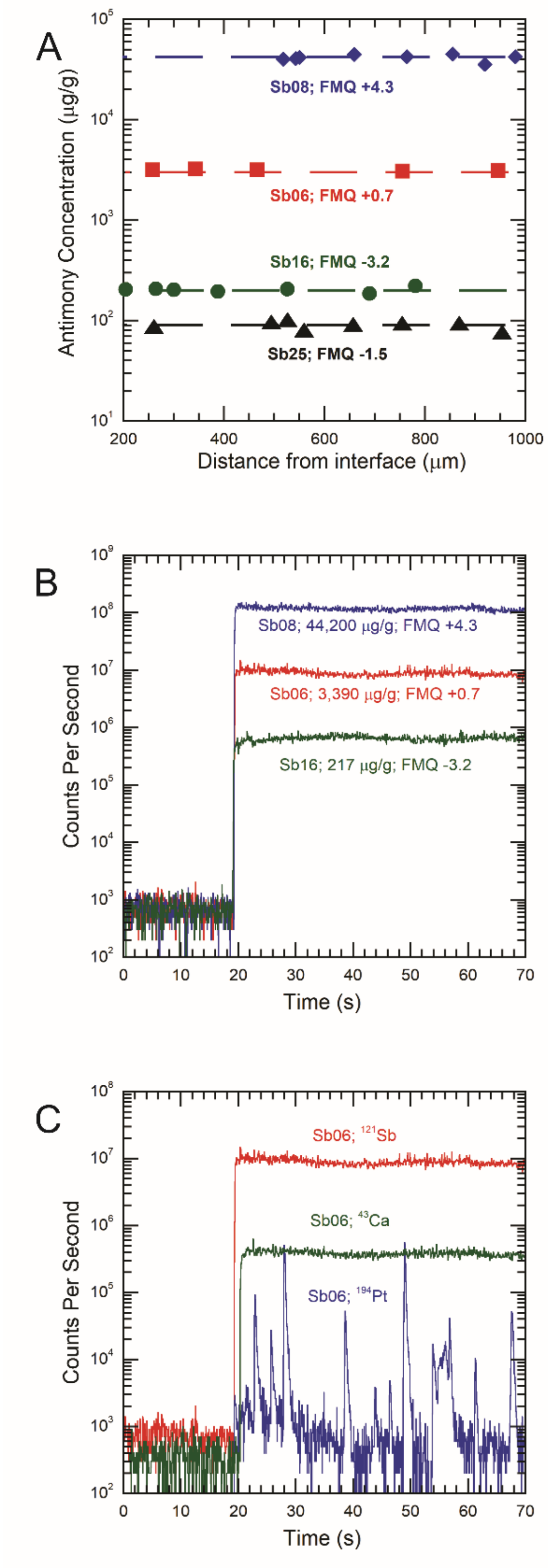

Figure 3.3 A) Analytical traverses across four samples synthesized at different *f*O$_2$ (as labelled) showing the Sb concentration as a function of distance from the melt-vapour interface. B) Examples of time-resolved LA-ICP-MS spectra from samples with different *f*O$_2$ and different Sb concentrations. C) Time-resolved spectra of ^{43}Ca, ^{194}Pt, and ^{121}Sb from experiment Sb06. Note the heterogeneity of the platinum signal in the glass, which is interpreted to reflect the presence of Pt micro-nuggets.

3.4.3. Approach to Equilibrium

The approach to chemical equilibrium was evaluated by analytical traverses of the run-product glasses from the bottom of the crucible to the melt-vapor interface. As shown in Fig. 3.3A, all the glasses were found to be homogeneous with respect to Sb concentration. Additionally, the time-resolved spectra of Sb from the individual analyses (Fig. 3.3B) are uniform indicating homogeneity within the depth of sampling, which is estimated to be 20 to 40 µm. The exception to this overall homogeneity is the distribution of platinum, which shows numerous oscillations in the time-resolved LA-ICP-MS spectra (Fig. 3.3C) due to the presence of micron-sized particles; however, these oscillations are not correlated with the Sb signal. Finally, the experiments of this study were of similar duration (96 hours), material, and method to that of the previous study of Canali et al. (2017), which found that 96 hours was sufficient to reach equilibrium. These authors reached this conclusion based upon sample homogeneity and reproducibility of results from runs of different durations.

3.4.4. XANES

3.4.4.1. Arsenic

The XANES spectrum of $As^{III}_2O_3$ is characterized by the main absorption peak (white line) at 11,870 eV, which is followed by an inflection on the back of the peak at 11,872 eV and a local minimum at 11,878 eV. In the post edge region, a second smaller (0.7 arbitrary units, a.u.) high by 3 eV wide) peak is located at 11,881 eV, which has been attributed to long-range distorted $As^{III}O_3$ groups and As-As backscatter (Borisova et al., 2010). The main absorption peak for the aqueous $As^{III}(OH)_3$ spectra from Borisova et al. (2010) is also located at 11,870 eV with a shoulder at 11,875 eV. The shape of this shoulder varies and appears to be a function of solution pH with higher pH resulting in a larger shoulder as As^{III} $(OH)_3$ becomes deprotonated to $As^{III}O_3^{3-}$ (Testemale et al., 2011). Scorodite and $As^{V}_2O_5$ are characterized by the white line positioned at 11,875 eV. The aqueous $As^{V}O(OH)_3$ reference materials (Borisova et al., 2010) are similar to the other As^{V} reference materials but contain a local minimum after the white line at 11,883 eV and a broad local maximum centred at 11,889 eV. The XANES spectrum of native As has the white line at 11,868.5 eV, which is much smaller than the $As^{III}_2O_3$ and $As^{V}_2O_5$

white line. Additionally, there is a small (0.06 a.u. high by 3 eV wide) post-edge feature at 11,878 eV.

Figure 3.4 shows the As K-edge XANES spectra of the basaltic glasses. All seven spectra are characterized by the peak absorption feature occurring at 11,870±1 eV, which corresponds to As^{III}. However, unlike the absorption peak in the $As^{III}_2O_3$ reference material, the basaltic glasses have a broader absorption peak that does not contain an inflection at 11,872 eV. Additionally, the post-edge peak at 11,877 eV is less pronounced (only 0.05 a.u.). Finally, the basaltic glasses do not have a local minimum after the absorption edge at 11,895 eV. Except for samples SP28 and SP7, the XANES spectra of the basaltic glasses are similar to that of the natural As-bearing rhyolite glass measured by Borisova et al. (2010). In that study, the differences between the rhyolite glass and reference materials spectra were ascribed to a lack of long-range distorted $As^{III}O_3$ groups and the absence of significant As-As backscatter in the volcanic glass. This reasoning is also likely the explanation for the differences between the basaltic glass in this study and the $As^{III}_2O_3$ reference material spectra.

The sample from the most oxidized experiment (SP28) and sample SP7 both have a shoulder peak located at 11,874±1 eV, which linear combination fitting determined to be a result of As^V in addition to As^{III} in these samples. The XANES spectrum of SP21, which was done at the most reduced conditions (FMQ -3.3), shows no evidence of zero-valent (As^0) or more reduced species (As^{-I} or As^{-III}) above minimum detection limits (estimated to be 10%). Table 3 provides a summary of the proportions of each oxidation state present in the glasses as determined by linear combination fitting, while Fig. 3.9 (supplementary information) shows the quality of the fit for two representative samples.

Despite having similar final experimental fO_2, there is a difference in the amount of As^V in SP28 and SP9, with SP28 containing ~15% As^V and less than detection limits (estimated to be 10%) in SP9. The difference in speciation between experiments SP9 and SP28 is attributed to the difference in their molar Fe/As ratio (see section 5.1). Samples SP8 and SP7 also have the same fO_2, but different proportions of As^V(11±4% in SP7 vs < 10% in SP8); however, in this case, the speciation is essentially the same when considering detection limits and associated errors.

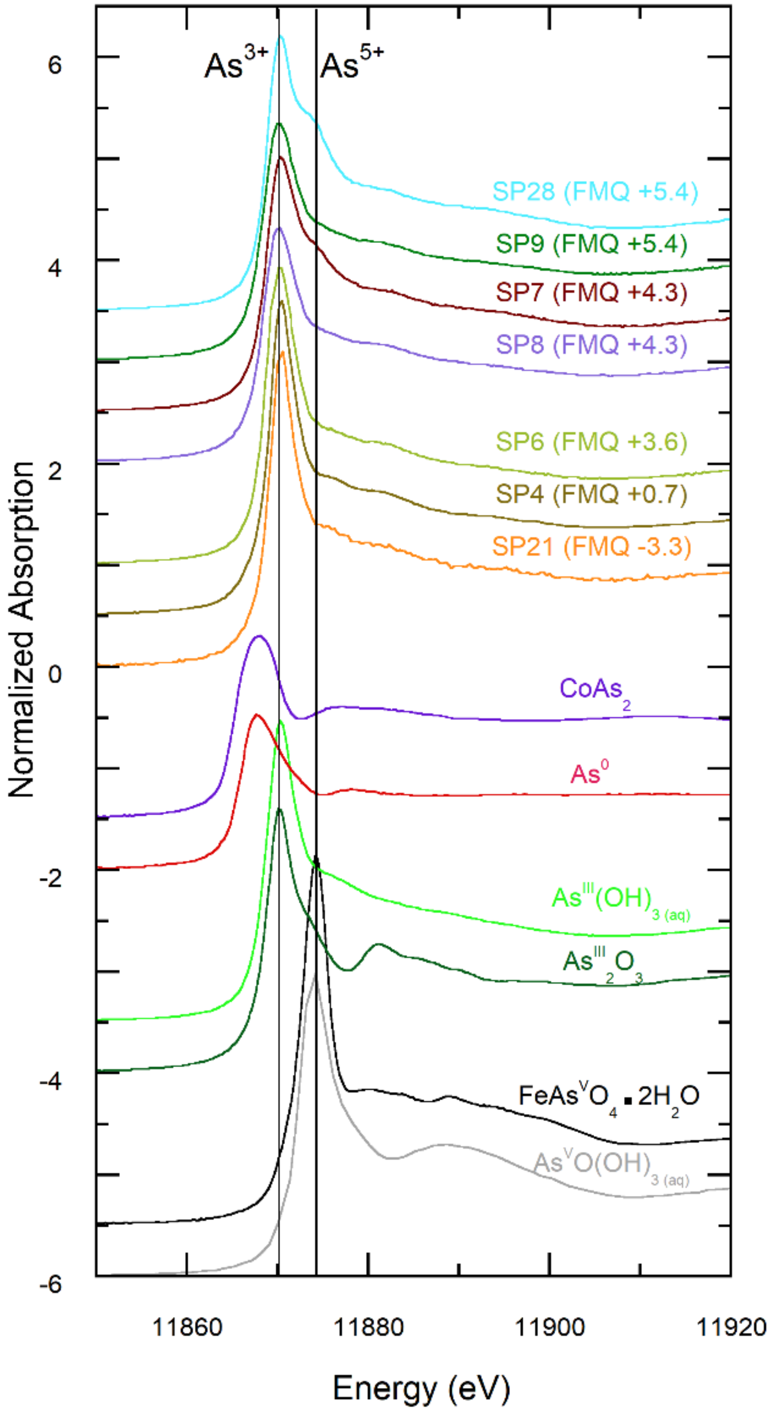

Figure 3.4 Normalized absorption at the As K-edge as a function of energy (eV) for As-bearing glasses synthesized at various fO_2 (as labelled). A selection of reference materials (As^0, $CoAs_2$, $As^{III}{}_2O_3$, aqueous $As^{III}(OH)_3$, aqueous $As^VO(OH)_3$, and $FeAs^VO_4{\cdot}2H_2O$) are also plotted for comparison. Spectra are offset vertically for clarity. Vertical lines indicate the white line position for As^{III} and As^V. Spectrum for $As^{III}{}_2O_3$ was obtained from the spectral library at the CLS. The spectra for aqueous As^{III} $(OH)_3$ and aqueous $As^VO(OH)_3$ are from Borisova et al. (2010).

3.4.4.2. *Antimony*

The XANES spectrum of $Sb^{III}{}_2O_3$ is characterized by a single broad (5 eV wide) peak centred at 30,518 eV and a small (0.01 a.u.) feature in the post edge region at 30,497 eV. The pre-edge region is characterized by a gradual rise in absorption. The peak position in the aqueous $Sb^{III}(OH)_3$ spectra has a similar energy to $Sb^{III}{}_2O_3$, but the peak of $Sb^{III}(OH)_3$ is less intense than $Sb^{III}{}_2O_3$. Additionally, the $Sb^{III}(OH)_3$ spectrum has a broad shoulder (14 eV wide), centred at 30,512 eV. The aqueous $Sb^{V}(OH)_5$ spectrum has a relatively intense absorption peak (1.6 a.u. compared to 1.4 a.u. for $Sb^{III}{}_2O_3$) at 30,504 eV and a shoulder peak at 30,520 eV. Metallic Sb does not have a pronounced absorption peak, instead, it is characterized by a small peak (0.1 a.u. above the edge) at 30,496 eV followed by strong oscillations throughout the post-edge region.

Figure 3.5 depicts the XANES spectra of the Sb-bearing glasses with each displaying a single broad peak centred at 30,497±1 eV, similar to the Sb^{III} reference materials. At energies greater than the peak absorption feature, the intensity of the spectrum gradually decreases until a minimum at 30,528 eV. Unlike the aqueous $Sb^{III}(OH)_3$ reference material, the basaltic glass samples do not show a shoulder near 30,518 eV.

Linear combination fitting (Fig. 3.9 in SI) was used to identify the different species of Sb present and their proportions (summarized in Table 3.3). Trivalent Sb was the only species found in the samples. Zero-valent (Sb^0) and reduced Sb species (Sb^{-III}) were below the minimum detection limits (estimated to be 7%) in the most reduced samples and Sb^V was below the minimum detection limits (estimated to be 10%) in the most oxidized samples.

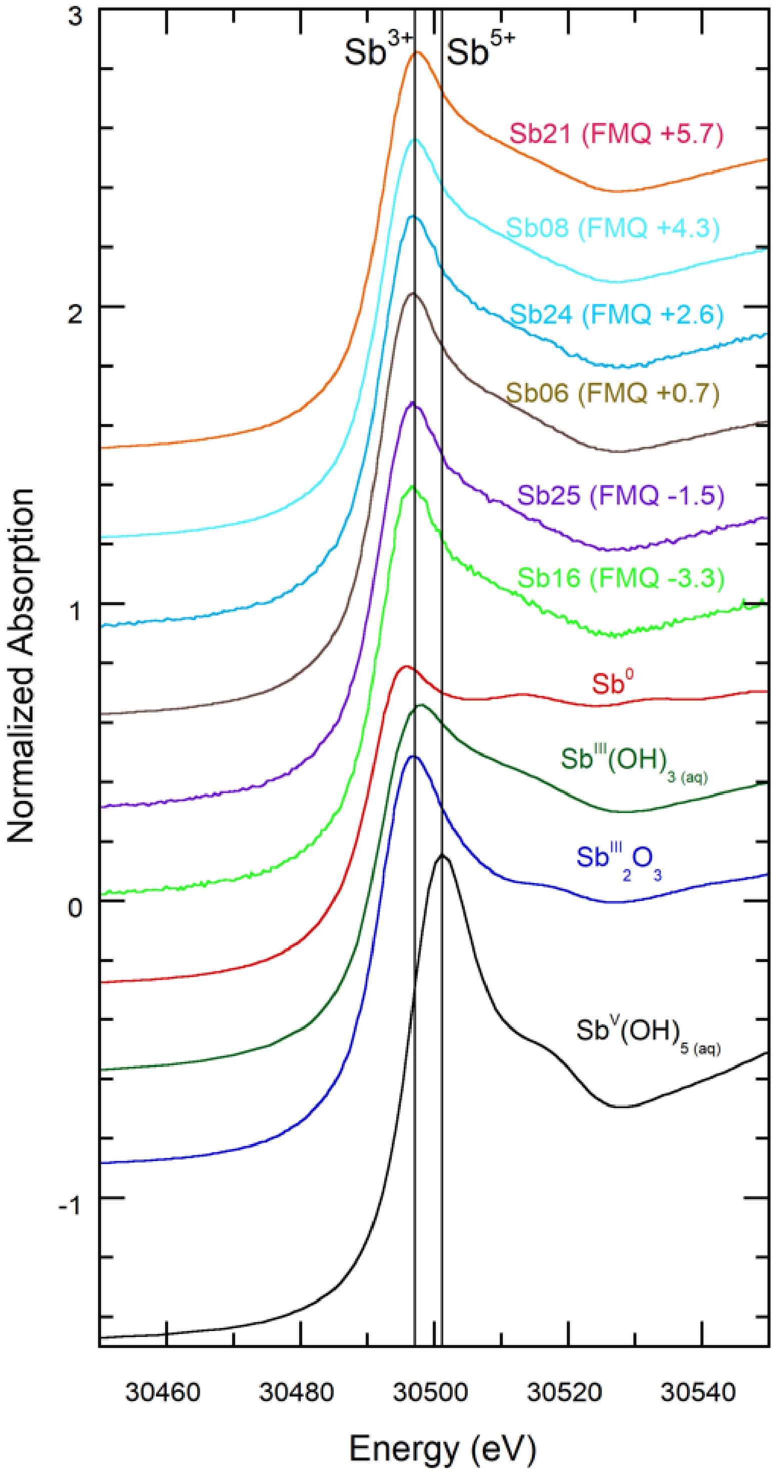

Figure 3.5 Normalized absorption at the Sb K-edge as a function of energy (eV) for Sb-bearing glasses synthesized at various *f*O2 (as labelled). A selection of reference materials (Sb0, $Sb^{III}_2O_3$, aqueous $Sb^{III}(OH)_3$ and aqueous $Sb^{V}(OH)_5$) are also plotted for comparison. Spectra are offset vertically for clarity. Vertical lines indicate the white line position for Sb^{III} and Sb^{V}. The aqueous $Sb^{III}(OH)_3$ spectrum is from Pokrovski et al. (2006) and the aqueous $Sb^{V}(OH)_5$ spectrum is from Tella and Pokrovski (2012).

Table 3.3 Results from linear combination fitting

Exp. ID	As or Sb	ΔFMQ	Trivalent Species (As^{III} or Sb^{III})	Pentavalent Species[b] (As^{V} or Sb^{V})	Fe/As or Fe/Sb Ratio (molar)	Goodness of Fit (R-factor[c])	Best Combination of linear combination fitting reference material [a]
SP21	As	-3.3	>90%	<10%	14200	0.00541	98% $As^{III}(OH)_3$, pH 5; 2% $As^{III}_2O_3$
SP4	As	+0.7	>90%	<10%	147	0.00253	100% $As^{III}(OH)_3$, pH 5
SP6	As	+3.6	>90%	<10%	6.67	0.00387	100% $As^{III}(OH)_3$, pH 5
SP8	As	+4.3	>90%	<10%	1.36	0.00470	61% $As^{III}(OH)_3$, pH 11; 39% $As^{III}_2O_3$
SP7	As	+4.3	90%±4%	10%±4%	6.52	0.000489	69% $As^{III}(OH)_3$, pH 5; 20% $As^{III}(OH)_3$, pH 11; 11% $As^{V}O(OH)_3$, pH 2
SP9	As	+5.4	>90%	<10%	1.36	0.00175	53% $As^{III}(OH)_3$, pH 11; 47% $As^{III}_2O_3$
SP28*	As	+5.4	85±7%	15±5%	0.38	0.00261	85% $As^{III}(OH)_3$, pH 5; 15% $As^{V}O(OH)_3$, pH 2
Sb16	Sb	-3.3	>90%	<10%	960	0.000259	43% $Sb^{III}_2O_3$; 57% $Sb^{III}(OH)_3$
Sb25	Sb	-1.5	>90%	<10%	1380	0.000132	62% $Sb^{III}_2O_3$; 38% $Sb^{III}(OH)_3$
Sb06	Sb	+0.7	>90%	<10%	77.8	0.0119	52% $Sb^{III}_2O_3$; 48% $Sb^{III}(OH)_3$
Sb24	Sb	+2.8	>90%	<10%	666	0.00318	54% $Sb^{III}_2O_3$; 46% $Sb^{III}(OH)_3$
Sb08	Sb	+4.3	>90%	<10%	4.32	0.000526	42% $Sb^{III}_2O_3$; 58% $Sb^{III}(OH)_3$
Sb21	Sb	+5.7	>90%	<10%	15.9	0.000577	48% $Sb^{III}_2O_3$; 52% $Sb^{III}(OH)_3$

*Spectra was corrected for self-absorption.

[a] Represents the best combination of the reference materials employed to replicate the basaltic glass spectra. The presence of a reference materials used in the linear combination fit does not imply this species is in the sample. The percentage of each oxidation state present in the sample is a combination of species identified by the linear combination fitting fits.

[b] Detection limits are estimated as 10%.

[c] Equation for the r-factor is provided in the Supplementary Information.

3.4.5. EXAFS

The structural parameters for the best fits of theoretical standards to the synthetic glasses are detailed in Table 3.4 and shown in Fig. 3.6. At reduced conditions, As appears to be coordinated by 3.1±0.7 oxygens at a bond distance of 1.78±0.01 Å, while at oxidized conditions As is coordinated by 3.5±1.0 oxygens at a bond distance of 1.75±0.02 Å. The small decrease in the average atomic bond length between these two samples is attributed to the two oxidation states present in this sample as As^V would hold oxygens closer than As^{III}. This would also explain the increase in coordination along with its associated larger error. Fitting an oxygen shell for each valence state did not result in a statistically better fit for the collected data. The interatomic Sb-oxygen bond distance is approximately the same at oxidized conditions (1.983±0.004 Å) and reduced conditions (1.974±0.004 Å). Additionally, the calculated coordination number of Sb decreases from 3.4±0.2 to 2.9±0.2 with increasing fO_2. Only the first shell was fit with confidence, as attempts to fit a second shell of Si, Ca, Mg, Fe, Al, As or O based on a diopside or olivine melt structure yielded unrealistic bond length disorder terms (σ^2), and coordination numbers (CN). Several multiple scattering paths were also attempted, but they did not improve the quality of fit.

Table 3.4 Best fit structural parameters from EXAFS for the first oxygen shell for As and Sb bearing basaltic glasses

Sample	As or Sb	Amplitude reduction Factor (S_0^2)	Coordination number*	Bond length (Å)	Bond disorder: $\sigma^2 \times 10^3$ (Å^2)	Energy shift (eV)	Goodness of fit (R-factor)	Degrees of Freedom in fit[a]
SP4	As	0.81±0.16	3.1±0.7	1.782±0.010	2.6±1.6	8.6±1.5	0.015	5
SP28	As	0.84±0.09	3.5±1.0	1.752±0.022	4.9±3.4	8.2±3.7	0.042	4
Sb06	Sb	0.98±0.07	3.4±0.2	1.973±0.004	5.7±0.6	6.5±0.6	0.0022	5
Sb21	Sb	0.98±0.07	2.9±0.2	1.981±0.004	3.4±0.6	8.6±0.6	0.0029	5

*Coordination number error includes the error from S_0^2.

[a] Degrees of Freedom equals the number of independent points in the spectrum minus the number of variables used in the fit

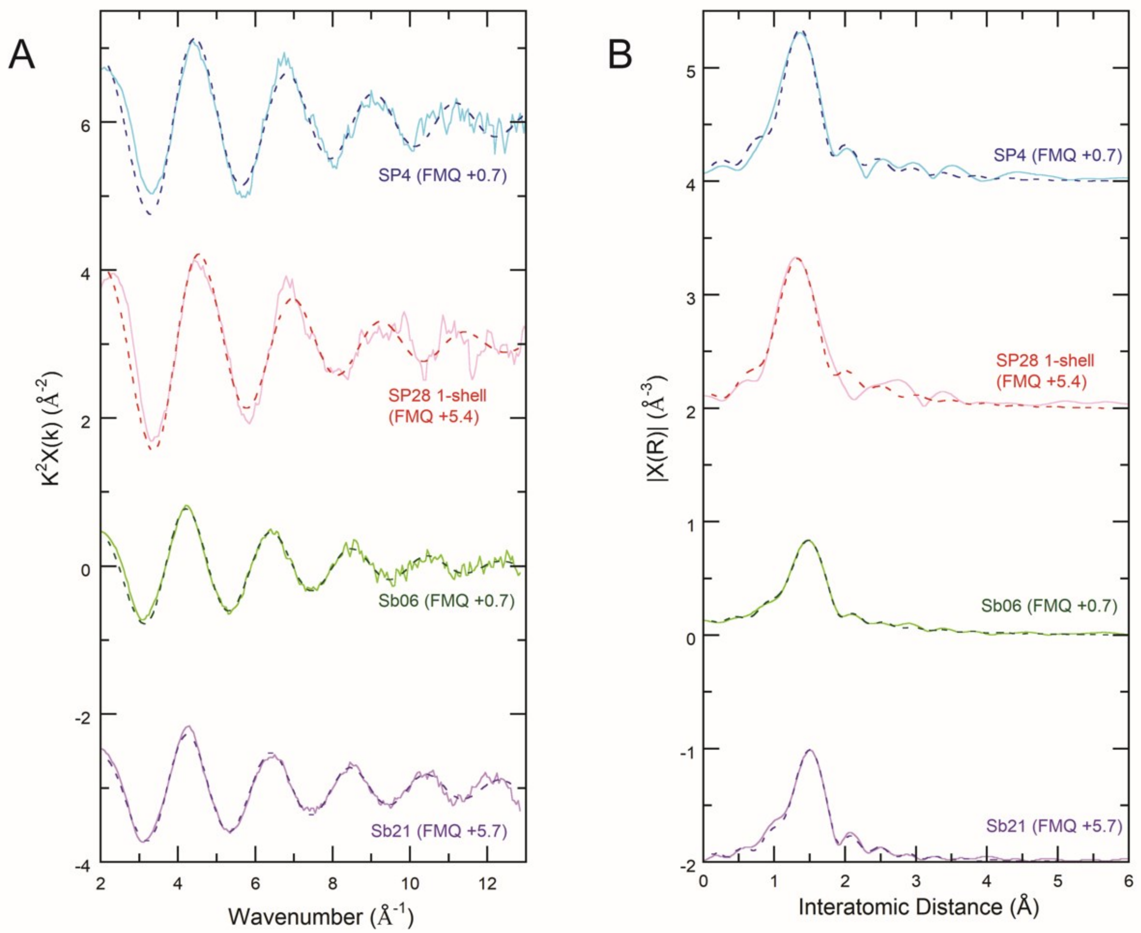

Figure 3.6 Arsenic (SP28 and SP4) and Sb (Sb21 and Sb06) EXAFS spectra (solid lines) and best theoretical model fit for each spectrum (dashed line) displayed in both (A) k-space and (B) in the Fourier transform (not corrected for phase shift).

3.5. Discussion

3.5.1. Correction for the Effect of Iron on the Measured Redox State

The presence of both ferric and ferrous iron in the experiments of this study means charge transfer reactions could occur during the quench and affect the speciation of As and Sb (Borisov, 2013). This charge transfer reaction has the form:

$$\mathrm{Me}^{5+} + 2\mathrm{Fe}^{2+} \leftrightarrow \mathrm{Me}^{3+} + 2\mathrm{Fe}^{3+} \quad (3.6)$$

Where Me is either As or Sb.

As the speciation measurements of this study are performed on quenched glasses and not the melt at 1200°C, the effect of iron on the quenched speciation needs to be considered so that the behavior of As or Sb at magmatic conditions can be determined. Borisov (2013) provides a quantitative evaluation of this correction, details of which can be found in the Supplementary Information. Other redox-sensitive elements such as chromium will also be involved in these redox reactions; however, due to its low concentration relative to iron its effect on arsenic speciation will be negligible.

The amount of reduction/oxidation that occurs will strongly depend on the molar iron to metalloid ratio (Fe/M). Higher ratios will result in a minor change to the ferric/ferrous ratio, but complete removal of a single metalloid species, while a lower ratio will have the opposite effect. Ratios near one may have an impact on the speciation of both elements. As the experiments of this study have different molar Fe/M ratios the effect of quenching will be different for each sample resulting in different speciation even for samples synthesized at the same fO_2. This effect is observed for samples SP9 and SP28. Figure 3.7a shows how the same melt speciation curve would be shifted at a fixed molar Fe/As ratio for these two experiments. Sample SP9 has a molar Fe/As ratio of 1.36 and the calculation shows that 41% of the As^V present would reduce to As^{III} upon quenching, whereas only 12% of the As^V present would be reduced to As^{III} in sample SP28 which was synthesized at the same fO_2 but has a Fe/As ratio of 0.381. Therefore, a change in the Fe/As ratio can explain the difference between the linear combination fitting results of SP9 and SP28 as seen in Table 3.4 and Fig. 3.7a. Regardless of the Fe/As ratio, quenching in the presence of iron results in the stabilization of As^{III} in the glass. Thus, the abundance of the oxidized species will be underestimated in the quenched glass compared to the melt phase.

After correcting for iron the ratio of As species present in the melt as a function of fO_2 (Fig. 3.7b) can be described assuming a two-electron transition as:

$$\log\frac{\mathrm{As^V}}{\mathrm{As^{III}}} = \frac{1}{2}\log fO_2 + \frac{6549}{T} - 3.8 \pm 0.9 \qquad (3.7)$$

This equation describes the sigmoidal change in As speciation as a function of fO_2. Details on how this equation was derived and the underlying thermodynamic values used are found in the Supplementary Information. Equation 3.7 along with Fig. 3.7b illustrates that at 1200°C the pentavalent species will not contribute to more than 1% of the As budget until the fO_2 is greater than FMQ +3.2±0.9. At FMQ +5.3±0.9 and FMQ +7.2±0.9, As^V will contribute to 10% and 50% of the total As budget at 1200°C, respectively.

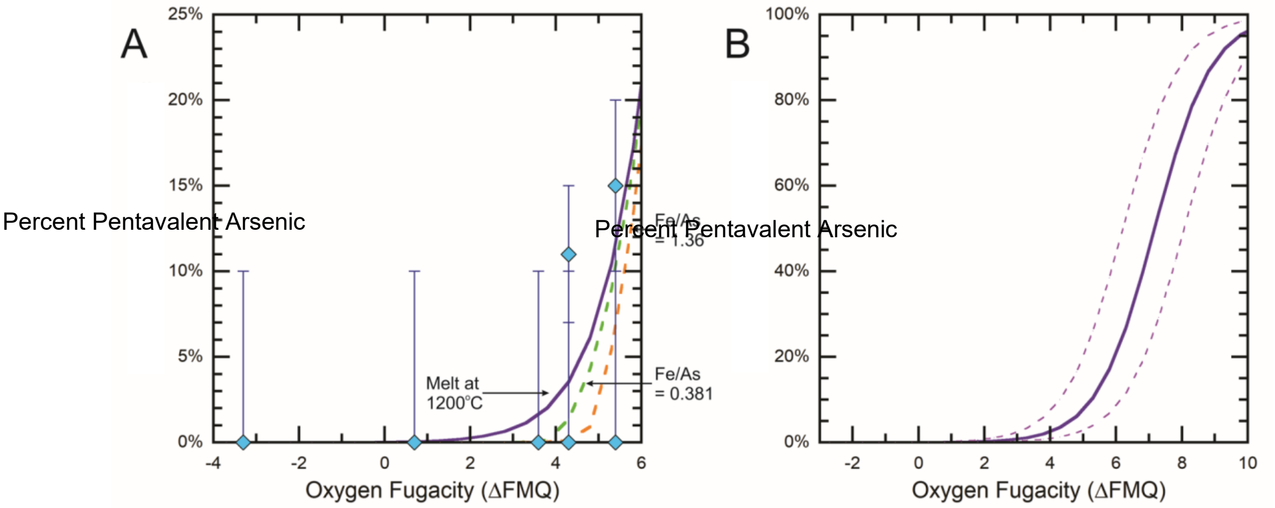

Figure 3.7 Speciation of As in basaltic glass. A) Effect of iron on As speciation. Diamonds correspond to the XANES linear combination fitting results. The solid curve represents the species in the melt, while the dashed curves are the speciation of quenched glass at different Fe/As ratios (Fe/As = 0.381 from SP28; Fe/As = 1.36 from SP9). Speciation in the glass was determined using the method of Borisov (2013) for a glass transition temperature of 700°C, calculated using the method of Giordano et al. (2008). B) The overall speciation-fO_2 relationship for As at 1200°C displayed relative to FMQ. The best-fit curve is the solid line ($\chi^2 = 0.085$), while the dashed lines represent the error in the fit ($\chi^2 > 0.12$).

As no pentavalent Sb was detected it is not possible to apply an iron correction to these experiments. However, the amount of pentavalent Sb measured in the glasses could be underestimated as a result of the reduction effect of iron. Assuming 10% Sb^V in the most oxidized sample and compensating for the iron effect could result in the melt phase containing up to 20% Sb^V at FMQ +5.7. Extrapolating this speciation-fO_2 relationship would result in only 1% Sb^V occurring at FMQ +2.8 and negligible Sb^V at conditions more reducing.

3.5.2. Comparison with Existing Speciation Measurements in Silicate Melts and Glasses

A comparison between the speciation-fO_2 results determined in this study to previous measurements on silicates melt and glasses for both As and Sb is provided in Table 3.5. For studies that determined a change in speciation as a function of fO_2, the fO_2 corresponding to the transition from trivalent dominant to pentavalent dominant is also reported in the table in brackets.

3.5.2.1. Arsenic

The As speciation determined in this study is consistent with the results from Borisova et al. (2010), and with all but samples SP7, and SP28 from Canali et al. (2017). The L_{III}-edge XANES spectra for these samples did not reveal any As^{V}, compared to the spectra reported here, which contained 10±4% As^{V} and 15±5% As^{V}, respectively. This discrepancy is attributed to the spectral interference from the magnesium K-edge on the As L_{III}-edge measured by Canali et al. (2017), which would mask the presence of As^{V}, at the levels measured in this study. Schreiber and Coolbaugh (1995) observed 4.7% As^{V} at FMQ +3.0 for which only 0.9% As^{V} was measured in this study. This difference is most likely related to the effect of melt composition on speciation, as the higher alkali content of the borosilicate glass (17.7% wt.% Na_2O vs. 0.82 wt.% Na_2O+K_2O) employed by Schreiber and Coolbaugh (1995), may have stabilized the oxidized species at lower fO_2 (Pyare and Nath, 1991). Guo (2008) did not report any As^{V} at conditions in which this species was detected here; however, the sensitivity of XPS for each species was not reported. The measurements from this study are inconsistent with the conclusions of Siebert et al. (2011), who used metal/silicate melt partitioning to suggest As^{V} as the dominant oxidation state for mafic silicate melts at fO_2 below the iron-wüstite buffer. The experimental conditions employed by Siebert et al. (2011) are quite different from this study (3 GPa vs 0.1 MPa; 1850-2200°C vs. 1200°C) and moreover, the small fO_2 range (1.5 log units) investigated would result in considerable uncertainty in their speciation estimation. An indirect method to determine As speciation can be obtained by investigating sulfide liquid/silicate melt partitioning as a function of either fO_2 or silicate melt FeO content (Li and Audétat, 2015; Li and Audétat, 2012). Although the speciation determined by such methods could be complicated by the presence of multiple valence states in both the silicate melt (As^{III} or As^{V}) and in the sulfide phases (As^{III} or As^{-I}), or activity coefficients changing as a function of fO_2, results of these studies are consistent with predominately As^{III} in the silicate melt at overlapping fO_2 conditions.

Table 3.5 Summary of oxidation state measurements for As and Sb from the literature

Redox State	Pressure (MPa)	Temperature (°C)	fO_2 (ΔFMQ)	Method	Melt Composition	Fe/As or Fe/Sb Ratio	Reference
Arsenic							
As^{III} & As^{V}	0.1	1200	-3.3 to +5.5 [+7.2±0.9*]	XANES (K-edge)	Synthetic basalt	0.38 to 14000	This Study
As^{III}	n/a	800	-3.6 to 0	XANES (K-edge)	Macusani Rhyolite	15	Borisova et al. 2010
As^{III}	0.1	1200	-3.3 to +5.5	XANES (L-edge)/ As solubility^{a}	Synthetic basalt	0.4 to 14000	Canali et al. 2010
As^{III} & As^{V}	0.1	1150	+5.6*	Colorimetric /complexometric titrations	Na-borosilicate glass^{b}	n/a	Schreiber and Coolbaugh 1995
As^{III}	200	800	+2.5 & +4.5	XPS	Haplogranite (Na_2O-K_2O - Al_2O_3-SiO_2 glass)^{b}	n/a	Guo, 2008
As^{V}	3000	1850 & 2200	-6.4 to -5.5	Metal/silicate melt Partitioning Vs. fO_2^{a}	Peridotite, and olivine tholeiite basalt	n/a	Siebert et al. 2011
As^{III}	1500	1175 to 1200	-3.1 to +1	Sulfide/Silicate Melt Partitioning Vs. fO_2^{a}	Hornblendite	n/a	Li and Audétat 2012
As^{III}	500 to 1500	1000 to 1200	-1.7 to +3	Sulfide/Silicate Melt Partitioning Vs. FeO^{a}	Synthetic MORB and, dacite plus natural andesite, and rhyolite	n/a	Li and Audétat 2015
Antimony							
Sb^{III}	0.1	1200	-3.3 to +5.5	XANES (K-edge)	Synthetic basalt	4.3 to 960	This Study
Sb^{III} & Sb^{V}	0.1 and 1000	1300 & 1400	-4.7 to +11 [+9.0±0.4*]	XANES (K-edge)	Alkali free synthetic MORB	2.6 to 23000	Miller et al. 2019
Sb^{III} & Sb^{V}	0.1	1300	-4.7 to 7.3 [+6.9±0.2*]	XANES (K-edge)	CaO-Al_2O_3-MgO-SiO_2 glass (Longhi2)^{b}	n/a	Miller et al. 2019
Sb^{III} & Sb^{V}	0.1	1300	-4.7 to 7.3 [+9.3±0.5*]	XANES (K-edge)	CaO-Al_2O_3-MgO-SiO_2 glass (Longhi3^{b}	n/a	Miller et al. 2019
Sb^{III} & Sb^{V}	0.1	1300 & 1400	-4.7 to +11 [+5.8±0.3*]	XANES (K-edge)	CaO-Al_2O_3-SiO_2 glass (CAS1)^{b}	n/a	Miller et al. 2019
Sb^{III} & Sb^{V}	0.1 and 1000	1300 & 1400	-4.7 to +11 [+7.6±0.1*]	XANES (K-edge)	CaO-Al_2O_3-SiO_2 glass (CAS4)^{b}	n/a	Miller et al. 2019

Redox State	Pressure (MPa)	Temperature (°C)	$f\mathrm{O}_2$ (ΔFMQ)	Method	Melt Composition	Fe/As or Fe/Sb Ratio	Reference
$\mathrm{Sb}^{\mathrm{III}}$ & Sb^{V}	0.1and 1000	1300 &1400	-4.7 to +11 [+8.2±0.4*]	XANES (K-edge)	CaO-$\mathrm{Al}_2\mathrm{O}_3$-$\mathrm{MgO}$-$\mathrm{SiO}_2$ glass (CMAS7G)[b]	n/a	Miller et al. 2019
$\mathrm{Sb}^{\mathrm{III}}$	1000 to 3000	1400	-1.2 to 0.2	XANES (K-edge)	Synthetic Andesite	130	Miller et al. 2019
$\mathrm{Sb}^{\mathrm{III}}$ & Sb^{V}	0.1	1150	+8.4*	Colorimetric /complexometric titrations	Na-borosilicate glass[b]	n/a	Schreiber and Coolbaugh 1995
$\mathrm{Sb}^{\mathrm{III}}$ & Sb^{V}	200	800	+6.8	XPS	Haplogranite ($\mathrm{Na}_2\mathrm{O}$-$\mathrm{K}_2\mathrm{O}$ -$\mathrm{Al}_2\mathrm{O}_3$-$\mathrm{SiO}_2$ glass)[b]	n/a	Guo, 2008
Sb^{V}	200	800	+5.2	XPS	Haplogranite ($\mathrm{Na}_2\mathrm{O}$-$\mathrm{K}_2\mathrm{O}$ -$\mathrm{Al}_2\mathrm{O}_3$-$\mathrm{SiO}_2$ glass)[b]	n/a	Guo, 2008
$\mathrm{Sb}^{\mathrm{III}}$	0.1 to 15000	1260 to 2150	-4.6 to -1.4	Metal/silicate melt Partitioning Vs. $f\mathrm{O}_2$[a]	Basalt, and eucritic basalt	n/a	Righter et al 2009
$\mathrm{Sb}^{\mathrm{III}}$ & Sb^{V}	0.1	1250	-3.5 to +7	Rutile/ silicate melt Partitioning $f\mathrm{O}_2$[a]	Synthetic andesite and rhyolite	n/a	Klemme et al. 2005
$\mathrm{Sb}^{\mathrm{III}}$	1500	1400	-0.9	Sulfide/Silicate Melt Partitioning Vs. FeO[a]	Synthetic MORB and CaO-$\mathrm{Al}_2\mathrm{O}_3$-$\mathrm{MgO}$-$\mathrm{SiO}_2$ glass[b]	n/a	Kiseeva and Wood 2013
$\mathrm{Sb}^{\mathrm{III}}$	1500	1400 to 1700	-0.9	Sulfide/Silicate Melt Partitioning Vs. FeO[a]		n/a	Kiseeva and Wood 2015
$\mathrm{Sb}^{\mathrm{III}}$	1500	1175 to 1200	-3.1 to +1	Sulfide/Silicate Melt Partitioning Vs. $f\mathrm{O}_2$[a]	Hornblendite (AG4)	n/a	Li and Audétat 2012
$\mathrm{Sb}^{\mathrm{III}}$	500 to 1500	1000 to 1200	-1.7 to +3	Sulfide/Silicate Melt Partitioning Vs. FeO[a]	Synthetic MORB and, dacite plus natural andesite, and rhyolite	n/a	Li and Audétat 2015

*$f\mathrm{O}_2$ value at which both oxidation states are present in equal proportions; [a]model dependent; [b]Iron free composition.; MORB stands for Mid ocean ridge basalt; n/a is not applicable or not available

3.5.2.2. Antimony

The results of this study show that Sb^{III} is the dominant oxidation state over the fO_2 range investigated, with less than 10% Sb^{V} indicated even for the most oxidized experiments (Sb21; FMQ +5.7). This speciation trend is consistent with the results of Schreiber and Coolbaugh (1995) which predict only a small contribution from Sb^{V} (<5%) at the highest fO_2 conditions reported here. When the results of the current study are extrapolated to 1300°C using the enthalpy of the Sb^{III} to Sb^{V} reaction (from Borisov, 2013 and reference therein), the absence of Sb^{V} in the glasses is also consistent with the speciation-optical basicity and speciation-wt.% CaO relationships determined by Miller et al. (2019) for alkali-free basaltic glasses. However, the NBO/T – speciation relationship determined by Miller et al. (2019) predicts > 30% Sb^{V} in the most oxidized sample reported here, which was not observed. This discrepancy indicates that NBO/T may not be an accurate predictor of speciation beyond the composition limits of the Miller et al. (2019) study.

Based upon the observed variation in sulfide liquid/silicate melt partitioning as a function of silicate melt FeO content, Kiseeva and Wood (2013) concluded that Sb^{III} is the dominant oxidation state in both the sulfide and silicate melt at FMQ -0.9. In contrast, Guo (2008) reported results with only Sb^{V} at FMQ +5.2 and mixed Sb^{III} and Sb^{V} at more oxidized conditions of FMQ +6.8. The stabilization of Sb^{V} in the experiments of Guo (2008) compared to the predominance of Sb^{III} reported in the current study, could be explained by the higher alkali content of the granitic melt employed. However, the alkali effect does not explain why significant Sb^{V} is stabilized in the Guo (2008) experiments when compared to those of Schreiber and Coolbaugh (1995).

As Sb^{V} should be more compatible than Sb^{III} in rutile based on ionic size and charge consideration, rutile/melt partitioning can also be used to infer speciation. Results of rutile/melt partitioning experiments done by Klemme et al. (2005) revealed an increase in the partition coefficient for Sb with increasing fO_2 (up to FMQ +6.8), suggesting the presence of Sb^{V} at the high end of the fO_2 range investigated. Assuming a maximum rutile/melt partition coefficient for Sb^{V} similar to Ta^{V} determined by Klemme et al. (2005), this would imply that only 2% Sb^{V} is needed to reach the observed partition coefficient of 2.1 at FMQ +6.8. Such a small amount of Sb^V is consistent with the results presented here.

3.5.3. Comparison with Arsenic and Antimony Speciation in Aqueous Fluids

This study has shown that As is predominantly in the trivalent state and coordinated to three oxygens over a large range of fO_2 in basaltic melts. Structural studies of As in hydrothermal fluids (Pokrovski et al., 2002, and Testemale et al., 2011) yield similar results in terms of oxidation state and coordination (Fig. 3.4 and Table 3.4). One small difference is that the XANES spectra of As^{III} in basaltic melts does not contain the intensity drop at the base of the white line, which is indicative of $As^{III}O_3^{3-}$ not $As^{III}(OH)_3$ (Testemale et al., 2011). In experiments involving hydrothermal fluids done at 500°C and 60 MPa, Pokrovski et al. (2002) determined that trivalent As is coordinated to 3 oxygens at a distance of 1.78-1.79 Å, which is the same bond distance and coordination determined by EXAFS in the current study. Testemale et al. (2011) also derived the same structural parameters for aqueous fluids at pH 5.4 and 11 at ambient temperatures and pressures (20°C, 0.1 MPa). The bond disorder or mean square relative displacement (σ^2) determined from all three studies overlap within error. For the case of hydrothermal fluids containing As^V, Testemale et al. (2011) measured bond lengths of 1.70 ± 0.01 Å with the coordination increasing to 4 oxygens. This is consistent with the decreased bond lengths in the glass from experiment SP28 as it contains components of both As^{III} and As^V.

The XANES spectra for Sb in basaltic melt are also similar to that determined for $Sb^{III}(OH)_3$ in hydrothermal fluid at 300°C and 60 MPa (Pokrovski et al., 2006), but with the amplitude of the melt white line 10-15% greater than that of $Sb^{III}(OH)_3$. Of the various hydrothermal fluids studied by Tella and Pokrovski (2009) the shape of the XANES spectrum for Sb in the basaltic glass is most similar to the fluid at a pH of ~0, as they both contain a more intense primary absorption peak relative to the hydrothermal fluid at pH 5 measured by Pokrovski et al. (2006). The large absorption peak in the more acidic fluid is attributed to 4-fold coordinated Sb with two oxygen bonds and two OH^- bonds, resulting in significant bond disorder (Tella and Pokrovski, 2009). There was also no evidence for a second OH^- shell observed in the EXAFS signal for the basaltic glass.

The average coordination number determined by EXAFS for the basaltic glass (3.1±0.4) is lower than the value found in the pH 13 fluid (4.9±0.6) determined by Tella and Pokrovski (2009), while the average bond length in the glass (1.98±0.01 Å) is approximately the same as the bond lengths in the pH 5 fluid (1.96±0.01 Å; Pokrovski et al., 2006).

As previously described by Borisova et al. (2010), the similarity of As speciation in both felsic silicate melts and aqueous fluids indicates that As partitioning behavior is controlled by the oxy-hydroxide species, thus partition coefficients should be near unity. This conclusion is supported by the experimental measurements of Guo (2008) and Simon et al. (2007). Guo (2008) found that the average fluid/melt partition coefficient between a granitic melt and an aqueous fluid was 1.4±0.5 at 800°C and 200 MPa, and was insensitive to changes in melt composition and fO_2 (up to FMQ +6.2). Simon et al. (2007) measured the fluid/melt partition coefficient between a rhyolite melt and a low salinity vapor to be 1.0±0.1 at 800°C, 120 MPa and FMQ +0.84 in the absence of sulfur. In sulfur-bearing experiments (0.7 molar S in the vapor) the fluid/melt partition coefficient increased to 2.5±0.3, which the authors attributed to the presence of an As-sulfur species in the vapor phase. The similarity of the As species in the basaltic melt found in this study and the As species in an aqueous fluid reported previously suggests that fluid/basalt partitioning should also be near unity. At very high fO_2, as As^V becomes more prevalent in the melt, it is possible for the fluid/melt partitioning to change due to dissimilarity of the fluid and melt species; however, if the fluid speciation changes with the melt speciation, which is the case up to FMQ +6.2 based on the measurements of Guo (2008), then the fluid/melt partitioning should remain near unity.

Owing to the similarity in the species of Sb in pH 5 hydrothermal fluids and basaltic melts, the partition coefficient should also be near unity. As the species in the fluid changes with pH, it is possible that the partitioning will also vary but in an unknown way. Guo (2008) found that the fluid/granitic-melt partitioning of Sb increased from 0.1 to 1.3 as the melt alumina saturation index increased from 0.65 to 1.31. Additionally, Zajacz et al. (2008) measured fluid/melt partition coefficients for Sb to be between 1-10 in naturally occurring coexisting melt and low chlorinity fluid inclusion pairs; however, they also found much greater partition coefficients (45.8±15.6) involving fluids with a chlorinity of m_{Cl}= 12.74.

3.5.4. Structure of Arsenic and Antimony in Silicate melt

The CN and associated bond length for As in basaltic glass determined here overlap the value for the Macusani rhyolitic glass determined by Borisova et al. (2010) and in volcanic ashes from Patagonia, Chile (Bia et al., 2017). The smaller bond length measured in sample SP28 is consistent with a mixture of valence states. This bond shortening was also observed in the ancient volcanic ash "T" measured by Bia et al. (2017). However, unlike these natural samples, the glasses investigated in this study are anhydrous and thus As^{III} would be present as $As^{III}O_3E$ trigonal pyramids (with E being the lone pair of electrons) rather than the $As^{III}(OH)_3$ molecule proposed by Borisova et al. (2010) and Bia et al. (2017). The triangular pyramidal structure of $As^{III}O_3E$ is consistent with the similarities in the XANES spectra measured for hydrothermal systems (Pokrovski et al., 2002; Borisova et al., 2010) and the calculated aqueous $As^{III}O_3$ spectra (Testemale et al., 2011). This geometry is also consistent with numerous studies of As in oxide glasses which have identified the structural component of $As^{III}_2O_3$ as $As^{III}O_3E$ trigonal pyramids (Papatheodorou and Solin, 1976, Lucacel and Ardelean, 2006, Soignard et al., 2008, Krishna et al., 2010, Shi et al., 2015, Durandurdu, 2016, Ahmmad et al., 2016, Zhao et al., 2017). This structure was identified using a variety of techniques including molecular dynamic simulations (Durandurdu, 2016), and based on the position of the Fourier Transform Infrared (FT-IR) spectra and Raman spectral bands in vitreous and liquid $As^{III}_2O_3$ relative to position of these bands in $As^{III}_2O_3$ minerals (Papatheodorou and Solin, 1976; Soignard et al., 2008). Other authors (Lucacel and Ardelean, 2006, Krishna et al., 2010, Shi et al., 2015, Ahmmad et al., 2016, Zhao et al., 2017) have also used the position of the FT-IR and Raman wavelength related to As-O bond stretching in binary and ternary As-bearing glasses to propose an $As^{III}O_3E$ pyramidal structure for As. The bond lengths (1.78 Å) determined in the current study fall within the accepted range of the bond lengths for the $As^{III}O_3E$ trigonal pyramid determined by Soignard et al. (2008). Based on an EXAFS study of a variety of antimonate-silicate/germinate/borate/arsenate glasses, Ellison and Sen (2003) concluded that Sb behaves as a classic network-forming cation. These authors also concluded that Sb in the form of trigonal pyramids ($Sb^{III}O_3E$) would be consistent with their results regardless of composition. However, several studies of Sb-bearing glasses have also inferred the presence of a 4-fold coordinated $Sb^{III}O_4E$ in addition to $Sb^{III}O_3E$ (Dubois et al., 1986, Terashima et al., 1996, Charton and Armand, 2003, Wood et al., 2004, Nalin et al., 2004, Koudelka et al., 2007). The presence of 4-fold coordinated Sb^{III} was primarily identified by either a change in the BO_3 to BO_4 ratio in boron-bearing glasses with increasing Sb content (Wood et al., 2004; Koudelka et al., 2007) or by the size of the pre-edge feature in Sb L_{III}-edge XANES with increasing glass phosphorous content (Franco et al., 2018; Nalin et al., 2004). Dubois et al. (1986) interpreted the $Sb^{III}O_4E$ molecules to be in the form of square-based pyramids. Another potential isomer for 4-fold coordinated Sb^{III} is pseudo-bipyramidal, which is the form of Sb^{III} in $Sb^{(III,V)}{}_2O_4$ oxide phases (Orman, 2010) and the geometry of Sb in acidic or basic hydrothermal fluids (Tella and Pokrovski, 2009). The bond length for $Sb^{III}O_3E$ is 1.973 Å (Orman, 2010), while Sb^{III} in pseudo-bipyramidal 4-fold coordination has a longer bond length at 2.079 Å (Orman, 2010). Based upon the bond lengths in these reference materials, the similarities of the spectra to hydrothermal species (see above), and the EXAFS parameters calculated for Sb06 and Sb21, the structure of Sb in basaltic melts is consistent with of $Sb^{III}O_3E$ trigonal pyramids. This configuration is consistent with the structural parameters reported in Miller et al. (2019) for Sb^{III} in andesite glasses at 1-3 GPa, although Miller et al. (2019) report a slightly shorter bond length of 1.94 Å compared to the 1.98 Å reported in the current study.

3.5.5. Implications for Mineral/Melt Partitioning in Magmas

There is now abundant evidence in the literature that verifies that the dominant controls on mineral/melt partitioning are ionic radius and charge, as formalized by Blundy and Wood (1994). Armed with this principle and information on As and Sb speciation measured in this study, it is possible to predict which phases may host these metalloids in igneous systems. However, caution needs to be used when using this approach as the lone pair of electrons on the trivalent forms and the covalent nature of the metalloids could also impose substitution limitations.

In general, both oxidation states of As are considered to be incompatible in silicate minerals. Based on the ionic radius, which unless otherwise stated ionic radii are from Shannon (1976), and charge of As^{V}(0.335Å; 4-fold), this cation is not expected to substitute for any major elements, although the limited replacement of As^{V} for Si^{IV} (0.26Å; 4-fold) has been documented for garnets rich in the andradite component (Charnock et al., 2007), and suggested for antigorite (Hattori et al., 2005). Trivalent As (0.58 Å) in 6-fold coordination could substitute for Fe^{III} (0.55 Å) or Al^{III} (0.535 Å) in 6-fold coordination, however, the lone pair of electrons on As^{III} could make it less compatible than other 3+ cations in 6-fold coordination, which is similar to how the lone pair of electrons on Pb^{II} affect the expected partitioning behavior between clinopyroxene and melt (Shannon, 1976, Blundy and Wood, 2003). Additionally, the tendency for trivalent As to form 3-fold coordinated oxyanions ($As^{III}O_3^{3-}$) in silicate systems further limits its compatibility in common rock-forming minerals.

Similar to As^{V}, Sb^{V} (0.6 Å; 6-fold) is not expected to substitute for any major elements, while Sb^{III} (0.76 Å; 6-fold) could substitute for Mg^{II} (0.72 Å) and Fe^{II} (0.78 Å) in 6-fold coordination sites if sufficient charge balance is available. Despite theoretical predictions, clinopyroxene/melt partition coefficients ($D^{Cpx/melt}$) for Sb (0.004 to 0.103; Hill et al., 2000, Adam and Green, 2006) are in fact lower than the $D^{Cpx/melt}$ for the similar-sized light rare earth elements (LREE) (eg. Neodymium: 0.15 to 0.38; Hill et al., 2000, Adam and Green 2006). This deviation from expectations for Sb may be related to its lone-pair of electrons, which depending on the extent of their involvement in bonding, can increase the effective ionic radius (Shannon, 1976). A high Ca-Tschermaks component has been shown to increase the $D^{Cpx/melt}$ for Sb to 1.67 (Hill et al., 2000), which is significantly greater than the $D^{Cpx/melt}$ of LREE in Ca-Tschermak-rich clinopyroxene (0.39 for praseodymium and 0.50 for neodymium; Hill et al., 2000). This increased compatibility in clinopyroxene may be due to the ability of Sb^{III} to substitute isovalently for Al^{III} or could result from structural distortions to the M sites caused by Al^{III}.

Compared to silicates there are several accessory phases that may impact the behavior of As and Sb in magmatic systems. Numerous experimental studies have shown that As and Sb are compatible in sulfides with sulfide liquid/silicate melt partition coefficients from 0.3 to 180 for As (Li and Audétat, 2015; Li and Audétat, 2012) and 1.4 to 110 for Sb (Li and Audétat, 2015; Li and Audétat, 2012; Kiseeva and Wood, 2013;

Kiseeva and Wood, 2015; Brenan, 2015). Thus, the presence of sulfide would increase the bulk rock/melt partition coefficient of Sb, similar to the effect proposed for Pb relative to Ce in mid-ocean ridge basalts (MORB) (Kiseeva and Wood, 2013). This would help to explain the similar behavior of Sb and praseodymium in MORB described by Jochum and Hoffmann (1997).

The similarity in ionic radius of Sb^{V} (0.6 Å) to Ti^{IV} (0.605 Å) in 6-fold coordination allows Sb^{V} to fit well into titanium phases such as rutile (Klemme et al., 2005), which holds the majority of the Sb budget in eclogites (Zack et al., 2002). Pentavalent As in the form of the oxyanion $As^{V}O_4^{3-}$ has been shown to replace PO_4^{3-} in phosphates, including the common accessory mineral apatite (Pan and Fleet, 2002). Experiments have determined that the oxyanion $As^{III}O_3^{3-}$ can also substitute for phosphate; however, this substitution was determined only in dynamic crystallization experiments, with all $As^{III}O_3^{3-}$ reverting to $As^{V}O_4^{3-}$ upon reaching equilibrium (Liu et al., 2017). As the trivalent state of both As and Sb is less compatible than the pentavalent state in both apatite and rutile, properly calibrated partitioning systematics for these elements could have value in oxygen barometry. As previously described, such systematics have been suggested for Sb partitioning into rutile (Klemme et al., 2005). Similar behavior for As was shown empirically by Sha and Chappell (1999) who found that As concentrations in apatites from oxidized I-type granite were greater than those from more reduced S-type granites of the Lachlan fold belt.

3.6.Summary of Conclusions

Based upon the systematic and direct measurement of speciation as a function of fO_2 performed in this study, several key points about the geochemistry of As and Sb in basaltic magmatic systems can be made:

Arsenic and Sb are primarily in the trivalent state over the range of terrestrial fO_2 (FMQ -3.0 to FMQ +5.7). Pentavalent As contributes to more than 10% of the As species at very high fO_2 (FMQ +5.3±0.9) after accounting for the effect of iron. No pentavalent Sb was observed in the samples produced in this study. Additionally, no anionic As or Sb (As^{n-} or Sb^{n-}) was found, even at low fO_2.

For the basaltic melts produced in this study, trivalent As was determined to be coordinated to 3.07±0.7 oxygens, at a bond length of 1.78±0.01 Å forming trigonal pyramids of $As^{III}O_3E$. Similarly, trivalent Sb appears to be coordinated to 3 oxygens at a distance of approximately 1.98 Å, suggesting that Sb^{III} forms trigonal pyramids of $Sb^{III}O_3E$. The structure of As and Sb in basaltic melt is similar to the $Me^{III}(OH)_3$ (where Me is As or Sb) geometry found in aqueous fluids, although the $Sb^{III}(OH)_3$ species is only stable at near-neutral pH.

As As and Sb will be in the trivalent state at the conditions of most basaltic magma differentiation processes, these elements will behave incompatibly with respect to crystallizing silicate assemblages.

As the speciation of As varies as a function of fO_2 and As^V is more compatible in apatite than As^{III}, this fO_2-apatite compatibility relationship could be used to generate an oxybarometer. Future experiments quantifying how the As-apatite/melt partition coefficient varies as a function of fO_2 are required.

3.7. Supplementary Information

3.7.1. Sliding Buffer Calculations

In order to achieve oxygen fugacity (*f*O$_2$) intermediate to end-member metal-metal oxides, "sliding" buffers were employed. These buffers attain a different *f*O$_2$ from the end-member compositions by dilution of the metal or the oxide with a second component. With the Ni-NiO buffer, the addition of MgO will displace the *f*O$_2$ to a more reduced *f*O$_2$ while the addition of Pd will create a more oxidizing buffer. The effect of the MgO and Pd on the Ni-NiO buffer has been quantified by Taylor et al. (1992), and Pownceby and O'Neill (1994) and can be described by the following equations:

$$\log f\mathrm{O_2}\,(\mathrm{Ni,Pd}) = logfO_{2\,(NiNiO)} - 2\,\log \mathrm{X_{Ni}} - \frac{1}{(2.3025\ \mathrm{RT})}\{2(1 - \mathrm{X_{Ni}})^2\,[(-2165 - 7.958\mathrm{T}) + (9409 - 0.888\mathrm{T})(4\mathrm{X_{Ni}} - 1) + 2089(6\mathrm{X_{Ni}} - 1)(2\mathrm{X_{Ni}} - 1)]\} \tag{3.8}$$

$$\log f\mathrm{O_2}\,(\mathrm{Ni,Mg})\mathrm{O} = 2\,\log \mathrm{X_{NiO}} - \frac{1}{(2.3025\ \mathrm{RT})}\{(480104 - 244.700\mathrm{T} + 21.1078\,\mathrm{T}\log\mathrm{T}) - [2(1 - \mathrm{X_{NiO}})^2(0.693 + 512.0(6\mathrm{X_{NiO}} - 1)(2\mathrm{X_{NiO}} - 1)]\} \tag{3.9}$$

where log*f*O$_{2(\mathrm{NiNiO})}$ is the oxygen fugacity of the Ni-NiO buffer calculated from O'Neill and Pownceby (1993), X$_{\mathrm{Ni}}$ is the mole fraction of nickel in the NiPd alloy, X$_{\mathrm{NiO}}$ is the mole fraction of nickel oxide in nickel-magnesium oxide, T is the temperature in kelvin and R is the gas constant.

This study employed the NiPd-NiO (equation 3.8) sliding buffer to attain an *f*O$_2$ of approximately FMQ +2.5, and the Ni-(Ni,Mg)O buffer (equation 3.9) to attain an *f*O$_2$ of FMQ -2. In both cases, the final *f*O$_2$ is shifted to more oxidized conditions relative to the target value. Table 3.6 details the final buffer compositions, the calculated mole fractions, and the calculated *f*O$_2$ values.

Table 3.6 Summary of buffer alloy and oxide compositions

Exp. ID	Alloy (wt.%)					Oxide (wt.%)						fO_2 Calculation		
	Sb	Pd	Ni	Total	N	MgO	Sb_2O_3	PdO	NiO	Total	N	X_{NiO} or X_{Ni}	$\log fO_2$	ΔFMQ
Sb24	1.59	87.2	12.1	100.9	7	n/a	0.00	0.22	98.9	99.1	4	0.199	-5.6	+2.8
σ	1.06	1.16	0.94	1.16			0.02	0.12	0.47	0.57		0.011	0.1	
Sb25	1.24	n/a	98.2	99.45	5	85.2	0.00	n/a	13.0	98.2	5	0.0761	-10.0	-1.5
σ	1.35		1.07	0.35		1.12	0.01		0.16	1.12		0.0062	0.1	

n/a is not analyzed; N =number of analysis

3.7.2. Statistical Tests

The quality of a model fit to a data set can be described by a number of fit statistics. This study used two primary statistics: the r-factor and the χ^2 value. The r-factor describes the quality of fit for X-ray absorption near-edge structures measurements as well as extended X-ray absorption near-edge structures and can be expressed by the following equation (Ravel and Newville, 2005):

$$\mathrm{R-factor} = \frac{\sum(\mathrm{U}-\mathrm{Y})^2}{\sum \mathrm{U}^2} \tag{3.9}$$

Where U is the measured value, and Y is the value of the model fit to the data.

The other statistical measure employed is the χ^2 value, which is the sum of the squares of the difference between the measured and modelled values. This parameter is calculated using the equation:

$$\chi^2 = \sum \frac{(\mathrm{U}-\mathrm{Y})^2}{\sigma} \tag{3.10}$$

Where U and Y are as described above and σ is the standard deviation of the measurement of U.

3.7.3. Correction for Iron and Fitting Procedure

The speciation of As and Sb corrected for the effect of iron upon quenching was done using the method of Borisov (2013), which can be described in four steps. First, the equilibrium redox ratios of iron and the metalloids at a given fO_2 and temperature of the melt are calculated. The speciation of a redox couple in the melt as a function of fO_2 is defined by the equation:

$$\mathrm{Me}^{y+}\mathrm{O}_{y/2} + \frac{n}{4}\mathrm{O}_2 \leftrightarrow \mathrm{M}^{(y+n)+}\mathrm{O}_{(y+n)/2} \tag{3.11}$$

Which can be rewritten in the form:

$$\log\frac{M^{(y+n)+}O_{(y+n)/2}}{M^{y+}O_{(y)/2}} = \frac{n}{4}\log fO_2 - \frac{\Delta_r H^\circ}{2.303RT} + \frac{\Delta_r S^\circ}{2.303R} + \Gamma \qquad (3.12)$$

where H is the entropy, S is the enthalpy, R is the gas constant, T is the temperature in Kelvin, n is the number of electrons being transferred, Me^{y+} and $Me^{(y+n)+}$ are the mole fraction of each species, y is the charge on the reduced cation and Γ is the activity factor defined as:

$$\Gamma = -\gamma_{M^{(y+n)+}O_{(y+n)/2}} / \gamma_{M^{y+}O_{(y)/2}} \qquad (3.13)$$

in which γ is the activity coefficient. Equation 3.12 describes a sigmoidal change in the percentage of species present as a function of $\log fO_2$. If the activity coefficients do not vary as a function of fO_2, then S and Γ can be combined into a single constant.

The second step involves repeating the above calculation for the redox ratios at the quenching temperature, assuming the same fO_2 as at magmatic conditions. The quenching temperature was assumed to be the glass transition temperature and was calculated using the method of Giordano et al. (2008). The third step involves calculating the total molar charge of the redox pair in both the melt and the glass. This is done using the following equation:

$$\sum e^- = (M^{x+}) + y(M^{y+}) + r(N^{r+}) + q(M^{q+}) \qquad (3.14)$$

where Σe^- is the total electrons in the system, M and N represent the moles of each species and x, y, r, and q are the corresponding charges. The fourth step involves subtracting the total charge of the quenched glass from the total charge of the melt. If the net charge is not zero, the fO_2 in step 2 (the glass) needs to be changed and the speciation and total charge recalculated. Steps 2-4 are repeated iteratively until the net charge is zero. For more details on this method see Borisov (2013). Calculating the total charge requires information on the concentration of iron and the metalloid in the system; thus, the molar iron to metalloid ratio (Fe/M) must be known for each sample.

To determine the correct melt speciation in the experiments of this study from the glass measurements, an initial melt speciation had to be assumed and converted to glass using the method detailed above for each experiment fO_2 and Fe/M ratio. For As, the initial melt speciation curve was determined using enthalpy and entropy values calculated from the thermodynamic data available for inorganic oxides (Barin and Platzki, 1995) assuming that the oxides are appropriate model analogues for the melt species. Estimated thermodynamic values for the melt species of iron and Sb were obtained from Borisov (2013). The activity factor of the initial melt curve was assumed to have an initial value of 0. The calculated glass values are then compared to the XANES measurements and the chi-squared (χ^2) value is calculated to determine the quality of fit. The activity factor was then changed, and the process was then repeated to minimize the χ^2 value. Table 3.7 contains the enthalpy and entropies for the redox pairs of Fe^{II} & Fe^{III}, As^{III} & As^{V}, and Sb^{III} & Sb^{V}. Table 3.8 provides the parameters to describe the best solution fit and bounding fits for As speciation.

Table 3.7 Thermodynamic values for redox pair reactions

Redox Pair	Enthalpy ($\Delta_r H°$; kJ/mol)	Entropy ($\Delta_r S°$; kJ/mol)	Number of electrons exchanged (n)
Fe^{II} --> Fe^{III}	-114	-0.0437	1
As^{III} --> As^{V}	-125	0.105	2
Sb^{III} --> Sb^{V}	-200	-0.129	2

Table 3.8 Activity factor values for end member As speciation-*f*O2 relationships and resulting χ2 values

Fit Type	Γ value	χ^2
Best fit As speciation	1.59	0.085
Upper bound As speciation	2.04	0.26185
Lower bound As speciation	1.14	0.12395
No As V fit (Max χ^2)	-4.53	0.16112
No As III fit (Max χ^2)	15.47	23.00301

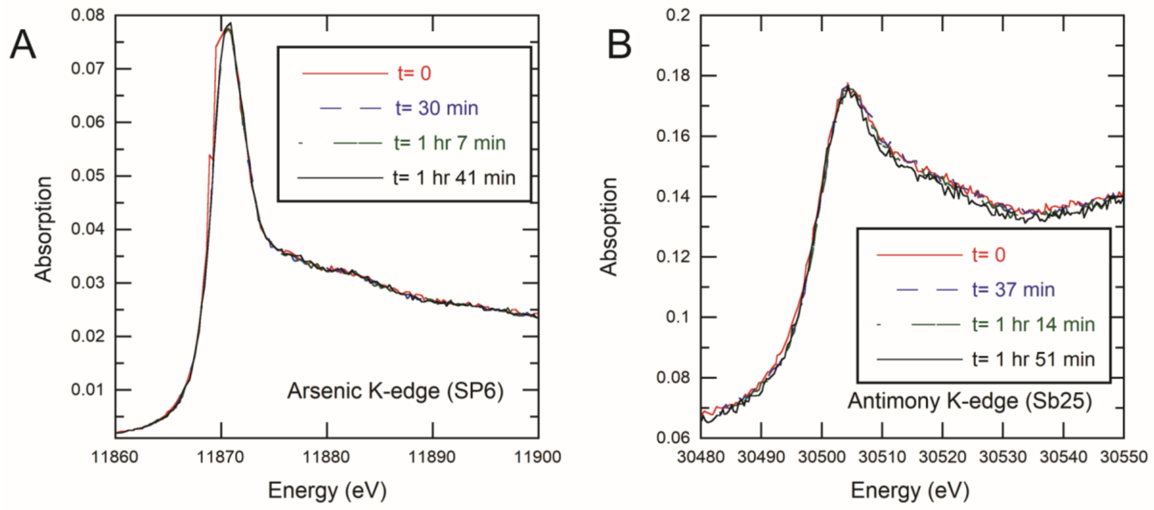

Figure 3.8 Plot of X-ray absorption as a function of energy (eV) for individual scans across the (A) As and (B) Sb K-edge. Spectra were collected at approximately 30-minute intervals over the course of two hours on the same spot. The lack of systematic variation with time suggests beam damage did not occur.

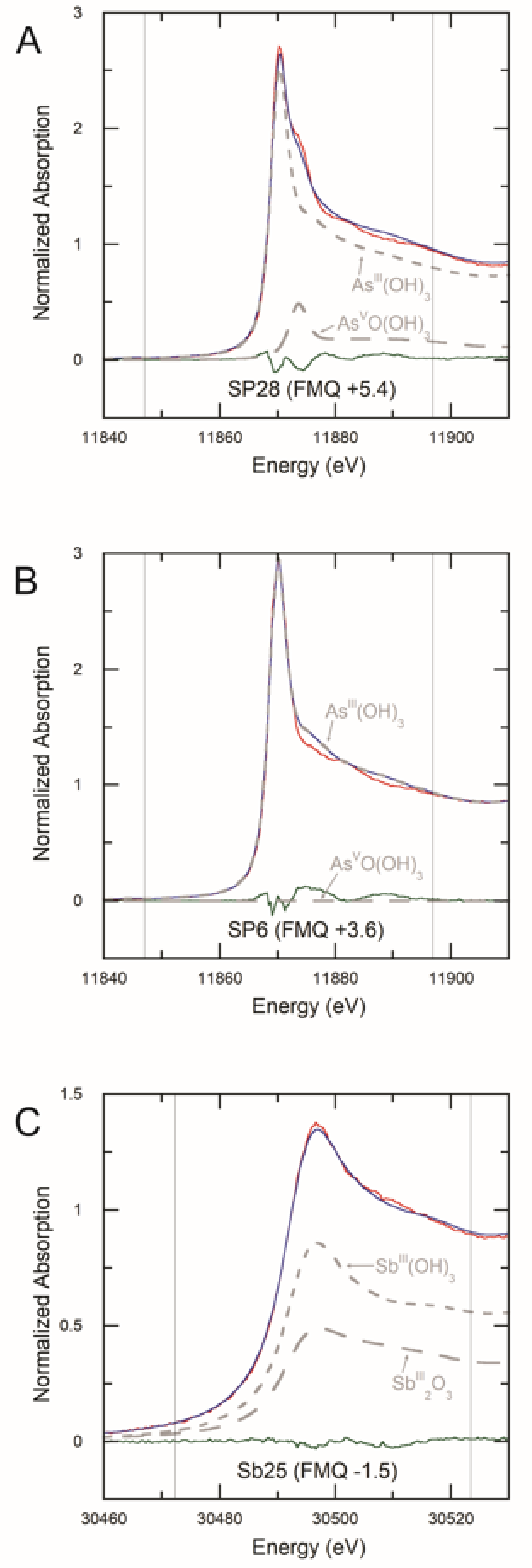

Figure 3.9 Examples of linear combination fits for As and Sb bearing glasses. The sample spectra are in red, the resultant spectra are in blue, and the residual is in green. Best fit species (labelled on the figure) are dashed lines in grey. Vertical grey lines are the fitting range. A) The fit of SP28 showing the peak for As^{III} with a shoulder at the As^{V} energy. B)) The fit of SP6 showing only As^{III}. D) The fit of Sb25 showing only a peak for Sb^{III}.

Acknowledgments

Part of the research described in this paper was performed at the Canadian Light Source, which is supported by the Canada Foundation for Innovation (CFI), Natural Sciences and Engineering Research Council of Canada (NSERC), the National Research Council (NRC), the Canadian Institutes of Health Research (CIHR), the Government of Saskatchewan, and the University of Saskatchewan. Additionally, this research used resources of the Advanced Photon Source, an Office of Science User Facility operated for the U.S. Department of Energy (DOE) Office of Science by Argonne National Laboratory, and was supported by the U.S. DOE under Contract No. DE-AC02-06CH11357, and the Canadian Light Source and its funding partners. The spectral reference materials used in this study were obtained using a 2017 Society of Economic Geologists Student Research Grant awarded to BJM. This work was supported by the NSERC Discovery Grant awarded to JMB. BJM acknowledges the receipt of support from the CLSI Graduate and Post-Doctoral Student Travel Support Program. We would also like to thank Dr. P Blanchard (beamline scientist) for access to his spectral library which was also used in the linear combination fitting fitting as well as David Morris and Dr. Peng Zhang from Dalhousie University for their guidance in processing and fitting EXAFS data. We would like to thank Ms. Erin Keltie along with the beamline scientists, Dr. Ning Chen, Dr. Weifeng Chen, Dr. Renfei Feng, Dr. Peter Blanchard, and Dr. Zou Finfrock for their assistance in acquiring the XANES and EXAFS data and guidance in processing the data. We would also like to thank Dr. Gleb Pokrovski for a thorough review that significantly improved the quality of the presentation and for providing us with the aqueous species spectra. Finally, we would like to thank Associate Editor L. Anovitz for providing feedback and handling our submission.

Research Data

Research data associated to this article can be accessed at https://doi.org/10.17632/w44srcbncg.1

Chapter 4

ARSENIC-RICH APATITE AS A RECORDER OF LOCAL CRYSTALLIZATION PROCESSES IN FELSIC PLUTONIC SYSTEMS

Bryan J. Maciag and James M. Brenan
Department of Earth and Environmental Sciences, Dalhousie University,
Halifax, Nova Scotia, Canada

Key words: Arsenic, Apatite, Oxygen fugacity, XANES
Prepared for Publication in American Mineralogist

Abstract

Arsenic can concentrate in phosphate minerals, such as apatite, with levels exceeding whole-rock concentrations in some felsic plutonic suites. This strong As-apatite association is ascribed to oxidizing conditions during crystallization, as arsenate [$As^VO_4^{3-}$] is expected to be more compatible than arsenite [$As^{III}O_3^{3-}$] in apatite. Previous spectroscopic measurements on mafic composition indicate that As^{III} is the dominant species over the range of terrestrial oxygen fugacity (fO_2), thus As should be incompatible in apatite. To understand this apparent contradiction, apatite-melt partitioning experiments using metaluminous, peraluminous, and peralkaline felsic melt compositions were performed at fO_2 ranging from ΔFMQ of -0.4 to +7.5 (ΔFMQ = log deviation from the Fayalite-Magnetite-Quartz redox buffer), 0.75 GPa, and 900-1050°C. These results were combined with the As speciation data obtained from X-ray absorption near edges structures spectroscopy (XANES) to generate an apatite-melt partitioning model that incorporates fO_2, temperature and melt composition. Results confirm the prediction based on the speciation measurements and underscore the need for unusually oxidizing conditions (ΔFMQ +4.7) for the As concentration of apatite to exceed the levels in the co-existing melt.

To understand elevated As concentrations in apatite, the trace element composition of apatite from thirty-two samples of the Devonian South Mountain Batholith of Nova Scotia, Canada was obtained by laser ablation inductively-coupled-plasma mass spectrometry. Samples yield apatite/whole-rock partition coefficients for As between 0.12 to 18. However, equilibrium partitioning cannot explain values above ~0.1

at the estimated fO_2 of the South Mountain Batholith. Instead, models of protracted crystallization (>85%) leading to the enrichment of As in the melt prior to apatite crystallization replicate the partition coefficients found in the South Mountain Batholith apatites. Modelling of additional trace elements supports this hypothesis. Apatite/whole-rock partition coefficients for As greater than ~0.74 represent apatite growth reflecting melt compositions affected by local enrichment processes and are not necessarily indicative of unusually oxidizing conditions.

4.1. Introduction

Arsenic is a redox-sensitive element with three oxidation states (-III, +III and +V) and is generally incompatible in most rock-forming minerals due to its small ionic radius, high charge, and the lone pair of electrons when present as As^{III}. One phase that may incorporate As during magma evolution is apatite, which can incorporate As^{V} by isovalent substitution for P^{V} (Pan and Fleet, 2002). Trivalent As is not compatible in apatite but may be included due to dynamic uptake (Liu et al., 2017). Previous studies have reported As concentrations in apatite associated with plutonic systems ranging from 1 µg/g to 1 wt.% (Sha and Chappell, 1999; Belousova et al., 2002; Marks et al., 2012; Wang et al., 2014; Teiber et al., 2015; Mao et al., 2016; Andersson et al., 2019). Due to the inferred higher compatibility of As^{V} relative to As^{III} in the apatite structure, the observed range of apatite As concentrations has been ascribed to variation in oxygen fugacity (fO_2) (Sha and Chappell, 1999; Belousova et al., 2002; Mao et al., 2016).

The speciation of As measured for basaltic compositions indicates that As is primarily As^{III} over the range in fO_2 recorded by most terrestrial magmas (Maciag and Brenan, 2020). Hence, As is predicted to be incompatible in apatite relative to the melt, and magmatic apatite should have lower As concentrations than the whole-rock, provided the latter is reflective of the melt from which the apatite formed. This prediction is in disagreement with the data from natural apatite and associated whole-rock compositions in granites of the Lachlan Fold Belt (Sha and Chappell 1999), the South Mountain Batholith (this study) and other well-studied granitic suites (Belousova et al., 2002; Mao et al., 2016), in which apatite can attain 80x the As level of the estimated whole-rock (Fig. 4.1). While contamination of the magma by As-rich sediments such as black shales (~100 µg/g; Ketris and Yudovich, 2009) could increase the As concentration in apatite, this process cannot change the partition coefficient. Thus, an apparent paradox exists, in which the concentration of As in apatite relative to the whole-rock (assumed melt) is significantly higher than predicted from the As speciation results.

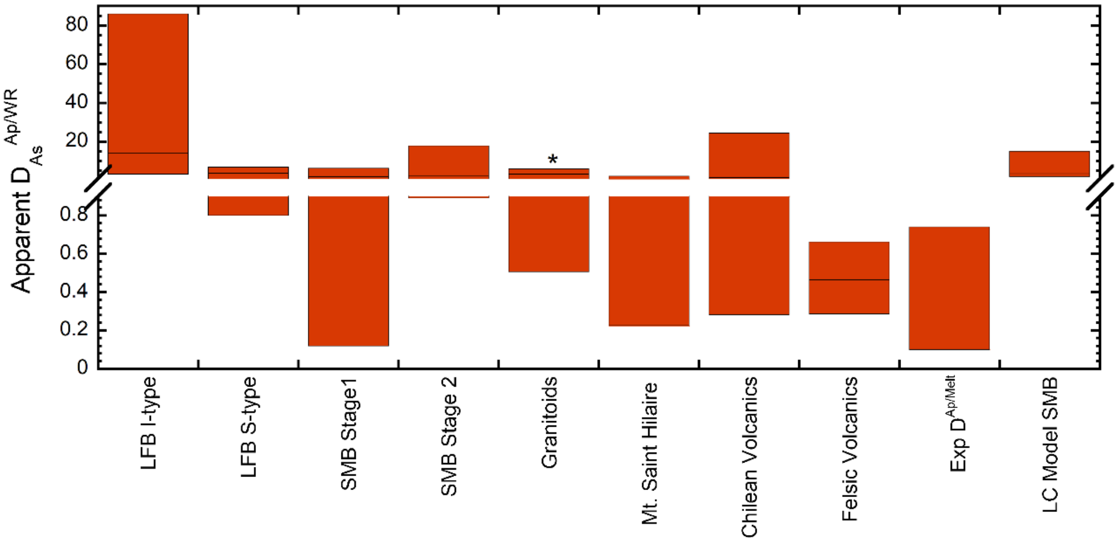

Figure 4.1 Box plot showing the median and range of apparent $D^{Apatite/Whole\text{-}rock}$ for As from various felsic systems including the Lachlan Fold Belt (LFB) belt (Sha and Chappell, 1999), South Mountain Batholith (SMB; this study), Mt. Saint Hilaire [Apatite (Marks et al., 2012), whole-rock (Tice, 2010)], felsic volcanics [Apatite (Belousova et al., 2002), whole-rock assumed to be 4.53 µg/g], Chilean Volcanics [Nathwani et al., 2020]. "Exp $D^{Apatite/Melt}$" is the experimental $D^{Apatite/Melt}$ for a melt with Ψ = 1 at 900°C calculated for the fO_2 range of FMQ -3 to FMQ +3.5. "LC" is the calculated $D^{Apatite/Whole\text{-}rock}$ for a model of apatite formation after As concentration by protracted crystallization. The model used a primitive South Mountain Batholith Stage 2 granite starting composition with 5wt.% H_2O, and 3 µg/g initial As. The fO_2 was held at FMQ -1. *The maximum value for the granitoids is calculated from the 3rd quartile of Belousova et al. (2002).

A lack of information on apatite/melt partitioning ($D^{Apatite/Melt}$) for As hampers the understanding of As enrichment in apatite. This study presents the results of experiments measuring $D^{Apatite/Melt}$ for As involving peraluminous, metaluminous, and peralkaline felsic melts over the fO_2 range of ΔFMQ -0.4 to +7.5. Experiments were done at 0.75 GPa under vapor-saturated conditions employing a piston-cylinder apparatus. The As content of run-product phases was measured by laser ablation inductively coupled plasma mass spectrometry (LA-ICP-MS). X-ray absorption near-edge structures (XANES) at the As K-edge determined the speciation in select samples. Combining the speciation data with the calculated partition coefficients resulted in an As-in-apatite partitioning model. This study also characterizes the As and other trace element concentrations in apatite of 32 samples collected from the peraluminous, late Devonian South Mountain Batholith, Nova Scotia, Canada (MacDonald, 2001). The predicted apatite compositions from the experimental results are compared against the South Mountain Batholith apatite suite and models of crystallization to explain the observed behavior.

4.2. Methods

4.2.1. Selection of Samples from the South Mountain Batholith

Mapping of the South Mountain Batholith has delineated 49 map units, assigned to at least 11 individual plutons which constitute two intrusive stages (MacDonald, 2001). Early (Stage 1) biotite granodiorites to monzogranites were emplaced between ~379 to 375 Ma and later (Stage 2), more chemically-evolved leucomonzogranite to leucogranite yield ages spanning ~375 to 372 Ma (autocrystic zircon U-Pb zircon; Bickerton et al. 2022). Samples were obtained from fieldwork in 2018 and 2019 conducted by B. Maciag, J. Brenan and J. Chavez, and from the NS Department of Natural Resources and Renewables sample archive at the Nova Scotia Core Library in 2020 and 2021. Sixteen samples from Stage 1 plutons and thirty samples from Stage 2 plutons were selected. Whole-rock data for most samples were available from the Nova Scotia Department of Energy and Mines bedrock mapping initiative; however, several samples collected in a separate sampling program (prefixed with 18JC and 19BM) were analyzed by ICP-MS by ACT-LABS (Ancaster, Ontario, Canada) using the 4LITHO analysis package. This method involved initial crushing, then pulverizing with mild steel to 95% passing 74-micron mesh. Samples were fused with lithium metaborate/tetraborate, then digested in nitric acid. The detection limit for As by this method is 5 µg/g, with REE-1 (containing 124 µg/g) as the As standard. The samples collected are the same as from Brenan et al. (Submitted) which contains details on the samples, including grid coordinates, pluton occurrence, lithology, and relevant textural information.

4.2.2. Experimental

Materials for experiments were synthesized by grinding analytical grade oxides (MgO, SiO_2, and Al_2O_3), carbonates (K_2CO_3, Na_2CO_3, and $CaCO_3$), and hydroxyapatite ($Ca_5(PO_4)_3OH$) under ethanol for at least 30 minutes in an agate mortar in proportions to achieve the compositions listed in Table 4.1 plus an extra 4-6 % apatite. The mixture was calcined for a minimum of 8 hrs at 1000°C. Once the mixture cooled it was homogenized by grinding, fused in a box furnace at 1500°C for 30 minutes, then quenched in cold water, homogenized and fused again for 30 minutes at 1500°C. Glasses were ground again and CaF_2 was added in stoichiometric proportions to the apatite added to the glass before fusion. Due to the volatility of As, 1 wt.% As_2O_3 or elmental As was also added to a 1 g aliquot and ground to homogeneity. Further, dilute aliquots were mixed, using doped and undoped starting materials to the desired As concentration. All mixtures were ground for at least 30 min under ethanol. The initial As content of each experiment is listed in Table 4.2. As past studies (Pyare and Nath, 1991) have shown that the oxidation state can be impacted by melt alkalinity (molar Al/(Na+K) or Ψ), three compositions of rhyolites were used: peraluminous (PAL; Ψ: 1.65; Alumina Saturation Index (ASI):1.2), metaluminous (MAL; modelled after Lake County Obsidian; Ψ: 1.15; ASI: 0.87) and peralkaline (ALK; Ψ:0.73; ASI: 0.60). Aside from As, no other redox-sensitive elements were added to the melts, to avoid potential changes in the As oxidation state during the quench (Berry et al., 2006; Borisov, 2013; Maciag and Brenan, 2020).

Table 4.1 Experiment Starting Material Compositions.

	Metaluminous (MAL)	**Peraluminous (PAL)**	**Peralkaline (ALK)**
SiO_2	76	71	71
Al_2O_3	13	18	13
CaO	2.0	2.0	2.0
MgO	0.5	1.0	0.5
Na_2O	3.7	4.0	6.5
K_2O	4.8	4.0	6.8
P_2O_5	0.10	0.25	0.25
Ψ*	1.15	1.65	0.73
ASI**	0.87	1.24	0.60

*Ψ = molar (Al/(Na+K))

**ASI = molar (Al/(Ca+Al+Na)

Experiments were done with an end-loaded piston-cylinder apparatus using 1.905 cm diameter salt-pyrex-graphite pressure cells. Three types of capsule configuration were used to achieve the different fO_2s in this study: double capsule (sample inner, buffer outer), internal buffer, and graphite-lined capsules (Fig. 4.2). In each configuration, prior to sealing the capsule containing the sample, water was added to oversaturate the melt by 10-20 wt.%. The conditions and configuration for each experiment are provided in Table 4.2. Experiments were first over-pressurized by 10% and then the pressure was maintained while ramping the temperature to the desired value. The pressure was then allowed to decrease during sample relaxation and held at a constant value thereafter. Experiments were quenched by terminating power to the assembly furnace. All experiments were run at 0.75 GPa plus a 10% friction correction. The pressure was calibrated using the melting point of salt (Bohlen, 1984) at 1 GPa method and the solubility of albite in water (Baker, 2004) at 0.5 GPa. No correction was needed at 1 GPa, however, a 20% correction was needed at 0.5 GPa, thus a 10% correction was used at 0.75 GPa. Details of the pressure calibration can be found in Drage (2022).

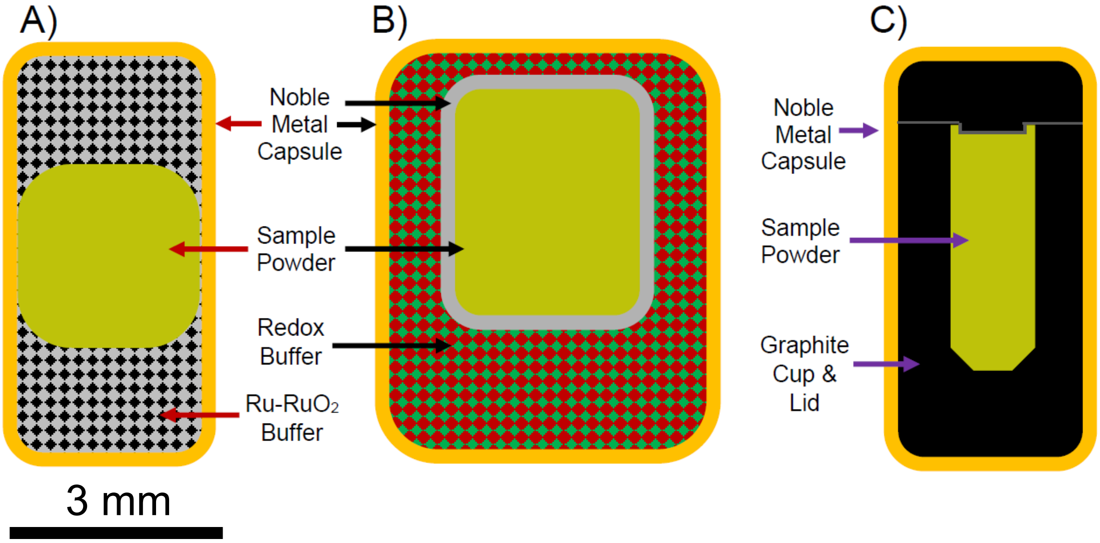

Figure 4.2 Capsule designs for partitioning experiments. A) Buffer sandwich in which the sample is between layers of the buffer assemblage; B) Double capsule consisting of an inner capsule holding the sample and an outer capsule with the buffer + H_2O; C) Graphite lined capsule. Configurations A and C used gold capsules. For the double capsule experiments, the inner capsule is platinum, and the outer capsule is gold. Redox buffers for the double capsule experiments were Fe_3O_4- Fe_2O_3, MnO-Mn_3O_4 and Re-ReO_2.

Table 4.2 Experiment Details.

Experiment ID	**Duration (hrs)**	**Capsule Configuration**	**Temperature (°C)**	**Oxygen Fugacity (ΔFMQ)**	**Starting Composition**	**Initial As_2O_3 Content (wt.%)**
AAO01	48	IB; Ru-RuO_2	1000	7.5	MAL	0.14*
AAO02	24	IB; Ru-RuO_2	1000	7.5	MAL	0.14*
AAO03	96	IB; Ru-RuO_2	1000	7.5	MAL	0.14*
AAO04	144	IB; Ru-RuO_2	1000	7.5	MAL	0.14*
AAO06	120	IB; Ru-RuO_2	1000	7.5	MAL	0.14*
AAO13	96	IB; Ru-RuO_2	1000	7.5	MAL	1.0
AAO19	72	IB; Graphite	1000	-0.4	MAL	0.10
AAO20	72	IB; Ru-RuO_2	900	8.1	MAL	0.10
AAO21	72	DC; Fe_3O_4-Fe_2O_3	1000	5.9	ALK	0.10
AAO24	72	IB; Graphite	1000	-0.4	ALK	0.10
AAO25	72	IB; Ru-RuO_2	1050	7.2	MAL	0.10
AAO26	72	IB; Ru-RuO_2	1000	7.5	PAL	0.10
AAO27	72	IB; Ru-RuO_2	1000	7.5	ALK	0.50
AAO29	72	IB; Ru-RuO_2	1000	7.5	ALK	0.050
AAO30	72	IB; Ru-RuO_2	1000	7.5	ALK	0.10
AAO32	72	DC; MnO-Mn_3O_4	1000	4.4	ALK	0.10
AAO33	72	DC; Re-ReO_2	1000	2.7	ALK	0.10
AAO39	72	DC; MnO-Mn_3O_4	1000	4.4	ALK	0.10
AAO47	24	Graphite Lined	1000	-0.4	MAL	0.10
AAO49	24	Graphite Lined	1000	-0.4	ALK	0.10
AAO50	24	Graphite Lined	1000	-0.4	PAL	0.10

*Added as As Metal

4.2.3. Analytical

4.2.3.1. X-ray Absorption Near Edge Structures

X-ray absorption spectra were collected at the sector 20-ID beamline of the Advanced Photon Source, Chicago, USA at the As K-edge. In addition to the K-B mirror, the monochromators were detuned by 10% to reduce harmonics. All unknown samples were measured in fluorescence mode *in situ* on polished samples using a 2 µm spot. Spectral reference materials were measured in transmission mode. Spectra for the trivalent and pentavalent aqueous species at various fluid pH were also used as reference materials, which are reported in Borisova et al. (2010). Energy calibration scans were done periodically on gold foil at the L_{III}-edge (edge position: 11,919 eV), with the edge position defined as the maximum in the first derivative of the absorption spectra. Energy drift during data acquisition was determined to be less than the spectral resolution of the beamline (1 eV). Spectral shifts caused by changes in speciation arising from beam-induced photo-oxidation/reduction of the sample or “beam damage” was of concern during the acquisition of the spectra. To minimize this effect, integration times were reduced to 0.1 seconds. In the cases where reduced integration times did not eliminate beam damage, the analysis spot was moved after each scan.

Individual scans for each unknown sample or reference material were merged, then calibrated and normalized. Linear combination fitting was performed on the individual spectra using data between -20 to +30 eV with respect to the absorption edge. Small shifts (±1 eV) in the energy spectra were allowed during linear combination fitting to account for energy drift during the collection of the spectra for samples and reference materials. The As reference materials considered were $As^{III}_2O_3$, arsenopyrite [FeAsS], native As, scorodite [$FeAs^{V}O_4 \cdot 2H_2O$], as well as aqueous $As^{V}O(OH)_3$ and $As^{III}(OH)_3$. The processing of the data was completed using ATHENA from the DEMETER software package, version 0.9.26 (Ravel and Newville, 2005).

4.2.3.2. Electron Microprobe

The major element composition of run-product phases was determined using the JEOL JXA-8200 EPMA housed in the Robert M. MacKay Electron Microprobe Laboratory at Dalhousie University. Silicate glass analyses used an accelerating voltage of 15 kV, a beam current of 10 nA and a 10 μm defocused beam to limit glass damage. Standards for silicate melt analysis were CAM66 rhyolite (Ca, K, Mg, Al, Si), albite (Na), and Durango apatite (P, F). Apatite analyses used an accelerating voltage of 15 kV, a beam current of 20 nA and a 1 μm focused beam. Standards for apatite analyses were Durango apatite (Ca, P, F), albite (Na), kaersutite (Mg), and sanidine (K, Si, Al). Additional standards for analysis of the natural apatite from the South Mountain Batholith were garnet (Fe), pyrolusite (Mn), kaersutite (Ti), and tugtupite (Cl) with synthetic fluorapatite substituting for Durango (Ca, P, F). Count times were 30 s (50 s for South Mountain Batholith apatite) on peak for fluorine and 20 seconds for all other elements. For the South Mountain Batholith apatite, the spectral interference from the Fe $L\alpha_{1,2}$ emission line (705 eV) on the F kα line (676.8 eV) was corrected by measuring Fe-metal. Due to the small Fe concentration in apatite, the magnitude of this correction was minimal. Raw count rates were converted to concentrations using the ZAF data reduction scheme.

4.2.3.3. Laser Ablation Inductively Coupled Plasma Mass Spectrometry

Trace element concentrations were determined using the laser ablation inductively coupled plasma mass spectrometry (LA-ICP-MS) facility located in the Health and Environments Research Centre (HERC) Laboratory at Dalhousie University. The system employs a frequency quintupled Nd: YAG laser operating at 213 nm, coupled to a Thermo Scientific iCAP Q ICP-MS quadrupole mass spectrometer with He flushing the ablation cell to enhance sensitivity (Eggins et al., 1998). Silicate glasses were analyzed using a laser repetition rate of 5-10 Hz and a spot size of 40-50 µm with the analysis area moving back and forth during ablation to reduce ablation depth. Apatite was measured using a repetition rate of 5-10 Hz and the largest spot size possible, up to a maximum of 40 µm, but typically 5-10 µm for experimental run-products. Factory-supplied time-resolved software was used for the acquisition of individual analyses. A typical glass analysis involved 20 seconds of background acquisition with the ablation cell being flushed with He, followed by ablation for 60 seconds, then 60 seconds of cell washout. Vapor bubbles were likely included in the glass analysis. Most of these vesicles were likely breached during polishing, given the fractured nature of the glass. Any remaining filled vesicles would contribute little to the signal due to low modal abundance (typical around 20%) and low mass. Apatite analysis typically had a much shorter ablation time (10-20 seconds) as the crystals were often completely consumed during ablation. Data were collected in a sequence in which two analyses were done on the standard reference material at the start of the acquisition cycle, then after every 16-18 analyses on the unknown samples. Four to five analyses were done on each run-product glass. Data reduction was done using the Iolite version 4.0 software package (Woodhead et al., 2007; Paton et al., 2011). For apatite analysis where the grain was completely ablated the integration area was reduced so that only the contribution of apatite is considered. Ablation yields were corrected by reference to the known concentration of Ca as determined by EPMA, using ^{43}Ca or ^{44}Ca as an internal standard. Arsenic concentrations were quantified using the NIST 610 silicate glass, which contains 325 µg/g of As (Jochum et al., 2011). The following isotopes were measured in apatite from the experiment run-products: ^{30}Si, ^{31}P, ^{43}Ca, ^{44}Ca, and ^{75}As, with all dwell times of 10 milliseconds. For apatite analysis in experiments AAO 47, 49, and 50 the dwell time for ^{75}As was increased to 30 milliseconds and the element list was simplified to ^{27}Al ^{31}P, ^{43}Ca, ^{44}Ca, and ^{75}As to achieve lower detection limits. The analysis of the natural apatite from the South Mountain Batholith included the following isotopes: ^{7}Li, ^{27}Al, ^{31}P, ^{43}Ca, ^{45}Sc, ^{47}Ti, ^{51}V, ^{52}Cr, ^{55}Mn, ^{57}Fe, ^{59}Co, ^{60}Ni, ^{61}Ni, ^{63}Cu, ^{65}Cu, ^{66}Zn ^{69}Ga, ^{73}Ge, ^{75}As, ^{85}Rb, ^{88}Sr, ^{89}Y, ^{90}Zr, ^{93}Nb, ^{95}Mo,^{111}Cd, ^{113}In, ^{115}In, ^{118}Sn, ^{121}Sb, ^{133}Cs, ^{137}Ba, ^{139}La, ^{140}Ce, ^{141}Pr, ^{146}Nd, ^{147}Sm, ^{153}Eu, ^{157}Gd, ^{159}Tb, ^{163}Dy, ^{165}Ho, ^{166}Er, ^{169}Tm, ^{172}Yb, ^{175}Lu, ^{178}Hf, ^{182}Ta, ^{186}W, ^{206}Pb, ^{208}Pb, ^{209}Bi, ^{232}Th, and ^{238}U. Dwell times for ^{27}Al, ^{43}Ca, ^{57}Fe were 5 milliseconds, while dwell times for ^{63}Cu, ^{66}Zn, ^{75}As, ^{95}Mo, ^{118}Sn were 20 milliseconds. All other isotopes used dwell times of 10 milliseconds. The accuracy of the LA-ICP-MS As concentration was assessed by measuring a natural Durango fluorapatite. The As concentration measured using our analytical protocol (992±64 µg/g) reproduces the values obtained on the same material measured by instrumental neutron activation analysis (1010 µg/g) at ACT-LABS (Ancaster, Ontario, Canada).

4.3. Results & Discussion

4.3.1. Textures and Composition of South Mountain Batholith Apatite

The South Mountain Batholith samples have two types of apatite. Type M apatites appear either homogenous or concentrically zoned (Fig. 4.3A) based on backscattered electron imaging (BSE) and exhibit consistent REE patterns, with elevated MREE, a significant negative Eu anomaly and unfractionated HREE compared to the LREE (Fig. 4.4 closed symbols). These patterns are consistent with crystallization from a melt, with similar whole-rock REE abundances as South Mountain Batholith samples based on available apatite-melt partition coefficients (Prowatke and Klemme, 2006) and are similar to apatite from other Siluro-Devonian granites in the northern Appalachians (Azadbakht et al., 2018). Type M apatite range from 5 to 100 µm, are euhedral to subhedral, and occur as inclusions or along the grain boundaries of primary biotite. Type H apatite is subhedral to anhedral and is often found in the matrix. Type H apatites exhibit irregular and patchy BSE zoning (Fig. 4.3B), along with variable REE patterns, and distinctly low Y content that is inconsistent with a magmatic source (Fig. 4.4; open symbols). The median As content of Type M apatite is 6.3µg/g and ranges from 1.5 to 47 µg/g. Type H apatite has a median As content of 4.3 µg/g and ranges from 0.90 to 26 µg/g.

Based on a correlation matrix the As concentration in apatite correlates most strongly with the other high-field strength elements Nb and Ta; however, it also correlates positively with the MREE and HREE's. The unusual REE chemistry and patchy zoning indicate that Type H apatite's are of non-magmatic origin and are not considered further. The full trace element geochemistry of the South Mountain Batholith apatites are available in the electronic supplementary information Dataset 4A.

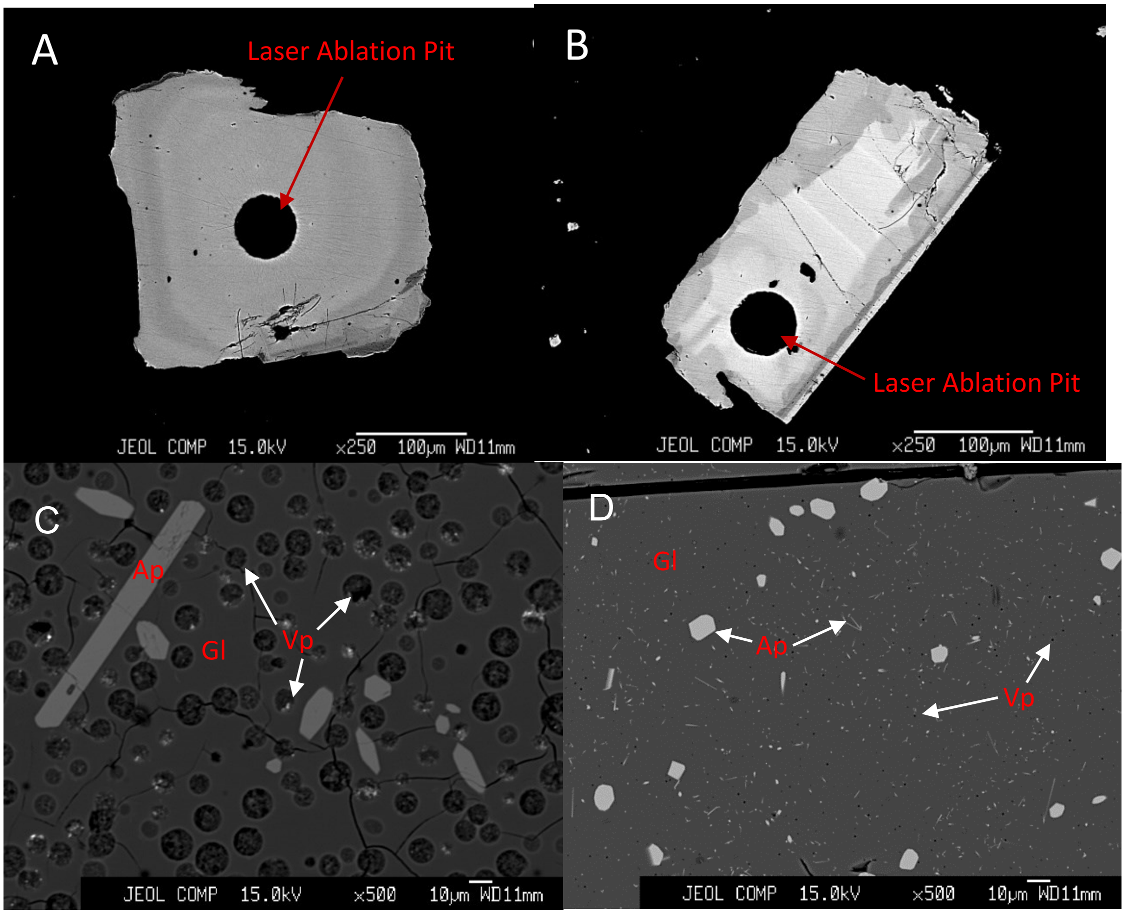

Figure 4.3 Backscatter electron image of A) type M apatite from the South Mountain Batholith Stage 2 New Ross Pluton, sample A16-1256, showing concentric zoning B) type H apatite from the South Mountain Batholith Stage 2 New Ross Pluton, sample A16-1256, showing irregular and patch zoning, C) experimental run-product AAO32 showing apatite (Ap), glass (Gl) and vapor (Vp) phase performed using a double capsule setup with the MnO-Mn_2O_3 buffer D) experimental run-product AAO50, performed in the graphite lined capsule showing apatite (Ap), glass (Gl) and vapor phase (Vp).

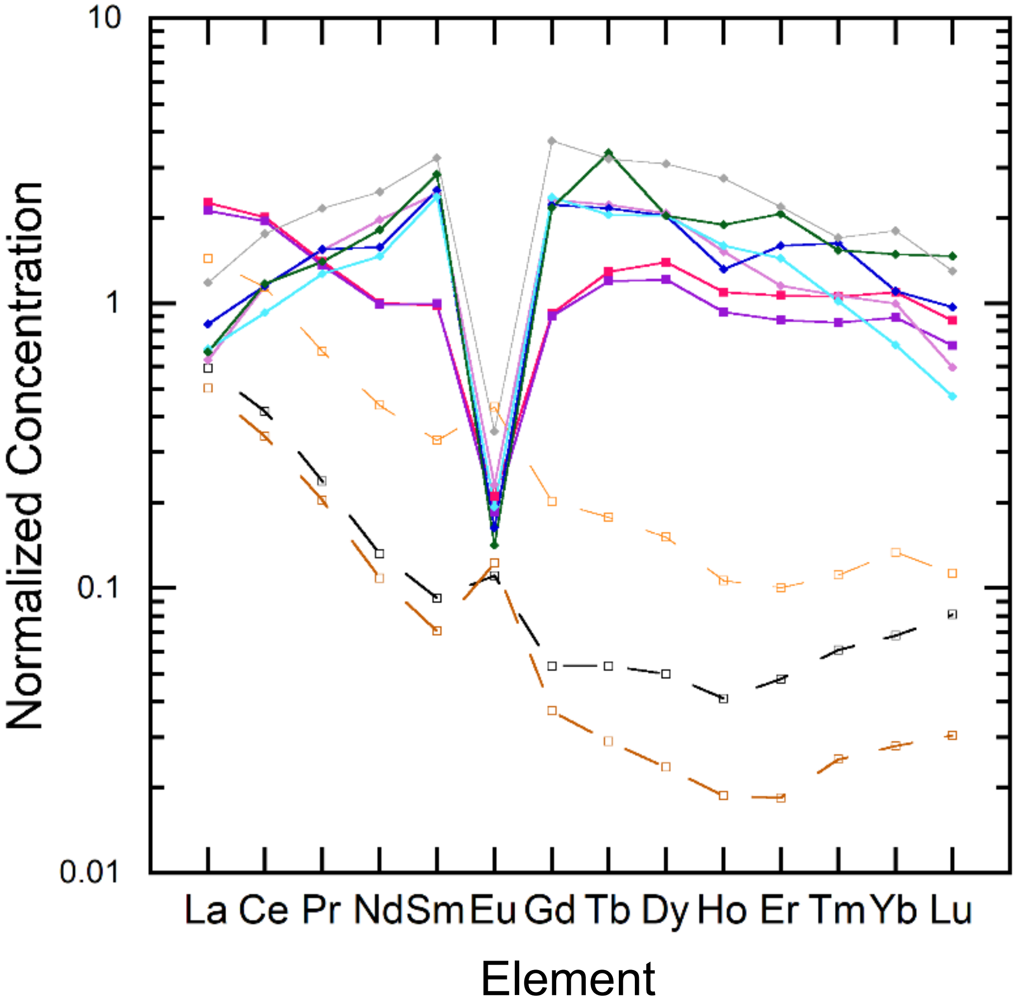

Figure 4.4 Chondrite-normalized rare earth element concentrations in apatite from South Mountain Batholith, samples A16-1256 (squares) from the New Ross Pluton and 18JC-0003 (diamonds) from the Halifax Pluton. The different sample prefixes are related to the sample collection (see section 4.2.1). The solid symbols and lines are apatites with concentric zoning (Fig 4.3A) and open symbols with dashed lines are apatites with irregular zoning (Fig 4.3B). The higher La/Sm ratio observed in the New Ross sample compared to the Halifax Pluton is interpreted as due to the absence of early crystallizing monazite in the New Ross magma, which would have sequestered the LREE (see text for further discussion).

4.3.2. Experimental Run-products

Run-products consisted of apatite, glass, and circular void spaces interpreted to have held a vapor phase at run conditions. Apatite makes up between 1 to 5 modal % of the samples. In experiments at an fO_2 greater than FMQ, apatite are euhedral and show hexagonal sections, although stubby and elongate rectangular apatites occur. These grains range in size from 5 µm to over 100µm, with most crystals 10-20 µm. In experiments done under reducing conditions, larger apatite (5-10µm) occur but most are acicular and under 1 µm in size. The vesicles make up between 15 to 40% of the volume of the run-products. Vesicles are 5-30 µm in diameter in most samples, but in some reduced experiments, the vesicles are mostly 1-2 µm. All phases are homogenous in appearance in backscatter electron images (Fig. 4.3C and D). In several of the experiments done with graphite-lined capsules a Pt-As metallic phase was observed suggesting As saturation was attained. The source of platinum in these experiments is likely contamination from the Pt-crucible used for sample fusion. Tables 4.3 and 4.4 provide the major element composition and As content of run-product glass and apatite, respectively.

4.3.3. Arsenic Loss and the Approach to Equilibrium

Except for the samples encased in graphite-lined capsules, mass balance indicates that As was lost to a varying extent over the course of experiments (Table 4.5). Samples equilibrated with the Ru-RuO_2 buffer lost 0-65% of the total As, with those having the highest initial As concentrations showing less As loss. For experiments involving a double capsule configuration, 18-94% of the As was lost by alloying with the noble metal capsule (Au or Pt), with a greater extent of As loss with decreasing fO_2. LA-ICP-MS analysis of the Ru-RuO_2 buffer and the noble metal capsules confirmed these observations.

Table 4.3 Summary of major and trace element abundances in run-product glasses.

	SiO_2 (Wt.%)	Al_2O_3 (Wt.%)	MgO (Wt.%)	CaO (Wt.%)	Na_2O (Wt.%)	K_2O (Wt.%)	P_2O_5 (Wt.%)	F (Wt.%)	Total (Wt.%)	N	LA-ICP-MS ^{75}As (µg/g)			
											Mean	σ	Mean LOD	N
AAO1	66.4	12.2	1.30	2.21	2.68	4.30	0.123	0.0629	89.3	20	540	14.1	0.515	4
σ	0.755	0.354	0.0904	0.105	0.216	0.0913	0.02	0.0365	0.834					
AAO2	67.5	12.1	1.29	2.17	2.77	4.42	0.108	0.0501	90.4	22	731	93.6	0.527	3
σ	0.49	0.141	0.157	0.0987	0.130	0.0950	0.02	0.0541	0.555					
AAO3	68.0	12.1	1.23	1.98	2.61	4.40	0.109	0.0537	90.5	18	501	23.7	0.432	5
σ	2.26	1.12	0.342	0.749	0.577	0.261	0.05	0.0490	1.58					
AAO4	65.6	12.7	1.49	2.34	2.74	4.29	0.145	0.0437	89.2	16	370	57.7		4
σ	0.556	0.453	0.253	0.180	0.112	0.132	0.03	0.0473	0.531					
AAO6	66.3	12.2	1.37	2.16	2.73	4.34	0.156	0.0642	89.3	17	486	51.6		6
σ	0.434	0.252	0.149	0.140	0.124	0.119	0.02	0.0464	0.591					
AAO13	64.8	13.4	2.10	1.80	2.29	4.18	0.191	0.0404	89.4	15	6658	875	0.813	4
σ	1.84	1.74	0.545	0.372	0.132	0.212	0.04	0.0294	0.872					
AAO19	67.8	12.2	0.497	1.81	2.68	4.71	0.151	0.0315	89.8	12	5.13	0.375	0.440	3
σ	0.412	0.0884	0.0240	0.135	0.0920	0.0861	0.10	0.0248	0.411					
AAO20	67.3	12.2	2.28	2.25	2.71	4.32	0.172	0.0395	91.2	13	365	26.2	0.250	2
σ	0.344	0.198	0.120	0.263	0.0659	0.116	0.14	0.0307	0.587					
AAO21	65.4	12.1	0.750	2.17	5.46	6.20	0.122	0.0932	92.2	15	485	47.5	0.600	4
σ	0.267	0.0943	0.0331	0.0391	0.0733	0.0611	0.02	0.0253	0.345					
AAO24	65.7	12.2	0.757	2.06	4.04	5.33	0.016	0.100	90.2	4	93.7	20.7	0.48	2
σ	0.738	0.196	0.0424	0.0862	0.0885	0.0898	0.01	0.0057	1.10					
AAO25	66.6	13.4	0.791	1.93	3.03	4.36	0.208	0.0101	90.4	20	584	44.5	0.263	6
σ	1.69	1.89	0.0490	0.0679	0.162	0.164	0.01	0.0317	0.685					
AAO26	61.2	16.1	1.58	3.13	3.02	3.39	0.960	0.0942	89.5	20	706	54.7	0.332	6
σ	0.478	0.303	0.0697	0.100	0.120	0.0607	0.05	0.0356	0.400					

	SiO_2 (Wt.%)	Al_2O_3 (Wt.%)	MgO (Wt.%)	CaO (Wt.%)	Na_2O (Wt.%)	K_2O (Wt.%)	P_2O_5 (Wt.%)	F (Wt.%)	Total (Wt.%)	N	LA-ICP-MS ^{75}As (μg/g)			
											Mean	**σ**	**Mean LOD**	**N**
AAO27	63.2	12.5	1.71	2.51	3.88	5.66	0.106	0.0912	89.6	17	1307	147	11.0	8
σ	0.465	0.128	0.111	0.133	0.186	0.165	0.03	0.0410	0.625					
AAO29	62.5	12.4	1.69	3.06	4.89	6.21	0.127	0.0356	90.9	28	74.7	5.64	1.18	7
σ	0.527	0.174	0.106	0.167	0.246	0.271	0.03	0.0308	0.758					
AAO30	64.3	12.5	1.49	1.79	3.52	7.00	0.064	0.0571	90.7	15	156	18.2	1.20	4
σ	0.566	0.142	0.227	0.538	0.274	0.212	0.02	0.0436	0.493					
AAO32	63.1	12.1	1.82	2.75	5.23	6.12	0.180	0.0892	91.3	17	244	45.7	1.75	6
σ	1.20	0.254	0.0823	0.172	0.718	0.162	0.03	0.0404	1.48					
AAO33	63.5	12.1	1.42	2.61	5.24	6.32	0.131	0.0737	91.3	17	39.6	12.8	0.500	5
σ	0.697	0.173	0.0910	0.0880	0.211	0.0872	0.02	0.0300	0.803					
AAO39	64.4	12.0	2.52	2.62	5.35	6.31	0.187	0.105	93.4	11	135	12.6	0.452	5
σ	0.536	0.150	0.124	0.0574	0.0845	0.0795	0.04	0.1640	0.710					
AAO47	64.7	12.0	2.05	4.54	2.34	3.71	1.74	0.102	91.1	14				
σ	1.00	0.479	0.191	0.720	0.0492	0.0756	0.39	0.0360	0.602					
AAO47*	67.6	12.3	1.96	1.96	2.43	3.90	0.166	0.0353	90.3	7	343	66.7	0.393	8
σ	0.154	0.151	0.0992	0.0696	0.0506	0.0636	0.04	0.0292	0.300					
AAO49	61.0	11.8	1.70	4.24	4.67	5.39	1.30	0.0812	90.1	20				
σ	0.973	0.180	0.0859	0.772	0.656	0.2890	0.50	0.0421	0.552					
AAO49*	62.9	12.1	1.62	2.34	5.27	5.72	0.111	0.0531	90.1	4	106	10.5	0.529	7
σ	0.861	0.130	0.115	0.0198	0.129	0.0852	0.01	0.0596	0.987					
AAO50	61.4	16.3	3.57	3.08	3.17	3.30	0.656	0.0703	91.5	20	158	39.8	0.577	7
σ	0.270	0.130	0.115	0.0723	0.0536	0.0561	0.04	0.0320	0.401					

* Represent microprobe analyses on glass without micro-apatites.

Table 4.4 Summary of major and trace element abundances in run-product apatites.

	CaO (Wt.%)	P_2O_5 (Wt.%)	F (Wt.%)	Na_2O (Wt.%)	K_2O (Wt.%)	SiO_2 (Wt.%)	Al_2O_3 (Wt.%)	MgO (Wt.%)	Total (Wt.%)	N	LA-ICP-MS ^{75}As (µg/g)			
											Mean	**σ**	**Mean LOD**	**N**
AAO1	55.1	40.5	1.55	0.0390	0.129	0.331	0.0289	0.225	98.6	18	5348	645	52.4	5
σ	0.496	0.285	0.0515	0.0178	0.0211	0.0677	0.0196	0.0151	0.630					
AAO2	54.6	40.5	1.46	0.0253	0.160	0.434	0.0455	0.216	98.4	12	5328	808	43.0	5
σ	0.562	0.309	0.0685	0.0187	0.0288	0.124	0.0261	0.0160	0.769					
AAO3	54.9	40.8	1.43	0.0181	0.101	0.281	0.0301	0.223	98.5	11	5722	568	73.4	5
σ	0.542	0.247	0.0797	0.0103	0.0300	0.0623	0.0176	0.0197	0.677					
AAO4	54.7	40.6	1.35	0.0210	0.0945	0.304	0.0387	0.217	98.0	13	4014	426	65.6	5
σ	0.404	0.381	0.0495	0.0115	0.0485	0.176	0.0410	0.0175	0.657					
AAO6	54.5	40.6	1.36	0.0170	0.131	0.355	0.0378	0.219	97.7	18	4368	526	49.8	5
σ	0.563	0.266	0.0583	0.0142	0.0297	0.160	0.0252	0.0170	0.616					
AAO13	54.6	38.0	1.34	0.0323	0.126	0.409	0.0624	0.270	98.7	7	40240	17060	192	5
σ	0.560	0.694	0.0448	0.0154	0.0291	0.165	0.0460	0.0261	0.557					
AAO19	55.2	41.7	1.63	0.0152	0.113	0.320	0.0205	0.224	99.2	13			6.8	
σ	0.579	0.315	0.0669	0.0080	0.0222	0.0514	0.0104	0.0143	0.759					
AAO20	54.8	40.1	1.54	0.0529	0.183	0.956	0.105	0.164	99.2	14	8324	1317	43.7	4
σ	0.613	0.516	0.0830	0.0328	0.0495	0.487	0.0818	0.0139	0.758					
AAO21	54.4	40.5	1.55	0.0908	0.145	0.428	0.0159	0.0498	97.6	17	3070	411	19.8	5
σ	0.700	0.249	0.0720	0.0541	0.0432	0.0972	0.0129	0.0143	0.959					
AAO24	55.0	41.1	2.11	0.0678	0.207	0.764	0.0719	0.0354	99.5	7			27.3	
σ	0.232	0.109	0.158	0.0170	0.0500	0.175	0.0272	0.00452	0.308					
AAO25	54.0	41.2	1.37	0.1176	0.0818	0.214	0.0191	0.216	97.9	19	5082	1305	23.0	5
σ	0.469	0.377	0.123	0.0644	0.0229	0.166	0.0337	0.0147	0.753					
AAO26	54.1	41.4	1.68	0.0448	0.0782	0.201	0.0491	0.486	98.3	15	1845	618	37.5	4
σ	0.612	0.239	0.0778	0.0307	0.0297	0.0776	0.0227	0.0137	0.831					

	CaO (Wt.%)	P_2O_5 (Wt.%)	F (Wt.%)	Na_2O (Wt.%)	K_2O (Wt.%)	SiO_2 (Wt.%)	Al_2O_3 (Wt.%)	MgO (Wt.%)	Total (Wt.%)	N	LA-ICP-MS ^{75}As (µg/g)			
											Mean	**σ**	**Mean LOD**	**N**
AAO27	55.4	38.8	1.49	0.0136	0.146	0.393	0.0239	0.0690	99.6	12	23986	477	20.0	5
σ	0.491	0.281	0.0398	0.0126	0.0318	0.0443	0.0185	0.00935	0.612					
AAO29	55.5	41.0	1.66	0.1595	0.139	0.444	0.0173	0.0544	99.1	16	1411	114	19.2	5
σ	0.667	0.256	0.0723	0.0273	0.0250	0.0612	0.0140	0.0126	0.901					
AAO30	55.5	40.6	1.55	0.0186	0.128	0.441	0.0143	0.0587	99.0	14	4525	311	49.5	5
σ	0.517	0.229	0.0764	0.0121	0.0660	0.0830	0.0189	0.0115	0.725					
AAO32	56.0	41.7	1.59	0.0145	0.122	0.439	0.0294	0.0528	100.1	15	819	110	32.0	5
σ	0.477	0.217	0.0559	0.0178	0.0312	0.0711	0.0160	0.0152	0.536					
AAO33	55.6	41.3	1.60	0.1086	0.119	0.355	0.00990	0.0470	99.2	12	55	12.9	59.4	8
σ	0.359	0.269	0.0659	0.0184	0.0245	0.0395	0.0123	0.0185	0.465					
AAO39	51.5	37.7	0.98	0.2070	0.187	1.60	0.0248	0.0695	92.3	11	645	57.7	53.2	5
σ	1.04	0.931	0.0691	0.0376	0.0256	0.387	0.0196	0.0181	1.47					
AAO47	54.9	41.3	1.85	0.0334	0.165	0.504	0.0656	0.356	99.2	8			44.4	7
σ	0.754	0.268	0.121	0.0300	0.0168	0.0683	0.0133	0.1198	0.789					
AAO49	55.5	41.2	1.79	0.0505	0.238	0.667	0.0452	0.0299	99.5	12			60.0	14
σ	0.722	0.250	0.0854	0.0172	0.0219	0.134	0.0287	0.00804	0.853					
AAO50	55.1	41.6	2.21	0.0238	0.120	0.296	0.0443	0.622	100.0	14			50.6	17
σ	0.667	0.217	0.127	0.0084	0.0125	0.0684	0.0138	0.0241	0.738					

To obtain accurate estimates of apatite/melt partitioning, a mass balance calculation was used to reconstruct the glass concentration of As at the time of apatite crystallization (details provided in the supplementary information (SI) section). These new partition coefficients are the Adjusted $D^{Apatite/Melt}$ values in Table 4.5. Briefly, the method assumes that the glass composition at the onset of the experiment is equal to the total As concentration added, minus the amounts apportioned to the apatite and vapor phase. This approach assumes that only the vapor and melt lose As. This assumption is reasonable since the loss of As from apatite once formed is expected to be negligible assuming volume diffusion parameters similar to S^{VI} (Li et al., 2020) or REE^{III} (Cherniak, 2000). A time-series conducted at 1000°C at the Ru-RuO_2 buffer involving the metaluminous melt composition shows the As concentration of the glass decreasing with time while the As content of apatite is constant until at least 96 hours (Fig. 4.12).

The resulting partition coefficients from this time series calculated using loss-corrected melt compositions are also constant within error for runs of 24, 48, and 96 hours (Table 4.6), implying apatite-melt equilibrium at 24 hours. This result is consistent with partitioning experiments involving other slow-diffusing cations such as the REE, in which Watson and Green (1981) demonstrated equilibrium by reversal experiments in as little as 12 hours at 950°C.

4.3.4. Arsenic Speciation Systematics

The speciation of As in the metaluminous glasses (MAL; Fig. 4.5, Table 4.6) synthesized at FMQ + 7.2 is mostly As^{V}, with linear combination fitting returning less than 30% As^{III}. Over the temperature range of 900-1050°C, there is negligible change in As speciation for this composition at the same redox buffer. The proportion of As^{V} decreases with decreasing fO_2, as the metaluminous glass sample synthesized at FMQ - 0.4 contains only As^{III}. In terms of melt composition effects, at the same temperature and fO_2, the peraluminous glass (PAL) contains a higher proportion of As^{III} than the metaluminous compositions (Table 4.6).

Table 4.5 Summary of measured and modelled As partitioning coefficients.

Experiment	$D^{Apatite/Melt}$	σ_D	Arsenic Lost	Adjusted $D^{Apatite/Melt}$	Adjusted σ_D	Modeled $D^{Apatite/Melt}$	Residuals
AAO01	9.91	1.22	28%	6.40	0.77	7.50	1.01
AAO02	7.29	1.45	11%	6.34	1.26	7.62	1.28
AAO03	11.4	1.26	30%	7.16	0.79	7.53	0.370
AAO04	10.9	2.05	50%				
AAO06	9.00	1.44	39%				
AAO13	6.04	2.68	0%	6.04	2.68	6.78	0.740
AAO19	1.31	Max	99%				
AAO20	22.8	3.97	11%	18.9	3.29	17.6	-1.35
AAO21	6.33	1.05	18%	4.97	0.82	4.95	-0.0154
AAO24	0.0726	Max	87%				
AAO25	8.70	2.33	0%	8.70	2.33	3.37	-5.32
AAO26	2.61	0.898	1%	2.58	0.89	6.05	3.47
AAO27	18.4	2.10	41%	8.52	0.98	8.26	-0.258
AAO29	18.9	2.09	65%	4.69	0.52	8.53	3.84
AAO30	29.0	3.94	55%	8.19	1.11	8.37	0.181
AAO32	3.36	0.776	62%	1.18	0.27	1.65	0.476
AAO33	1.40	0.559	94%	0.078	0.03	0.335	0.256
AAO39	4.76	0.614	78%	0.948	0.12	1.70	0.750
AAO47	0.0788	Max				0.100	0.0230
AAO49	0.285	Max				0.100	-0.181
AAO50	0.0563	Max				0.100	0.0448

The XANES spectra determined 43% As^{III} for the peralkaline composition (ALK) synthesized at FMQ +5.9. This amount of As^{III} is similar to the peraluminous composition but higher than the metaluminous composition, both of which are more oxidized at FMQ +7.2. Considering that higher fO_2 will stabilize more As^{V} and less As^{III}, there should be <43% As^{III} if the peralkaline composition was at FMQ +7.2, indicating that peralkaline compositions stabilize more As^{V} than peraluminous compositions. A more general assessment of the effects of both melt composition and fO_2 on As speciation can be gained by considering the equilibrium constant for the homogeneous speciation reaction:

$$As^{III}O_{3/2} + \frac{1}{2}O_2 \leftrightarrow As^{V}O_{5/2} \qquad (4.1)$$

expressed as:

$$\mathrm{K_{eq}} = \frac{a_{\mathrm{As^V}O_{5/2}}}{a_{\mathrm{As^{III}}O_{3/2}} \cdot fO_2{}^{1/2}} \tag{4.2}$$

where $\mathrm{K_{eq}}$ is the equilibrium constant, a_i is the activity of phase i, and $f\mathrm{O_2}$ is the oxygen fugacity.

$$a_i = \gamma_i \cdot X_i \tag{4.3}$$

Converting activities to mole fractions, X_i, by multiplying by each phase's activity coefficient, γ_i, yields:

$$\mathrm{K} = \frac{X_{\mathrm{As^V}O_{5/2}}}{X_{\mathrm{As^{III}}O_{3/2}} \cdot fO_2{}^{1/2}} \cdot \frac{\gamma_{AsIII}}{\gamma_{AsV}} \tag{4.4}$$

Assuming:

$$\Gamma = \frac{\gamma_{AsV}}{\gamma_{AsIII}} \tag{4.5}$$

then

$$\mathrm{logK} = -\log X_{\mathrm{As^{III}}O_{3/2}} + \log X_{\mathrm{As^V}O_{5/2}} - \frac{1}{2}\log f\mathrm{O_2} + \log\Gamma \tag{4.6}$$

which can be arranged as

$$\mathrm{logK'} = \log\frac{X_{\mathrm{As^V}O_{5/2}}}{X_{\mathrm{As}^{III}O_{3/2}}} - \frac{1}{2}\log f\mathrm{O_2} \tag{4.7a}$$

where

$$\mathrm{logK'} = \mathrm{logK} - \log\Gamma \tag{4.7b}$$

The effective equilibrium constant of this reaction, K', can be used to describe the speciation in quantitative terms. Lower K' values indicate that $\mathrm{As^{III}}$ is more abundant at a given $f\mathrm{O_2}$. Thus, the peralkaline compositions stabilize more $\mathrm{As^V}$ than either metaluminous or peraluminous compositions (Table 4.6). Felsic melts have slightly more $\mathrm{As^V}$ than basaltic melts. At FMQ +3, there is 0.2% $\mathrm{As^V}$ in basaltic melts (Maciag and Brenan, 2020), while peraluminous felsic melts contain 1% and peralkaline felsic melts contain 7%.

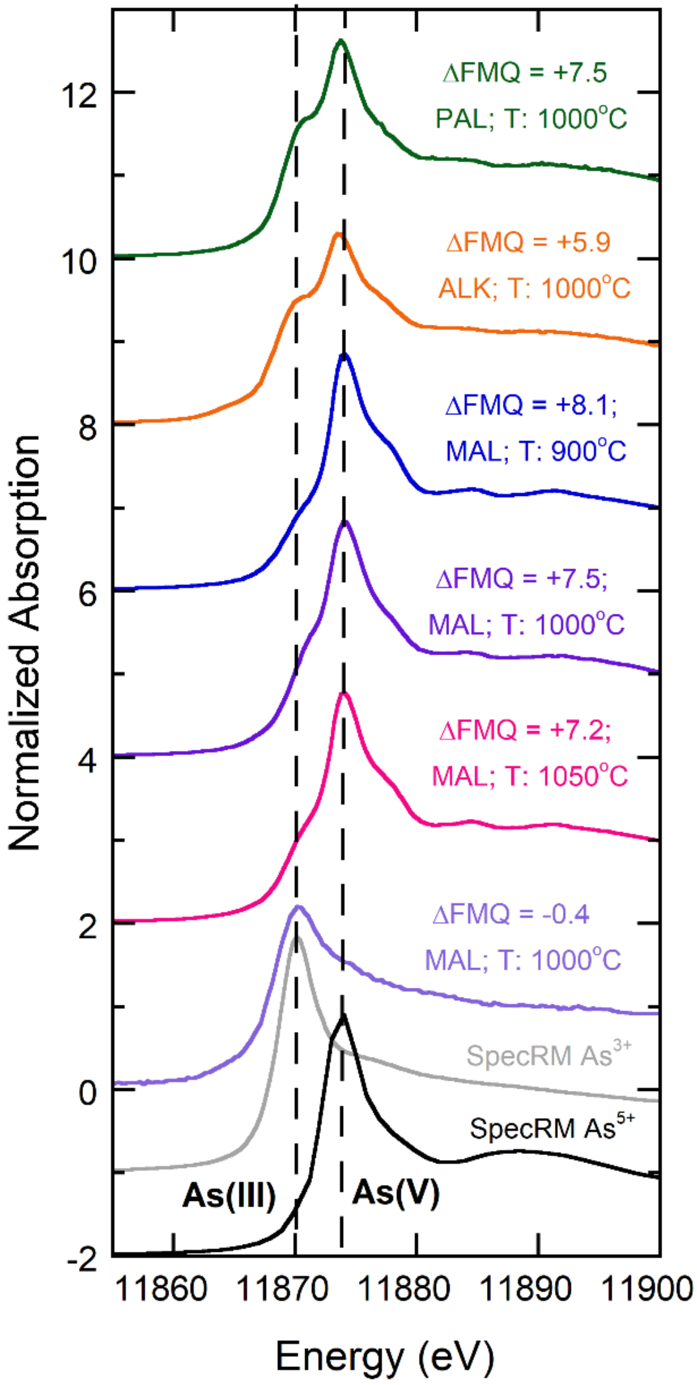

Figure 4.5 Normalized absorption spectra at the As K-edge as a function of energy (eV) for As-bearing glasses synthesized at various fO_2 and compositions (as labelled). Spectral reference materials for $As^{III}(OH)3$ and $As^{V}O(OH)3$ are from Borisova et al. (2010). Vertical lines show the white line position for As^{III} and As^{V}

Table 4.6 - Linear combination least squares fitting results from XANES for experimental run - products.

Exp. ID	Comp.	ΔFMQ	T (°C)	As(III)			As(V)			logK'	$\sigma_{LogK'}$	R-factor
AAO01	MAL	7.5	1000	26%	±	1.0%	74%	±	2.5%	2.26	0.111	0.00642
AAO03	MAL	7.5	1000	22%	±	1.0%	78%	±	1.8%	2.33	0.126	0.00712
AAO19	MAL	-0.4	1000	100%	±	5.0%				N/A		0.00637
AAO20	MAL	8.1	900	18%	±	1.2%	82%	±	0.8%	2.96	0.123	0.00578
AAO21	ALK	5.9	1000	52%	±	0.6%	47%	±	0.6%	2.59	0.067	0.00385
AAO25	MAL	7.2	1050	23%	±	1.8%	77%	±	0.1%	2.10	0.103	0.00468
AAO26	PAL	7.5	1000	43%	±	2.0%	57%	±	0.7%	1.91	0.071	0.00392

4.3.5. Arsenic Partitioning Systematics

The adjusted experimentally determined partition coefficients (Table 4.5) vary in three ways. First, the $D^{Apatite/Melt}$ increases with increasing fO_2 (Fig. 4.6A). In reduced experiments at FMQ -0.4, the amount of As in apatite was below the analytical detection limits and thus only maximum values are plotted. Second, the $D^{Apatite/Melt}$ increases with increasing alkalinity or decreasing ASI (Fig. 4.6B), as As^{V} is more stable in alkaline melts (Table 4.6). This stabilization is probably related to the greater abundance of non-bridging oxygen which is favourable for oxidized species (Pyare and Nath, 1991). Finally, the $D^{Apatite/Melt}$ increases with decreasing temperature if fO_2 is fixed at the same redox buffer (Fig 4.6C).

4.3.6. Arsenic Partitioning Model

The partition coefficient for As can be modelled as a combination of the partition coefficients for each oxidation state, described by the equation:

$$D_{As}^{Apatite/Melt} = D_{As(III)}^{Apatite/Melt}\left(\frac{X_{AsIII}}{X_{\Sigma As}}\right) + D_{As(V)}^{Apatite/Melt}\left(1 - \frac{X_{AsIII}}{X_{\Sigma As}}\right) \qquad (4.8)$$

in which $D_{As}{}^{Apatite/Melt}$ is the partition coefficient for As between apatite and melt, $D_{As(III)}$, $D_{As(V)}$ are the partition coefficient for the indicated species, X_{AsIII} is the mole fraction of As^{III} and $X_{\Sigma As}$ is the total As mole fraction in the melt.

Results of the XANES measurements of run-product glasses define the effects of melt composition and temperature on As speciation. The XANES measurements also allow for the calculation of the endmember values of $D_{As(V)}$ for the analyzed experiments. Linear regression analysis calculated the speciation as a function of melt composition and temperature, and $D_{As(V)}$ as a function of temperature. Combining these results with equation 4.8 yields (see SI for a full derivation):

$$D_{As}^{\frac{Apatite}{Melt}}(\pm 0.42) = \frac{178{,}000(\pm 42{,}600)}{\mathrm{T}} - 130\ (\pm 33.8) + \left(\frac{0.1 - \left(\frac{178{,}000(\pm 42{,}600)}{\mathrm{T}} - 130\ (\pm 33.8)\right)}{(1 + 10^{(\frac{1}{2}\log fO_2 + \frac{9{,}500(\pm 1{,}210)}{\mathrm{T}} - 0.579(\pm 0.0805)\Psi - 4.40(\pm 0.960))}} \right) \tag{4.9}$$

in which T is the temperature in Kelvin, fO_2 is oxygen fugacity in bars, and Ψ is the melt molar (Al/(Na+K)). Comparing each experiment modelled $D^{Apatite/Melt}$ determined from equation 4.9 against the adjusted values (Table 4.5) results in a standard error of 0.42 based on the variance of the residuals and an unweighted R^2 value of 0.86 (Fig. 4.7).

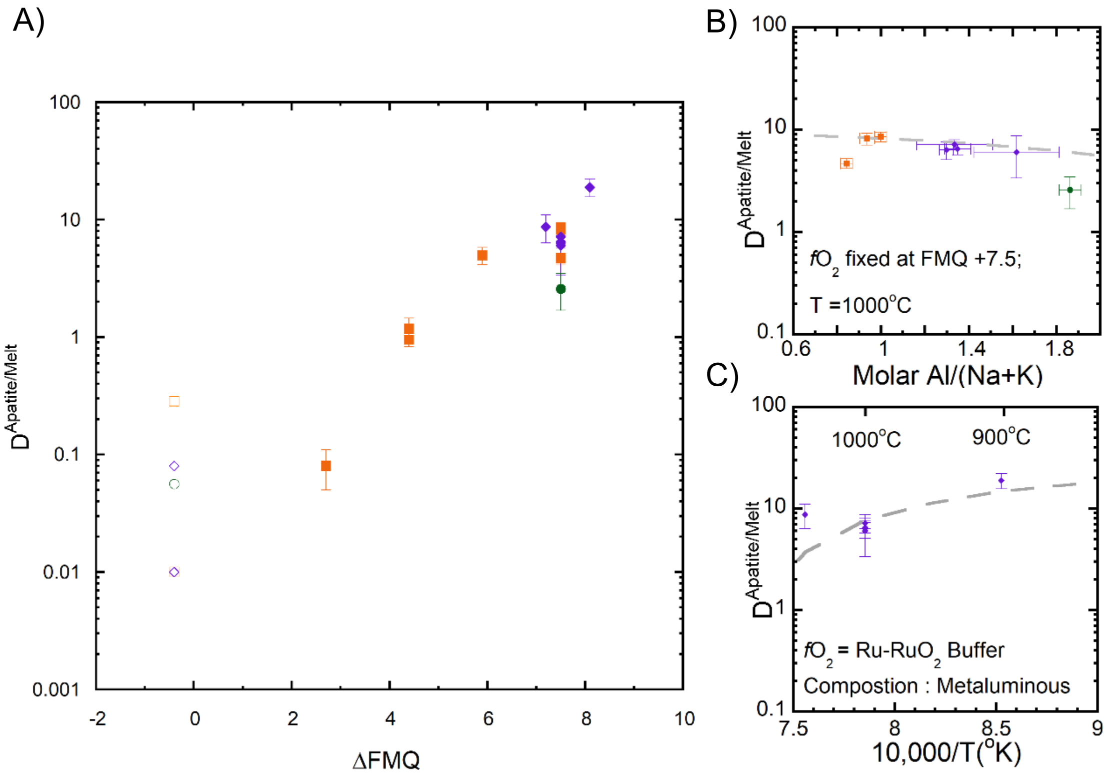

Figure 4.6 Experimentally determined $D^{Apatite/Melt}$ for As as a function of A) oxygen fugacity; B) the molar (Al/Na+K); and C) the inverse of temperature. Partition coefficients are corrected for the As loss from the sample using the method described in the supplementary text. Green (circle), purple (diamonds) and orange (square) symbols correspond to peraluminous, metaluminous and peralkaline composition, respectively. Open symbols are maximum partition coefficients as the As content of the run-product apatite is below detection limits. Variation in maximum values is due to the size of the apatite grains, with larger apatites giving lower minimum detection limits. The gray line in plots B) and C) are the model predictions from the regression.

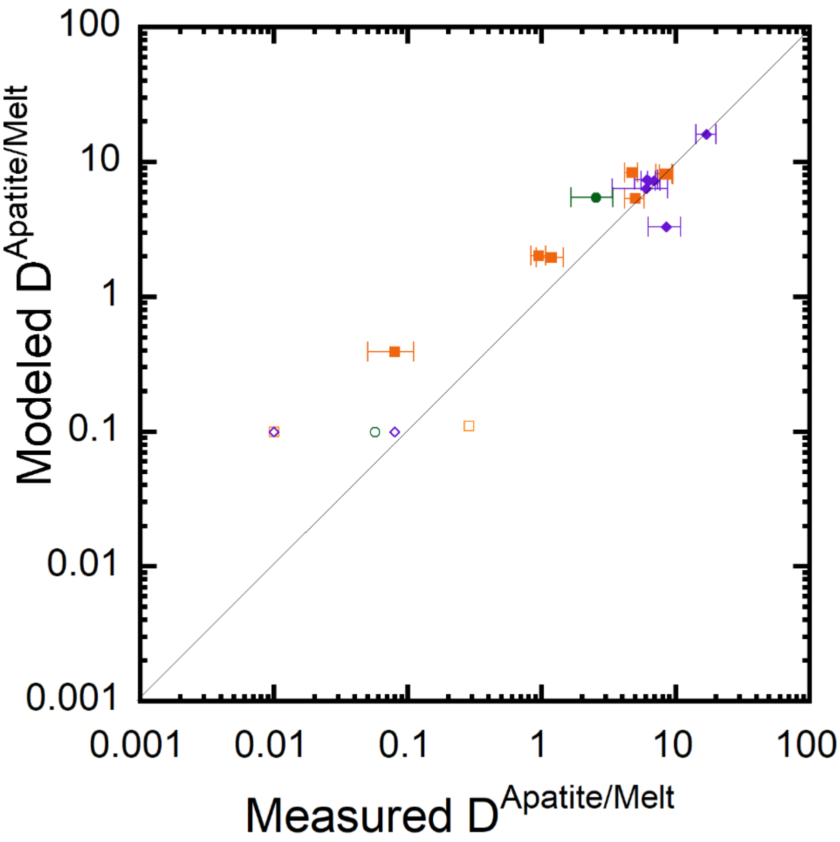

Figure 4.7 Comparison between model and adjusted apatite/melt partition coefficients for As. Model values are calculated from equation 4.9 in the text.

Modelled values of $D^{Apatite/Melt}$ increase from a minimum of ~0.1 at FMQ -2 or lower to a maximum of 20 at FMQ +8.5 and above (Fig. 4.8). For the range of fO_2 estimated for terrestrial felsic magmas (FMQ -3 to FMQ +3.5; Carmichael 1991; Černý et al. 2005) the maximum $D^{Apatite/Melt}$ is ~0.74 or less for metaluminous to peraluminous compositions ($\Psi > 1$), and ~1.3 in peralkaline compositions ($\Psi = 0.5$). These calculations show that As is generally incompatible in apatite crystallized from a range of felsic magma compositions, except under highly oxidizing conditions that exceed the natural fO_2 range.

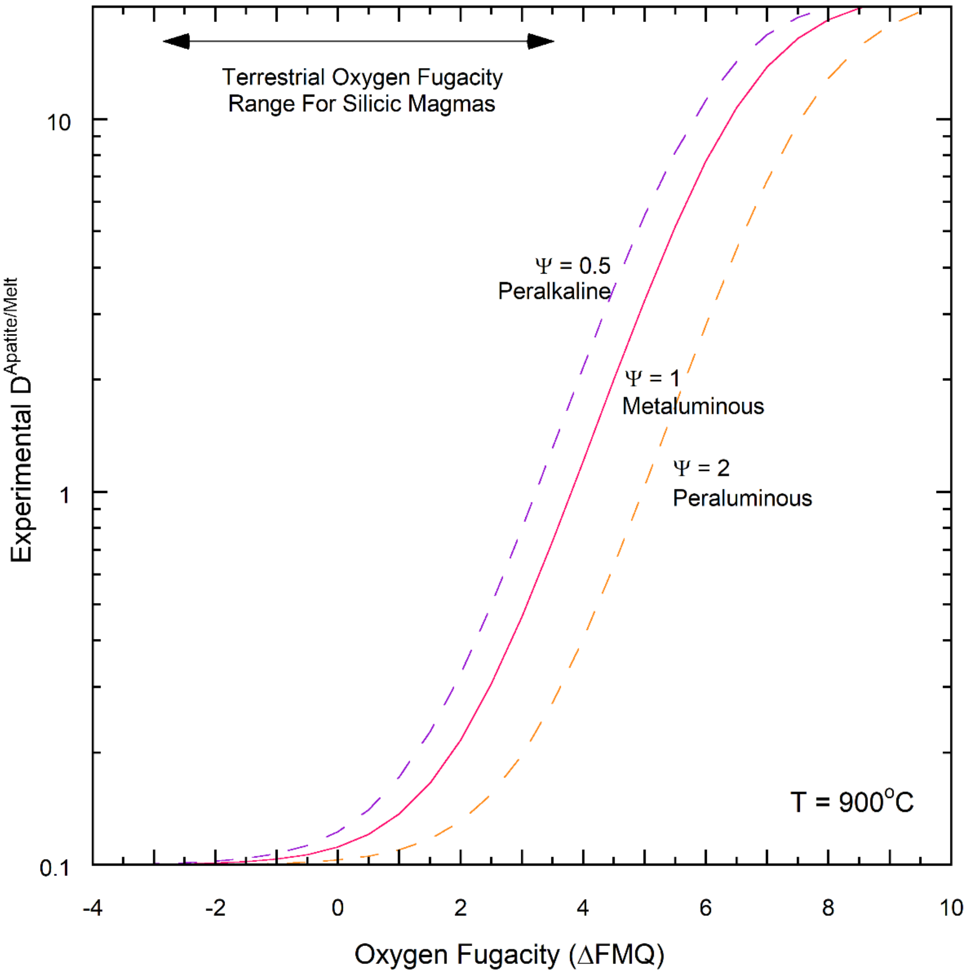

Figure 4.8 Modeled apatite/melt partition coefficient as a function of oxygen fugacity for different melt compositions (Ψ= molar (Al/Na+K)) at 900°C. The approximate alumina saturation index (ASI = molar (Al/(Na+K+Ca)), for each Ψ are at Ψ=0.5 AS I= 0.35 to 0.4; Ψ = 1, ASI = 0.6 to 0.8; Ψ= 2.0, ASI = 0.9 to 1.4.

4.3.7. Comparison to Natural Apatite/Melt Concentration Ratios

For plutonic and extrusive samples, whole-rock analyses can serve as a proxy for the melt composition, assuming the sample was not formed by crystal accumulation. While this assumption may not hold for all plutonic rocks, it provides a simple starting point that can be used to assess trace element behavior that can be expanded upon with more elaborate models. The results of this study predict that apatite/whole-rock partition coefficients ($D^{Apatite/Whole\text{-}rock}$) will range between ~0.1 and ~0.6 assuming an fO_2 between FMQ -3 and FMQ +3.5 and melt compositions with Ψ ≥ 1. Some samples from the South Mountain Batholith (this study), and Mt St. Hilaire (Tice, 2010; Marks et al., 2012) yield values of $D^{Apatite/Whole\text{-}rock}$ that are consistent with this predicted range (Fig. 4.1), but also include samples that extend to higher values. All the granitoids from the Lachlan Fold Belt (Sha and Chappell, 1999) exceed the predicted $D^{\text{Apatite/Whole-rock}}$ and have values up to 80. This study also estimated $D^{\text{Apatite/Whole-rock}}$ from three compilations of apatite compositions (Belousova et al., 2002; Guo and Audétat, 2017; Nathwani et al., 2020) for which whole-rock As concentrations are unavailable. Calculations assumed a value of 4.5 µg/g As for these whole-rocks. This value represents a compilation of 895 felsic volcanic rock analyses from the East China Craton (Gao et al., 1998). The estimated $D^{\text{Apatite/Whole-rock}}$ for felsic volcanic rocks is in the range expected from the experiments. The higher As content in some of the apatite's from the Chilean volcanics is likely due to some rocks forming from melts that have higher As concentrations. The As content of the Chilean apatite's loosely correlates negatively with the apatite Mg content. As a lower Mg content indicates a greater degree of fractionation before eruption (Nathwani et. al., 2020) a higher As content in these apatites is consistent with the incompatible behavior of As. Some of the granitoid compilation values are consistent with the experimental $D^{\text{Apatite/Whole-rock}}$, but the majority are anomalously high. Calculations based on the experimental calibration of $D^{\text{Apatite/Melt}}$ provided in this study require fO_2 of FMQ +8.2 and +5.0 to reproduce the median observed $D^{\text{Apatite/Whole-rock}}$ for samples from the Lachlan Fold Belt and the South Mountain Batholith, respectively. For comparison, Whalen and Chappell (1988) summarised the opaque and mafic mineral characteristics of the Lachlan Fold Belt granites with results indicating that most ilmenite-bearing peraluminous granites (S-type) formed at fO_2 less than FMQ, although some magnetite-bearing S-type granites may reflect conditions at ~FMQ. Based on the presence of magnetite, and other indicators, estimates suggest that the associated metaluminous granites (I-type) formed at an fO_2 greater than FMQ but below the magnetite-hematite buffer. The fO_2 needed to produce the median values of $D^{\text{Apatite/Melt}}$ would be consistent with hematite as the primary oxide, which is present in some Lachlan Fold Belt samples. However, this phase occurs as exsolution in primary magnetite, and is related to late deuteric alteration. Estimates for the fO_2 at which the South Mountain Batholith crystallized are at FMQ and below, based on biotite compositional relations (Brenan et al., Submitted) and Ce-in-zircon oxygen barometry (Chavez Cabrera, 2019; Bickerton et al., 2022). These measured values are much less than the extremely oxidized conditions of FMQ +5.0 suggested by apatite/melt partitioning.

Ruling out unusually high *f*O_2, the only plausible reason for apatite As concentrations to exceed whole-rock values is if the whole-rock composition does not represent the melt that crystallized apatite. Therefore, conditions must exist during magma crystallization at the sample scale that allow the melt to achieve extreme As concentrations which can lead to the observed As-enriched apatite.

4.3.8. Mechanism for Arsenic Enrichment in Apatite

The results of this study show that the speciation of As in felsic melt compositions is primarily as As^{III}. Previous work (Maciag and Brenan, 2020) found that this form of As is incompatible in most rock-forming silicates due to size and charge mismatch with common octahedral and tetrahedral sites. This is consistent with the uniformly low As concentrations determined in minerals from the South Mountain Batholith and other granite occurrences (Chapter 5; this thesis). Arsenic should therefore behave incompatibly and concentrate in the melt during crystallization (the exception to this would be significant sulfide crystallization, causing As depletion in the melt). Therefore, the later in the crystallization sequence that apatite saturation occurs, the more enriched in As the apatite will become.

Experiments have shown that the solubility of apatite depends on temperature, melt SiO_2 and CaO concentrations (Harrison and Watson, 1984; Wolf and London, 1994; Tollari et al., 2006); thus, the timing of apatite saturation strongly depends on the evolving melt composition.

To determine if the necessary level of As enrichment can be achieved to produce the observed elevated $D^{Apatite/Whole\text{-}rock}$ in natural suites, this study simulated the fractional crystallization behavior of a South Mountain Batholith granitic liquid composition using the MELTS thermodynamic model. A complicating effect is that plutonic rocks that contain a significant proportion of accumulated crystals will have whole-rock element contents either lower or higher (depending on the element compatibility in the accumulated crystals) than values corresponding to 100% liquid. To evaluate if whole-rock compositions are an accurate representation of a liquid, a comparison is made to available low pressure phase equilibria (Fig. 4.9) in the quartz+albite+orthoclase system

(Tuttle and Bowen, 1958; and Steiner et al., 1975). Estimates for the pressure of formation for the South Mountain Batholith range from 250 to 400 MPa (Brenan et al., Submitted), and a value of 350 MPa was chosen for the correction applied here. The whole-rock compositions from the South Mountain Batholith do not plot on the trace of the multiple saturation points, but rather are shifted to more quartz and orthoclase-rich composition, suggesting that there is a component of crystal accumulation. The melt component of these samples can be reconstructed by subtracting off the composition of the accumulated crystals. By removing 12.5% quartz and 12.5% orthoclase from sample 18JC-0010 (Fig. 4.9, Red square) the composition shifts to the multiple saturation point at 350 MPa (Fig. 4.9 black square). The whole-rock As concentration was also corrected from a value of 3 μg/g to a value of 4 μg/g assuming that quartz and k-spar are nominally As-free. This reconstructed composition was used in the MELTS models (Table 4.8). Models used rhyolite-melts v1.1 and rhyolite-melts v1.0 algorithms in the MELTS for Excel package to track the liquid composition, with the apatite solubility determined at each step using the calibration of Tollari et al. (2006). Equation 4.9 was used to calculate the As concentration of apatite once saturation was achieved. Further details of the model are provided in the supplemental text. Figure 4.10 shows the variation in the As content of apatite and melt as a function of percent crystallization and Fig. 4.1 displays the calculated $D^{\text{Apatite/Whole-rock}}$ range. Calculations assumed initial water contents of 2 and 5 wt%, with the highest value consistent with estimates for vapor saturation of the South Mountain Batholith. Crystallization models yield apatite at 650°C after ~80% crystallization containing 2.2 to 39.7 μg/g of As and $D^{\text{Apatite/Whole-rock}}$ between 0.75 and 13. An additional constraint to this model are the petrographic relationships that reflect the relative timing of apatite crystallization compared to other phases. In this case, biotite-apatite textural associations are unambiguous, as the common occurrence of apatite included in biotite indicates that apatite must form before biotite finished crystallizing. This relationship can mean that either apatite precedes biotite or that biotite and apatite co-crystallize followed by biotite-only crystallization. The hydrous MELTS model indicates that biotite forms at 865°C and continues to crystallize until 550°C, although the highest proportion of biotite crystallization (> 13 wt.%) occurs above 700°C. Titanium-in-biotite thermometry on the same South Mountain Batholith samples (Brenan et al., Submitted), yield biotite crystallization temperatures from ~725°C to ~600°C, consistent with the MELTS model. Crystallization of biotite at lower temperatures than 600°C is likely, as indicated by the presence of low Ti, high Fe biotite within the sampled suite, but those compositions are outside the calibrated range for the Ti-in-biotite thermometer (Henry et al., 2005). The large crystallization interval of biotite and the high solubility of apatite in peraluminous melts (Harrison and Watson, 1984; Bea et al., 1992; Pichavant et al., 1992; Wolf and London, 1994; Tollari et al., 2006) suggest that apatite must have co-crystalized with biotite, rather than forming early.

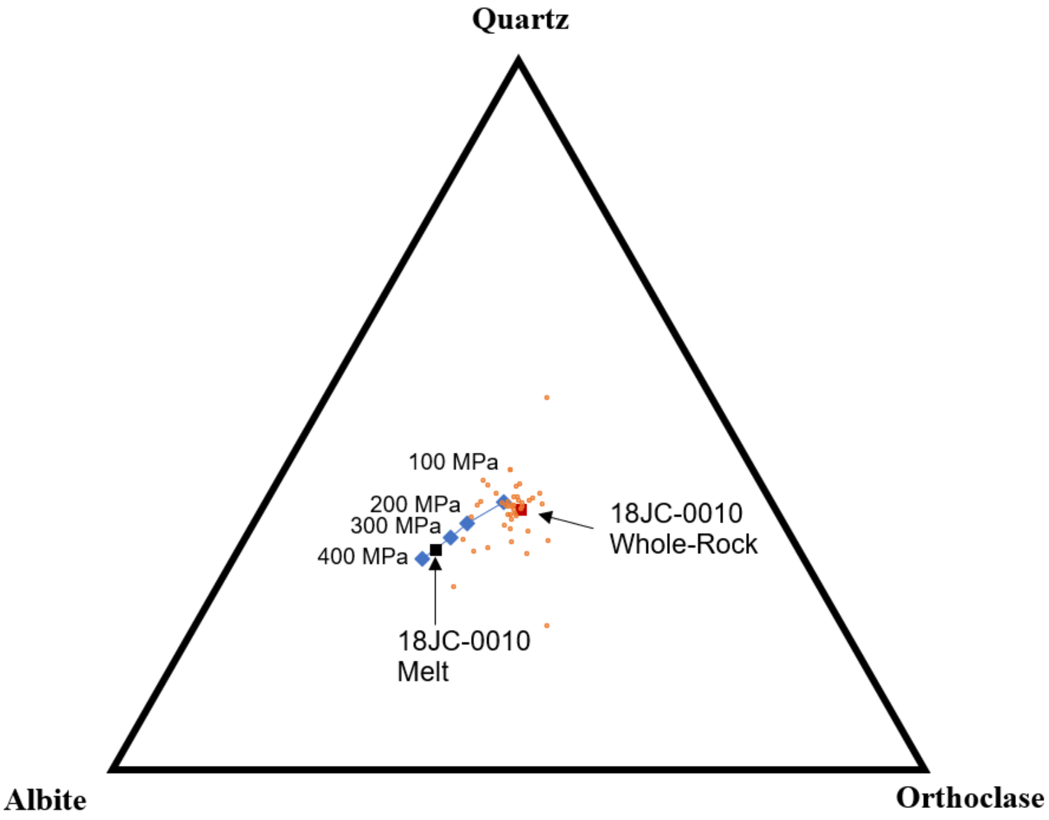

Figure 4.9 Quartz-Albite-Orthoclase ternary plot showing the trace of the hydrous granitic eutectic from 400 MPa to 100 MPa (blue diamonds; data from Tuttle and Bowen, 1958; and Steiner et al., 1975). Orange circles are South Mountain Batholith whole-rock compositions. The red square is the projected whole rock composition of 18JC-0100, and the black square is the same composition after subtracting 12.5% quartz and 12.5% orthoclase to bring it to the point of multiple saturation at ~400 MPa.

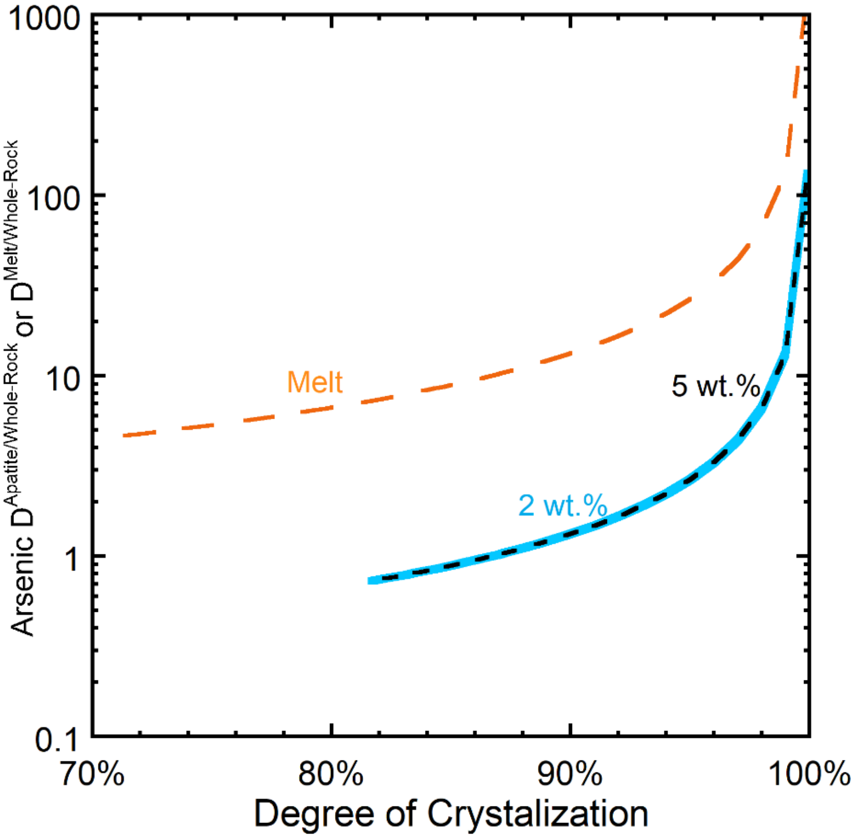

Figure 4.10 Modeled As apatite/whole-rock and melt/whole-rock partition coefficients as a function of the degree of crystallization. The modelled melt is from sample 18JC-0010. This melt represents a Stage 2 leucomonzogranite from the South Mountain Batholith, and the whole rock composition of the sample was modified to remove the crystal accumulation contribution. The melt has an initial As concentration of 4 µg/g. Crystallization models were run assuming 2 and 5 wt.% water.

An alternative method for enriching the melt in P and As is by pile-up diffusion next to a growing crystal (Holycross and Watson, 2018) or in a trapped pore space (Bea et al., 2022). To accurately evaluate these models, detailed information on the diffusion of As in silicate melts is needed, which is not available. The process of pile-up diffusion may cause apatite to saturate before 650°C; however, due to the high solubility of apatite in peraluminous melts, the pile-up of P at a growing crystal face will not cause saturation until after significant crystallization. Similarly, the formation of trapped pore spaces in a granitic system also requires a significant amount of crystallization (Vigneresse et al., 1996). Thus, in a peraluminous melt both of these models would only have secondary effects on the timing of apatite and its associated arsenic content. Pile-up diffusion may play a more significant role in metalumnious melts due to the lower apatite solubility in such compositions.

4.3.9. Modelling of Other Trace Elements

Further support for the late apatite crystallization model is if the concentration of other trace elements incorporated into apatite follow a similar pattern of enrichment for the same extent of crystallization. As MELTS does not consider trace elements, models for the evolution of REEs, Y, Nb, Ta, U and Th used the Rayleigh equation to simulate fractional crystallization:

$$C_l = C_0 \mathrm{F}^{(\mathrm{D}^{\mathrm{Bulk}}-1)} \tag{4.10}$$

where C_l is the melt concentration, C_0 is the initial melt composition (assumed to be that of the whole-rock), F is the fraction of liquid remaining and $\mathrm{D}^{\mathrm{Bulk}}$ is the bulk partition coefficient calculated as:

$$\mathrm{D}^{\mathrm{Bulk}} = \sum\nolimits_{\mathrm{Minerals}} \left[\mathrm{B}_{\mathrm{Mineral}} \cdot D^{\frac{Mineral}{Melt}} \right] \tag{4.11}$$

where $\mathrm{B}_{\mathrm{Mineral}}$ is the mass fraction of the mineral in the crystallizing assemblage and $\mathrm{D}^{\mathrm{Mineral/Melt}}$ is the partition coefficient between the mineral and the melt. The models used a fixed mineral mode to calculate $\mathrm{D}^{\mathrm{Bulk}}$, corresponding to an average South Mountain Batholith granodiorite (MacDonald, 2001) 30% quartz, 40% plagioclase, 25% K-feldspar, and 5% biotite. Petrographic observations also require the presence of zircon and monazite in the crystallizing assemblage (Fig. 4.11), whose abundances were fixed at 0.05% and 0.04%, respectively (but the effect of different monazite proportions was also tested; Fig. 4.11). The mineral/melt partition coefficients for plagioclase and K-feldspar are from the Fish Canyon Tuff (Bachmann et al., 2005), biotite from the Toba Tuff (Brenan et al., 2020), monazite and zircon from the experimental work of Stepanov et al. (2012) and Rubatto and Hermann (2007), respectively. The composition of coexisting apatite was calculated using the apatite/melt partition coefficients from Prowatke and Klemme (2006; their experiment 77). The initial trace element concentrations are from 18JC-0010, which was corrected for containing 25% accumulated crystals and is the same composition used in the MELTs models. This sample is a Stage 2 South Mountain Batholith granite with a complete trace element dataset and also records biotite with relatively high biotite crystallization temperature suggesting an early-formed Stage 2 magma (Brenan et al., Submitted). Thus, this composition is a representative melt composition for all Stage 2 plutons. As the As concentration of this sample was below the detection limit of 5 µg/g, the model uses the median South Mountain Batholith As content of 3 µg/g which was increased to 4 µg/g to account for crystal accumulation. As the models are meant to simulate the formation of all Stage 2 apatites, not just the apatites from 18JC-0010, this assumption is reasonable. Models require both whole-rock concentrations and apatite/melt partition coefficients; thus, calculations were restricted to REEs, Y, As, Nb, Ta, U and Th.

Model results are provided in Fig. 4.11 and show that progressive fractional crystallization produces apatite with trace element concentrations higher than those formed from the initial liquid (whole-rock; purple line labelled 0%), with relative enrichments of HREE, As, and U compared to the LREE and other high field strength elements. Notably, small amounts of monazite crystallization are required to suppress LREE and Th enrichment to reproduce the observed fractionation in the South Mountain Batholith apatite. At 85% solidification (line with squares) the calculated As content matches the observed value.

At 85% crystallization, the models underestimate the average HREE, Y and U abundances in Stage 2 apatite (orange line), requiring a further 10-15% crystallization for all elements to be in good agreement with the range of apatite compositions (shaded area). The failure for 85% crystallization to reproduce all of the trace elements considered could be the result of uncertainties in the initial melt concentration or in the partition coefficients used in the model; for example, Prowatke and Klemme (2006) noted that the REE partition coefficient increase with melt polymerization. Nonetheless, as these models can replicate both the overall level of trace element enrichment, and the interelement fractionation patterns (Fig. 4.11), strongly suggests that apatite compositions represent significant extents of crystallization.

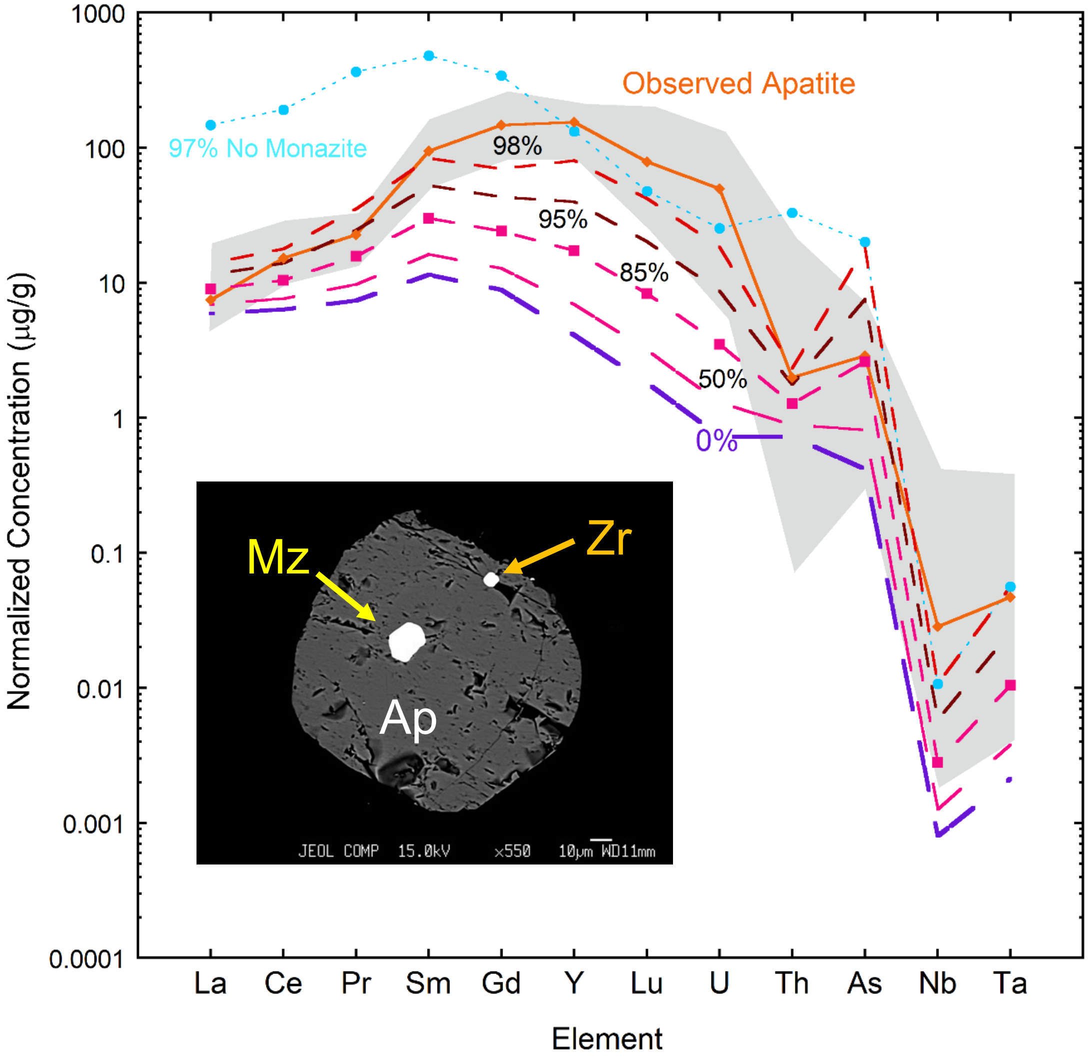

Figure 4.11 Trace element concentrations normalized to upper continental crust (Rudnick and Gao, 2003) comparing all Stage 2 South Mountain Batholith apatite compositions (average is orange diamonds; range of data is the shaded area) with modelled apatite compositions at different degrees of crystallization (dashed lines). The apatite formed in equilibrium with the assumed melt is at 0% crystallization (thick dashed purple). The assumed melt composition is the whole-rock composition of sample 18JC-0010 with 3 µg/g initial As minus 25% quartz and K-feldspar crystallization. At 85% fractional crystallization (squares) the As content of the modelled apatite is the same as observed in the South Mountain Batholith sample. The apatite composition after 97% crystallization in which monazite is not a part of the crystalizing assemblage is the dotted blue circle line. The Insert is a backscattered electron image of an apatite (Ap) grain taken from sample 19BM-0006, from the Stage 1 Scragg lake pluton, showing the typical textural relationship between apatite (Ap) monazite (Mz) and zircon (Zr) in the South Mountain Batholith.

4.4. Implications

The apatite/melt partitioning model (equation 4.9) indicates that As is generally incompatible in apatite crystallized for a range of felsic magma compositions, except under unusually oxidizing conditions. Comparison between apatite/whole-rock partitioning from suites of felsic igneous rocks and the apatite/melt partitioning model are in good agreement (i.e., apatite concentrations are less than whole-rock values) for felsic volcanics and some plutonic rocks. For the occurrences in which there is enrichment of As in apatite relative to the whole-rock suggests that apatite formed after protracted crystallization within the sample. The magnitude of the difference between the $D^{\text{Apatite/Whole-rock}}$ and the $D^{\text{Apatite/Melt}}$ reflects the amount of crystallization needed prior to apatite formation. Fractional crystallization calculations involving both As and other trace elements support this model.

The South Mountain Batholith results imply the formation and crystallization of liquid trapped in the interstices of major-rock forming minerals (in this case, quartz, and feldspar). These late melts are not likely to be mobile (Vigneresse et al., 1996) but the application of external deviatoric stresses (Vigneresse et al., 1996; Vigneresse and Tikoff, 1999) could transport the trapped liquids depending on the permeability, melt wetting characteristics and viscosity. The removed melt has higher As and other trace element concentrations, while the residual crystal pile will have an even greater $D^{\text{Apatite/Whole-rock}}$. The extensive window of crystallization for the South Mountain Batholith-forming magmas, as indicated by the models presented here, would be possible if melts contain a high volatile content, or enrichment in "fluxing" elements that would serve to suppress the solidus (Manning, 1981; Chen et al., 2014; Pichavant et al., 2016; Feisel et al., 2022).

In this context, it is interesting to note that the range of $D^{\text{Apatite/Whole-rock}}$ values for the Stage 2 South Mountain Batholith granites is systematically higher than the Stage 1 samples (Fig. 4.1). Higher abundances of incompatible elements in Stage 2 vs. Stage 1 biotites support the hypothesis that a greater extent of within-sample differentiation occurred in the Stage 2 granites (Clark, 2022). In support of the fluxing hypothesis, Clark (2022) also reports significantly higher levels of both F and Li in biotite from Stage 2 vs Stage 1 granites. Paradoxically, the whole-rock major and trace element systematics are similar between the two magmatic stages (MacDonald, 2001), so the contrasting behavior of As and other trace elements suggests other factors have played a role during the later stages of crystallization.

4.5. Supplementary Information

Dataset 4A- All Mineral Trace Element Analyses.

Digital Excel file containing LA-ICP-MS analysis of minerals. Data is presented by Lithology, Pluton, Stage, Sample number, and analysis ID. Reported for each isotope is the concentration in µg/g, the 2σ error, and the limit of detection.

Dataset 4D- South Mountain Batholith Sample Information.

Digital Excel file containing details on the South Mountain Batholith samples, including location data, pluton occurrence, and lithology.

4.5.1. Method for Correcting Arsenic Loss

It is possible to correct the As concentration of run-product glasses to approximate the level present during the growth of apatite, which is assumed to occur early in the experiment history. The As loss was corrected using a mass balance approach in which:

$$M_{As}^{Total} = M_{As}^{Apatite} + M_{As}^{Glass} + M_{As}^{Vapor} + M_{As}^{Lost} \tag{4.12}$$

and M^{Total} is the total mass of As added to the experiment, M^{Lost} is the mass of As lost to either the capsule or the buffer material and $M^{Apatite}$, M^{Glass} and M^{Vapor} are the mass of As in either apatite, glass or vapor. $M^{Apatite}$, M^{Glass} and M^{Vapor} can be calculated as:

$$M_{As}^{Phase} = m^{phase} \cdot C_{As}^{phase} = \rho^{phase} \cdot \forall^{phase} \cdot C_{As}^{phase} \tag{4.13}$$

where m is the mass of the phase in grams, C is the concentration of As in the phase in µg/g, ρ is the density of the phases in g/cm^3 and ∀ is the volume of the phase in cm^3. As the vapor composition was not measured in this study, the concentration of As in the vapor is calculated from the vapor/melt partition coefficient, assumed to be 2, which is within the range of previous experimental measurements of 0.8 to 6 (Guo, 2008; Simon et al., 2007; Guo and Audetat, 2017; D'Souza and Canil, 2018). For the case of 100 g melt, mass balance dictates:

$$m^{Total} = 100\ g = m^{Apatite} + m^{Glass} + m^{Vapor} \tag{4.14}$$

The mass of apatite was calculated as the difference in P_2O_5 of the starting material and the P_2O_5 content (Table 4.7) of the melt then converting melt P_2O_5 to apatite equivalent using the reaction:

$$10CaO + 3P_2O_5 + F \rightarrow Ca_{10}(PO_4)_6F_2 + ½O_2 \tag{4.15}$$

The mass of glass and vapor were calculated using the ratio between the volume of glass to the volume of vapor, $R^{Glass/Vapor}$:

$$R^{Glass/Vapour} = \frac{\forall^{Glass}}{\forall^{Vapor}} \tag{4.16}$$

with the value of $R^{Glass/Vapor}$ determined by measuring the bubble to glass ratio from sample images using the imageJ software package. Table 4.7 contains the $R^{Glass/Vapor}$ used in this study. Substituting equation 4.16 into 4.14 for mass vapor, results in:

$$100\ g - m^{Apatite} = m^{Glass} + \frac{\forall^{Glass}}{R^{Glass/Vapor}} \cdot \rho^{Vapor} \tag{4.17}$$

and

$$100\ g - m^{Apatite} = m^{Glass} + \frac{\frac{m^{Glass}}{\rho^{Glass}}}{R^{Glass/Vapour}} \cdot \rho^{Vapor} \tag{4.18}$$

The density of the vapor and glass were assumed to be 0.75 g/cm^3 and 2.65 g/cm^3, respectively. With the above calculations, the amount of As lost can be determined using equation 4.12. A time series done at the Ru-RuO$_2$ buffer and 1000°C shows that the As content of apatite stays constant, for at least 96 hours, although the As content of the melt decreases continuously (Fig. 4.12). This behavior is taken to mean that apatite forms early in the experiment when the As content of the melt is still high, and the apatite does not re-equilibrate during As loss. Therefore, assuming that no As is lost from the apatite, M^{Lost} can be written as:

$$M_{As}^{Lost} = m^{Glass} \cdot C_{As}^{LostGlass} + m^{Vapor} \cdot C_{As}^{LostVapor} \tag{4.19}$$

in which $C^{LostGlass}$ and $C^{LostGlass}$ are the concentrations missing from the glass and vapor. At assumed vapor-melt equilibrium, the amount lost from the glass relative to vapor is related by the $V^{apor/melt.}$ This leads to:

$$M_{As}^{Lost} = m^{Glass} \cdot C_{As}^{LostGlass} + m^{Vapor} \cdot C_{As}^{LostGlass} \cdot D_{As}^{Vapor/Melt} \tag{4.20}$$

which can be solved for $C^{LostGlass}$. Adding the missing glass concentration back, then the corrected apatite/melt partition coefficient is calculated as:

$$D_{As}^{Apatite/Melt} = \frac{C_{As}^{Apatite}}{(C_{As}^{LostGlass} + C_{As}^{Glass})} \tag{4.21}$$

Table 4.7 Variables needed to calculate As loss in experiments.

Experiment	Starting Material P_2O_5 (wt.%)	Run-Product P_2O_5 (wt.%)	$R^{Glass/Vapor}$	Arsenic Loss %
AAO01	1.60	0.123	4.56	28%
AAO02	1.60	0.108	7.73	11%
AAO03	1.60	0.109	3.55	30%
AAO04	1.60	0.145	5.39	50%
AAO06	1.60	0.155	9.96	39%
AAO13	1.60	0.191	5.00	0%
AAO19	1.71	0.151	4.00	99%
AAO20	1.60	0.172	2.60	11%
AAO21	1.71	0.122	3.17	18%
AAO24	1.60	0.016	4.00	87%
AAO25	1.60	0.208	4.56	0%
AAO26	1.88	0.960	5.67	1%
AAO27	1.71	0.106	2.46	41%
AAO29	1.71	0.183	1.81	65%
AAO30	1.71	0.064	2.60	55%
AAO32	1.71	0.180	2.96	62%
AAO33	1.71	0.131	2.21	94%
AAO39	1.71	0.187	2.03	78%

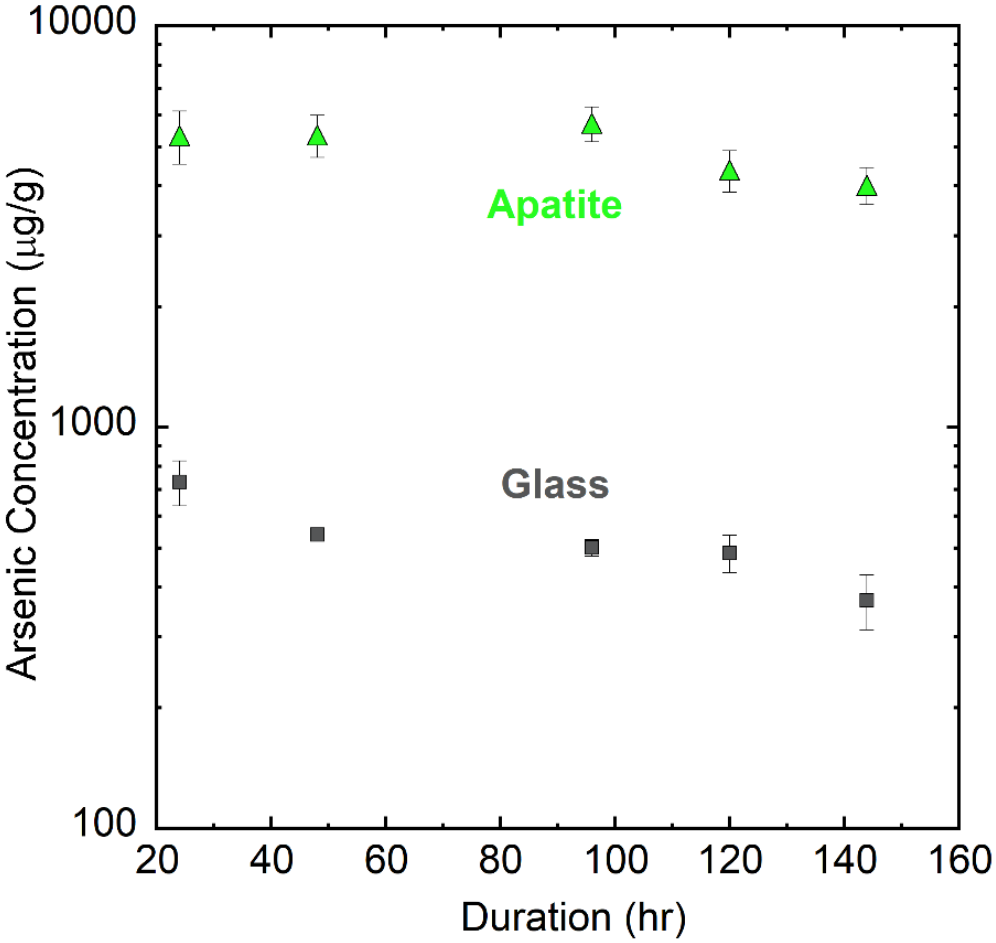

Figure 4.12 Arsenic concentration in run-product glass and apatite as a function of experiment length in hours. Data are for experiments done at 0.75 GPa, 1000°C using a metaluminous composition and buffered with Ru-RuO$_2$.

4.5.2. Derivation of the Apatite/Melt Partitioning Equation for Arsenic

As As is a multivalent element, its partition coefficient is a combination of the partition coefficients for each species.

$$D_{As}^{Apatite/Melt} = D_{As(III)}^{Apatite/Melt}\left(\frac{X_{AsIII}}{X_{\Sigma As}}\right) + D_{As(V)}^{Apatite/Melt}\left(1-\frac{X_{AsIII}}{X_{\Sigma As}}\right) \quad (4.22)$$

$D_{As}^{Apatite/Melt}$ is the partition coefficient for As between apatite and melt, $D_{As(III)}$, $D_{As(V)}$ are the partition coefficient for the indicated species, X_{AsIII} is the mole fraction of As^{III} and $X_{\Sigma As}$ is the total As mole fraction in the melt. The ratio of X_{AsIII}/ $X_{\Sigma As}$ is imposed by the speciation of the system and can also be expressed by the reaction:

$$As^{III}O_{3/2} + \frac{1}{2}O_2 \leftrightarrow As^{V}O_{5/2} \qquad (4.23)$$

which, by considering the equilibrium constant for this reaction, K_{eq}, can be solved for the relative proportion of species as:

$$\log \frac{a_{\mathrm{As^{V}}O_{5/2}}}{a_{\mathrm{As^{III}}O_{3/2}}} = \frac{1}{2}\log fO_2 + \log K_{eq} \qquad (4.24)$$

where quantities in *a* are activities, and fO_2 is the oxygen fugacity. Considering that the activity of component i is the mole fraction of phase i *(X_i)* multiplied by the activity coefficient (γ) equation 4.24 can be rewritten as:

$$\log\left(\frac{X_{\mathrm{As^{V}}O_{5/2}} \cdot \gamma_{AsV}}{X_{\mathrm{As^{III}}O_{3/2}} \cdot \gamma_{AsIII}}\right) = \frac{1}{2}\log fO_2 + \log K_{eq} \qquad (4.25)$$

$$\log\left(\frac{X_{\mathrm{As^{V}}O_{5/2}}}{X_{\mathrm{As^{III}}O_{3/2}}}\right) + \log\left(\frac{\gamma_{AsV}}{\gamma_{AsIII}}\right) = \frac{1}{2}\log fO_2 + \log K_{eq} \qquad (4.26)$$

Assuming that the activity coefficients are constant with changing fO_2, the apparent equilibrium constant, K', which incorporates only mole fractions, can be written as:

$$\log K' = \log K_{eq} - \log\left(\frac{\gamma_{AsV}}{\gamma_{AsIII}}\right) \qquad (4.27)$$

Substituting 4.27 into 4.26 yields:

$$\log\left(\frac{X_{\mathrm{As^{V}}O_{5/2}}}{X_{\mathrm{As^{III}}O_{3/2}}}\right) = \frac{1}{2}\log fO_2 + \log K' \qquad (4.28)$$

and substituting equation 4.28 into 4.22 gives:

$$D_{As}^{Apatite/Melt} = D_{As(V)}^{Apatite/Melt} + \left(\frac{D_{As(III)}^{Apatite/Melt} - D_{As(V)}^{Apatite/Melt}}{(1 + 10^{(\frac{1}{2}\log fO_2 + \log K')})}\right) \qquad (4.29)$$

Which is the general partitioning equation in terms of fO_2, K', $D_{As(V)}$ and $D_{As(III)}$.

4.5.2.1. Estimation of the apparent equilibrium constant (K')

The apparent equilibrium constant, K', was calculated from 6 experiments at known fO_2 for which the As^{III} to As^{V} ratio was determined by XANES using linear combination fitting based on the $AsO(OH)_3$ and $As(OH)_3$ spectral reference materials (Table 4.6). Examination of logK' in relation to the other intensive parameters shows a dependence on 1/T (Fig. 4.13A) and melt composition (Fig. 4.13B). Weighted linear regressions were performed using the R code (R Studio, 2018) with R Studio (R Core Team, 2013). Regressions on logK' assume that 1/T and molar Al/(Na+K) are independent, resulting in the empirical expression:

$$\log K' = \frac{9{,}500(\pm 1{,}210)}{\mathrm{T}} - 0.579(\pm 0.0805)\Psi - 4.40(\pm 0.960) \tag{4.30}$$

in which Ψ is the melt molar (Al/(Na+K)). This regression has an adjusted R^2 value of 0.954 and a p-value of 0.00452.

4.5.2.2. Constraints on the trivalent partition coefficient ($D_{As(III)}$)

The As speciation measured in experiment AAO19, which was performed at reducing conditions (graphite-CO_2 buffer; FMQ -0.4), only shows the presence of As^{III} meaning that the partition coefficient measured from this experiment is an accurate representation of $D_{As(III)}$. Unfortunately, this experiment experienced significant As loss. Other experiments were performed at the same fO_2 using graphite-lined capsules to prevent As loss. The concentration of As within the apatites from these experiments is too low to be quantified given their small crystal sizes, and only maximum partition coefficients could be estimated. A conservative upper limit value of 0.1 is used to represent $D_{As(III)}$. Additionally, although experiments AAO 47, 49 and 50 all involved different melt compositions, the effect of this parameter on the $D_{As(III)}$ is not resolvable, and therefore the estimated value for $D_{As(III)}$ is assumed to be the same for all the compositions studied.

4.5.2.3. Constraints on the pentavalent partition coefficient ($D_{As(V)}$)

$D_{As(V)}$ can be calculated from equation 4.29 for experiments with known logK'. Examination of $D_{As(V)}$ shows a dependence on the temperature of the system (Fig. 4.13C) where the partition coefficient increases with decreasing temperature and can be expressed as:

$$D_{As(V)}^{Apatite/Melt} = \frac{178{,}000(\pm 42{,}600)}{\mathrm{T}} - 130\ (\pm 33.8) \tag{4.31}$$

This regression has an adjusted R^2 value of 0.768 and a p-value of 0.0138.

4.5.2.4. Apatite-melt partitioning model for As.

Substituting Equation 4.30, 4.31 and the assumed $D_{As(III)}$ value into Equation 4.29 gives the generalized equation for As partitioning between apatite and melt:

$$D_{As}^{Apatite/Melt} = \frac{178{,}000(\pm 42{,}600)}{\mathrm{T}} - 130\ (\pm 33.8) + \left(\frac{0.1 - \left(\frac{178{,}000(\pm 42{,}600)}{\mathrm{T}} - 130\ (\pm 33.8)\right)}{(1 + 10^{(\frac{1}{2}\log fO_2 + \frac{9{,}500(\pm 1{,}210)}{\mathrm{T}} - 0.579(\pm 0.0805)\Psi - 4.40(\pm 0.960))}} \right) \tag{4.9}$$

in which T is the temperature in Kelvin, fO_2 is oxygen fugacity in bars and Ψ is the melt molar (Al/(Na+K)). The partition coefficients calculated from equation 4.9 have a standard error of 0.42 based on the variance of the residuals. Comparison between calculated and measured partition coefficients yields an unweighted R^2 value of 0.86 (Fig. 4.7).

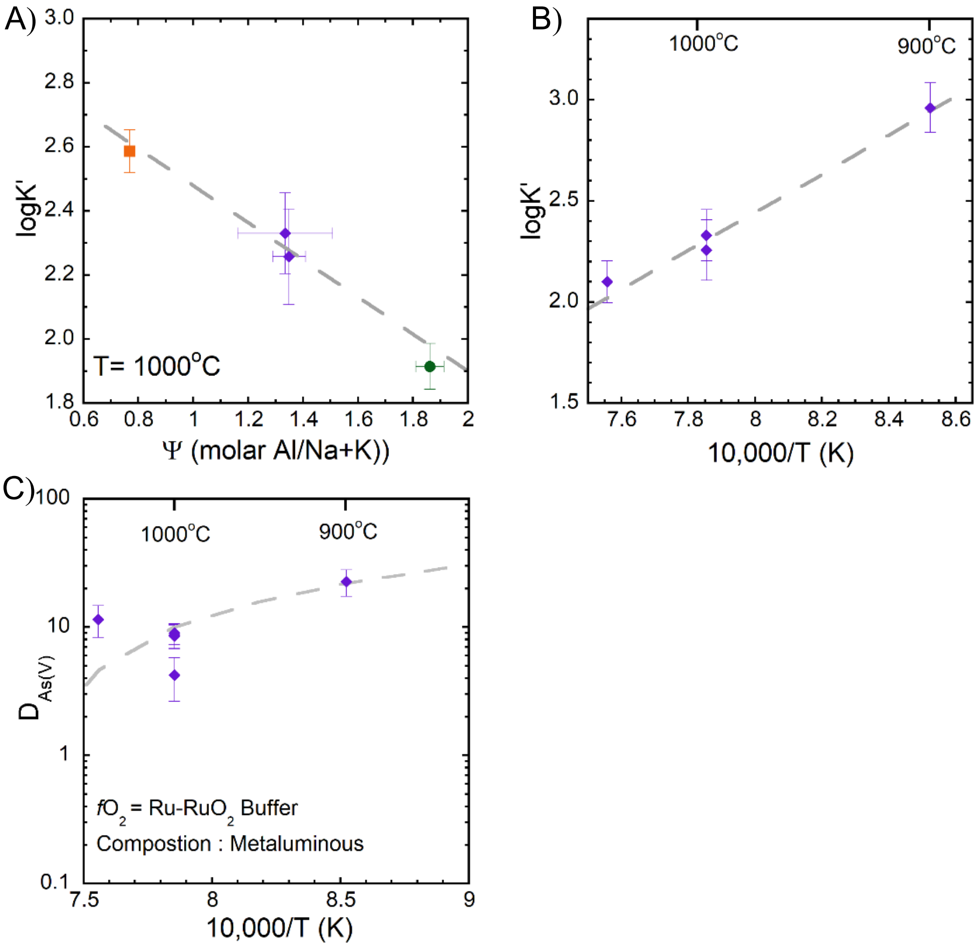

Figure 4.13 Bivariant diagrams showing the relationship between regression parameters and independent variables used to generate equation 4.9 (A to C). Green (circle), purple (diamonds) and orange (square) symbols correspond to peraluminous, metaluminous and peralkaline composition, respectively. The gray lines in the plots are the model predictions from the regression.

4.5.3. Modelling of Arsenic Uptake During Apatite Crystallization

MELTS thermodynamic algorithms were used to model the crystallization of a selected South Mountain Batholith magma composition to determine the point of apatite saturation and the resulting distribution of As between apatite and melt. Models were done using the rhyolite-melts v1.1 and rhyolite-melts v1.0 algorithms in the MELTS for Excel package updated on April 24th, 2018 (Gualda et al., 2012; Ghiorso and Gualda, 2015; Gualda and Ghiorso, 2015). The initial South Mountain Batholith melt composition is a Stage 2 leucomonzogranite (sample 18JC-0010) for which a full suite of As, REE and other trace element data are available (see Brenan et al.,(submitted) for details). In all models, the pressure was held constant at 200 MPa, fO_2 was held at FMQ -1 and the temperature was decreased in increments of 2ºC.

Mass balance calculations are used to determine the temperature and melt fraction at which apatite saturation occurs, and the resulting average amount of As in apatite. Mass balance was done on phosphorous at each temperature step with the assumption that phosphorous is perfectly incompatible in the crystallization assemblage. The following steps were used:

1. Calculate the concentration of P_2O_5 in the melt assuming no apatite forms (C_{P*}).
2. Check the P_2O_5 concentration for apatite saturation (C_{sat}) using the calibration of Tollari et al. (2006):

$$X_{P2O5}^{Sat} \cdot 100 = e^{\left[T\left(\frac{-0.879}{139.0-100 \cdot X_{SiO2}^{melt}}+0.0165\right)-3.33 \ln 1\left(00 \cdot X_{CaO}^{Melt}\right)\right]} \qquad (4.32)$$

where T, is the temperature in K, and X is the mole fraction of SiO_2, CaO, or P_2O_5 at saturation in the melt.

3. If $C_{sat} > C_{P*}$ then $M_P^{apatite} = m_{melt} * (C_{P*} - C_{sat})$

Where $M_P^{apatite}$ is the mass of phosphorus in apatite, and m^{melt} is the mass of melt.

4. The mass of apatite is calculated as $M_P^{apatite} / C_{Apatite}$, in which $C_{Apatite}$ is the concentration of P_2O_5 in stoichiometric fluorapatite (42.22 wt.%).
5. The mass of P in the melt (M_P^{Melt}) is set equal to M_P^{System} - $M_P^{apatite}$

6. At the next temperature step, the new phosphorus mass is calculated as $M_P^{System} = M_P^{Melt}$ from the previous step. The mass of the system (m_{system}) is also reduced by the mass of apatite formed ($m_{Apatite}$).

To determine the amount of As in apatite the following procedure was used:

1. $D_{As}^{Apatite/Melt}$ was calculated using equation 4.9.
2. The concentration of As in the apatite ($C_{Apatite}$) was calculated as $D_{As}^{Apatite/Melt} * C_{Melt}$, in which C_{Melt} is the As concentration in the melt.
3. The mass of As in the apatite ($M_{As}^{Apatite}$) for this step was calculated as $C_{Apatite}*m_{Apatite}$, in which $m_{Apatite}$ is the mass of apatite, determined by the phosphorous mass balance.
4. The mass of As in the melt (M_{As}^{Melt}) is $M_{As}^{System} - M_{As}^{Apatite}$
5. At the next temperature step, $M_{As}^{System} = M_{As}^{Melt}$ from the previous step then, $C_{Melt} = M_{As}^{System} / m_{Melt}$

Table 4.8 Anhydrous composition used in models taken from of 18JC-0010 from the New Ross Pluton

Oxide or element	Whole Rock Concentration	Melt Concentration
SiO_2 (wt.%)	71	65.4
TiO_2 (wt.%)	0.48	0.62
Al_2O_3 (wt.%)	15	16.3
Fe_2O_3 (wt.%)	3.7	4.89
MnO (wt.%)	0.070	0.10
MgO (wt.%)	0.90	1.2
CaO (wt.%)	1.4	1.9
Na_2O (wt.%)	3.1	4.1
K_2O (wt.%)	4.6	3.2
P_2O_5 (wt.%)	0.21	0.28
As (µg/g)	3	4
La (µg/g)	28.4	37.9
Ce (µg/g)	60.8	81.1
Pr (µg/g)	7.23	9.64
Sm (µg/g)	6.5	8.7
Gd (µg/g)	5	6.7
Y (µg/g)	25	33.3
Lu (µg/g)	0.41	0.547
U (µg/g)	2.8	3.73
Th (µg/g)	11.4	15.2
Nb (µg/g)	6	8
Ta (µg/g)	1.2	1.6

Acknowledgements

BJM thanks Debroa Motta Meira for her assistance at the beamline and Claire Boteler for her assistance with R-software. Support for this project was provided by CSEG student research grant and the GSA graduate student research grant obtained by BJM and the NSERC discovery grand obtained by JMB. This research used resources of the Advanced Photon Source, an Office of Science User Facility operated for the U.S. Department of Energy (DOE) Office of Science by Argonne National Laboratory and was supported by the U.S. DOE under Contract No. DE-AC02-06CH11357, and the Canadian Light Source and its funding partners. BJM acknowledges the receipt of support from the CLSI Graduate and Post-Doctoral Student Travel Support Program. BJM thanks Alexandra Arnott for her aid in proofreading this manuscript.

Chapter 5

SOURCES OF GEOGENIC ARSENIC IN WELL WATER ASSOCIATED WITH GRANITIC BEDROCK FROM NOVA SCOTIA, CANADA

Bryan J. Maciag[a]*, James M. Brenan[a], Michael B. Parsons[b], and Gavin W. Kennedy[c]

[a]Department of Earth and Environmental Sciences, Dalhousie University, Halifax, NS, Canada

[b]Geological Survey of Canada, Dartmouth, NS, Canada

[c]Nova Scotia Department of Natural Resources and Renewables, Halifax, NS, Canada

*Corresponding author: Bryan J. Maciag (bmaciag@dal.ca)

Key Words: Geogenic Arsenic, Granites, South Mountain Batholith, Groundwater

Prepared for Publication in Environmental Science and Technology

Abstract

Arsenic toxicity in drinking water is a global issue, with chronic exposure causing cancer and other health concerns. Groundwater from geochemically similar granites from mainland Nova Scotia, Canada, can have high and low levels of As. The origin of this variation is uncertain, but different mineral hosts for As could explain the disparity. The lability of As from different minerals was assessed using laser ablation inductively coupled plasma mass spectrometry combined with calculations based upon well water data. Pyrite has the highest As concentration (mean: 2,300 μg/g, N=9) of all minerals analyzed, is unstable in the groundwater system, and can release As during oxidation. However, oxidation products replacing pyrite can adsorb As, modifying the amount released. Cordierite has low As concentrations (mean: 7.3 μg/g, N=5) but is abundant and relatively soluble, as are some of its alteration products, which may contain up to 500 μg/g As. As cordierite can be abundant in metapelitic rocks it could be a previously unrecognized source of As in metamorphic terranes. Pyrite from one of the granites studied is not oxidized, which could result from lower host rock permeability. This observation, in addition to the absence of cordierite in these same granites, may

account for the lower As levels observed in the associated well water. The results of this study can be used to identify geogenic sources of As in other granitic terranes and assess the risks of As release when modifying granitic bedrock for construction or mining.

5.1.Introduction

Arsenic is a multivalent element with different behaviors depending on the geochemical conditions. It is also an environmental contaminant and Group I (IARC Working Group on the Evaluation of Carcinogenic Risks to Humans, 2012) carcinogen with the potential to cause several different types of cancer (Hughes et al., 2011; Saint-Jacques et al., 2014; Sri et al., 2016; Health Canada, 2020) and birth defects (Shi et al., 2015). In 2019 As was ranked as the most significant potential threat to human health at contaminated sites in the United States by the Agency for Toxic Substance and Disease Registry (2019). Arsenic contamination is a global issue with the greatest impact occurring in the West Bengal Basin, where over 50 million people (Mukherjee et al., 2008; Shamsudduha et al., 2008; von Brömssen et al., 2008) are at risk of exposure to drinking water over the Maximum Acceptable Concentration (MAC) of 10 µg/L As (World Health Organization, 2008; Health Canada, 2020). Groundwater As contamination may originate from anthropogenic activity (i.e., waste from wood preservation, glass manufacturing, mining activities, and runoff from pesticides) or geogenic sources (i.e., dissolution of As-bearing minerals, or mixing with geothermal fluids; Ali et al., 2018).

Barring anthropogenic influences, As levels in drinking water sourced from surface waters and groundwater are typically below the MAC; however, groundwater can have a large range of naturally sourced As concentrations (< 0.5 to 5000 µg/L (Smedley and Kinniburgh, 2002). Toxic metals that dissolve as divalent cations become less soluble at high pH. However, As is a metalloid that forms oxyanions making it more soluble in circumneutral pH waters, where its mobility is generally controlled by sorption rather than precipitation of metal oxides (Smedley and Kinniburgh, 2002). Arsenic is also mobile and released from different minerals over a broad range of redox conditions. Sulfides such as pyrite and arsenopyrite are the most common As-bearing minerals and can serve as geogenic sources of As in aquifers (Smedley and Kinniburgh, 2002). Ferric oxides and oxyhydroxides such as goethite are also common geogenic sources of As in loess and alluvial aquifers as they not only incorporate As into their structure upon precipitation (Smedley and Kinniburgh, 2002) but also have a high sorption capacity for As that is sensitive to the groundwater chemistry (Dixit and Hering, 2003). The combination of diverse geochemical behavior and high toxicity makes identifying the source of elevated As critical to assessing the risk of drinking water contamination.

Arsenic contamination in Nova Scotia groundwater was first identified in the community of Waverley in 1976 when a case of chronic As poisoning was diagnosed (Grantham and Jones, 1977). The groundwater in question contained 5000 µg/L of As and led to the further scrutiny and testing of drinking water across the province. A 2017 study (Kennedy et al., 2017) linking well water chemistry to bedrock lithology found that over 20% of well water exceeds the MAC and that 42% of the population relies on domestic well water for drinking, which is unregulated (Kennedy et al., 2017). Over 37% of the private wells are located in bedrock aquifers with a high risk of As contamination (Kennedy et al., 2017). This area includes the South Mountain Batholith (SMB) and the Meguma Supergroup (Fig. 5.1), where over 30% and 39% of well water samples exceeded the MAC, respectively (Kennedy et al., 2017).

The origin of As-enriched well water related to granitic bedrock is sometimes enigmatic. Typically, As in granites is derived from sulfides (Bondu et al., 2016; Mukherjee et al., 2019) or their secondary minerals (Acharyya et al., 2005; Shukla et al., 2010), which is what has been suggested for the Nova Scotian granites (Kennedy et al., 2017) based on observed arsenopyrite or As-bearing pyrite in xenoliths, quartz veins, fractures or pegmatites. However, no association between As and dissolved sulfate was identified in the well water (Kennedy et al., 2017), which is typical of As derived from sulfide minerals. An additional unexplained observation is the absence of elevated As in well water associated to a series of smaller satellite granite plutons, south of the central granites (Fig. 5.1) (Kennedy et al., 2017), despite their similar whole rock geochemistry to the central granites. Thus, this study seeks to identify the origin(s) of elevated As in groundwater associated with granitic terranes by contrasting the character of selected intrusions that have very different well water As concentrations. This investigation considers the mineralogical controls on the As distribution and the susceptibility of phases to dissolution in the local groundwater and also identifies minerals that could release As if exposed to acid rock drainage.

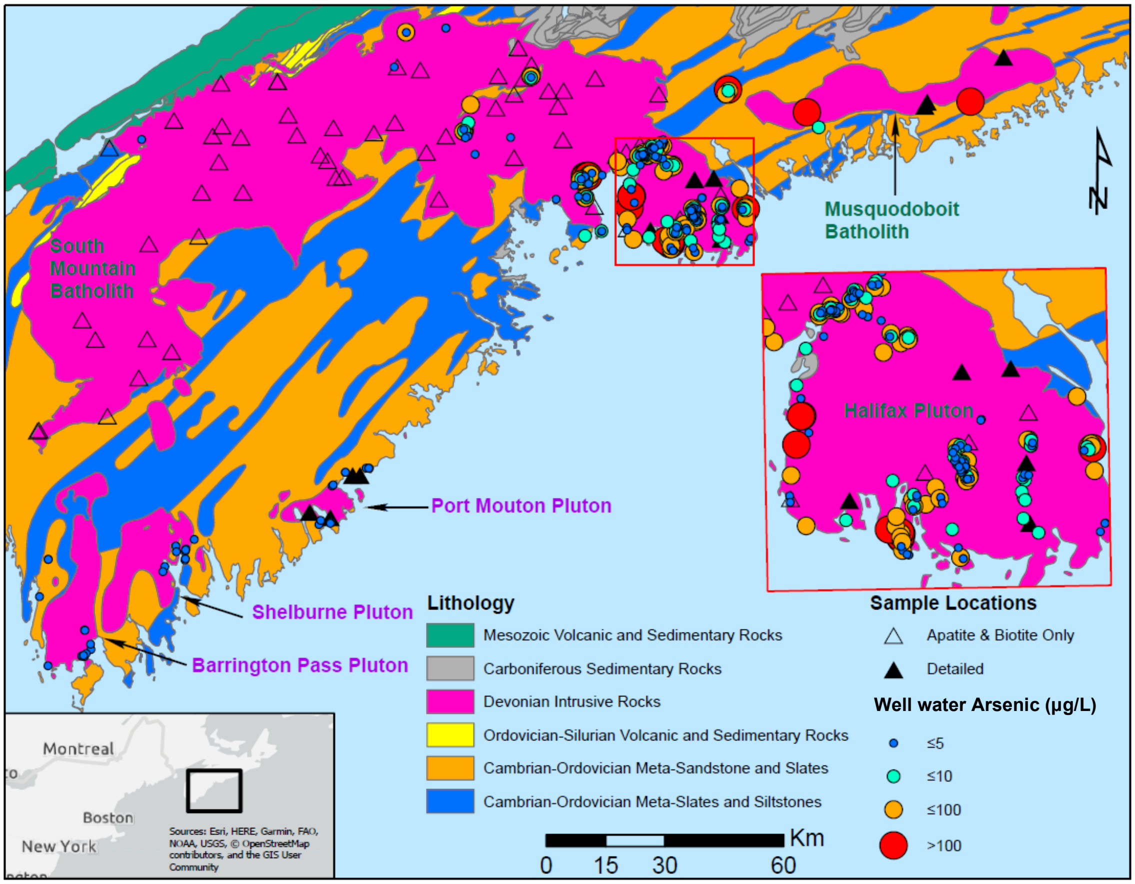

Figure 5.1 Simplified geological map of southwestern Nova Scotia (Canada) modified from Fisher and Poole (Fisher and Poole, 2006). Well water chemistry is depicted as circles with the color and size indicating the As concentration (Nova Scotia Department of Natural Resources and Renewables, 2021). Sample locations for this study are shown as solid triangles while additional samples taken from a study on apatite and biotite geochemistry in the South Mountain Batholith (Brenan et al., Submitted) are shown as open triangles. Names of the central granitic plutons are in green, while the southern satellite plutons are in purple.

5.1.1. Study Area

The regional geology of southwestern Nova Scotia is dominated by the Cambrian-Ordovician Meguma Supergroup, comprised of the Goldenville Group (meta-sandstones, slates) and the overlying Halifax Group (meta-siltstones and slates; Schenk, 1997) (Fig. 5.1). These sediments were folded and metamorphosed during the Acadian Orogeny between 354 and 399 Ma (Shellnutt et al., 2019). Both the Goldenville and Halifax Groups contain lithologies with over 1,000 μg/g As (White, 2010). The granitic rocks under study intruded the Meguma Supergroup during the waning stages of the Acadian Orogeny. These granites range from monzogranites to tonalites and are distinctive in that most exhibit molar $Al_2O_3/(CaO+Na_2O+K_2O) > 1$, termed peraluminous. This compositional type results in a high abundance of Al-rich phases, such as muscovite, biotite, and cordierite. Common accessory phases found in these granites include rutile, ilmenite, titanite, zircon, apatite, monazite, and xenotime. Table 5.2 (found in the supplementary information (SI) section) contains general descriptions of the 12 samples collected for this study, and Table 5.3 (in SI) summarizes the model abundance of accessory phases for each sample.

In addition to geogenic As, acid rock drainage (ARD), is another well-known geohazard occurring in Nova Scotia. Oxidation of naturally occurring sulfide minerals has led to acidic runoff at many sites, including the Robert Stanfield International Airport where runway construction resulted in significant fish kills downstream in the 1970s and 1980s (Wargon, 1987; Fox et al., 1997). Several formations within the Meguma Supergroup were identified as acid-producing mainly due to their high pyrrhotite contents, while the granites of the South Mountain Batholith are not considered to have a high capacity for ARD (Fox et al., 1997; White and Goodwin, 2011).

5.2.Methods & Materials

5.2.1. Sample

Four samples were collected from the Port Mouton Pluton, which represents the southern satellite granites. The central granites are the South Mountain Batholith and Musquodoboit Batholith (MB). Three samples were obtained from the Musquodoboit Batholith, also analyzed in a study by MacDonald and Clarke (MacDonald and Clarke, 1985). Five samples were taken from the Halifax Pluton member of the South Mountain Batholith, one of which was collected near the contact between the South Mountain Batholith and the Meguma supergroup metasediments. Analysis of apatite and biotite plus several other minerals in an additional 45 South Mountain Batholith samples from a separate study (Brenan et al., Submitted) were also included in the dataset. Analyses occurred on 30 or 100 μm polished rock slides made from unweathered samples collected from surface outcrops.

5.2.2. Analytical Techniques

The major element composition of apatite, monazite, epidote, cordierite, goethite, and pyrite grains were determined by wavelength dispersive spectroscopy, using a JEOL

JXA-8200 electron probe microanalyzer at Dalhousie University (Halifax). Analyses were done using an accelerating voltage of 15 kV, a beam current of 20 nA and a 1 μm focused beam. Raw count rates were converted to concentrations using the ZAF data reduction scheme. Other analytical details can be found dataset 5A in the electronic supplementary information. The major element chemistry of all other phases was determined by semi-quantitative energy dispersive spectroscopy using a Thermo Scientific™ UltraDry EDS Detector mounted on the microprobe or calculated by mineral stoichiometry.

Arsenic and other trace element concentrations were determined by laser ablation inductively coupled plasma mass spectrometry (LA-ICP-MS) at Dalhousie University (Halifax). The instrument consists of a frequency quintupled Nd: YAG laser operating at 213 nm coupled to a Thermo Scientific iCAP Q ICP-MS quadrupole mass spectrometer. Helium was used as a carrier gas to enhance sensitivity. Laser repetition rate (5-15 Hz) and spot size (5-40 μm) were varied to maintain signal longevity. Likewise, a line raster was used instead of a spot. The typical analysis involved 20 seconds of background acquisition with the ablation cell being flushed with He, followed by ablation for 60 seconds, then 45 seconds of cell washout. The As concentrations of a fluorapatite reference material measured on the LA-ICP-MS (992±64 μg/g) reproduced the values obtained on the same material measured by instrumental neutron activation analysis (1010 μg/g) at a commercial laboratory. Data reduction was done using the Iolite version 4.0 software package. Other analytical details are found in the SI under dataset 5A. Detection limits vary based on the spot size of the analysis and can be found listed with the analytical results in electronic supplementary information dataset 5B.

Raman spectroscopy was used to determine the identity of the ferric oxide/hydroxide phases (Fig. 5.1 in the SI). Analyses were done at Saint Mary's University (Halifax) using a 532 nm Nd:YAG diode laser operated at 0.1 to 1 mW with 600 groves/mm gratings resulted in a spectral resolution of ±2 cm^{-1}. Frequency calibration utilized a Horiba Scientific SP-RCO-XP calibration objective employing a NIST-traceable compound (patent reference: FR2934367) in a sealed objective body.

To calculate accessory phase modes (Table 5.3), X-ray fluorescence (XRF) maps of Al, Ca, Ce, Fe, S, P and Zr produced on a Bruker M4 tornado benchtop XRF at Saint Mary's University, were reclassified at set thresholds to generate binary elemental maps. These binary maps were combined through raster overlay to produce unique mineral signature maps, using at least two binary maps, when possible, to reduce the effects of spectral interference. However, the zircon content may be overestimated as no second element was available to constrain the data.

5.2.3. Well Water Calculations

The Nova Scotia Department of Natural Resources and Renewables (DNRR) provided well water chemistry data including As, uranium, manganese, iron, fluoride, aqueous silica, calcium, nitrite, nitrate, carbonate, and sulfate concentrations along with pH and alkalinity for 938 well water samples associated with the granitic bedrock in this study (Nova Scotia Department of Natural Resources and Renewables, 2021). The Nova Scotia groundwater chemistry database consists of untreated samples taken from both surficial and bedrock aquifers since 1954 and is maintained by the Nova Scotia DNRR and was compiled from federal, provincial, and municipal sources (Kennedy, 2021). The chemistry of the well water was measured by a variety of methods but typically consisted of total metal digestion followed by ICP-MS analysis on unfiltered water samples (Kennedy, 2021). The Geochemist's Spreadsheet and SpecE8, applications of the Geochemist's Workbench community edition platform v. 15.0 (Bethke, 2022), were used to calculate mineral saturation indices and Eh. Well water Eh was calculated using the nitrite/nitrate ratio, with a range of Eh varying from 0.22 to 0.45 V. These values are considered minimum estimates as nitrite concentrations are sometimes below detection limits. Well water concentrations of cerium, phosphorus and aluminum were assumed to be 0.0074 μg/L (Noack et al., 2014), 20 μg/L (Holman et al., 2008) and 10 μg/L (Hart et al., 2021), respectively, to calculate the mineral saturation indices. These values were considered reasonable as they are median concentrations of aluminum in Nova Scotia groundwater and the median cerium concentration from a compilation of thirty-one studies with groundwater REE concentrations. The phosphorus concentration is a conservative estimate based on a typical detection limit as most phosphorus data is not detected. Saturation indices for all minerals except monazite were calculated using the

LLNL thermodynamic database included with the Geochemist's Workbench software. The MinTeq database (Gustafasson, 2011) was used to calculate the monazite saturation index. For this study, mineral saturation indices are only used as an indication of each mineral's degree of undersaturation or supersaturation and are not used to evaluate phases in equilibrium with the groundwater. Minerals with saturation indices > 1 are supersaturated and thus considered to be stable in groundwater while values <1 are undersaturated and may dissolve.

5.3.Results & Discussion

A summary of the As content of the whole-rock analyses, as well as As concentrations and mineral saturation indices of minerals containing over 5% of the As budget for any pluton (Fig. 5.2) are provided in Table 5.1. For Table 5.1 concentrations below analytical detection limits were assumed to be one-half the detection limit when computing the median unless the detection limit for the analysis was significantly greater than quantified values, in which case the analysis was excluded. Trace element data for all minerals analyzed (including major silicates) in this study are available in the SI dataset 5B. The Port Mouton Pluton has less As than the South Mountain Batholith. Although the South Mountain Batholith granites contain more As than the Port Mouton Pluton granites, these plutonic rocks are not anomalous in As, with concentrations below the average concentration found in the upper continental crust, which is 4.8 µg/g As (Rudnick and Gao, 2003). Additionally, excluding the extreme As values, the As concentrations of granites from this study are within the range typical for granitic rocks (Smedley and Kinniburgh, 2002).

5.3.1. Silicates

Major rock-forming minerals comprise greater than 92% of all samples and include quartz [SiO_2], potassium feldspar [$KAlSi_3O_8$], plagioclase feldspar [$NaAlSi_3O_8$ – $CaAl_2Si_2O_8$], muscovite [$KAl_2(AlSi_3O_{10})(F,OH)_2$] and biotite [$K(Mg,Fe)_3(AlSi_3O_{10})(F,OH)_2$]. Arsenic is typically below 1 µg/g for these minerals, although there are exceptions. Retrograde chlorite [$(Mg,Fe)_5Si_3Al_2O_{10}(OH)_8$] replacing biotite typically has less than 1 µg/g As but some partially chloritized grains contain up to 8 µg/g. Such low levels of As are within the range of values reported previously for silicate minerals (Onishi, 1969; Smedley and Kinniburgh, 2002; Seddique et al., 2008). Despite the low concentrations, due to their high modal abundance, the major rock-forming silicates contain the majority (>50%) of the As budget (Fig. 5.2). This conclusion is similar to observations in sedimentary aquifers (Alam et al., 2014).

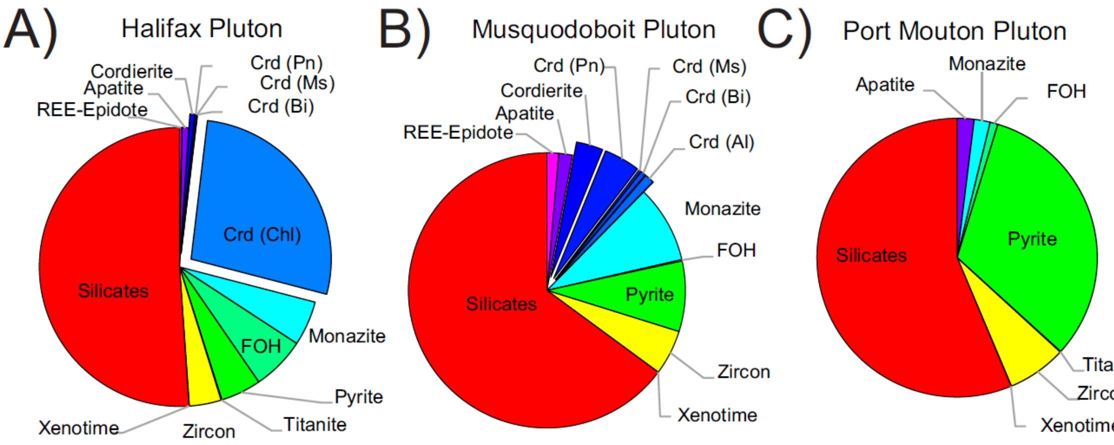

Figure 5.2 Pie diagrams illustrating the mass percentage of As contained in each mineral phase for each pluton. The proportion of As contained within the major rock-forming silicates is calculated by assuming an average concentration of 0.5 µg/g As (half of the 1 µg/g detection limit for major silicates measured in this study). The cordierite (Crd) pseudomorph products are subdivided by alteration type, and pseudomorph products that were not analyzed were assumed to contain 0.5 µg/g As. Pn is Pinite, Ms is muscovite, Bi is Biotite, Al is hydrous aluminosilicates, Chl is chlorite and FOH are ferric oxyhydroxides.

Cordierite [$(Mg,Fe)_2Al_2Si_5O_{18}$] is only present in three of the samples selected for study, however, it is considered a common accessory phase (up to 10 modal%; Erdmann et al., 2004) in both the Musquodoboit Batholith and the South Mountain Batholith. Cordierite is absent from the Port Mouton Pluton except for grains contained within Meguma Group xenoliths (Tate, 1994). Cordierite occurs as >1 mm size subhedral to euhedral grains, partially to completely replaced by a combination of alteration products. The primary alteration product is pinite (Fig. 5.7 in SI), a fine-grained allochemical retrograde alteration, whose mineral composition is poorly defined but believed to consist of muscovite, biotite, and hydrous phyllosilicates (Ogiermann, 2002). This alteration assemblage replaces over 25% of the cordierite grains. Other alteration products include muscovite + biotite ± chlorite ± hydrous aluminosilicates (possibly kaolinite or a zeolite) (Fig. 5.7 in SI). Analysis of the least altered cordierite yields an average primary value of 7.2 µg/g As which is significantly greater than concentrations in the major silicates. The biotite, muscovite and pinite pseudomorph products of cordierite have less As than the unaltered sections while the hydrous aluminosilicate and chlorite alteration have a greater As concentration.

Table 5.1 Summary of whole-rock and mineral concentrations of As and mineral saturation indices.

Arsenic Concentration (µg/g)					Mineral Saturation Index		
Mineral Pluton	Min	Max	Median	N	Min	Max	Median
Whole Rock	**<0.5**	**3000**	**2.4**	**56**			
Halifax Pluton	<0.5	7	3.1	8			
Musquodoboit Batholith	<0.5	4.5	0.8	3			
Port Mouton Pluton	<0.5	1.7	0.25	4			
South Mountain Batholith	0.7	3000	2.6	41			
Cordierite (Unaltered)[1]	**2.7**	**16**	**6.3**	**5**	**-30.7**	**-12.6**	**-14.3**
Halifax Pluton	6.3	6.5	6.4	2	-30.7	-12.7	-14.3
Musquodoboit Batholith	2.7	16	5.3	3			
Port Mouton Pluton					-21.6	-12.9	-14.3
Cordierite (Altered)[2]	**<0.77**	**500**	**22[3]**	**10**	**-33.8**	**4.66**	**0.135**
Halifax Pluton	1.9	500	87[3]	2	-33.8	4.66	0.214
Musquodoboit Batholith	<0.77	20	2.7[3]	8			
Port Mouton Pluton					-23.8	3.56	0.184
Monazite	**280**	**1200**	**530**	**72**	**0.286**	**4.06**	**2.77**
Halifax Pluton	320	770	500	31	0.286	3.65	2.76
Musquodoboit Batholith	280	1200	630	13			
Port Mouton Pluton	370	800	570	23	1.52	4.06	2.64
South Mountain Batholith	400	790	520	5	2.15	3.18	2.94
Goethite	**20**	**3400**	**690**	**15**	**5.52**	**10.4**	**7.61**
Halifax Pluton	20	3400	700	14	5.52	10.4	7.86
Musquodoboit Batholith			300	1			
Port Mouton Pluton					6.07	9.11	7.57
Pyrite	**<14**	**15000**	**490**	**9**			
Halifax Pluton	<14	15000	460	6			
Musquodoboit Batholith			2700	1			
Port Mouton Pluton	490	490	490	2			

[1] Measurement of the least altered cordierite sections

[2] Measurements of the altered cordierite grain represented by a combination of alteration products in the following proportions: Muscovite (22.7%), Biotite (26.6%), Chlorite (8.16%), Pinite (41.2%), and hydrous aluminosilicate (1.25%).

[3] Due to the heterogeneous nature of the alteration, no median value is provided, a mean weighted by the proportion of each phase in the plutons is displayed. The mean for all altered grains is calculated using the proportions listed above.

Cordierite has a mineral saturation index <1 (Table 5.1) in the groundwater from Nova Scotian granites, as do related chlorite and biotite alteration products. Insufficient data is available on the dissolution rates of cordierite in natural groundwaters, but recent surface exposures of the South Mountain Batholith (<50 years) show preferential weathering of cordierite over the major silicates (Fig. 5.6 in the SI). Although qualitative, these weathering pits and observed alteration products suggest that cordierite is relatively reactive in the surface environment. Despite the low concentrations of As, cordierite and its alteration products are a significant reservoir for As in the Halifax Pluton and Musquodoboit Batholith (Fig. 5.2). In some of the well water samples from the Halifax Pluton, there is an increase in the uranium or manganese content with As in proportion to the ratio of these elements contained within cordierite, as would be expected if the dissolution of this mineral was the source of As (Fig. 5.3A and B). The mass of As stored in cordierite coupled with the solubility of this phase and its alteration products in well water makes the dissolution of cordierite a potential source for geogenic As at the South Mountain Batholith. Outside the study area, cordierite is abundant in lithologies that are transformed by thermal metamorphism from shales and in granites that are either derived from or have assimilated these sedimentary rocks. As shales may have high As content (Smedley and Kinniburgh, 2002; Ketris and Yudovich, 2009), the resulting cordierite is more likely to have high As. Given that cordierite is reactive in acidic waters (Palandri and Kharaka, 2004) and it may have elevated As concentration, this mineral may release As into ground or surficial waters if subjected to acid rock drainage. Thus, cordierite is a potential source of geogenic As in many metamorphic and igneous aquifers.

Zircon [$ZrSiO_4$] is a common accessory phase (~0.5 to 2 modal %), found as euhedral inclusions in biotite. The As concentration of zircon in this study varies from a maximum value of 4.6 µg/g and a minimum detected value of 0.46 µg/g. Due to the size of these grains, the detection limits vary from less than 0.24 µg/g to over 10 µg/g. Other studies have found that zircons from highly evolved granites can reach up to 1.1 wt.% As due to hydrothermal alteration (Breiter et al., 2014). Zircon is typically considered to be insoluble but significant radiation damage can increase its solubility in aqueous fluids (Tromans, 2006). Incongruent dissolution of damaged zircon may release loosely bound

^{234}U over ^{238}U in granites (Papageorgiou et al., 2022). This incongruent dissolution could make zircon a potential geogenic source of As. Due to the low As content, if zircon was the As source in Nova Scotia, then the U concentrations should be much higher than observed (Fig. 5.3A), even with incongruent dissolution.

The four grains of *titanite* [$CaTiSiO_5$] in this study are 10-20 µm in size, subhedral and hold between 1.5 to 12 µg/g. Titanite from the Roxby Downs granite, Australia, includes up to 10-50 µg/g As, with the highest concentrations in the magmatic cores of the grains (Kontonikas-Charos et al., 2019). At other granitic intrusions, titanite could be a minor geogenic source of As, if concentrations are like those found in the Roxby Downs granite.

In total, eleven grains of *rare earth element (REE)-enriched epidote* [$(REE,Ca,Y)_2(Fe^{3+},Al)_3(SiO_4)_3(OH)$] were found in four of the samples from the Halifax Pluton and Musquodoboit Batholith. The epidote grains have 10-13 wt.% total REE in the Musquodoboit Batholith and 18-21 wt.% in the Halifax Pluton. Epidote from the Halifax Pluton has 62 to 190 µg/g As and epidote from the Musquodoboit Batholith contains <46 to 96 µg/g. These concentrations are slightly higher than epidotes recorded in other studies (Spiegel et al., 2002; Cooke et al., 2014; Ahmed et al., 2020; Pacey et al., 2020) but are similar to values reported by Jantos et al. (2011) for metamorphic allanite (50-130 µg/g). In the present study, epidote occurs as either lenses (Fig. 5.7C in SI) or bladed crystals along the cleavages of biotite. The mineral saturation index of epidote ranges from -12.5 to 4.72 thus epidote may dissolve under some conditions but is not considered a significant reservoir of As (Fig. 5.2) despite high As concentrations. Well water concentrations of uranium do not correlate with concentrations of As according to the ratio of As to uranium in epidote (Fig. 5.3A), further suggesting this mineral is not a source for As in groundwater associated with the granites of Nova Scotia, as congruent dissolution of epidote should release these elements in proportion to their abundance in the mineral. However, the high concentration of As in REE-epidote and lower stability suggest this mineral could be a geogenic source of As in granitic bodies with higher modal abundances of epidote.

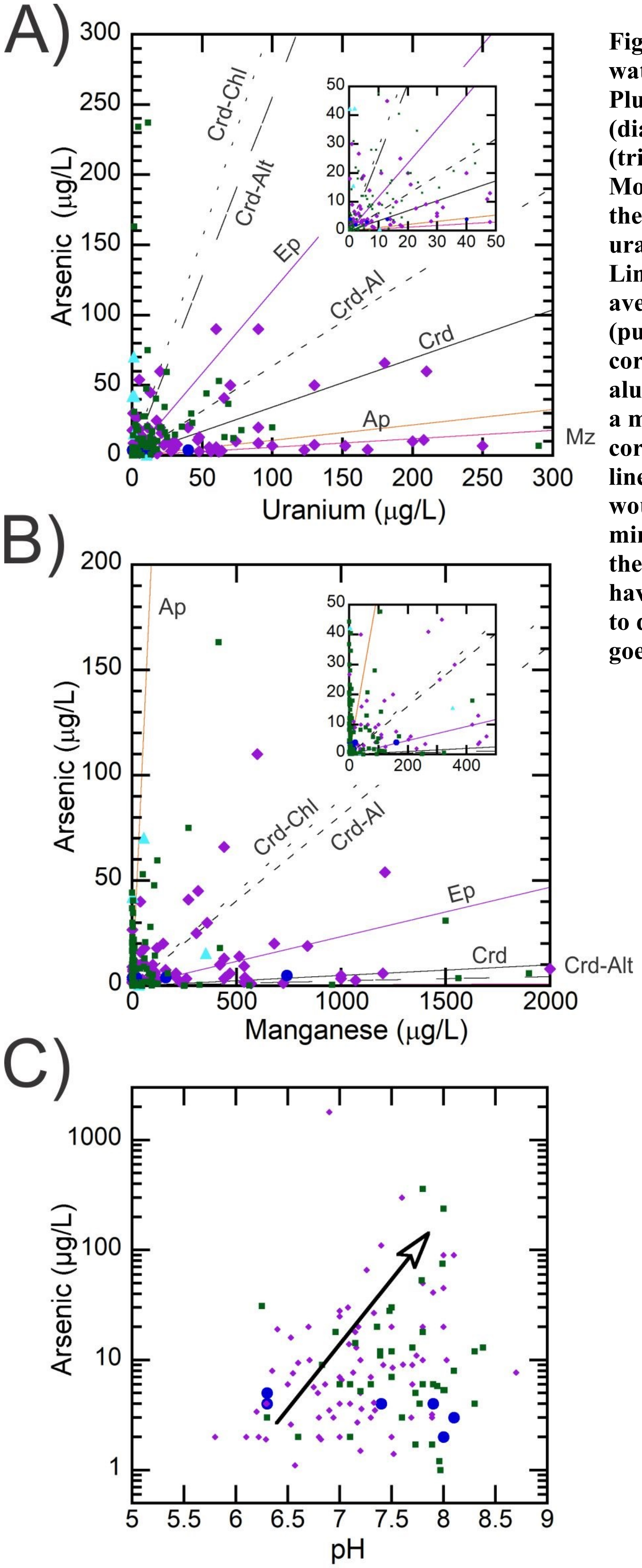

Figure 5.3 Concentration of As from well water associated with the Port Mouton Pluton (circles), the Halifax Pluton (diamonds), Musquodoboit Batholith (triangle) and the remainder of the South Mountain Batholith (squares) plotted versus the A) manganese concentration, B) uranium concentration, C) well water pH. Lines plotted in figures A and B are the average elemental ratios found in epidote (purple), apatite (red), monazite (orange), cordierite (black solid), cordierite altered to aluminosilicate (short-dash), cordierite with a mat-like alteration (long-dash) and cordierite altered to chlorite (dot). These lines reflect the well water chemistry that would occur if congruent dissolution of the mineral was dominant. The arrow shows the anticipated effect increasing pH would have on the well water As concentration due to desorption of pentavalent As from goethite.

5.3.2. Phosphates

Apatite [$Ca_5(PO_4)_3(F,Cl,OH)$] is the most common phosphate mineral in the studied samples with modal amounts varying from 0.01-0.46%. Grains are 5 to 500 µm and typically occur as euhedral inclusions in biotite but also as separate subhedral to anhedral crystals in the rock matrix. Apatite is predominantly the fluorapatite end member. The As content of apatite ranges from 1.5 to 58 µg/g with most grains containing less than 7.5 µg/g. Apatite from the Port Mouton Pluton has the lowest As concentration with a median value of 2.4 µg/g, while the apatites from the Musquodoboit Batholith and Halifax Pluton have medians of 4.3 µg/g and 5.7 µg/g, respectively. The As concentrations of apatite in this study are on the lower end of those reported for other granitic bodies (Belousova et al., 2002; Wang et al., 2014; Teiber et al., 2015; Mao et al., 2016) which range from less than 0.5 µg/g (Teiber et al., 2015) up to 11,355 µg/g (Belousova et al., 2002). The mineral saturation index for fluorapatite is greater than 1 (ranging from 1.96 to 11.8) thus apatite should be stable in local groundwaters. The insoluble nature of phosphates in groundwater is supported by most natural groundwaters being below analytical detection limits (Holman et al., 2008). This is consistent with the uranium-As and manganese-As systematics in the well water analyzed, with only a few samples that have U/As ratios that correspond to apatite dissolution, and only at low As concentrations (Fig. 5.3A and B). There is no correlation between dissolved As and fluoride in the well water.

Monazite [$CePO_4$] is a rare mineral in the samples studied, typically making up less than 0.01 modal %. Grains of monazite are euhedral to subhedral with occasional corrosion at the edges and can be zoned and/or pitted (Fig. 5.7E in SI). Like apatite, this phosphate is included in biotite or occurs along biotite grain boundaries. In some cases, monazite forms micron-scale inclusions in apatite and rarely do these inclusions comprise most of the phosphate grain. Most monazites are 10-30 µm in size but can be as large as 100 µm. The average As concentration of monazite is 550 µg/g with most of the data between 450 to 630 µg/g (1st and 3rd quartile). Monazite As concentrations are uniform across all three plutons, although the variability in the Musquodoboit Batholith is slightly greater. Such high As concentrations are consistent with experimental measurements of monazite-melt partitioning (Stepanov et al., 2012). Additionally, high As in monazite is expected as a solid solution between monazite and gasperite [$CeAsO_4$] has been documented in REE-enriched granites (Majzlan et al., 2014 and references therein). Calculated mineral saturation index for monazites using estimated phosphate concentrations (Table 5.1) indicates that this phase is stable (supersaturated) under the observed well water chemistry. Uranium-As well water concentrations (Fig. 5.3A) could suggest congruent monazite dissolution in some samples in contrast to the mineral saturation index. The manganese concentration of monazite ranges from < 1 µg/g to over 900 µg/g, thus Mn-As systematics cannot assess monazite dissolution. At acidic conditions, monazite becomes more soluble and combined with its high concentration of As (Fig. 5.2) indicates that a decrease in well water pH, such as from seepage related to acid rock drainage outflows, could trigger a significant release of As.

Xenotime [YPO_4] is the rarest of the three phosphates in the samples studied, at < 0.001 modal %. Xenotime is subhedral to anhedral, 20 to 100 µm, and occurs on biotite grain edges but may also be present as inclusions. In some cases, xenotime forms zoned overgrowths on monazite (Fig. 5.7D in SI). Like monazite, in REE-enriched granites xenotime exhibits a solid solution with an arsenate endmember, in this case, chernovite [$YAsO_4$] (Majzlan et al., 2014 and references therein). However, the As concentrations of xenotimes in this study ranged between 31 and 78 µg/g.

5.3.3. Sulfides

Pyrite [FeS_2] is the predominant sulfide in the samples studied, with lesser amounts of chalcopyrite occurring as inclusions (Fig. 5.4A) in the pyrite from the Port Mouton Pluton. This contrasts with the work of Clarke et al. (2009) where pyrrhotite [$Fe_{(1-x)}S$] was identified as the primary sulfide. However, these pyrrhotite grains are from near the Meguma-South Mountain Batholith contact and are believed to be xenocrysts (Clarke et al., 2009). The modal amount of pyrite is highly variable from trace (<0.01 modal %) to 0.1 modal %. Pyrite in central plutons is partially to completely replaced by hydrous ferric oxides and ferric hydroxides (Fig. 5.4B, C and D). Based on replacement morphologies, the original pyrite crystals are anhedral and range up to 200 µm in size. Pyrite contains from <14 µg/g up to 15,000 µg/g As (Table 5.1). Such higher concentrations are not unusual, as levels up to 10 wt.% (Fakhreddine et al., 2021) have been reported. Magmatic pyrrhotite is not expected to have high As concentrations as the partition coefficient between monosulfide solution (the high-temperature phase of pyrrhotite) and silicate melt should be near unity (Li and Audétat, 2015). Xenocryst metamorphic pyrrhotite is also expected to have low As concentrations as metamorphism can convert high-As pyrite into low-As pyrrhotite (O'Shea et al., 2015). Although pyrite can host significant amounts of arsenic, its variable concentration and low modal abundance suggest it does not the control the whole-rock arsenic content. Based on the estimated Eh and measured pH of the local well water, pyrite is unstable and expected to oxidize with iron re-precipitating as a ferric oxyhydroxide, in agreement with textural evidence. The As released from pyrite should be correlated with sulfur or iron based on the ratio of these elements in this mineral, however, this is not observed in the well water chemistry. This discrepancy may relate to sorption of As onto secondary minerals, as discussed below. The high concentrations of As in pyrite make it a significant reservoir for this element despite low model abundances (Fig. 5.2). The textural evidence of pyrite dissolution and oxide replacement in the Halifax Pluton and MP indicates that this mineral is likely contributing to As in the associated well water.

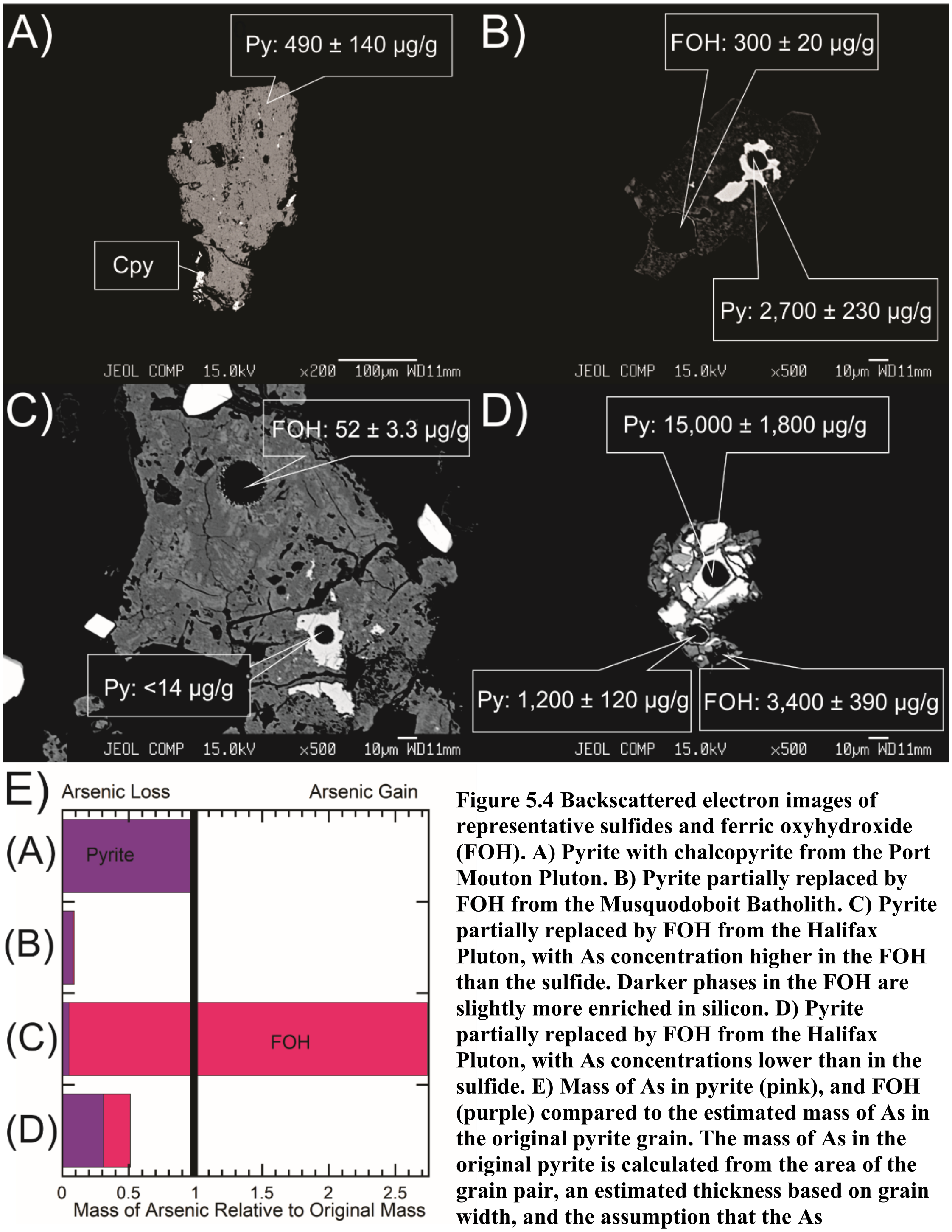

Figure 5.4 Backscattered electron images of representative sulfides and ferric oxyhydroxide (FOH). A) Pyrite with chalcopyrite from the Port Mouton Pluton. B) Pyrite partially replaced by FOH from the Musquodoboit Batholith. C) Pyrite partially replaced by FOH from the Halifax Pluton, with As concentration higher in the FOH than the sulfide. Darker phases in the FOH are slightly more enriched in silicon. D) Pyrite partially replaced by FOH from the Halifax Pluton, with As concentrations lower than in the sulfide. E) Mass of As in pyrite (pink), and FOH (purple) compared to the estimated mass of As in the original pyrite grain. The mass of As in the original pyrite is calculated from the area of the grain pair, an estimated thickness based on grain width, and the assumption that the As concentration of pyrite was homogenous and has remained unchanged since replacement by FOH.

5.3.4. Oxides

Rutile [TiO_2] occurs as 50-100 μm euhedral inclusions in biotite, subhedral to anhedral grains included in chlorite or as large (>100 μm) anhedral grains included within or along the margins of ilmenite crystals. Rutile is present in the samples at trace levels (< 0.1 modal %) The As concentrations of rutile are below 1 μg/g.

Ilmenite [$FeTiO_3$] occurs as discrete 300 μm subhedral to anhedral grains or as 10 to 50 μm long needles often included in biotite. Similar to rutile, the concentration of As in ilmenite is less than 1 μg/g, consistent with previously reported values (Onishi, 1969; Smedley and Kinniburgh, 2002). Ilmenite is the dominant titanium phase present in the samples at minor (< 1 modal %) to trace levels.

Hydrous ferric oxide and ferric hydroxides (Goethite [α-$Fe^{3+}O(OH)$] and lepidocrocite [γ-$Fe^{3+}O(OH)$]), henceforth called ferric oxides and hydroxides (FOH), partially to completely replace pyrite in samples from the Musquodoboit Batholith (Fig. 5.4B) and Halifax Pluton (Fig. 5.4C and D), but not the Port Mouton Pluton. These phases mantle the pyrite and have either a mottled or botryoidal texture. The analytical totals of the FOH, assuming all Fe^{3+}, are often less than 100%, suggesting hydration in most of the grains. Additionally, the FOH contained 1-2 wt.% Si, with one sample having up to 5 wt.% Si which may be related to porosity and silicate inclusions formed during the alteration of the pyrite. Within the Port Mouton Pluton, a single 30 μm goethite crystal included in plagioclase feldspar was observed. This grain did not have any associated pyrite, suggesting goethite replaced the sulfide. Most of the sulfide oxidation products have As concentrations between 120 and 840 μg/g, similar to values reported for other localities (Smedley and Kinniburgh, 2002). Whether this As is sorbed or structurally bound is unknown. Mass balance calculations (Fig. 5.4E) of pyrite-FOH pairs demonstrate that the concentration of As in two of the FOH grains is greater than could have been achieved by the replacement of the original sulfide. To explain this discrepancy either the remaining sulfide was depleted in As compared to the original grain or the FOH has acquired more As than available from the original sulfide, possibly through adsorption. If the acquired As is present as an adsorbed component, then several mechanisms can lead to the release of As from FOH including a change in pH, a change in the sorption strength, the reduction of hydroxide surface area (possible through phase transformation), or hydroxide dissolution (Smedley and Kinniburgh, 2002; Dixit and Hering, 2003). Dissolution is unlikely as mineral saturation indicess suggest goethite is stable in the groundwater system (Table 5.1); however, this may change if the groundwater were to become reduced.

In terms of the effect of pH, the sorption behavior depends on the speciation of As in groundwater. At the estimated Eh-pH conditions As is predicted to be mainly in the pentavalent form, and a previous study demonstrated a 15-30% drop in the sorption capacity of As^V on goethite for a change from pH 6 to 8 with a larger decrease in sorption capacity associated with lower initial As concentrations (Dixit and Hering, 2003). The As concentration of the well water from the Halifax Pluton shows a weak increase with increasing pH (Fig. 5.3C) consistent with this behavior. A similar relationship exists for the other South Mountain Batholith samples, although there is considerable scatter in the data. The well water As concentrations related to the Port Mouton Pluton do not increase with increasing pH, which is consistent with a lack of a regulating role for FOH. The spread seen in Fig. 5.3 C may be related to the other factors affecting As sorption. Dissolution of other potential sources of As such as cordierite may cause the variation in well water concentrations of As, as some of the well water U/As and Mn/As ratios (Fig. 5.3A and B) correspond to the dissolution of this phase.

5.3.5. Geogenic Controls on Arsenic in Groundwater

While the absolute As content of a granite may influence the associated groundwater, this does not appear to be the case with Nova Scotian granites. The whole-rock As concentration of the central and southern plutons does not scale with the well water As content straightforwardly, implying a more complex control. Thus, this study considers sample mineralogy to explain the observed variation. The main mineralogical differences between the granitic bodies are 1) the presence of cordierite and its alteration products in the central plutons and its absence in the southern granites and, 2) the observed evidence for pyrite oxidation resulting in the formation of FOH rims in the Halifax Pluton and Musquodoboit Batholith, while pyrite in the Port Mouton Pluton is pristine. In both cases, the phases identified in the central granites may have labile As and therefore release As into infiltrating groundwater. The absence of cordierite and its alteration products from the Port Mouton Pluton can partially explain the lower As concentrations in the southern plutons. However, As-rich pyrite is present in all the granites studied. The presence of FOH replacement of pyrite seems to provide the most obvious mechanism for As release/retention into groundwater, with pH as a contributing factor. As groundwater Eh-pH conditions are similar for both the central and southern granites, the lack of FOH in the Port Mouton Pluton implies these sulfides were not exposed to oxidizing groundwater, reflecting a permeability control on As release. In general, factors that control permeability in crystalline rocks are fractures, joints, and the degree of weathering. Hydrothermal alteration increases the porosity of granitic rocks by the alteration of plagioclase to illite and biotite to chlorite, but the permeability only increases with extensive alteration (Staněk and Géraud, 2019). The central pluton samples in this study appear to have high degrees of chloritization and sericitization relative to the Port Mouton Pluton (Table 5.2 in SI). Additionally, intense weathering has formed saprolites in the South Mountain Batholith (O'Beirne-Ryan and Zentilli, 2006) indicating associated areas of increased permeability (Lachassagne et al., 2021). Thus, the central plutons have greater permeability than the southern plutons.

Owing to the moderate to high concentrations of As in both pyrite and cordierite and the evidence for their instability, both phases are potential geogenic sources of As in granitic terranes. However, these geogenic sources are influenced by other factors, with cordierite limited to granites with peraluminous compositions (Clarke, 1995), and sulfides, while ubiquitous, requiring destabilization by oxidized, high pH waters for efficient release.

5.4. Conclusions

Cordierite and pyrite are the main sources of As to groundwater in the central granites of Nova Scotia. The replacement of pyrite by FOH is a secondary control that can inhibit or limit the release of As into groundwater. Pyrite is also a potential geogenic source at the Port Mouton Pluton; however, lower permeability caused by less intense hydrothermal alteration impedes oxidation and in turn prevents As release.

In addition to the above minerals, zircon, REE-epidote, and monazite are potential geogenic sources at other locations with granitic bedrock. Of these three phases, monazite is the highest risk mineral. It contains a significant amount of As and is soluble under acidic conditions, such as those that occur during ARD. Acid rock drainage could infiltrate the granites in Nova Scotia near the contacts with the Meguma metasediments. Exposure of sulfide mineralization by mining/construction activities could also generate ARD in the South Mountain Batholith that could release As from monazite. The results of this study emphasize the importance of understanding bedrock mineralogy in predicting well water contamination.

5.5. Supplementary Information

Dataset 5A- Analytical Details for EMPA and LA-ICPMS.

Digital Excel file. In tab 1 labelled EMPA is a table listing the X-ray line, Count time, Crystal, and standard for each element and mineral pair analyzed. Tab 2 labelled LA-ICP-MS contains dwell time, and standard for each isotope, and if the isotope was used an internal standard.

Dataset 5B- All Mineral Trace Element Analyses.

Digital Excel file containing LA-ICP-MS analysis of minerals. Data is presented by Pluton, Sample number, mineral and analysis ID. Reported for each isotope is the concentration in μg/g, the 2σ error, and the limit of detection.

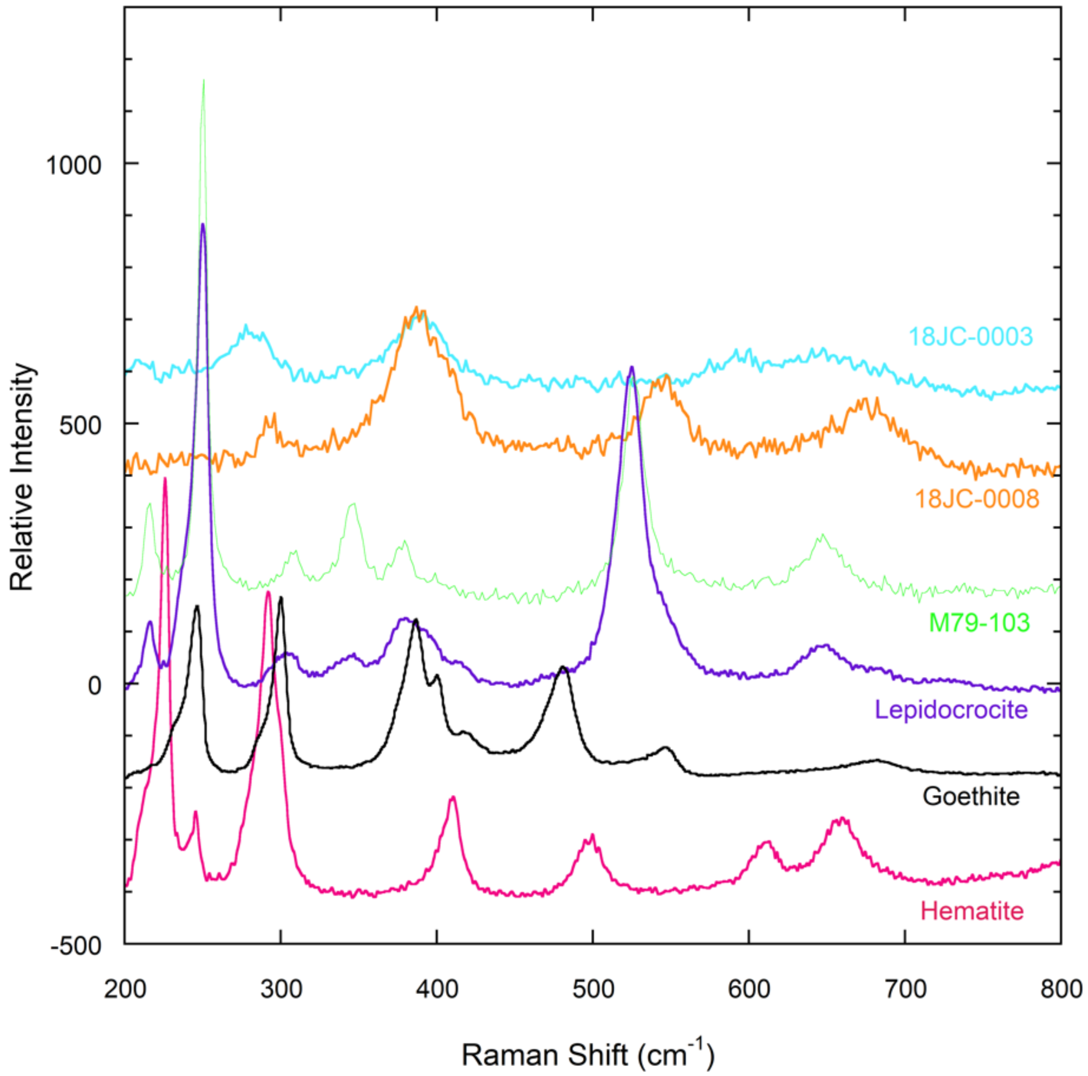

Figure 5.5 Representative Raman spectra of ferric oxides and hydroxides from the Halifax Pluton and the Musquodoboit Batholith, with reference spectra of goethite (RRUFFID: R120086), hematite (RRUFFID: R050300) and lepidocrocite (RRUFFID: R050454) for comparison.

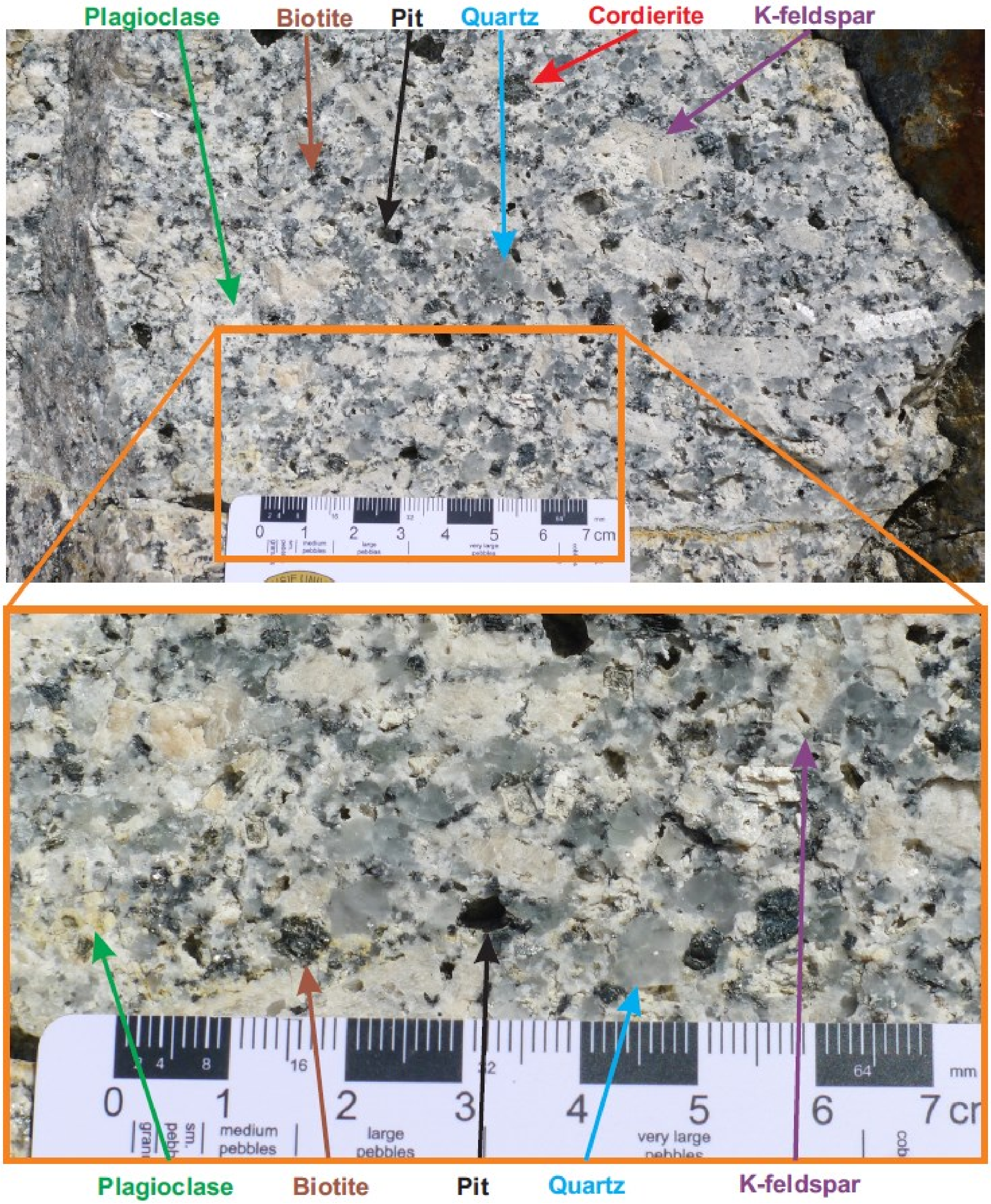

Figure 5.6 Photograph of South Mountain Batholith outcrop face located on roadcut 650 m past Exit 5 on NS-Hwy 103 W, in Upper Tantallon, Nova Scotia. Latitude: 44°42’07.7” Longitude:63°52’04.1”.The pits in the granite are caused by the selective weathering of cordierite.

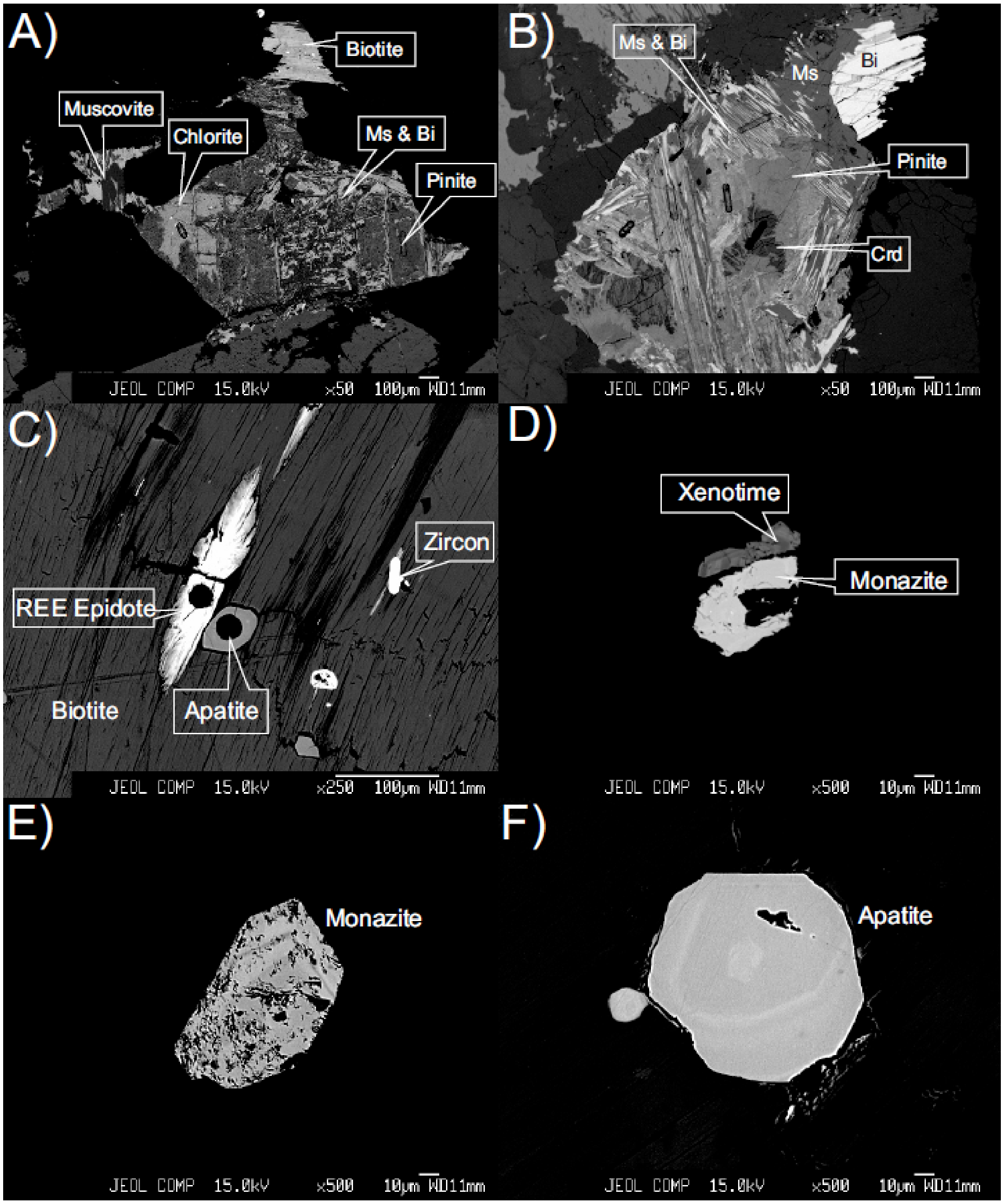

Figure 5.7 Backscatter electron images of representative As-bearing accessory minerals: A) cordierite (Crd) pseudomorphs from the Halifax Pluton showing domains with partial to complete replacement by chlorite (Chl), muscovite (Ms), biotite (Bi), and domains of altered cordierite to pinite; B) cordierite pseudomorphs from Musquodoboit Batholith showing partial to complete replacement by chlorite (Chl), muscovite (Ms), biotite (Bi), and domains of chlorite altered to pinite; C) REE-epidote from the Musquodoboit Batholith D) Monazite with xenotime mantle from the Halifax Pluton; E) monazite from the Musquodoboit Batholith; F) apatite from the Musquodoboit Batholith.

Table 5.2 Summary of Samples

Sample	Texture	Easting	Northing	Lithology	Pluton	Central or Southern Pluton	Cordierite Bearing	Grain Size	Degree of Chloritization	Degree of Plagioclase Alteration
18JC-0003	Porphyritic K-Feldspar	449154	4933734	MBMG	HP	Central	N	MG	1	3
18JC-0004	Porphyritic K-Feldspar + Plagioclase	449507	4927713	MBMG	HP	Central	N	FG	1	2
18JC-0008	Equigranular	447604	4943099	BGD	HP	Central	N	CG	0	2
D12-0103-2	Equigranular (Excluding Biotite)	442747	4942774	LMG	HP	Central	N	CG to MG	3	3
D12-3082	Equigranular	431593	4929963	LMG	HP	Central	Y	CG	1	2
21BM-0020	Prophyritic Plagioclase & Quartz	358201	4867941	MBT	PMP	Southern	N	MG	0	2
21BM-0021	Equigranular with poikilitic K-Feldspar	356333	4867913	MBMG	PMP	Southern	N	FG	0	2
21BM-0022	Equigranular (Excluding Biotite)	350696	4857270	BT	PMP	Southern	N	CG	0	1
21BM-0023	Poikilitic Porphyritic K-Feldspar, Anhedral Micas	345468	4858636	MBMG	PMP	Southern	N	MG	0	1
M79-010	Equigranular	520854	4973701	LMG	MB	Central	Y	CG	1	2
M79-022	Porphyritic K-Feldspar	500983	4961278	LMG	MB	Central	Y	CG	1	2
M79-103	Porphyritic K-Feldspar	501557	4962311	LMG	MB	Central	N	CG	1	2

BGD= Biotite Granodiorite; BMG= Biotite Monzogranite; MBMG= Muscovite Biotite Monzogranite; LMG= Leucomonzogranite; MBT= Muscovite Biotite Tonalite; BT= Biotite Tonalite; HP =Halifax Pluton; PMP = Port Mouton Pluton; MB= Musquodoboit Batholith; CG: Coarse grained (>2 mm); MG: Medium grained (1-2mm); FG: Fine Grained (<1 mm)

Coordinates are in UTM 20 NAD 83

Table 5.2 – footnote continued.

Degree of Chloritization

0) Negligible: No alteration to one or two grains with minor alteration on grain boundaries
1) Minor alteration: Most grains have alteration on grain boundaries or a few grains have been completely replaced by chlorite
2) Significant alteration: Almost all grains have alteration with multiple grains being completely altered.
3) Intense alteration: Almost no Biotite remains

Degree of Plagioclase Alteration

0) Negligible: No alteration to one or two grains with minor alteration
1) Minor alteration: Some grains have alteration in cores
2) Significant alteration: Almost all grains are altered but most are below 50%
3) Intense alteration: All grains are over 50% altered

Table 5.3 Modal Abundances of Accessory Phases

Sample Number	REE-Epidote	Apatite	Cordierite	Cordierite (Pinite)	Cordierite (Muscovite)	Cordierite (Biotite)	Cordierite (Hydrous-Aluminosilicate)	Cordierite (Chlorite)
18JC-0003	0.012%	0.12%	0.0%	0.0%	0.0%	0.0%	0.0%	0.0%
18JC-0004	0%	0.15%	0.0%	0.0%	0.0%	0.0%	0.0%	0.0%
18JC-0008	0%	0.22%	0.0%	0.0%	0.0%	0.0%	0.0%	0.0%
D12-0103-2	0.0010%	0.079%	0.0%	0.0%	0.0%	0.0%	0.0%	0.0%
D12-3082	0.0010%	0.012%	0.42%	0.55%	0.32%	0.32%	0.0%	0.25%
21BM-0020	0.0%	0.19%	0.000%	0.0%	0.0%	0.0%	0.0%	0.0%
21BM-0021*	0.0%	0.11%	0.000%	0.0%	0.0%	0.0%	0.0%	0.0%
21BM-0022	0.0030%	0.21%	0.000%	0.0%	0.0%	0.0%	0.0%	0.0%
21BM-0023	0.0%	0.16%	0.000%	0.0%	0.0%	0.0%	0.0%	0.0%
M79-010	0.025%	0.46%	0.000%	0.0%	0.0%	0.0%	0.0%	0.0%
M79-022	0.000%	0.073%	0.920%	2.3%	1.2%	1.6%	0.12%	0.0%
M79-103	0.0030%	0.11%	0.000%	0.0%	0.0%	0.0%	0.0%	0.0%

* Modes estimated from backscatter electron image not XRF maps

** Overestimate due to spectral interference

Table 5.3 Continued.

Sample Number	Monazite	Goethite	Pyrite	Titanite	Zircon**	Xenotime	Rock-forming Silicates
18JC-0003	0.0020%	0.016%	0.0070%	0.045%	0.51%	0.0010%	99.2%
18JC-0004	0.0080%	0.0%	0.0%	0.000%	1.4%	0.0%	98.4%
18JC-0008	0.010%	0.023%	0.0020%	0.0010%	0.86%	0.0010%	98.9%
D12-0103-2	0.0010%	0.0010%	0.0010%	0.0050%	0.51%	0.0010%	99.4%
D12-3082	0.0040%	0.011%	0.0%	0.000%	0.16%	0.0010%	98.0%
21BM-0020	0.0030%	0.0%	0.001%	0.0%	1.1%	0.0%	98.8%
21BM-0021*	0.0060%	0.0%	0.000%	0.0%	0.10%	0.0%	99.8%
21BM-0022	0.0060%	0.0%	0.101%	0.0090%	0.78%	0.0010%	98.9%
21BM-0023	0.0010%	0.003%	0.0%	0.010%	1.7%	0.0%	98.2%
M79-010	0.0020%	0.048%	0.0%	0.032%	0.38%	0.0010%	99.1%
M79-022	0.015%	0.0%	0.0%	0.0%	1.6%	0.0%	92.2%
M79-103	0.0010%	0.0010%	0.0040%	0.0080%	0.56%	0.0%	99.3%

* Modes estimated from backscatter electron image not XRF maps

** Overestimate due to spectral interference

Acknowledgements

This work was supported by the NSERC Discovery Grant awarded to JMB. BJM thanks the Nova Scotia Department of Natural Resources and Renewables for providing access to the Nova Scotia groundwater chemistry database. BJM thanks Gavin Kennedy for his advice in approaching this study as well as feedback on the manuscript. BJM thanks Erin Adladka for her assistance and use of the Bruker M4 tornado benchtop XRF at Saint Mary's University and Mitchell Kerr for his help with the Raman spectrometer at Saint Mary's University

Chapter 6

CONCLUSIONS

The goal of this thesis was to determine the high-temperature geochemical properties of As and Sb in order to understand the compositional evolution of these elements during magmatic processes and their mineralogical distribution in the solidification products of felsic melts. Results of this work established the speciation of As and Sb in silicate melts by direct measurements with XANES. The seemingly paradoxical As enrichment of apatite in plutonic rocks was also explored by determining the apatite/melt partition coefficient for As under controlled laboratory conditions. Finally, this thesis determined the distribution of As in granitic bedrock samples from southwestern Nova Scotia and identified the geogenic sources of As contamination in associated well water. The main conclusions of this thesis are:

- *The speciation of As and Sb in magmatic systems:* Over the range of oxygen fugacity (fO_2) encountered in terrestrial magmas (FMQ -3 to FMQ +3.5) both As and Sb were identified as trivalent cations in mafic melts, with the same As species found in felsic melts. Owing to the charge/size mismatch of this oxidation state with most major element crystallographic cation sites, both As and Sb are likely to be excluded from common rock-forming minerals during crystallization.
- *Partition coefficient between apatite and felsic melts for As:* Over the range of fO_2 for felsic magmas (FMQ-3 to FMQ +3.5) the apatite/melt partition coefficient for As is expected to vary from ~0.1 to ~1 in peralkaline melts, with values <1 in metaluminous and peraluminous compositions. Therefore, As is incompatible in apatite, except under extraordinarily oxidizing conditions. The high concentrations of As observed in apatite from terrestrial rocks are not a reflection of oxidizing conditions. Instead, high As in apatite and elevated apatite/whole partition coefficients for As indicate late apatite saturation after extreme degrees of crystallization.
- *The distribution of As in granites:* Pyrite, cordierite and monazite have elevated As concentrations in representative samples of the southwestern Nova Scotian granites. Arsenic release may occur by either oxidation (pyrite) or dissolution (cordierite), although As released by oxidation is modulated by the formation of

secondary ferric oxides. In granitic terranes, the nature of the As-bearing mineralogy, not the As whole-rock content, controls geogenic sources of contamination. Other factors such as groundwater chemistry and permeability may play a critical role in determining As mobility.

Taken together, these results tell a story of As and Sb incompatibility in magmatic minerals. In the absence of sulfides, both elements will concentrate in the residual melt during the crystallization process. Late crystallizing phases will equilibrate with melts having higher As and Sb concentrations, becoming enriched in these elements. If these phases are unstable under surface conditions, then they can provide geogenic sources of contamination in groundwater.

This thesis provides a starting point for further research into the behavior of arsenic and antimony in magmatic systems. Below is a brief list of questions raised for future work.

- *The Antimony Paradox:* The geochemistry of Sb in subduction zones is somewhat enigmatic as Sb is expected to be sequestered by rutile in the slab, similar to Nb. This idea is supported by studies showing that rutile holds the entire Sb budget in eclogites (Zack et al., 2002). However, Sb is enriched in arc magmas when compared to Nb (Zack et al., 2002) and this thesis found that in basaltic magmatic systems that Sb is in the Sb^{III} form which is incompatible in rutile. Trivalent antimony explains the fractionation from Nb in arcs magmas, but not the high Sb concentration in rutile. Thus, further experiments exploring Sb, Nb partitioning at subduction zone conditions are needed.
- *Arsenic in Apatite Paradox: Other compositions*: This thesis revealed the As in apatite paradox, which was explained to be a result of melt enrichment caused by extreme degrees of fractional crystallization. However, this model was only applied to samples from the peraluminous South Mountain Batholith. Data for apatite and whole-rock As concentrations in peralkaline and metaluminous plutonic systems could be used to verify the proposed enrichment model in systems where apatite is expected to crystallize earlier. Also, data on coexisting apatite and volcanic glass could be used to verify magma redox state determined using other oxygen barometers.
- *Arsenic in Apatite Paradox: Pile-up Diffusion*: This study suggested extreme degrees of fractional crystallization as the mechanism for As to become enriched in the

melt prior to apatite formation. However other processes such as pile-up diffusion (Holycross and Watson, 2018) or trapped residual melts (Bea et al., 2022) could potentially cause extreme arsenic enrichment. These models require As diffusion coefficients, which have not been measured for felsic systems. Thus, future experimental studies investigating As diffusion could be done to evaluate these alternative mechanisms.

- *Arsenic in Apatite Paradox: Mineralized Systems:* Chapter 4 focused on the As content of apatite associated with unmineralized magmatic systems. However, the highest levels of As in apatite are associated with iron-oxide-apatite deposits (IOA; Belousova et al., 2002; Mao et al., 2016). Unfortunately, these apatite analyses do not have the corresponding whole-rock As contents available. The origin of these deposits is still debated, and the process(es) that enrich As in apatite may help to understand the associated metal enrichment. Apatite and whole-rock analysis for arsenic for samples from these deposits would be of use in this context. Additionally, targeted experiments to evaluate apatite/melt partitioning involving phosphate, carbonate or sulphate melts, which are proposed ore-forming agents, would be of benefit.
- *Arsenic in Cordierite:* The unexpectedly high arsenic content of cordierite relative to other silicates from the South Mountain Batholith raises several questions which could have significant environmental relevance.
    - Where is the arsenic in the structure of cordierite? Is it in the cyclosilicates column, or is it substituting for Al or Si?
    - Are the South Mountain Batholith cordierites unique, or does all magmatic cordierite have high As?
    - Does metamorphic cordierite have elevated As? If so, is it the source of elevated As in groundwater associated with Meguma Terrane bedrock (Kennedy and Drage, 2017)?
    - How fast does cordierite react with neutral waters and how labile is As in cordierite? What about in acidic waters?
- *Geogenic Arsenic Model of Nova Scotia:* Chapter 5 found that geogenic arsenic could be linked to the mineralogy of the granitic samples, however, this study did not attempt to explore the spatial link between bedrock mineralogy, and groundwater

chemistry. Future research could focus on replicating Chapter 5’s approach but use more systematic water and bedrock sampling over a limited spatial area. Alternatively, further work could explore any geospatial link between whole-rock geochemistry, mineralogy and groundwater chemistry using publicly available data for the entire batholith. Both of these studies would be useful in evaluating geogenic arsenic risks.

REFERENCES

Acharyya S. K., Shah B. A., Ashyiya I. D. and Pandey Y. (2005) Arsenic contamination in groundwater from parts of Ambagarh-Chowki block, Chhattisgarh, India: Source and release mechanism. *Environ. Geol.* **49**, 148–158.

Adam J. and Green T. (2006) Trace element partitioning between mica-and amphibole-bearing garnet lherzolite and hydrous basanitic melt: 1. Experimental results and the investigation of controls on partitioning behaviour. *Contrib. Miner. and Petrol.* **152,** 1-17.

Agency for Toxic Substances and Disease Registry (2019) Substance Priority List. *https://www.atsdr.cdc.gov/SPL/#2019spl*.

Ahmed A. D., Fisher L., Pearce M., Escolme A., Cooke D. R., Howard D. and Belousov I. (2020) A Microscale Analysis of Hydrothermal Epidote: Implications for the use of laser ablation-inductively coupled plasma-mass spectrometry mineral chemistry in complex alteration environments. *Econ. Geol.* **115**, 793–811.

Ahmmad S. K., Samee M., Taqiullah S. and Rahman S. (2016) FT-IR and Raman spectroscopic studies of ZnF_2–ZnO–As_2O_3–TeO_2 glasses. *J. Taibah Univ. Sci.* **10,** 329-339.

Alam M. S., Wu Y. and Cheng T. (2014) Silicate minerals as a source of As contamination in groundwater. *Water. Air. Soil Pollut.* **225**, 1–15.

Ali W., Rasool A., Junaid M. and Zhang H. (2018) A comprehensive review on current status, mechanism, and possible sources of As contamination in groundwater: a global perspective with prominence of Pakistan scenario. *Environ. Geochemistry Heal. 2018 412* **41**, 737–760.

Anderson G. (2017) *Thermodynamics of Natural Systems: Theory and Applications in Geochemistry and Environmental Science*. 3rd ed., Cambridge University Press, Cambridge.

Andersson S. S., Wagner T., Jonsson E., Fusswinkel T. and Whitehouse M. J. (2019) Apatite as a tracer of the source, chemistry and evolution of ore-forming fluids: The case of the Olserum-Djupedal REE-phosphate mineralisation, SE Sweden. *Geochim. Cosmochim. Acta* **255**, 163–187.

Azadbakht Z., Lentz D. R. and McFarlane C. R. M. (2018) Apatite chemical compositions from Acadian-related granitoids of New Brunswick, Canada: Implications for petrogenesis and metallogenesis. *Miner. 2018, Vol. 8, Page 598* **8**, 598.

Bachmann O., Dungan M. A. and Bussy F. (2005) Insights into shallow magmatic processes in large silicic magma bodies: The trace element record in the Fish Canyon magma body, Colorado. *Contrib. to Mineral. Petrol.* **149**, 338–349.

Bai L., Barnes S. J. and Baker D. R. (2017) Sperrylite saturation in magmatic sulfide melts: Implications for formation of PGE-bearing arsenides and sulfarsenides. *Am. Mineral.* **102**, 966–974.

Ballhaus, C. (1993). Redox states of lithospheric and asthenospheric upper mantle. *Contrib. to Mineral. Petrol*., **114**, 331-348.

Ballirano P. and Maras A. (2002). Refinement of the crystal structure of arsenolite, As_2O_3. *Z. Kristallogr.* **217**, 177-178.

Baker, D.R. 2004. Piston-cylinder calibration at 400 to 500 MPa: A comparison of using water solubility in albite melt and NaCl melting. *Am. Min.* **89**, 1553- 2318.

Barin I. And Platzki (1995) *Thermochemical data of pure substances. Third Edition Vol. 1: Ag-Kr and Vol. II: La-Zr.* VCH Publishers Inc. NewYork, USA and VCH Verlagsgesellschaft mbH, Weinheim, Germany.

Bea F, Fershtater G, Corretge LG (1992) The geochemistry of phosphorus in granite rocks and the effect of aluminum. *Lithos* **29**, 43–56

Bea, F., Bortnikov, N., Cambeses, A., Chakraborty, S., Molina, J.F., Montero, P., Morales, I., Silantiev, S. and Zinger, T. (2022) Zircon crystallization in low-Zr mafic magmas: Possible or impossible? *Chem. Geol.* **602**, 120898

Belousova E. A., Griffin W. L., O'Reilly S. Y. and Fisher N. I. (2002) Apatite as an indicator mineral for mineral exploration: trace-element compositions and their relationship to host rock type. *J. Geochemical Explor.* **76**, 45–69.

Berry A. J., O'Neill H. S. C., Scott D. R., Foran G. J. and Shelley J. M. G. (2006) The effect of composition on Cr2+/Cr3+ in silicate melts. *Am. Mineral.* **91**, 1901–1908.

Bethke C. (2022) *Geochemical and biogeochemical reaction modeling*. Cambridge university press.

Bia G., García M. and Borgnino L. (2017) Changes in the As solid speciation during weathering of volcanic ashes: A XAS study on Patagonian ashes and Chacopampean loess. *Geochim. Cosmochim. Acta* **212,** 119-132.

Bickerton M. L., Kontak D. D. J., Murphy D. J. B., Kellett D. D. A.-M., Samson D. I. M., Marsh D. J., Dunning D. G. R. and Stern D. R. A. (2022) The Age and Origin of the South Mountain Batholith (Nova Scotia, Canada) as Constrained by Zircon U-Pb Geochronology, Geochemistry and O-Hf Isotopes. *Can. J. Earth Sci.* **Just-In**

Blundy J. and Wood B. (1994) Prediction of crystal-melt partition coefficients from elastic moduli. *Nature* **372,** 452-454.

Blundy J. and Wood B. (2003) Mineral-melt partitioning of uranium, thorium and their daughters. *Rev. Mineral.* **52,** 59-123.

Bohlen, S. R. (1984). Equilibria for precise pressure calibration and a frictionless furnace assembly for the piston-cylinder apparatus. *Neu. Jb. Mineral, Mh* 404-412.

Bondu R., Cloutier V., Rosa E. and Benzaazoua M. (2016) A review and evaluation of the impacts of climate change on geogenic As in groundwater from fractured bedrock aquifers. *Water. Air. Soil Pollut.* **227**.

Borisov A. A. (2013) Mutual interaction of redox pairs in silicate melts: V5+/V4+/V3+/V2+ tetrad and other equilibria. *Petrol. 2013 214* **21**, 305–315.

Borisova A. Y., Pokrovski G. S., Pichavant M., Freydier R. and Candaudap F. (2010) Arsenic enrichment in hydrous peraluminous melts: Insights from femtosecond laser ablation-inductively coupled plasma-quadrupole mass spectrometry, and in situ X-ray absorption fine structure spectroscopy. *Am. Mineral.* **95**, 1095–1104.

Boström D. (1987) Single-crystal X-ray diffraction studies of synthetic Ni-Mg olivine solid solutions. *Am. Mineral.* **72,** 965-972.

Bowell R. J., Alpers C. N., Jamieson H. E., Nordstrom D. K. and Majzlan J. (2014) The environmental geochemistry of As — An overview —. *Rev. Mineral. Geochemistry* **79**, 1–16.

Boyce J. W. and Hervig R. L. (2008) Apatite as a monitor of late-stage magmatic processes at Volcán Irazú, Costa Rica. *Contrib. to Mineral. Petrol.* **157**, 135.

Brandon, A. D., & Draper, D. S. (1996). Constraints on the origin of the oxidation state of mantle overlying subduction zones: an example from Simcoe, Washington, USA. *Geochim. Cosmochim. Acta*, **60**, 1739-1749.

Breiter K., Lamarão C. N., Borges R. M. K. and Dall'Agnol R. (2014) Chemical characteristics of zircon from A-type granites and comparison to zircon of S-type granites. *Lithos* **192–195**, 208–225.

Brenan J. M. (2015) Se–Te fractionation by sulfide–silicate melt partitioning: Implications for the composition of mantle-derived magmas and their melting residues. *Earth Planet. Sci. Lett.* **422,** 45-57.

Brenan J. M., Maciag B. J. and Hanley J. J. (2020) *Development of new mineralization pathfinders for the South Mountain Batholith (NS) using biotite and apatite trace element geochemistry: Report Mineral Deposits Reserch Fund.*, Halifax.

Brenan J. M., Maciag B. J. and Hanley J. J. (Submitted) Geochemical variation in biotite from the Devonian South Mountain Batholith, Nova Scotia: Constraints on intensive parameters and the development of a magmatic vapour phase. *Am. Mineral.*

Bromiley G. D. (2021) Do concentrations of Mn, Eu and Ce in apatite reliably record oxygen fugacity in magmas? *Lithos* **384–385**, 105900.

von Brömssen M., Häller Larsson S., Bhattacharya P., Hasan M. A., Ahmed K. M., Jakariya M., Sikder M. A., Sracek O., Bivén A., Doušová B., Patriarca C., Thunvik R. and Jacks G. (2008) Geochemical characterisation of shallow aquifer sediments of Matlab Upazila, Southeastern Bangladesh - Implications for targeting low-As aquifers. *J. Contam. Hydrol.* **99**, 137–149.

Bryndzia, L. T., & Wood, B. J. (1990). Oxygen thermobarometry of abyssal spinel peridotites: the redox state and C–O–H volatile composition of the Earth's sub-oceanic upper mantle. *Am. J. Sci.*, **290**, 1093-1116.

Buerger M. and Hendricks S. B. (1938) The crystal structure of valentinite (orthorhombic Sb_2O_3) 1. *Z. Kristallogr.* **98,** 1-30.

Calvin S. (2013) *XAFS for Everyone*., CRC Press.

Cameron M., Sueno S., Prewitt C. T. and Papike J. J. (1973) High-temperature crystal chemistry of acmite, diopside, hedenbergite, jadeite, spodumene, and ureyite. *Am. Mineral.* **58,** 594-618.

Campbell L. S. and Henderson P. (1997) Apatite paragenesis in the Bayan Obo REE-Nb-Fe ore deposit, Inner Mongolia, China. *Lithos* **42**, 89–103.

Canali A. C., Brenan J. M. and Sullivan N. A. (2017) Solubility of platinum-arsenide melt and sperrylite in synthetic basalt at 0.1 MPa and 1200 °C with implications for As speciation and platinum sequestration in mafic igneous systems. *Geochim. Cosmochim. Acta* **216**, 153–168.

Cao M., Li G., Qin K., Seitmuratova E. Y. and Liu Y. (2012) Major and trace element characteristics of apatites in granitoids from central Kazakhstan: Implications for petrogenesis and mineralization. *Resour. Geol.* **62**, 63–83.

Carmichael I. S. E. (1991) The redox states of basic and silicic magmas: a reflection of their source regions? *Contrib. to Mineral. Petrol. 1991 1062* **106**, 129–141.

Černý P., Blevin P. L., Cuney M. and London D. (2005) Granite-Related ore deposits. *One Hundredth Anniv. Vol.*

Charnock J., Polya D., Gault A. and Wogelius R. (2007) Direct EXAFS evidence for incorporation of As^{5+} in the tetrahedral site of natural andraditic garnet. *Am. Mineral.* **92,** 1856-1861.

Charton P. and Armand P. (2003) Glasses in the TeO_2–$Sb2O_4$ binary system. *J. Non Cryst. Solids* **316,** 189-197.

Chavez Cabrera J. (2019) Redox state of the South Mountain Batholith: A reconnaissance study using zircon geochemistry. B.Sc. Thesis. Dalhousie University.

Chen, B., Ma, X., and Wang, Z. (2014). Origin of the fluorine-rich highly differentiated granites from the Qianlishan composite plutons (South China) and implications for polymetallic mineralization. *Asian J. Earth Sci.* **93**, 301-314.

Chen X., Zeng X. C., Wang J., Deng Y., Ma T., Guoji E., Mu Y., Yang Y., Li H. and Wang Y. (2017) Microbial communities involved in As mobilization and release from the deep sediments into groundwater in Jianghan plain, Central China. *Sci. Total Environ.* **579**, 989–999.

Cherniak D. J. (2000) Rare earth element diffusion in apatite. *Geochim. Cosmochim. Acta* **64**, 3871–3885.

Chew D. M. and Spikings R. A. (2015) Geochronology and thermochronology using apatite: time and temperature, lower crust to surface. *Elements* **11**, 189–194.

Clark K. (2022) Trace element geochemistry of biotite from the Scrag Lake and New Ross plutons of the South Mountain Batholith, Nova Scotia, Canada: Implications for magma differentiation. B.Sc. Thesis Dalhousie University.

Clarke D. B. (1995) Cordierite in felsic igneous rocks: a synthesis. *Mineral. Mag.* **59**, 311–325.

Clarke D. B., Erdmann S., Samson H. and Jamieson R. A. (2009) Contamination of the South Mountain Batholith by sulfides from the country rocks. *Can. Mineral.* **47**, 1159–1176.

Clarke D. B., Grujic D., McCuish K. L., Sykes J. C. P. and Tweedale F. M. (2013) Ring schlieren: Description and interpretation of field relations in the Halifax Pluton, South Mountain Batholith, Nova Scotia. *J. Struct. Geol.* **51**, 193–205.

Cooke D., Baker M., Hollings P., Sweet G. and Chang Z. (2014) New advances in detecting the distal geochemical footprints of porphyry systems—epidote mineral chemistry as a tool for vectoring and fertility assessments.

Craw D., Wilson N. and Ashley P. M. (2004) Geochemical controls on the environmental mobility of Sb and As at mesothermal Sb and gold deposits. *Appl. Earth Sci.* **113**, 3–10.

Dixit S. and Hering J. G. (2003) Comparison of As(V) and As(III) sorption onto iron oxide minerals: Implications for As mobility. *Environ. Sci. Technol.* **37**, 4182–4189.

D'Souza, R. J., & Canil, D. (2018). The partitioning of chalcophile elements between sediment melts and fluids at 3 GPa, 950–1050 C with implications for slab fluids in subduction zones. *Earth Planet. Sci. Lett*. **498**, 215-225.

Drage N. (2022) An experimental study of the effect of pressure on the formation of chromite deposits. M.Sc. Thesis Dalhousie University.

Dubois B., Videau J., Couzi M. and Portier J. (1986) Structural approach of the ($xPbCl_2$−(1−x) Sb_2O_3) glass system. *J. Non Cryst. Solids* **88,** 355-365.

Durandurdu M. (2016) Local structure of As_2O_3 glass from first principles simulations. *J. Non Cryst. Solids* **436,** 18-21.

Eggins S. M., Kinsley L. P. J. and Shelley J. M. G. (1998) Deposition and element fractionation processes during atmospheric pressure laser sampling for analysis by ICP-MS. *Appl. Surf. Sci.* **127–129**, 278–286.

Ellison A. and Sen S. (2003) Role of Sb^{3+} as a network-forming cation in oxide glasses. *Phys. Rev. B* **67,** 052203.

Erdmann S., Clarke D. B. and MacDonald M. A. (2004) Origin of chemically zoned and unzoned cordierites from the South Mountain and Musquodoboit Batholiths, Nova Scotia. *Spec. Pap. Geol. Soc. Am.* **389**, 99–110.

Fakhreddine S., Prommer H., Scanlon B. R., Ying S. C. and Nicot J. P. (2021) Mobilization of As and other naturally occurring contaminants during managed aquifer recharge: A critical review. *Environ. Sci. Technol.* **55**, 2208–2223.

Fawcett S. E., Gordon R. A. and Jamieson H. E. (2009) Optimizing experimental design, overcoming challenges, and gaining valuable information from the Sb K-edge XANES region. *Am. Mineral.* **94,** 1377-1387.

Feisel, Y., Castro, J.M., Helo, C., Dingwell, D.B. (2022) The effect of halogens (F, Cl) on the near-liquidus crystallinity of a hydrous trachyte melt. *Am. Mineral.* **107**, 1007-1017.

Ferguson J. F. and Gavis J. (1972) A review of the As cycle in natural waters. *Water Res.* **6,** 1259-1274.

Filella M., Belzile N. and Lett M. (2007) Antimony in the environment: a review focused on natural waters. III. Microbiota relevant interactions. *Earth-Sci. Rev*. **80,** 195-217.

Fisher B. E. and Poole J. C. (2006) *DP ME 043 Version 2, Digital version of Nova Scotia Department of Natural Resources Map ME 2000-1, geological map of the Province of Nova Scotia, scale 1:500 000.*, Halifax, Nova Scotia, Canada.

Foster A. L. and Kim C. S. (2014) Arsenic speciation in solids using x-ray absorption spectroscopy. *Rev. Mineral. Geochemistry* **79**, 257–369.

Fox D., Robinson C. and Zentilli M. (1997) Pyrrhotite and associated sulphides and their relationship to acid rock drainage in the Halifax Formation, Meguma Group, Nova Scotia. *Atl. Geol.* **33**, 87–103.

Franco D. F., Fares H., de Souza A. E., Santagneli S. H. and Nalin M. (2018) Glass formation in the Sb_2O_3-$SbPO_4$-WO_3 system. *Eclét. Quím. J.* **42,** 51-59.

Gao S., Luo T. C., Zhang B. R., Zhang H. F., Han Y. W., Zhao Z. D. and Hu Y. K. (1998) Chemical composition of the continental crust as revealed by studies in East China. *Geochim. Cosmochim. Acta* **62**, 1959–1975.

Gebel T. (1997) Arsenic and Sb: comparative approach on mechanistic toxicology. *Chem. Biol. Interact.* **107**, 131-144.

Gervilla F., Leblanc M., Torres-Ruiz J. and Fenoll Hach-Ali P. (1996) Immiscibility between arsenide and sulfide melts; a mechanism for concentration of noble metals. *Can. Mineral.* **34**, 485–502.

Ghiorso M. S. and Gualda G. A. R. (2015) An H2O–CO2 mixed fluid saturation model compatible with rhyolite-MELTS. *Contrib. to Mineral. Petrol.* **169**, 1–30.

Giordano D., Russell J. K. and Dingwell D. B. (2008) Viscosity of magmatic liquids: a model. *Earth Planet. Sci. Lett.* **271,** 123-134.

Goldschmidt V. M. (1954) *Geochemistry.*, LWW.

Grantham D. A. and Jones J. F. (1977) Arsenic contamination of water wells in Nova Scotia. *J. AWWA* **69**, 653–657.

Gualda G. A. R. and Ghiorso M. S. (2015) MELTS_Excel: A Microsoft Excel-based MELTS interface for research and teaching of magma properties and evolution. *Geochemistry, Geophys. Geosystems* **16**, 315–324.

Gualda G. A. R., Ghiorso M. S., Lemons R. V. and Carley T. L. (2012) Rhyolite-MELTS: A modified calibration of MELTS pptimized for silica-rich, fluid-bearing magmatic systems. *J. Petrol.* **53**, 875–890.

Guo H. and Audétat A. (2017) Transfer of volatiles and metals from mafic to felsic magmas in composite magma chambers: An experimental study. *Geochim. Cosmochim. Acta* **198**, 360–378.

Guo Q. (2008) Some aspects of As and Sb geochemistry in high temperature granitic melt-aqueous fluid system and in low temperature permeable reactive barrier-groundwater system. Ph.D. Thesis, University of Waterloo

Gustafasson J. . (2011) Visual MINTEQ – Visual MINTEQ – a free equilibrium speciation model. *KTH, Department of Land and Water Recources,* Stockholm, Sweden.

Hamilton W. C. (1965) Significance tests on the crystallographic R factor. *Acta Crystallogr.* **18,** 502-510.

Hanley J. J. (2007) The role of arsenide-rich melts and mineral phases in the development of high-grade Pt-Pd mineralization within komatiite-associated magmatic Ni-Cu sulfide horizons at Dundonald Beach South, Abitibi Subprovince, Ontario, Canada. *Econ. Geol.* **102**, 305–317.

Harlov D. E. and Förster H.-J. (2003) Fluid-induced nucleation of (Y+REE)-phosphate minerals within apatite: Nature and experiment. Part II. Fluorapatite. *Am. Mineral.* **88**, 1209–1229.

Harrison T. M. and Watson E. B. (1984) The behavior of apatite during crustal anatexis: Equilibrium and kinetic considerations. *Geochim. Cosmochim. Acta* **48**, 1467–1477.

Hart K. A., Kennedy G. W., Sterling S. M., Nakamura F., Negishi J. and Ishiyama N. (2021) Distribution, drivers, and threats of aluminum in groundwater in Nova Scotia, Canada. *Water 2021, Vol. 13, Page 1578* **13**, 1578.

Hattori K., Takahashi Y., Guillot S. and Johanson B. (2005) Occurrence of As (V) in forearc mantle serpentinites based on X-ray absorption spectroscopy study. *Geochim. Cosmochim. Acta* **69,** 5585-5596.

Hawthorne F. (1976) The hydrogen positions in scorodite. *Acta Crystallogr. B.* **32,** 2891-2892.

Health Canada (2020) Guidelines for Canadian drinking water quality summary table. https://www.canada.ca/en/health-canada/services/environmental-workplace-health/reports-publications/water-quality.html (accessed 25 Febuary 2022)

Helmy H. M., Ballhaus C., Fonseca R. O. C. and Nagel T. J. (2013) Fractionation of platinum, palladium, nickel, and copper in sulfide-arsenide systems at magmatic temperature. *Contrib. to Mineral. Petrol.* **166**, 1725–1737.

Henry D. J., Guidotti C. V and Thomson J. A. (2005) The Ti-saturation surface for low-to-medium pressure metapelitic biotites: Implications for geothermometry and Ti-substitution mechanisms. *Am. Mineral.* **90**, 316–328.

Hill E., Wood B. J. and Blundy J. D. (2000) The effect of Ca-Tschermaks component on trace element partitioning between clinopyroxene and silicate melt. *Lithos* **53,** 203-215.

Holycross, M. E., & Watson, E. B. (2018). Trace element diffusion and kinetic fractionation in wet rhyolitic melt. *Geochim. Cosmochim. Acta*, **232**, 14-29.

Holman I. P., Whelan M. J., Howden N. J. K., Bellamy P. H., Willby N. J., Rivas-Casado M. and McConvey P. (2008) Phosphorus in groundwater - An overlooked contributor to eutrophication? *Hydrol. Process.* **22**, 5121–5127.

Holtz F., Johannes W., Tamic N. and Behrens H. (2001) Maximum and minimum water contents of granitic melts generated in the crust: a reevaluation and implications. *Lithos* **56**, 1–14.

Hughes J. M. and Rakovan J. F. (2015) Structurally robust, chemically diverse: Apatite and apatite supergroup minerals. *Elements* **11**, 165–170.

Hughes M. F., Beck B. D., Chen Y., Lewis A. S. and Thomas D. J. (2011) Arsenic exposure and toxicology: A historical perspective. *Toxicol. Sci.* **123**, 305–332.

IARC Working Group on the Evaluation of Carcinogenic Risks to Humans (2012) *Arsenic, metals, fibres, and dusts. IARC monographs on the evaluation of carcinogenic risks to humans*.

Jain C. K. and Ali I. (2000) Arsenic: occurrence, toxicity and speciation techniques. *Water Res.* **34**, 4304–4312.

Janots E., Berger A. and Engi M. (2011) Physico-chemical control on the REE minerals in chloritoid-grade metasediments from a single outcrop (Central Alps, Switzerland). *Lithos* **121**, 1–11.

Jansen M. (1979) Die Kristallstruktur von Antimon (V)-oxid. *Acta Crystallogr. B* **35,** 539-542.

Jenner F. E. and O'Neill H. S. C. (2012) Analysis of 60 elements in 616 ocean floor basaltic glasses. *Geochemistry, Geophys. Geosystems* **13**, 2005.

Jochum K. P. and Hofmann A. W. (1997) Constraints on earth evolution from Sb in mantle-derived rocks. *Chem. Geol.* **139**, 39–49.

Jochum K. P., Weis U., Stoll B., Kuzmin D., Yang Q., Raczek I., Jacob D. E., Stracke A., Birbaum K., Frick D. A., Günther D. and Enzweiler J. (2011) Determination of Reference Values for NIST SRM 610–617 Glasses Following ISO Guidelines. *Geostand. Geoanalytical Res.* **35**, 397–429.

Jugo, P. J., Wilke, M., & Botcharnikov, R. E. (2010). Sulfur K-edge XANES analysis of natural and synthetic basaltic glasses: Implications for S speciation and S content as function of oxygen fugacity. *Geochim. Cosmochim. Acta* **74**, 5926-5938

Kennedy G. W. (2021) *A Manganese in Well Water Risk Map for Nova Scotia Open File Report ME 2021-002* ., Halifax.

Kennedy G. W., Drage J. M. and Scotia N. (2017) *An Arsenic in Well Water Risk Map for Nova Scotia based on Observed Patterns of Well Water Concentrations of Arsenic in Bedrock Aquifers Open File Report ME 2017-003*.,

Ketris M. P. and Yudovich Y. E. (2009) Estimations of Clarkes for Carbonaceous biolithes: World averages for trace element contents in black shales and coals. *Int. J. Coal Geol.* **78**, 135–148.

Kiseeva E. S. and Wood B. J. (2013) A simple model for chalcophile element partitioning between sulphide and silicate liquids with geochemical applications. *Earth Planet. Sci. Lett.* **383**, 68–81.

Kiseeva E. S. and Wood B. J. (2015) The effects of composition and temperature on chalcophile and lithophile element partitioning into magmatic sulphides. *Earth Planet. Sci. Lett.* **424**, 280–294.

Klemme S. and Dalpé C. (2003) Trace-element partitioning between apatite and carbonatite melt. *Am. Mineral.* **88**, 639–646.

Klemme S., Prowatke S., Hametner K. and Günther D. (2005) Partitioning of trace elements between rutile and silicate melts: Implications for subduction zones. *Geochim. Cosmochim. Acta* **69**, 2361–2371.

Konecke B. A., Fiege A., Simon A. C., Linsler S. and Holtz F. (2019) An experimental calibration of a sulfur-in-apatite oxybarometer for mafic systems. *Geochim. Cosmochim. Acta* **265**, 242–258.

Kontonikas-Charos A., Ehrig K., Cook N. J. and Ciobanu C. L. (2019) Crystal chemistry of titanite from the Roxby Downs Granite, South Australia: insights into petrogenesis, subsolidus evolution and hydrothermal alteration. *Contrib. to Mineral. Petrol.* **174**, 1–20.

Koudelka L., Šubčík J., Mošner P., Montagne L. and Delevoye L. (2007) Structure and properties of Sb_2O_3-containing zinc borophosphate glasses. *J. Non Cryst. Solids* **353,** 1828-1833.

Krishna S. B. M., Babu A. R., Ch R. S. and Rao D. K. (2010) Influence of molybdenum ions on the structure of $ZnO–As_2O_3–Sb_2O_3$ glass system by means of spectroscopic and dielectric studies. *J. Non Cryst. Solids* **356,** 1754-1761.

Lachassagne P., Dewandel B. and Wyns R. (2021) Review: Hydrogeology of weathered crystalline/hard-rock aquifers—guidelines for the operational survey and management of their groundwater resources. *Hydrogeol. J.* **29**, 2561–2594.

Li W., Chakraborty S., Nagashima K. and Costa F. (2020) Multicomponent diffusion of F, Cl and OH in apatite with application to magma ascent rates. *Earth Planet. Sci. Lett.* **550**, 116545.

Li Y. and Audétat A. (2015) Effects of temperature, silicate melt composition, and oxygen fugacity on the partitioning of V, Mn, Co, Ni, Cu, Zn, As, Mo, Ag, Sn, Sb, W, Au, Pb, and Bi between sulfide phases and silicate melt. *Geochim. Cosmochim. Acta* **162**, 25–45.

Li Y. and Audétat A. (2012) Partitioning of V, Mn, Co, Ni, Cu, Zn, As, Mo, Ag, Sn, Sb, W, Au, Pb, and Bi between sulfide phases and hydrous basanite melt at upper mantle conditions. *Earth Planet. Sci. Lett.* **355–356**, 327–340.

Liu W., Mei Y., Etschmann B., Brugger J., Pearce M., Ryan C. G., Borg S., Wykes J., Kappen P., Paterson D., Boesenberg U., Garrevoet J., Moorhead G. and Falkenberg G. (2017) Arsenic in hydrothermal apatite: Oxidation state, mechanism of uptake, and comparison between experiments and nature. *Geochim. Cosmochim. Acta* **196**, 144–159.

Lucacel R. C. and Ardelean I. (2006) Comparative structural investigation of B_2O_3-MO-CuO glasses (MO→ TeO_2 or As_2O_3) by FTIR and Raman spectroscopies. *J. Optoelectron. Adv. Mater.* **8,** 1124.

MacDonald M. A. (2001) *Geology of the South Mountain Batholith, Southwestern Nova Scotia*., Nova Scotia Natural Resources, Minerals and Energy Branch.

MacDonald M. A. and Clarke D. B. (1985) The petrology, geochemistry, and economic potential of the Musquodoboit Batholith, Nova Scotia. *Can. J. Earth Sci.* **22**, 1633–1642.

Maciag B. J. and Brenan J. M. (2020) Speciation of As and Sb in basaltic magmas. *Geochim. Cosmochim. Acta* **276**, 198–218.

Maier, W.D., Rasmussen, B., Fletcher, I.R., Godel, B., Barnes, S.J., Fisher, L.A., Yang, S.H., Huhma, H. and Lahaye, Y.(2015). Petrogenesis of the~ 2· 77 Ga Monts de Cristal Complex, Gabon: evidence for direct precipitation of Pt-arsenides from basaltic magma. *J. Petrol*. **56**, 1285-1308.

Majzlan J., Drahota P. and Filippi M. (2014) Parageneses and crystal chemistry of As minerals. *Rev. Mineral. Geochemistry* **79**, 17–184.

Mallmann G. and O'Neill H. S. C. (2007) The effect of oxygen fugacity on the partitioning of Re between crystals and silicate melt during mantle melting. *Geochim. Cosmochim. Acta* **71**, 2837–2857.

Manning, D.A.C. (1981). The Effect of Fluorine on Liquidus Phase Relationships in the System Qz-Ab-Or with Excess Water at 1 kb. *Contrib. to Mineral. Petrol*. **76**, 206 - 215.

Mao M., Rukhlov A. S., Rowins S. M., Spence J. and Coogan L. A. (2016) Apatite trace element compositions: A robust new tool for mineral exploration. *Econ. Geol.* **111**, 1187–1222.

Marks M. A. W., Wenzel T., Whitehouse M. J., Loose M., Zack T., Barth M., Worgard L., Krasz V., Eby G. N., Stosnach H. and Markl G. (2012) The volatile inventory (F, Cl, Br, S, C) of magmatic apatite: An integrated analytical approach. *Chem. Geol.* **291**, 241–255.

McDonough W. F. and Sun S. s. (1995) The composition of the Earth. *Chem. Geol.* **120**, 223–253.

McInnes, B. I., Gregoire, M., Binns, R. A., Herzig, P. M., & Hannington, M. D. (2001). Hydrous metasomatism of oceanic sub-arc mantle, Lihir, Papua New Guinea: petrology and geochemistry of fluid-metasomatised mantle wedge xenoliths. *Earth Planet. Sci. Lett*. **188**,169-183.

Miller L. A., O'Neill H. S. C., Berry A. J. and Glover C. J. (2019) The oxidation state and coordination environment of Sb in silicate glasses. *Chem. Geol.* **524**, 283–294.

Mukherjee A., von Brömssen M., Scanlon B. R., Bhattacharya P., Fryar A. E., Hasan M. A., Ahmed K. M., Chatterjee D., Jacks G. and Sracek O. (2008) Hydrogeochemical comparison and effects of overlapping redox zones on groundwater As near the Western (Bhagirathi sub-basin, India) and Eastern (Meghna sub-basin, Bangladesh) margins of the Bengal Basin. *J. Contam. Hydrol.* **99**, 31–48.

Mukherjee A., Gupta S., Coomar P., Fryar A. E., Guillot S., Verma S., Bhattacharya P., Bundschuh J. and Charlet L. (2019) Plate tectonics influence on geogenic As cycling: From primary sources to global groundwater enrichment. *Sci. Total Environ.* **683**, 793–807.

Nalin M., Messaddeq Y., Ribeiro S., Poulain M., Briois V., Brunklaus G., Rosenhahn C., Mosel B. and Eckert H. (2004) Structural organization and thermal properties of the Sb_2O_3–$SbPO_4$ glass system. *J. Mater. Chem.* **14,** 3398-3405.

National Research Council (1977a) Committee on Medical and Biological Effects of Environmental Pollutants, Arsenic. *National Academy of Sciences,* Washington DC

National Research Council (1977b) Arsenic: medical and biological effects of environmental pollutants.

Nathwani, C. L., Loader, M. A., Wilkinson, J. J., Buret, Y., Sievwright, R. H., & Hollings, P. (2020). Multi-stage arc magma evolution recorded by apatite in volcanic rocks. *Geology* **48**, 323-327.

Nearing M. M., Koch I. and Reimer K. J. (2014) Complementary As speciation methods: A review. *Spectrochim. Acta Part B At. Spectrosc.* **99**, 150–162.

Newville M. (2014) Fundamentals of XAFS. *Rev. Mineral. Geochemistry* **78**, 33–74.

Newville M. (2001) IFEFFIT: interactive XAFS analysis and FEFF fitting. *J. Synchrotron Radiat.* **8,** 322-324.

Nickson R. T., Mcarthur J. M., Ravenscroft P., Burgess W. G. and Ahmed K. M. (2000) Mechanism of As release to groundwater, Bangladesh and West Bengal. *Appl. Geochemistry* **15**, 403–413.

Noack C. W., Dzombak D. A. and Karamalidis A. K. (2014) Rare earth element distributions and trends in natural waters with a focus on groundwater. *Environ. Sci. Technol.* **48**, 4317–4326.

Nova Scotia Department of Natural Resources and Renewables (2021) *Nova Scotia Groundwater Atlas; Well water chemistry (available in part)*., Halifax, Nova Scotia.

O'Beirne-Ryan A. M. and Zentilli M. (2006) Weathering of Devonian monzogranites as recorded in the geochemistry of saprolites from the South Mountain Batholith, Nova Scotia, Canada. *Atl. Geol.* **42**, 153–159.

O'Neill H. S. C. (1988) Systems Fe-O and Cu-O; thermodynamic data for the equilibria Fe-"FeO," Fe-Fe_3O_4,"FeO"-Fe_3O_4, Fe_3O_4-Fe_2O_3, Cu-Cu_2O, and Cu_2O-CuO from emf measurements. *Am. Mineral.* **73**, 470-486.

O’Neill H. S. C. (1987) Quartz-fayalite-iron and quartz-fayalite-magnetite equilibria and the free energy of formation of fayalite (Fe2SiO4) and magnetite (Fe3O4). *Am. Mineral.* **72**, 67–75.

O'Neill H. S. C. (1986) Mo-MoO_2 (MOM) oxygen buffer and the free energy of formation of MoO_2. *Am. Mineral.* **71**, 1007-1010.

O'Neill H. S. C. and Pownceby M. I. (1993a) Thermodynamic data from redox reactions at high temperatures. I. An experimental and theoretical assessment of the electrochemical method using stabilized zirconia electrolytes, with revised values for the Fe-“FeO”, Co-CoO, Ni-NiO and Cu-Cu_2O oxygen buffers, and new data for the W-WO_2 buffer. *Contrib. Miner. and Petrol.* **114,** 296-314.

O'Neill H. S. C. and Pownceby M. I. (1993b) Thermodynamic data from redox reactions at high temperatures. II. The MnO-Mn_3O_4 oxygen buffer, and implications for the thermodynamic properties of MnO and Mn_3O_4. *Contrib. Miner. and Petrol.* **114**, 315-320.

O’Shea B., Stransky M., Leitheiser S., Brock P., Marvinney R. G. and Zheng Y. (2015) Heterogeneous As enrichment in meta-sedimentary rocks in central Maine, United States. *Sci. Total Environ.* **505**, 1308–1319.

Ogiermann J. C. (2002) Cordierite and its retrograde breakdown products as monitors of fluid-rock interaction during retrograde path metamorphism : case studies in the Schwarzwald and the Bayerische Wald (Variscan belt, Germany). Ph.D. Thesis.University of Heidelberg.

Ohtsuka T., Yamaguchi N., Makino T., Sakurai K., Kimura K., Kudo K., Homma E., Dong D. T. and Amachi S. (2013) Arsenic dissolution from Japanese paddy soil by a dissimilatory arsenate-reducing bacterium geobacter sp. OR-1. *Environ. Sci. Technol.* **47**, 6263–6271.

Onishi H. (1969) Chapter 33: Arsenic. Wedepohl, KH, Handbook of Geochemistry.

Orman R. G. (2010) Characterisation of novel Sb (III) oxide-containing glasses. Ph.D. thesis, University of Warwick.

Pacey A., Wilkinson J. J. and Cooke D. R. (2020) Chlorite and epidote mineral chemistry in porphyry ore systems: A case study of the Northparkes District, New South Wales, Australia. *Econ. Geol.* **115**, 701–727.

Palandri J. and Kharaka Y. (2004) A compilation of rate parameters of water-mineral interaction kinetics for application to geochemical modeling. OPEN REPORT 2004-1068. U.S. Geological Survey.

Palme H. and O’Neill H. S. C. (2003) 3.1 Cosmochemical estimates of mantle composition. *Treatise on geochemistry* **2**, 1–38.

Pan Y. and Fleet M. E. (2002) Compositions of the apatite-group minerals: Substitution mechanisms and controlling factors. *Phosphates Geochemical, Geobiol. Mater. Importance* **48**, 13–50.

Papageorgiou F., McDermott F. and Van Acken D. (2022) Uranium in groundwaters: Insights from the Leinster granite, SE Ireland. *Appl. Geochemistry* **139**, 105236.

Papatheodorou G. and Solin S. (1976) Vibrational excitations of As_2O_3. I. Disordered phases. *Phys. Rev. B* **13,** 1741.

Parkinson, I. J., & Arculus, R. J. (1999). The redox state of subduction zones: insights from arc-peridotites. *Chem. Geo.* **160**, 409-423.

Patiño Douce A. E. and Roden M. (2006) Apatite as a probe of halogen and water fugacities in the terrestrial planets. *Geochim. Cosmochim. Acta* **70**, 3173–3196.

Paton C., Hellstrom J., Paul B., Woodhead J. and Hergt J. (2011) Iolite: Freeware for the visualisation and processing of mass spectrometric data. *J. Anal. At. Spectrom.* **26**, 2508–2518.

Piccoli P. and Candela P. (1994) Apatite in felsic rocks; a model for the estimation of initial halogen concentrations in the Bishop Tuff (Long Valley) and Tuolumne Intrusive Suite (Sierra Nevada Batholith) magmas. *Am. J. Sci.* **294**, 92–135.

Pichavant, M., Montel, J. M., & Richard, L. R. (1992). Apatite solubility in peraluminous liquids: Experimental data and an extension of the Harrison-Watson model. *Geochim. Cosmochim. Acta* **56**, 3855-3861.

Pichavant, M., Villaros, A., Deveaud, S., Scaillet, B., and Lahlafi, M. (2016). The influence of redox state on mica crystallization in leucogranitic and pegmatitic liquids. *Can. Mineral.* **54**, 559-581

Piña R., Gervilla F., Barnes S. J., Ortega L. and Lunar R. (2015) Liquid immiscibility between arsenide and sulfide melts: evidence from a LA-ICP-MS study in magmatic deposits at Serranía de Ronda (Spain). *Miner. Depos.* **50**, 265–279.

Pokrovski G. S., Borisova A. Y. and Bychkov A. Y. (2013) Speciation and Transport of Metals and Metalloids in Geological Vapors. *Rev. Mineral. Geochemistry* **76**, 165–218.

Pokrovski G. S., Borisova A. Y., Roux J., Hazemann J. L., Petdang A., Tella M. and Testemale D. (2006) Antimony speciation in saline hydrothermal fluids: A combined X-ray absorption fine structure spectroscopy and solubility study. *Geochim. Cosmochim. Acta* **70,** 4196-4214.

Pokrovski, G. S., Zakirov, I. V., Roux, J., Testemale, D., Hazemann, J. L., Bychkov, A. Y., and Golikova, G. V. (2002) Experimental study of As speciation in vapor phase to 500°C: Implications for As transport and fractionation in low-density crustal fluids and volcanic gases. *Geochim. Cosmochim. Acta* **70,** 3453-3480.

Pownceby M. I. and O'Neill H. S. C. (1994a) Thermodynamic data from redox reactions at high temperatures. III. Activity-composition relations in Ni-Pd alloys from EMF measurements at 850–1250 K, and calibration of the NiO+ Ni-Pd assemblage as a redox sensor. *Contrib. Miner. and Petrol.* **116,** 327-339.

Pownceby M. I. and O'Neill H. S. C. (1994b) Thermodynamic data from redox reactions at high temperatures. IV. Calibration of the Re-ReO_2 oxygen buffer from EMF and NiO Ni-Pd redox sensor measurements. *Contrib. Miner. and Petrol.* **118,** 130-137.

Prowatke S. and Klemme S. (2006) Trace element partitioning between apatite and silicate melts. *Geochim. Cosmochim. Acta* **70**, 4513–4527.

Pyare R. and Nath P. (1991) Free oxygen ion activity in binary alkali silicate glasses. *J. Non. Cryst. Solids* **128**, 154–161.

R Core Team (2013) R: A language and environment for statistical computing.

R Studio (2018) Integrated development environment. *saddlebrookcontrols.com*

Railsback L. B. (2003) An earth scientist's periodic table of the elements and their ions. *Geology* **31**, 737–740.

Ravel B. and Newville M. (2005) ATHENA, ARTEMIS, HEPHAESTUS: data analysis for X-ray absorption spectroscopy using IFEFFIT. **12**, 537–541.

Ravenscroft P., Brammer H. and Richards K. (2011) *Arsenic pollution: a global synthesis*., John Wiley & Sons.

Righter K., Humayun M., Campbell A. J., Danielson L., Hill D. and Drake M. J. (2009) Experimental studies of metal–silicate partitioning of Sb: Implications for the terrestrial and lunar mantles. *Geochim. Cosmochim. Acta* **73**, 1487–1504.

Roeder P. L. and Reynolds I. (1991) Crystallization of chromite and chromium solubility in basaltic melts. *J. Petrol.* **32**, 909-934

Rubatto D. and Hermann J. (2007) Experimental zircon/melt and zircon/garnet trace element partitioning and implications for the geochronology of crustal rocks. *Chem. Geol.* **241**, 38–61.

Rudnick R. L. and Gao S. (2003) Composition of the continental rust. *Treatise on Geochemistry* **3–9**, 1–64.

Sacerdoti M., Parodi G. C., Mottana A., Maras A. and Ventura G. D. (1993) Asbecasite: crystal structure refinement and crystal chemistry. *Mineral. Mag.* **57,** 315-322.

Saint-Jacques N., Parker L., Brown P. and Dummer T. J. (2014) Arsenic in drinking water and urinary tract cancers: A systematic review of 30 years of epidemiological evidence. *Environ. Heal. A Glob. Access Sci. Source* **13**.

Schenk P. E. (1997) Sequence stratigraphy and proveance on Gondwana's margin: The Meguma Zone (Cambrian to Devonian) of Nova Scotia, Canada. *Geol. Soc. Am. Bull.* **109**, 395–409.

Schiferl D., Cromer D. and Jamieson J. (1981) Structure determinations on Sb up to 85×10^2 MPa. *Acta Crystallogr. B* **37,** 807-810.

Schreiber H. D. and Coolbaugh T. M. (1995) Solvations of redox ions in glass-forming silicate melts. *J. Non. Cryst. Solids* **181**, 225–230.

Seddique A. A., Masuda H., Mitamura M., Shinoda K., Yamanaka T., Itai T., Maruoka T., Uesugi K., Ahmed K. M. and Biswas D. K. (2008) Arsenic release from biotite into a Holocene groundwater aquifer in Bangladesh. *Appl. Geochemistry* **23**, 2236–2248.

Sha L. K. and Chappell B. W. (1999) Apatite chemical composition, determined by electron microprobe and laser-ablation inductively coupled plasma mass spectrometry, as a probe into granite petrogenesis. *Geochim. Cosmochim. Acta* **63**, 3861–3881.

Shamsudduha M., Uddin A., Saunders J. A. and Lee M. K. (2008) Quaternary stratigraphy, sediment characteristics and geochemistry of As-contaminated alluvial aquifers in the Ganges-Brahmaputra floodplain in central Bangladesh. *J. Contam. Hydrol.* **99**, 112–136.

Shannon R. D. (1976) Revised effective ionic radii and systematic studies of interatomic distances in halides and chalcogenides. *Acta Crystallogr. A* **32**, 767.

Shellnutt J. G., Owen J. V., Yeh M. W., Dostal J. and Nguyen D. T. (2019) Long-lived association between Avalonia and the Meguma terrane deduced from zircon geochronology of metasedimentary granulites. *Sci. Reports 2019 91* **9**, 1–11.

Shi M., Liang Y., Chai L., Min X., Zhao Z. and Yang S. (2015) Raman and FTIR spectra of modified iron phosphate glasses containing As. *J. Mol. Struct.* **1081,** 389-394.

Shi Xun, Ayotte Joseph D, Onda Akikazu, Miller S., Rees Judy, Gilbert-Diamond Diane, Onega Tracy, Gui Jiang, Karagas Margaret, Moeschler John, Shi X, Onda Á. A., Onda A, Ayotte J D, Miller Á Rees Á D Gilbert-Diamond Á T Onega Á J Gui Á M Karagas Á J Moeschler S. J., Rees J, Gilbert-Diamond D, Onega T, Gui J, Karagas M and Moeschler J (2015) Geospatial association between adverse birth outcomes and As in groundwater in New Hampshire, USA. *Springer* **37**, 333–351.

Shukla D. P., Dubey C. S., Singh N. P., Tajbakhsh M. and Chaudhry M. (2010) Sources and controls of As contamination in groundwater of Rajnandgaon and Kanker District, Chattisgarh Central India. *J. Hydrol.* **395**, 49–66.

Siebert J., Corgne A. and Ryerson F. J. (2011) Systematics of metal–silicate partitioning for many siderophile elements applied to Earth's core formation. *Geochim. Cosmochim. Acta* **75**, 1451–1489.

Simon A. C., Pettke T., Candela P. A., Piccoli P. M. and Heinrich C. A. (2007) The partitioning behavior of As and Au in S-free and S-bearing magmatic assemblages. *Geochim. Cosmochim. Acta* **71**, 1764–1782.

Smedley P. L. and Kinniburgh D. G. (2002) A review of the source, behaviour and distribution of As in natural waters. *Appl. Geochemistry* **17**, 517–568.

Soignard E., Amin S. A., Mei Q., Benmore C. J. and Yarger J. L. (2008) High-pressure behavior of As2 O3: Amorphous-amorphous and crystalline-amorphous transitions. *Phys. Rev. B - Condens. Matter Mater. Phys.* **77**, 144113.

Spiegel C., Siebel W., Frisch W. and Berner Z. (2002) Nd and Sr isotopic ratios and trace element geochemistry of epidote from the Swiss Molasse Basin as provenance indicators: implications for the reconstruction of the exhumation history of the Central Alps. *Chem. Geol.* **189**, 231–250.

Sri M. M., Murthy S., Madhukar M., Murthy B. M. S. and Udayashankara T. H. (2016) Article in Nature Environment and Pollution Technology. **15**, 971–979.

Staněk M. and Géraud Y. (2019) Granite microporosity changes due to fracturing and alteration: Secondary mineral phases as proxies for porosity and permeability estimation. *Solid Earth* **10**, 251–274.

Steiner, J. C., Jahns, R. H., & Luth, W. C. (1975). Crystallization of alkali feldspar and quartz in the haplogranite system $NaAlSi_3O_8$–$KAlSi_3O_8$–SiO_2–H_2O at 4 kb. *Geol. Soc. Am. Bull*, **86**, 83-98.

Stepanov A. S., Hermann J., Rubatto D. and Rapp R. P. (2012) Experimental study of monazite/melt partitioning with implications for the REE, Th and U geochemistry of crustal rocks. *Chem. Geol.* **300–301**, 200–220.

Stern C. R. and Wyllie P. J. (1973) Water-saturated and undersaturated melting relations of a granite to 35 kilobars. *Earth Planet. Sci. Lett.* **18**, 163–167.

Stoeppler M. (1992) *Hazardous metals in the environment*., Elsevier.

Tate M. C. (1994) The nature and origin of enclaves in four peraluminous granitoid intrusions from the Meguma Zone, Nova Scotia. *Atl. Geol.* **30**, 205–215.

Taylor J. R., Wall V. J. and Pownceby M. I. (1992) The calibration and application of accurate redox sensors. *Am. Mineral.* **77**, 284-295.

Teiber H., Marks M. A. W., Arzamastsev A. A., Wenzel T. and Markl G. (2015) Compositional variation in apatite from various host rocks: Clues with regards to source composition and crystallization conditions. *Neues Jahrb. fur Mineral. Abhandlungen* **192**, 151–167.

Tella M. and Pokrovski G. S. (2012) Stability and structure of pentavalent Sb complexes with aqueous organic ligands. *Chem.Geol.* **292**, 57-68.

Tella M. and Pokrovski G. S. (2009) Antimony (III) complexing with O-bearing organic ligands in aqueous solution: an X-ray absorption fine structure spectroscopy and solubility study. *Geochim. Cosmochim. Acta* **73,** 268-290.

Terashima K., Hashimoto T., Uchino T., Kim S. and Yoko T. (1996) Structure and nonlinear optical properties of Sb_2O_3-B_2O_3 binary glasses. *J. Ceram. Soc. Jpn.* **104,** 1008-1014.

Testemale D., Pokrovski G. S. and Hazemann. J. L. (2011) Speciation of AsIII and AsV in hydrothermal fluids by in situ X-ray absorption spectroscopy. *Eur. J. Mineral.* **23**, 379-390.

Tice P. E. (2010) Petrology and geochemical evolution of the East Hill Suite of the Mont Saint-Hilaire alkaline plutonic Complex. Ph.D. Thesis. University of New Orleans.

Tollari N., Toplis M. J. and Barnes S. J. (2006) Predicting phosphate saturation in silicate magmas: An experimental study of the effects of melt composition and temperature. *Geochim. Cosmochim. Acta* **70**, 1518–1536.

Tromans D. (2006) Solubility of crystalline and metamict zircon: A thermodynamic analysis. *J. Nucl. Mater.* **357**, 221–233.

Tuttle, O. F., & Bowen, N. L. (1958). Origin of granite in the light of experimental studies in the system $NaAlSi_3O_8$–$KAlSi_3O_8$–SiO_2–H_2O. *Mem. Geol. Soc. Amer*. **74**

Vigneresse J. L., Barbey P. and Cuney M. (1996) Rheological transitions during partial melting and crystallization with application to felsic magma segregation and transfer. *J. Petrol.* **37**, 1579–1600.

Vigneresse J. L. and Tikoff B. (1999) Strain partitioning during partial melting and crystallizing felsic magmas. *Tectonophysics* **312**, 117–132.

Wang L.-X., Marks M. A. W., Wenzel T., Von Der Handt A., Keller J., Teiber H. and Markl G. (2014) Apatites from the Kaiserstuhl Volcanic Complex, Germany: new constraints on the relationship between carbonatite and associated silicate rocks. *Eur. J. Mineral.* **26**, 397–414.

Wargon J. (1987) Acid mine drainage in reactive slates,"The Halifax International Airport Case". Transport Canada Perspective. In *Proceedings, Acid Mine Drainage Seminar/Workshop* pp. 127–135.

Webster J. D. and Piccoli P. M. (2015) Magmatic Apatite: A Powerful, Yet Deceptive, Mineral. *Elements* **11**, 177–182.

Whalen J. B. and Chappell B. W. (1988) Opaque mineralogy and mafic mineral chemistry of I-and S-type granites of the Lachlan fold belt. southeast Australia*. *Am. Mineral.* **73**, 281–296.

White C. E. (2010) Compilation of geochemical and petrographic data from the western and southern parts of the Goldenville and Halifax groups., Nova Scotia.: *Nova Scotia Natural Resources, Mineral Resources Branch, Open File Report ME*, *1*(9)

White C. and Goodwin T. (2011) Lithogeochemistry, petrology, and the acid-generating potential of the Goldenville and Halifax groups and associated granitoid rocks in metropolitan Halifax Regional Municipality, Nova Scotia, Canada. *Atl. Geol.* **47**, 158–184.

Winship K. A. (1987) Toxicity of Sb and its compounds. *Adv. Drug React. Ac. Pois. Rev.* **6,** 67-90.

Wolf M. B. and London D. (1994) Apatite dissolution into peraluminous haplogranitic melts: An experimental study of solubilities and mechanisms. *Geochim. Cosmochim. Acta* **58**, 4127–4145.

Woodhead J. D., Hellstrom J., Hergt J. M., Greig A. and Maas R. (2007) Isotopic and elemental imaging of geological materials by laser ablation inductively coupled plasma-mass spectrometry. *Geostand. Geoanalytical Res.* **31**, 331–343.

Wood, B. J., & Virgo, D. (1989). Upper mantle oxidation state: Ferric iron contents of Iherzolite spinels by 57Fe Mössbauer spectroscopy and resultant oxygen fugacities. *Geochim. Cosmochim. Acta*, **53**, 1277-1291.

Wood J. G., Prabakar S., Mueller K. T. and Pantano C. G. (2004) The effects of Sb oxide on the structure of alkaline-earth alumino borosilicate glasses. *J. Non Cryst. Solids* **349,** 276-284.

World Health Organization (2008) *Guidelines for drinking-water quality.*, Geneva.

World Health Organization (2006) *Guidelines for drinking-water quality (third ed.), incorporating first addendum Volume 1 - Recommendations*. World Health Organization Press, Geneva.

Wyckoff R. (1963), *Crystal Structures Vol.1.* Interscience Publishers, New York

Zack T., Kronz A., Foley S. F. and Rivers T. (2002) Trace element abundances in rutiles from eclogites and associated garnet mica schists. *Chem. Geol.* **184,** 97-122.

Zajacz Z., Halter W. E., Pettke T. and Guillong M. (2008) Determination of fluid/melt partition coefficients by LA-ICPMS analysis of co-existing fluid and silicate melt inclusions: Controls on element partitioning. *Geochim. Cosmochim. Acta* **72**, 2169–2197.

Zhao Z. W., Chai L. Y., Peng B., Liang Y. J., He Y. and Yan Z. H. (2017) Arsenic vitrification by copper slag based glass: Mechanism and stability studies. *J. Non Cryst. Solids* **466,** 21-28.